Accelerating the Deployment of Oxy-Fuel Combustion Technology for Victorian Brown Coal

Dr Lian Zhang

Department of Chemical Engineering,

Monash University, Clayton,

Vic 3800, Australia

Tel: 61-3-9905-2592, Fax: 61-3-9905-5686

Email: lian.zhang@monash.edu

July 15, 2017

Disclaimer

Copyright

Acknowledgement

The authors are grateful to Australian National Low Emission Coal (ANLEC) R&D and Brown Coal Innovation Australia (BCIA) for financial support. The project partners including Shanghai Boiler Works Co Ltd, Chubu University, and Shanghai Jiao Tong University are acknowledged for their support and collaboration throughout the project. The Shanghai University of Electric Power, Chubu University Japan, and Huazhong University of Science and Technology are also thanked for on-site flue gas analysis.

Contents

Chapter 1 Investigation on sulphur emission during air- and oxy-firing of Victorian brown coal

1.1 Sulphur emission during pyrolysis

Since pyrolysis is the first step regarding the emission of sulfur, four coal samples have been tested for sulphur emission mechanism during pyrolysis, including two air-dried Victorian brown coal sample (A, B), Kailuan brown coal and Kailuan black coal as reference. The proximate and ultimate analyses of these coals are shown in ***Table 1.1***. The overall ash content in the two Victorian brown coals is similar, ranging from 1.65 to 2.35 ar-wt%. The total sulphur content shows a large variation from 0.50 ar-wt% in coal A to 0.80 ar-wt% in coal B.

Table1.1 Properties of coal samples in sulphur emission experiments

	Vic brown coal -A	Vic brown coal-B	Kailuan brown coal	Kailuan black coal
Proximate analysis, ar				
Ash	1.65	2.35	17.1	35
Volatile Matter	44.95	42.55	38.7	25.2
Fixed Carbon	41.40	42.10	44.2	39.8
Moisture	12.00	13.00	26.7	3.3
ultimate analysis, ar				
C	65.70	69.30	59.8	50.3
H	6.80	7.00	3.80	3.4
O	12.15	6.85	18.06	9.75
N	0.60	0.60	0.77	0.84
S	0.50	0.80	0.47	0.71
Cl	0.60	0.10	-	-

Coal pyrolysis was carried out in a lab-scale drop-tube furnace. And the experimental conditions are tabulated in ***Table 1.2***. Through this mild pyrolysis period, char particle was collected. The char achieved was sieved into four sizes: >153 μm, 106-153 μm, 63-105 μm and <63 μm, as used for testing the influence of particle size on sulphur distribution in char.

Table 1.2 Experimental cases of coal pyrolysis

Experimental cases	
furnace temperature	400^{o}C, 800^{o}C, 1000^{o}C
coal feeding rate	0.5 g/min
gas rate	Pure nitrogen, 10L/min
Particle residence time in DTF	2 s

For the major metals including Al, Fe, Ca, Mg, Na and K, they were measured by inductively coupled plasma optical emission spectroscopy (ICP-OES, Optima 7000 DV Series, Perkin Elmer). And total sulphur content in samples was measured by XRF. The sulphur K-edge XANES spectra were tested at Synchrotron Radiation Research Centre, Taiwan, for the coal and char samples. The acquired S K-edge spectra were subjected to self-absorption correction function in ATHENA software to quantify the distribution of sulphur components in coal and char samples, including inorganic sulphur (mono- and poly-Sulphides, e.g. FeS, $Fe_{1-x}S$, FeS_2), organic sulphur (e.g. thiophene) and sulphate. Each spectrum measured is principally composed of one large and sharp peak located at ~ +1.0 eV, one minor peak at +3.0 eV, and another large but broad peak at +9.0 eV. The three peaks are indicative of the prevalence of sulphide, thiophene and sulphate. The experimental results, e.g. total sulphur content and sulphur forms, are summarized in ***Table1.3***.

Table 1.3 Percentages for different forms of sulphur in raw coal and char samples derived through pyrolysis

	Total S content in as-received raw coal sample, wt%	Sulphur Forms, %		
		mono or poly-Sulphide	Thiophene	Sulphate
Vic brown coal-A				
raw coal	0.38	42	36	22
400ºC char	0.29	15	64	21
800ºC char	0.10	0	54	46
1000ºC char	0.10	30	57	13
Vic brown Coal-B				
raw coal	0.66	10	88	2
800ºC char	0.23	15	50	35
1000ºC char	0.09	23	64	13
Kailuan brown coal				
raw coal	0.47	10	52.1	46.9
1000ºC char	0.37	0	52	48
Kailuan black coal				
raw coal	0.72	28.9	60.1	11
1000ºC char	0.502	39.4	46.8	13.8

Table 1.4 demonstrated the variation of sulphur content and speciation on account of coal particle size, as verified the insignificant variation and an even distribution of sulphur entities in the Victorian brown coal.

Table 1.4 Percentages for different forms of sulphur with respect to coal particle size for raw Victorian brown coals, A and B.

	Total S content in as-received raw coal sample, wt%	Sulphur Forms, %		
		mono or poly-Sulphide	Thiophene	Sulphate
Vic brown Coal A				
<53 *μm*	0.37	20	56	24
106-153 *μm*	0.38	28	36	22
153-300 *μm*	0.32	28	61	11
300-600 *μm*	0.30	20	63	17
Vic brown Coal B				
106-153 *μm*	0.66	10	88	2
153-300 *μm*	0.77	28	72	0

Figure 1.1 illustrates the changes on individual sulphur content in raw coal and yielded chars, as derived from K-edge spectra of samples and fitting calculation by ATHENA. For coal A in panel (a), its pyrolysis at 400^{o}C led to the removal of approximately half of the sulphidic sulphur, whereas the thiophenic sulphur remained rather constant, and the sulphate-like structure was even slightly increased. Increasing the pyrolysis temperature to 800oC resulted in a substantial reduction of the total S content from 0.38 wt% to 0.1 wt% in the resulting char, owing to the disappearance of sulphidic sulphur and the removal of a large quantity of thiophene sulphur. The total sulphur content in 1000^{o}C char was similar with that of 800oC char, for Victorian brown coal A. However, the total sulphur content of other 1000oC chars are decreased further, compared to the 800^{o}C char, shown in panel (b). Regarding 1000^{o}C chars, the fraction of thiophene in the residues is predominant. Panel (c) (d) shows the similar trend of sulphur evolution for Kailuan brown coal and black coal.

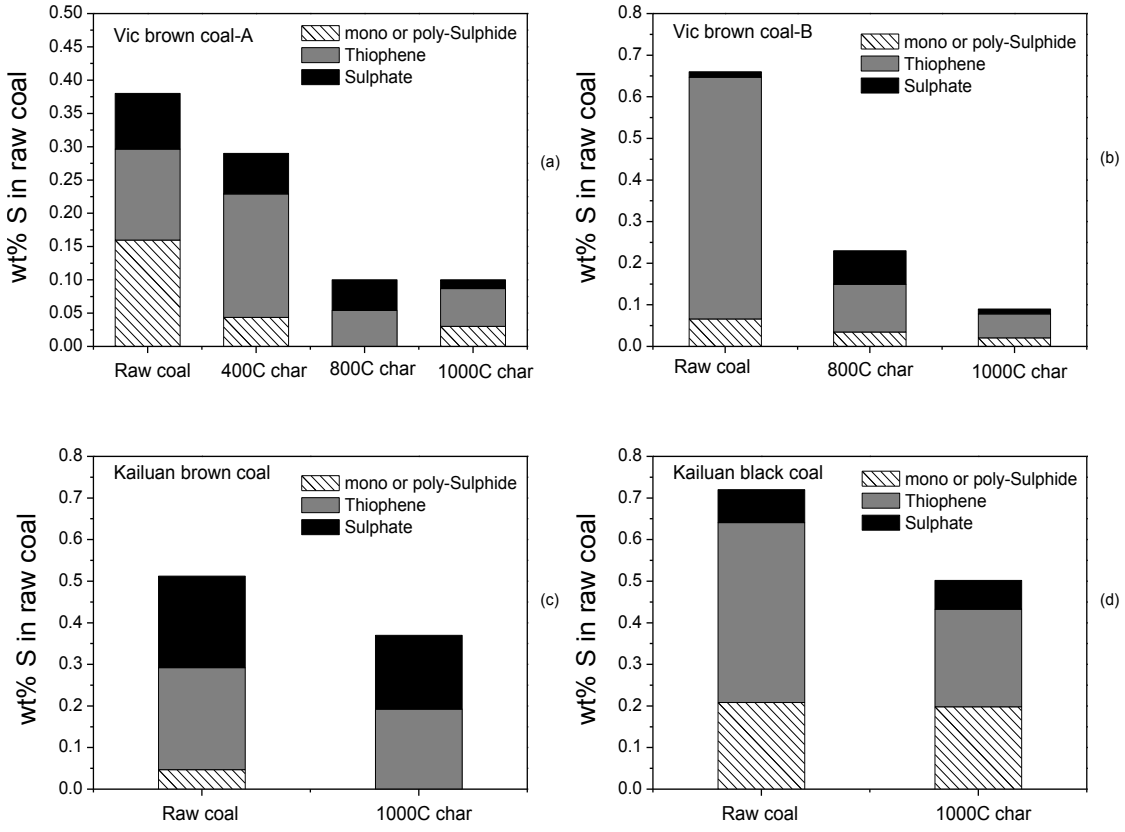

Figure 1.1 Sulphur contents in raw coal and derived chars upon pyrolysis at varying temperature. (a) Victorian brown coal A; (b) Victorian brown coal B, (c) Kailuan brown coal, (d) Kailuan black coal.

Figure1.2 shows the influence of furnace temperature on the released sulphur percentage in raw coal. It witnesses that most sulphur was released during pyrolysis for Victorian brown coal, about 78-85% sulphur emission from the residual char at 1000°C. However, only 20-30wt% of sulphur was emitted from Kailuan brown coal and black coal, which is due to the lower pyrolysis kinetics for these two coals than Victorian brown coal.

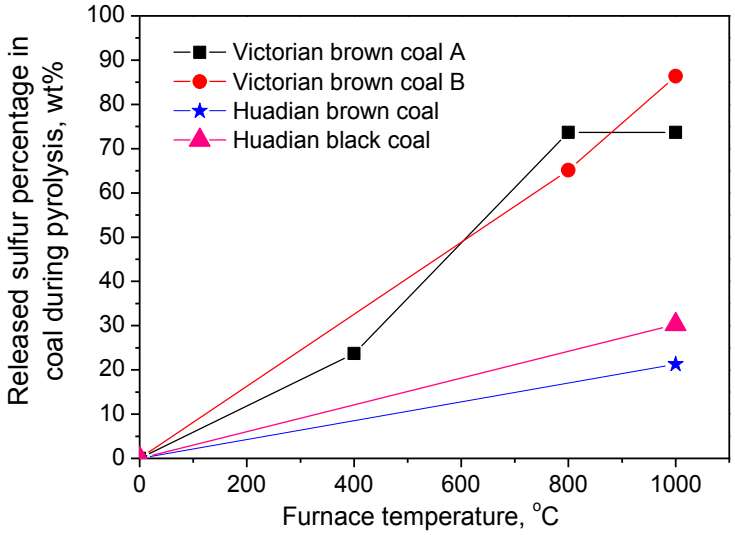

Figure 1.2 Influence of pyrolysis temperature on released sulphur percentage in coal

1.2. Sulphur emission during char oxidation during air- versus oxy-firing

Char oxidation experiments in DTF were conducted by varying a number of parameters in ***Table 1.5***. Here 1000°C chars yielded from Victorian brown coal B (Loy Yang) were examined.

Table 1.5 Experiments of sulphur emission during char oxidation

Experimental cases	Details
furnace temperature	1000°C
coal feeding rate	0.5 g/min
gas rate	10L/min, 0-5 vol% O_2 in N_2 versus CO_2
Particle residence time in DTF	2s, 4s, 6s
Particle size	63-105 μm versus 106-153 μm

Table 1.6 Total sulphur content and percentages for different forms of sulphur with respect to coal particle size for 1000°C char samples derived from Victorian brown B.

Samples	size, μm	S in air-dried coal, wt%	sulphide	Thiophene	Sulfate
Raw coal	105-153	0.66	10	88	2
Char	<63	0.104	15	71.3	13.7
Char	63-105	0.086	12.8	65.3	21.9
Char	106-153	0.090	16.2	72.7	11.1
Char	>153	0.099	5.2	61.2	33.6

The char samples were sieved into four sizes: >153 μm, 106-153 μm, 63-105 μm and <63 μm. As shown in ***Table 1.6***, there is an even distribution of sulphur total content and entities in the different size particles.

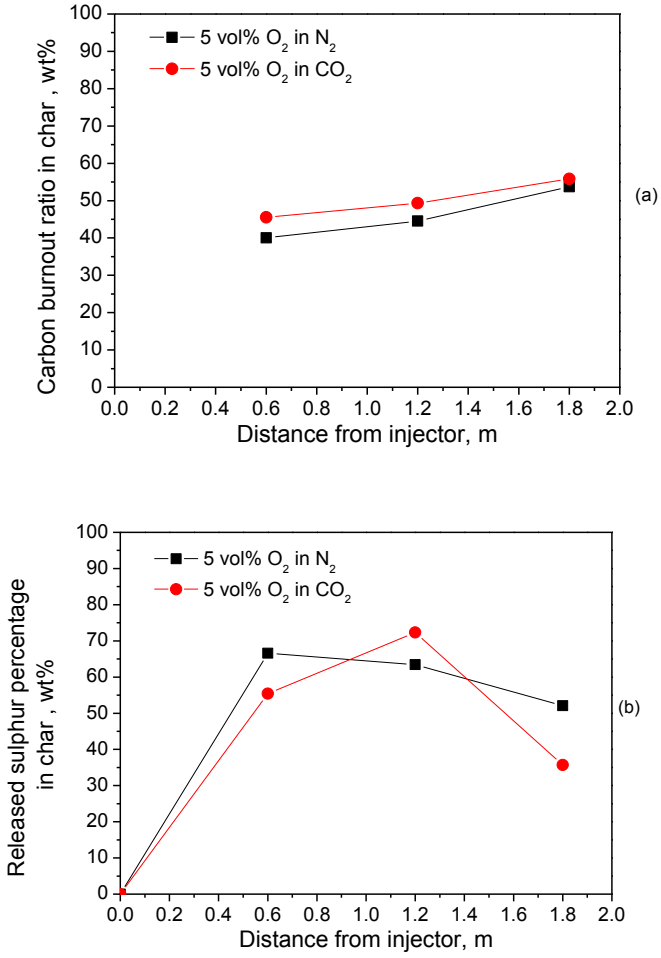

Figure 1.3 Carbon burnout ratio (a) and released sulphur percentage in char (b) during Victorian brown char combustion in O_2/N_2 and O_2/CO_2

Figure 1.3 shows the carbon burnout ratio and sulphur emission percentage in char samples versus particle motion distance upon the combustion of char in 5% O_2 diluted by N_2 versus CO_2. Within 0.6 m away from injector inlet, all the volatile matter remaining in char were burnt out, with a burnout ratio ~40-45wt%. The carbon burnout ratio is increased slowly over time. The sulphur emission was maximized at the height of 0.6-1.2 m. After it, the vaporised sulphur vapor was partly captured back into solid phase. It was found 40-60 wt% sulphur remained in char at the furnace exit.

Based on sulphur XANES analysis, sulphur content in char samples was plotted as a function of particle motion distance, shown in ***Figure 1.4***. Thiophene is still the largest fraction for sulphur remained in the unburnt residues after char combustion. After a decrease of total sulphur extent in the first stage, the total sulphur content and thiophene were subsequently increased in the second stage. This is a re-capture of its vaporized species via oxidation into solid residue. More sulphate was formed in CO_2 rather than in N_2, comparing panel (a) and (b).

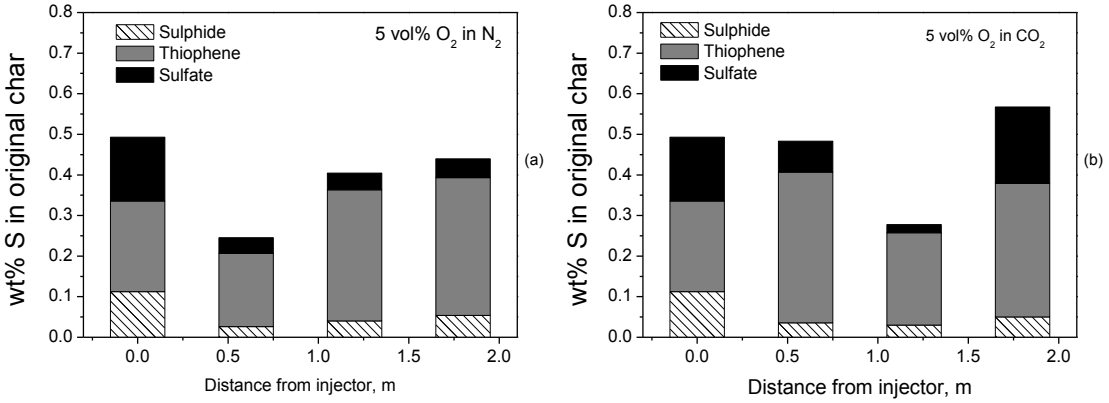

Figure 1.4 Sulphur contents in chars upon combustion in air-firing and oxy-firing mode. (a) 5vol% O_2 in N_2; (b) 5 vol% in CO_2.

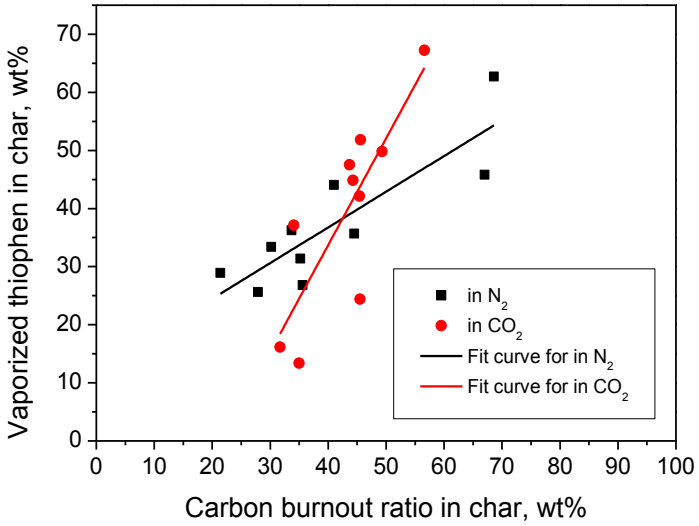

Figure 1.5 Vaporized thiophene in chars versus carbon burnout ratio

For both O_2/N_2 and O_2/CO_2 cases, ***Figure 1.5*** depicts the correlation for the mass losses between thiophene and carbon burnout ratio in char collected in 0.6 m and 1.2 m location. It shows a linear relationship between these two variables. However, the oxy-firing mode results in a higher thiophene loss rate than the conventional air-firing case. ***Figure 1.5*** also supplies the kinetic decomposition rate of thiophene for Victorian brown coal, which can/will be used for future modelling approach.

1.3 Ash sulfation experiments

The experiments of ash sulphation and tube corrosion are being conducted in a horizontal furnace in Chubu University. The photographs are shown in ***Figure 1.6.*** Panel (a) is the furnace, the temperature of which is fixed to mimic flue gas temperature in an industrial furnace. In panel (b), one can see a CCD camera installed on the right-hand side of the furnace to capture the tube corrosion during experiments. (c) shows a steam generator to produce steam to be injected into flue gas. (d) shows the sample holder, under which there is a thermocouple to record the real temperature for the sample. (e) shows the tube specimen which were made by ion milling of water tubes. The dimension of the tube specimen is 1.2×1.2×0.2cm. (f) demonstrates the quartz-made supporter, to carry several ash specimens that can be tested simultaneously in the furnace chamber. This lab-scale bench is designed to mimic the real tube wall with higher temperature 500-800^{o}C, e. g. super-heater, reheater and so on. Each ash specimen is tested for 50 -100 hr. To date, test on one tube material (T91) and one ash sample

(Hazelwood) has been finished. The rest conditions are underway and will be reported in next milestone report.

Two experimental trials have been successfully performed. T91 tube specimen were tested at the temperature of 700 ºC and 600 ºC. The tube specimen was embedded within coal fly ash, which was then pushed into the pre-heated furnace with flue gas flow continuously for 50 hr. The gas concentration was controlled with 5.0 vol% O_2, 8.0 vol% CO_2 and 5.0% H_2O, which is diluted in N_2. The preliminary results are shown below.

For the ash deposit samples attached on the specimen, the elemental distribution tested is shown in ***Table 1.7***. After the test, the loose ash particles (namely gas side ash hereafter) were carefully swept away and analyzed separately, whereas those (tube side ash) that have stuck to and penetrated into tube were analyzed with tube together. As can be seen, there were little difference for alkali metals and Cl at the different collection locations. However, a noticeable increase in the SO_3 content in ash was observed for the tube specimen tested at 600ºC, which demonstrates that the sulfates are prone to deposit on and even penetrate into tube to cause corrosion. These sulfates include Na_2SO_4, K_2SO_4, $CaSO_4$ and $PbSO_4$ that are predominant in brown coal fly ash, increasing temperature to 700ºC.

Table 1.7 Elemental components of ash deposits on the T91 tray at 700ºC and 600ºC. Apart from SO_2, HCl was also injected into the flue gas to manipulate an accumulated HCl upon flue gas recirculation during oxy-fuel combustion.

Specimen temp.	Ash location	N_2O +K2O	SO3	Cl	CaO	PbO	CuO
700ºC	gas side	16.79	3.19	16	29.7	0.087	1.47
	tube side	23	3.75	19.8	22.3	0.394	2.5
600ºC	gas side	28.2	15.2	17.7	19.4	0.166	0.387
	tube side	23.31	27.2	5.52	15.8	8.55	0.997

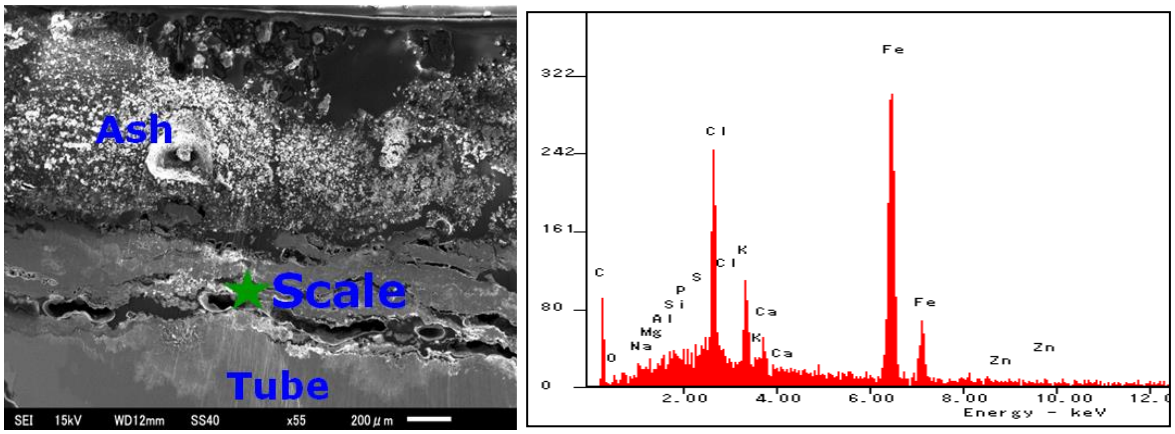

(a)

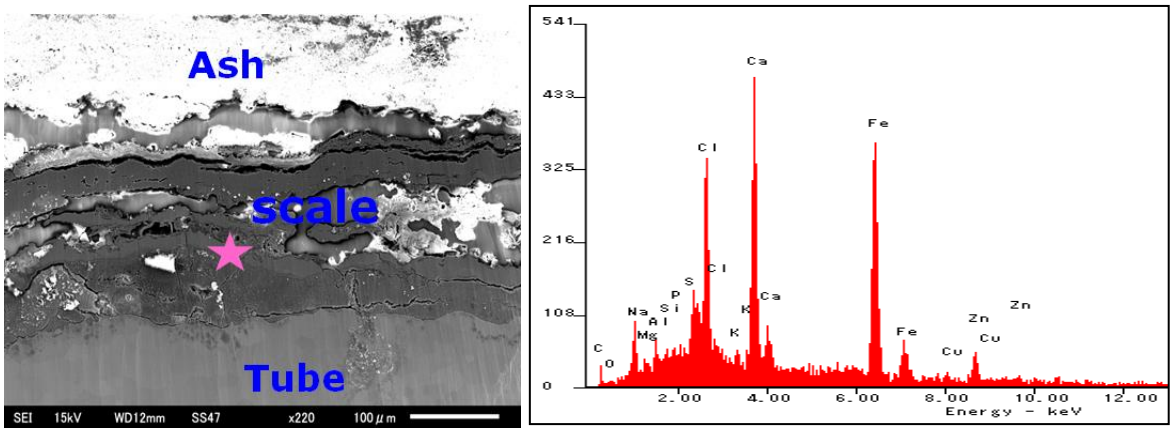

(b)

Figure 1.6 SEM-EDS analysis of ash deposits, which collected at 700°C (a) and 600°C (b)

The SEM-EDS analysis was conducted to measure the elemental mapping in the scale part between tube surface and ash deposit, shown in ***Figure1.6***. Clearly, the higher concentrations for Na, K and Cl can be found in this location, in which a lot of Fe also co-exists, indicating the inward penetration of Na, K and S, and an outward distribution (thus loss) of iron metal upon corrosion.

The elemental distributions of ash layer section were also tested via SEM for the ash deposits collected at 700°C and 600°C, respectively, as shown in ***Figure 1.7*** and ***Figure 1.8***. More Cl and S contents were found in the 700°C steel tube, as compared with those at 600°C. It witnessed that the corrosion extent of tube surface was enhanced at elevated temperature.

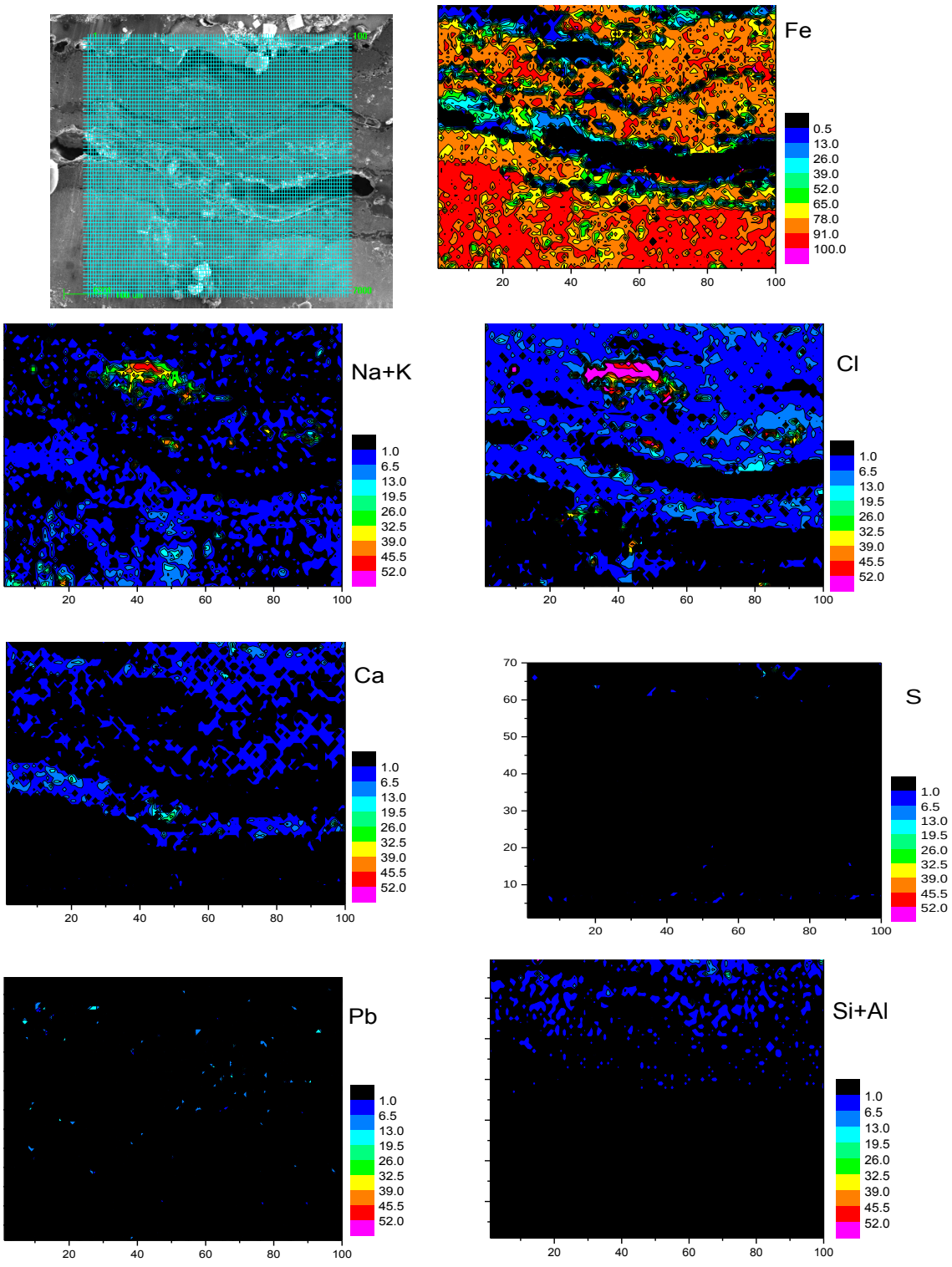

Figure 1.7 Element distributions of ash deposits at 700°

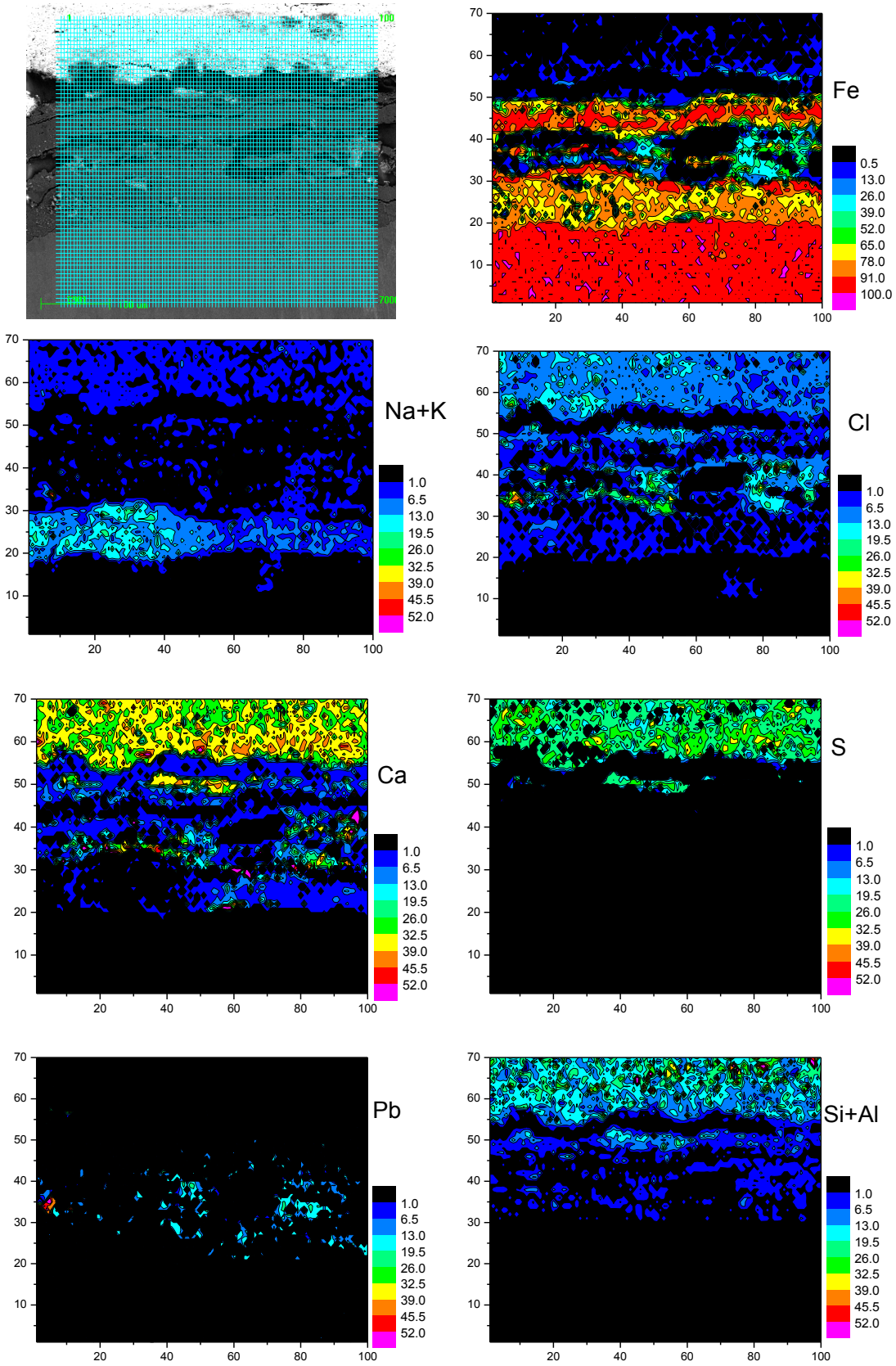

Figure 1.8 Element distributions of ash deposits at 600°C case

Chapter 2 Experiments and CFD modelling to refine the kinetics of char-H_2O and char-CO_2 reactions during oxy-fuel combustion

2.1 Thermo-gravimetric experiments for char-H_2O kinetics of Victorian brown coal

In previous studies, the kinetic reactivates of C-O_2 and C-CO_2 reactions of Victorian brown coal were measured. To determine another C-H_2O reaction rate of Victorian brown coal, experiments were conducted on an updated thermo-gravimetric analyzer (TGA), in which a controlled steam injection apparatus was added. The Victorian brown (Loy Yang) coal char yielded at 1000 ^oC was tested. The steam concentration was kept at 5-20 vol% in nitrogen. A non-isothermal heating program was run with the heating rate varying from 10 to 50 K/min. The weight loss curves are shown in ***Figure 2.1 panel (a)*** is for the cases with 5vol% H_2O. ***Panel b*** is the comparison of different steam concentration at the identical heating rate of 40^oC/min.

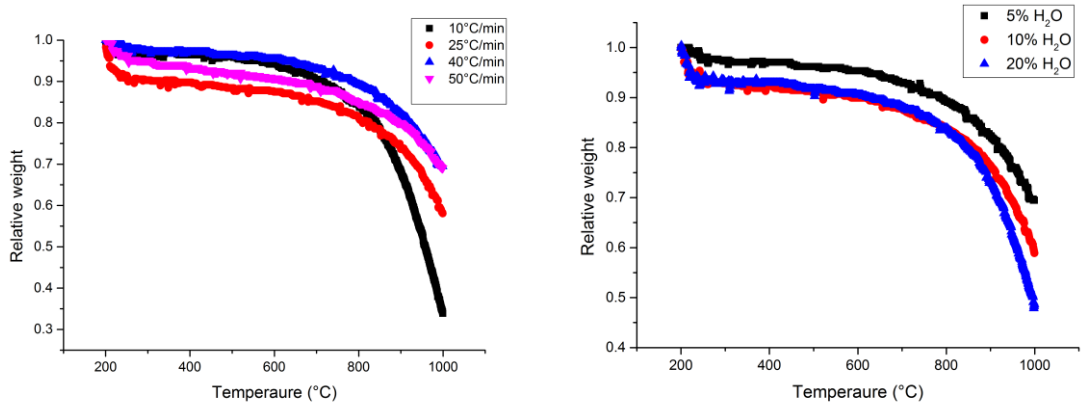

(a) (b)

Figure 2.1 Weight loss curves of Victorian brown char in H_2O/N_2. (a) influence of heating rate; (b) influence of steam concentration.

The reaction order of C-H_2O reaction was not 1.0, as is well known. The first work is to determine this order parameter. Based on the general Arrhenius equation (Eq. 2-1), the C-H_2O reaction rate is supposed to be proportional upon the nth power of steam concentration. Through trials of n value, the maximum deviation of three terms in (Eq. 2-2) was calculated, as used to solve this equation for n. This calculation was conducted based on the data in ***Figure 2.1 (b***). And the final result suggested an n of 0.68 giving the least fitting error.

$$r = AP_{H_2O}^{n} \exp(-E/RT) \qquad (2\text{-}1)$$

$$\frac{Rate_{5\%}}{(5\%)^n} = \frac{Rate_{10\%}}{(10\%)^n} = \frac{Rate_{20\%}}{(20\%)^n} \qquad (2\text{-}2)$$

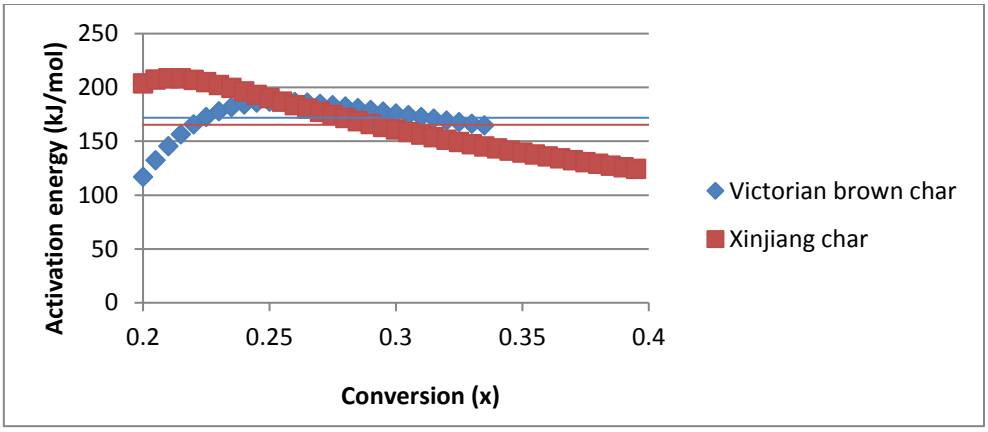

Figure. 2.2 Activation energy was determined by the Friedman method

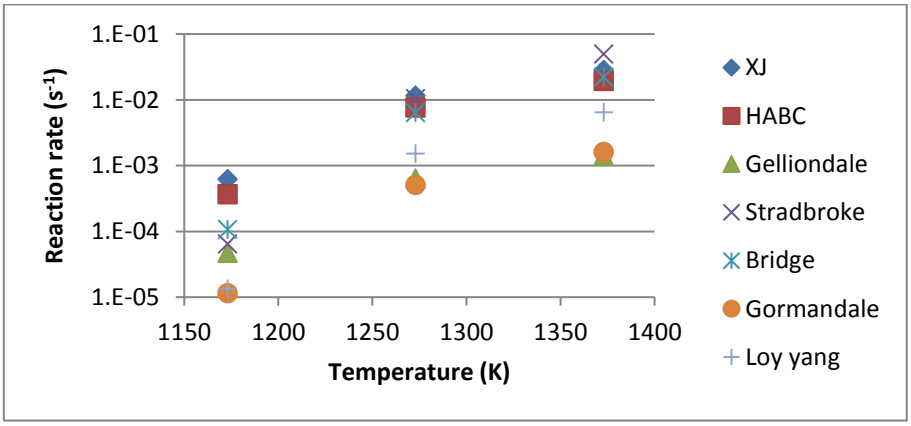

Figure 2.3 The comparison of C-H_2O reaction rate of different coal samples. HABC means the high ash Victorian brown coal that we tested. Other kinetics comes from literatures.

The C-H_2O reaction rate is hard to measure because of lower steam concentration as test atmosphere. Too higher steam level could damage the TGA device. Therefore, this is a fact that the peak value of reaction rate could not be observed within 1000^{o}C, corresponding to ***Figure 2.1***. In other words, the conversional maximum rate method could not be used to calculate A and E. Hereby another differential method (Friedman method) was used in this section.

$$\ln(\frac{dX}{dt}) = \ln[A(1-X)] - \frac{E}{RT} \quad (2\text{-}3)$$

Eq. (2-3) is a general rate description used in a grain model. For a given conversion ratio (X), the correlation between the reaction rate (dX/dt) and the sample temperature (T) can be derived, which can be derived from the experimental data in ***Figure 2.1 panel (a***). In the Friedman method, the activation energy (E) is a function of X, as is a calculative result shown in ***Figure 2.2***. The maximum value of E, 187.0 KJ/mol, occurs at the case X = 0.23. When X is above 0.23, E seems to decrease slightly. In the grain model, the influence of pore structure on the rate was not taken into account. In another word, this model can only predict the decline zone of reaction rate or activation energy, in which X > 0.23. Hence, the average activation energy, 172.5 KJ/mol, was chosen to depict all cases. Furthermore, the exponential parameter can be calculated through used of Eq. 2-3, A= 2.467 kg/m^2.s.Pan.

The C-H_2O reaction reactivity was compared with other coals, as shown in ***Figure 2.3***. The gas environment is 5% H_2O/ 95% N_2. It can be found that Victorian brown coal and another sub-bituminous coal, Xinjiang coal (XJ), bear higher reactivity of C-H_2O gasification reaction than other bituminous coals.

2.2 CFD modellings to verify the kinetics of char-H_2O and char-CO_2 reactions

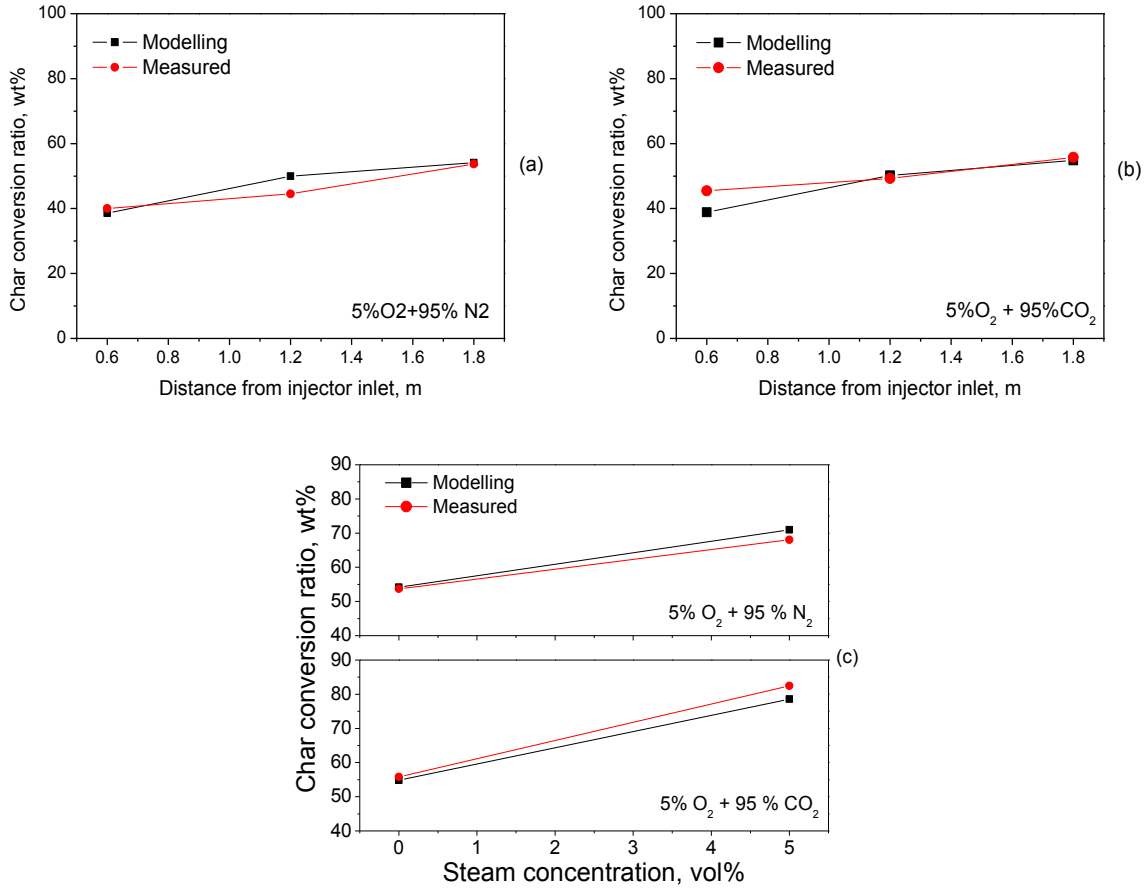

Figure 2.4 Validation of kinetic data of Char-CO_2 and Char-H_2O reactions. (a) 5% O_2 in N_2; (b) 5% O_2 in CO_2; (c) influence of H_2O concentration.

The kinetic data from TG was obtained in the experimental cases with low temperature and low heating rate, which does not present the actual flame conditions in industrial furnace. However, the kinetic data from TGA can be theoretically extended to cover the cases with higher temperature and higher heating rate, as is due to the strict linear relationship between reaction rate and the reciprocal of temperature (1/T) in Arrhenius description of Eq. 2-1. Hereby, further CFD modelling was conducted by incorporating the accurate TG kinetic data. Its accuracy was validated by comparing the measured data of char conversion in a drop tube furnace versus the CFD prediction.

The furnace temperature was kept at 1000^{o}C. The pyrolysis char was further injected into the drop tube furnace for different gas atmospheres. A good agreement has been obtained through comparing the measured data, char conversion ratio, with the modelling results, as shown in ***Figure 2.4***. All these witnessed the accuracy of char gasification kinetics in CO_2 and H_2O.

2.3 Model establishment of sulphur emission and sulfation

In previous works, we have been successful in conducting oxy-firing tests in a 3 MW_{th} pilot-scale furnace. For a 5 hr exposure time, abundant ash deposits were collected on the tube surface in the oxy-firing case of Victorian brown coal. The distinct and potentially severe slagging on fire-side wall/tube has been observed for the oxy-firing case. SEM observation confirmed the abundance of S and Fe in the ash deposit, which also possesses a fusion temperature 200^{o}C lower than the air case. The reason causing this is complex and unknown. It can be assigned to various discrepancies between air-firing and oxy-firing modes, such as flame temperature, gas environment in the vicinity of coal burner, flue gas amount /velocity /property (e.g. SOx, H_2O and HCl), ash particle density and trajectory. To clarify the influence of individual facts and their combined effect, a refinement of CFD modelling by adding sulphur emission model and ash slagging/fouling prediction model are underway.

The first step focused on the mathematical description of sulphur emission and sulphates used in CFD modelling. Sulphur exits in coal as organic sulphur, pyretic, and sulfates. During the combustion process, fuel sulphur is oxidized to SO_2 and SO_3. A portion of the gaseous SOx will condense on particle surface to combine with water condensate forming sulphuric acid, or may react further to form sulphates.

The sulphur emission and sulphation model incorporates the following three stages:

(a) Sulphur release from coal;

(b) Sulphur oxidation in gas phase and

(c) sulphur capture on ash particle surface.

2.3.1 Sulphur release from coal

2.3.1.1 Inorganic sulphur emission

Experimental studies have shown that pyrite (FeS_2) experiences a series of decomposition and oxidation reactions under combustion conditions, as was summarized in [1]. In the observations

by Thompson and Tilling, the reduction of FeS_2 does not occur until after 550 ^oC [2]. The decomposition of FeS_2 is intensified between 550 and 600 ^oC [3]. FeS_2 is unstable at temperatures above 600C. The gaseous species are released in the form of molecular sulphur (Sn) and H_2S, COS, SO_2. The pyrite transformation may be simply described by the following reaction. [4, 5]

$$FeS_2(s) \rightarrow FeS\,(s) + 0.5S_2 \quad (2\text{-}4)$$

In kinetic model of above decomposition [6, 7], this reaction was assumed to occur at 600 oC. This rate was assumed to be heat transfer limited, because of the rapid kinetics of this reaction. When oxygen reaches particle surface, poly-sulphide yielded (FeS, Fe1-xS) can further release additional sulphur. The reaction is

$$1.14\,Fe_{0.877}S(s) + 1.2367\,O_2 \rightarrow 0.33Fe_3O_4\,(s) + 1.14SO(g) \quad (2\text{-}5)$$

In Asaki's research [8], its rate can be described by

$$r = 5\times10^7 \cdot [O_2] \cdot \exp(-150\times10^6 / RT)$$

It totally depends on the oxygen diffusion. For extracted fine pyrite particle, this reaction is predominant [9]. However, regarding an ignited coal particle, most of oxygen is consumed by the released volatile matter, and hence, the included pyrite particle within a burning char particle has less opportunity to react with oxygen via above reaction equation. It would not be oxidized until after the complete oxidation of char particle.

2.3.1.2 Organic sulphur emission

The decomposition of organic sulphur (thiophene) can be simplified as overall reactions:

$$C_4H_4S\,(s) \rightarrow C_4H_3\,(s) + HS \quad (2\text{-}6)$$

$$2HS + 2.5O_2 \rightarrow 2SO_2 + H_2O \quad (2\text{-}7)$$

The decomposition of thiophene under pyrolysis in N_2 can be described by a first-order kinetic equation, such as

$$\frac{d[HS]}{dt} = 1.60\times10^{11}\exp(-265.04\times10^{6}/RT) \quad [10]$$

$$\frac{d[HS]}{dt} = 2.34\times10^{12}\exp(-316.26\times10^{6}/RT) \quad [11]$$

The decomposition reaction reactions (2-6), (2-7) mainly occurs above 900°C. Furthermore, the thiophenic structure was more complex, the decomposition reaction of which turns difficult from 1000°C onwards. When coal particle is ignited at 900-1100°C, the increase in sulphur emission was found to bear a proportional relationship with the oxidation extent of char. The oxidation becomes the main reason to break the C-S bond.

$$C_4H_4S + 1.5O_2 \rightarrow C_4H_2 + SO_2 + H_2O \qquad (2\text{-}8)$$

This understanding agrees well with our experimental results, shown in ***Figure 1-5***. The sulphur emission rate of Victorian brown coal has been measured in our above work.

2.3.2 Sulphur oxidation in gas phase

In oxygen-rich flames (e.g. oxy-fuel combustion), the predominant sulphur species are SO, SO_2 and SO_3. At lower oxygen concentrations, e.g. in coal gasification process, H_2S, S_2, and SH are also present in significant proportions, while SO_3 becomes negligible.

2.3.2.1 Detailed mechanism of sulphur oxidation

A detailed reaction mechanism for sulphur oxidation has been proposed by Kramlich [12]. The mechanism consists of 20 reversible reactions and includes 12 species (S, S_2, SH, SO, SO_2, H_2S, H, H_2, OH, H_2O, O, O_2. The mechanism has been reduced to 8 steps and 10 species (with S and S_2 removed), and validated in Perfectly Stirred Reactor (PSR) and Plug Flow

Reactor (PFR) simulations. Each reaction of the eight-step reduced mechanism is reversible, for each adjacent pair of reactions given in following Table, in which the kinetics are shown in ***Table 2.1***.

$$r = AT^{b}\exp(-E/RT)$$

Table 2-1 Eight-step reactions of sulphur oxidation [12]

Reaction	A	b	E
$H_2S+H \rightarrow SH+H_2$	1.819702E+07	0.0E+00	7.484300E+03
$SH+H_2 \rightarrow H_2S+H$	9.375623E+06	0.0E+00	6.253660E+04
$OH+H_2S \rightarrow H_2O+SH$	1.380385E+02	0.0E+00	3.742150E+03
$H_2O+SH \rightarrow OH+H_2S$	3.104557E+07	0.0E+00	1.218543E+05
$SO+OH \rightarrow H+SO_2$	1.621810E+08	0.0E+00	2.565926E+03
$H+SO_2 \rightarrow SO+OH$	7.691299E+09	0.0E+00	1.187023E+05
$SH+O \rightarrow SO+H$	3.548135E+08	0.0E+00	2.687316E+03
$SO+H \rightarrow SH+O$	2.985385E+09	0.0E+00	1.694600E+05
$O+H_2S \rightarrow SH+OH$	4.365162E+03	0.0E+00	1.380493E+04
$SH+OH \rightarrow O+H_2S$	9.885528E+08	0.0E+00	6.035996E+04
$SO+O_2 \rightarrow SO_2+O$	4.466832E+05	0.0E+00	2.703222E+04
$SO_2+O \rightarrow SO+O_2$	1.663412E+06	0.0E+00	7.613643E+04
$H+SH+M \rightarrow H_2S+M$	1.096478E+03	0.0E+00	0.000000E+00
$H_2S+M \rightarrow H+SH+M$	8.669613E+14	0.0E+00	3.819463E+05
$SO+O+M \rightarrow SO_2+M$	8.709647E+09 k	-1.8E+00	0.000000E+00
$SO_2+M \rightarrow SO+O+M$	1.905464E+14	0.0E+00	5.207365E+05

In addition, SO_3 formation can be considered by following two reactions, with the rate constants taken from Hunter's work [13]. M means one catalyst gas such as argon, nitrogen and oxygen.

$$SO_2 + O + M \rightarrow SO_3 + M \qquad (2\text{-}9)$$

$k_{f1} = 3.63 \times 10^{2} \exp(+4185.85/RT)\ m^6/mol^2/sec$, where R = 8.313 J/mol-K

$$SO_3 + O \rightarrow SO_2 + O_2 \qquad (2\text{-}10)$$

$k_{f2} = 1.2 \times 10^{6} \exp(-39765.575/RT)\ m^3/mol/sec$

2.3.2.2 Overall reaction description for S emission and speciation in CFD modelling

A detailed oxidation mechanism covering the full mechanisms including all the reactions mentioned above is unnecessary for CFD modelling, as it will significantly increase the computing time. Therefore, the overall reaction description is normally simplified as follows:

$$H_2S + 1.5O_2 \rightarrow SO_2 + H_2O \qquad (2\text{-}11)$$

$$SO_2 + 0.5O_2 \rightarrow SO_3 \qquad (2\text{-}12)$$

The kinetic rates can be described as follows, respective [14, 15].

$$\frac{d[SO_2]}{dt} = 1.5\times10^{10}[H_2S][O_2]\exp(-1.3\times10^5 / RT)$$

$$\frac{d[SO_3]}{dt} = -0.011\cdot[SO_2]\cdot[O_2]^{0.5}\exp(-70.3\times10^6 / RT) - 0.01069[SO_3]\cdot\exp(-168.5\times10^6 / RT)$$

2.3.3 Sulphur capture on ash particle

Sulphur oxide in flue gas can be absorbed by ash particles. The sorbent particles include residual ashes and some additional particles in furnace, *e.g.* limestone.

The sulphur vapour, SO_2 and SO_3, can be quickly captured by the abundant alkali and alkaline earth metals (CaO, MgO). The desulfurization temperature ranges are 980-1230ºC for CaO, 650-820 ºC for MgO. [16]

$$MO(s) + SO_2 + 0.5O_2 \rightarrow MSO_4(s) \qquad (2\text{-}10)$$

$$MO(s) + SO_3 \rightarrow MSO_4(s) \qquad (2\text{-}11)$$

The symbol M denotes a metal of alkali and alkaline earth metal such as Ca, Mg, and Na. The diffusion of gaseous reactants (SO_2, O_2) was considered through the surrounding gas film to the outer particle surface. And the diffusion of reactants is through the product shell (e.g. $CaSO_4$)

into the reactant into the reaction layer [17]. Furthermore, the reverse reaction for *Reaction 2-10* and *Reaction* 2-11 become significant above the decomposition temperature such as about 1610 ^{o}C for $CaSO_4$, and 1041 ^{o}C for $MaSO_4$.

Above all is the model establishment of sulphur emission and sulphate. Till today, as far as the authors are aware, there is only one code (in a German institute) around the world can cover above details. The CFD work in our group will be generating a code with independent intellectual property rights, which can be further verified by our plenty of experimental data of Victorian brown coal. Now the code writing and debugging are ongoing.

In the future work of this project, this code will be incorporated in CFD modelling to study the ash formation, slagging and fouling, combining other chemical database of Factsage software via ChemApp software. This will be employed to reveal the influence of CO_2 / steam –rich environment of oxy-firing on the evolution of ash of Victorian brown coal.

2.4 CFD simulation on ash formation during Victorian brown coal combustion

2.4.1 Experimental set up

Experiments were set up in the lab-scale 2 *m* drop tube furnace with the following parameters:

Table 2.2 Experimental cases in drop-tube furnace (DTF)

Char sample	Victorian brown coal char (Loy Yang)
Particle size	63-106 μm
Gas residence time	6 seconds
Gas feeding rate	10 L/min total
Temperature	1000°C
Oxygen concentrations	0, 1, 5%
Balance gas	Either N_2 or CO_2

Metal release is determined by dissolving with microwave digestion and quantitative analysis by ICP-OES.

$$Metal\ release\ (\%) = \frac{Metal\ concentraiton\ initial - metal\ concentraiton\ final * product\ yield}{Metal\ concentration\ intial}$$

Metals analysed: Aluminium, Sodium, Iron, Calcium, Potassium, and Magnesium.

2.4.2 Properties of Victorian brown coal (VBC) char

Victorian brown coal (VBC) char was generated in the drop tube furnace at a temperature of 1000°C and gas residence time of 2 seconds. As shown in ***Table 2.3***, this char is relatively high in sodium.

Table 2.3 Metal composition of Victorian brown coal (VBC) char sample

Element	Concentration (ppm)
Al	6506.23
Ca	805.43
Fe	1166.19
K	101.09
Mg	1175.18
Na	2030.11

2.4.3 Metal release as determined by ICP-OES and integration into Fluent

Metal release was determined to be a function of char burnout and plotted in ***Figure 2.4***. Volatility of each element can be compared by the proportion of metal released compared to the amount of char burnout. Elements Ca, Mg, Na, K are more volatile while Al and Fe are released in lower quantities.

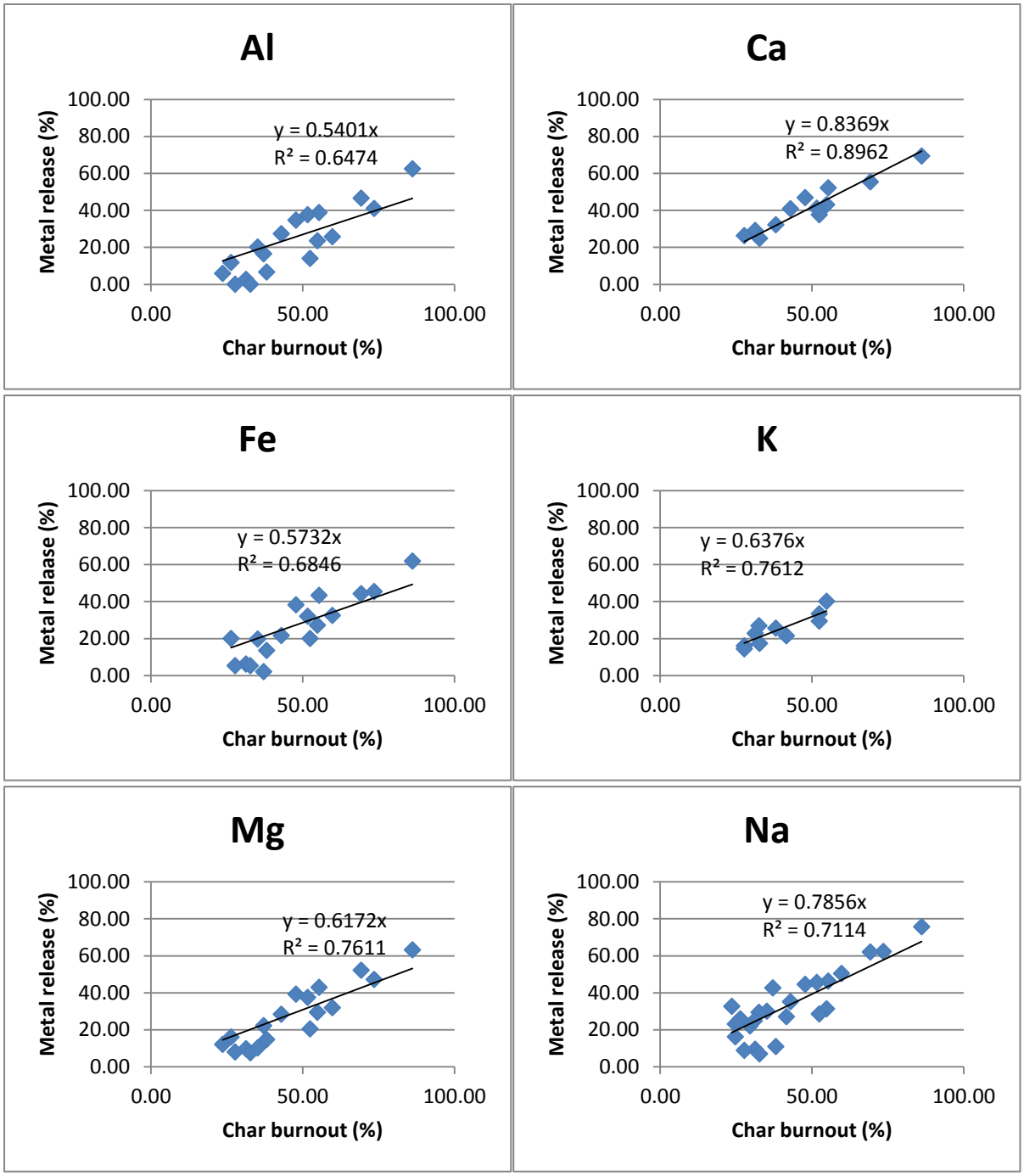

Figure 2.4 Metal release as a function of char burnout.

2.4.4 Integration of FactSage with Fluent through ChemApp

2.4.4.1 Brief introduction of ChemApp

FactSage software is widely employed to research mineral evolution in coal ash and fusion behaviour. It possesses an abundant and confirmed database of chemical reactions and reactive equilibriums. To achieve a coupling of CFD simulation programs and FactSage software, one third-party software, ChemApp, is required. ChemApp is essentially a library of subroutines for calculating complex, multicomponent, multiphase chemical equilibria, which can be combined with CFD codes through a user defined function (UDF) written in C programming language.

It is developed by GTT Technologies (FactSage, ChemSage, ChemSheet) in Aachen, Germany. The licence was purchased in June 2014. ChemApp is used by a large number of commercial and academic organisations for simulation of a wide range of processes including waste treatment, slags, corrosion and mineral extraction.

2.4.4.2 Usage of ChemApp

ChemApp software is used on a platform of Microsoft Visual Studio. Performing a calculation within ChemApp consists of three steps:

(1) Initialisation and reading a data file
(2) Setting initial conditions (temperature, pressure, concentrations of reactants)
(3) Performing equilibrium calculation and obtaining results

2.4.4.3 Usage of user defined function (UDF) in FLUENT

In CFD modelling of pulverized-coal flame, gas phase and particle phase are considered in different system, e.g. Euler system and Lagrange system. The chemical equilibrium in two phases should be regarded, respectively. The brief introduction of calculation procedure is shown below.

For a gas phase analysis:

- Gas phase conditions are calculated by CFD software FLUENT.
- A user defined function (UDF), “DEFINE_ON_DEMAND” is implemented which allows a one-time calculation to be performed.

- The UDF will:
  - Initialise ChemApp and read data file
  - Begin a loop over every cell in simulation
- Read gas phase conditions
- Pass these conditions to ChemApp
- Calculate equilibrium concentrations of products
- Export these concentrations to a user defined memory (UDM) macro
  - End loop
- Variables stored in UDM locations can then be analysed or displayed in a contour graph in fluent.

For a particle analysis:

- Particle progression is tracked by CFD software Fluent, including trajectory, temperature, and local gas environment.
- A virtual ash composition can be held by every particle, stored in a user defined which will be updated at every particle update. (About every 0.005 m for every tracked particle).
- UDFs for particles automatically loop over every particle update, therefore ChemApp can be initialised and data file can be read in a separate UDF to speed up process. Initial mineral concentrations are also being pre-defined. The UDF, "DEFINE_DPM_SCALAR_UPDATE" will then:
  - Read particle mineral concentrations
  - Read particle temperature and surrounding gas environment
  - Pass these conditions to ChemApp
  - Calculate equilibrium concentrations of products
  - Retrieve this information and update user scalar quantities
  - Calculate particle stickiness based on the determined mineral composition
- This information can then be combined with a UDF for particle contact with a surface. Using data such as previously calculated stickiness, particle velocity, particle momentum, and contact angle, it can be determined how likely the particle is to attach to the wall or reflect off the wall.

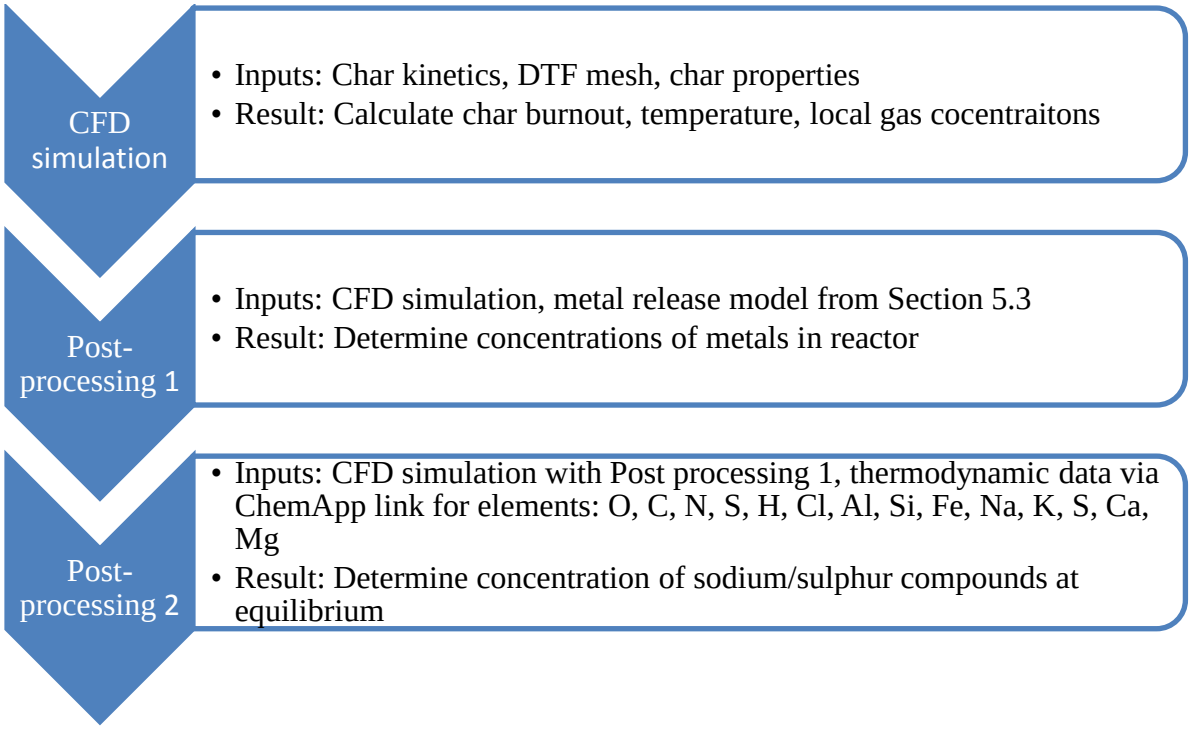

Figure 2.5 Flow sheet of thermodynamic data integration into Fluent

The flowsheet for the calculation upon the combination of Fluent and ChemApp is further depicted in ***Figure 2.5***, and the interaction between the two software is further schemed in ***Figure 2.6***.

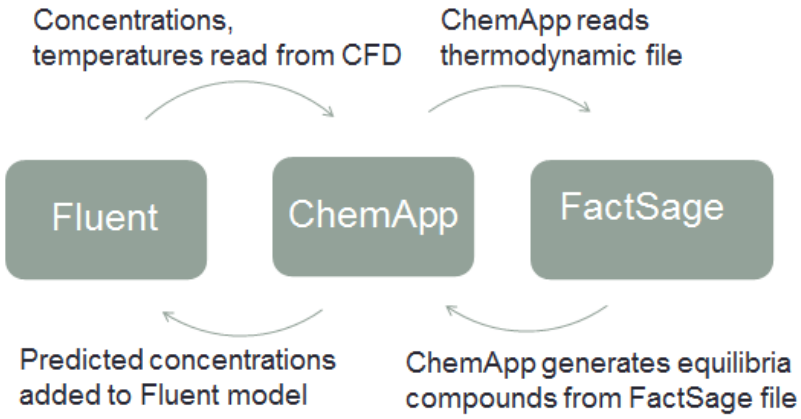

Figure 2.6 Flow sheet of thermodynamic data integration into Fluent

2.4.5 Effect of oxygen concentration on sodium and sulphur compounds with balance gas N_2

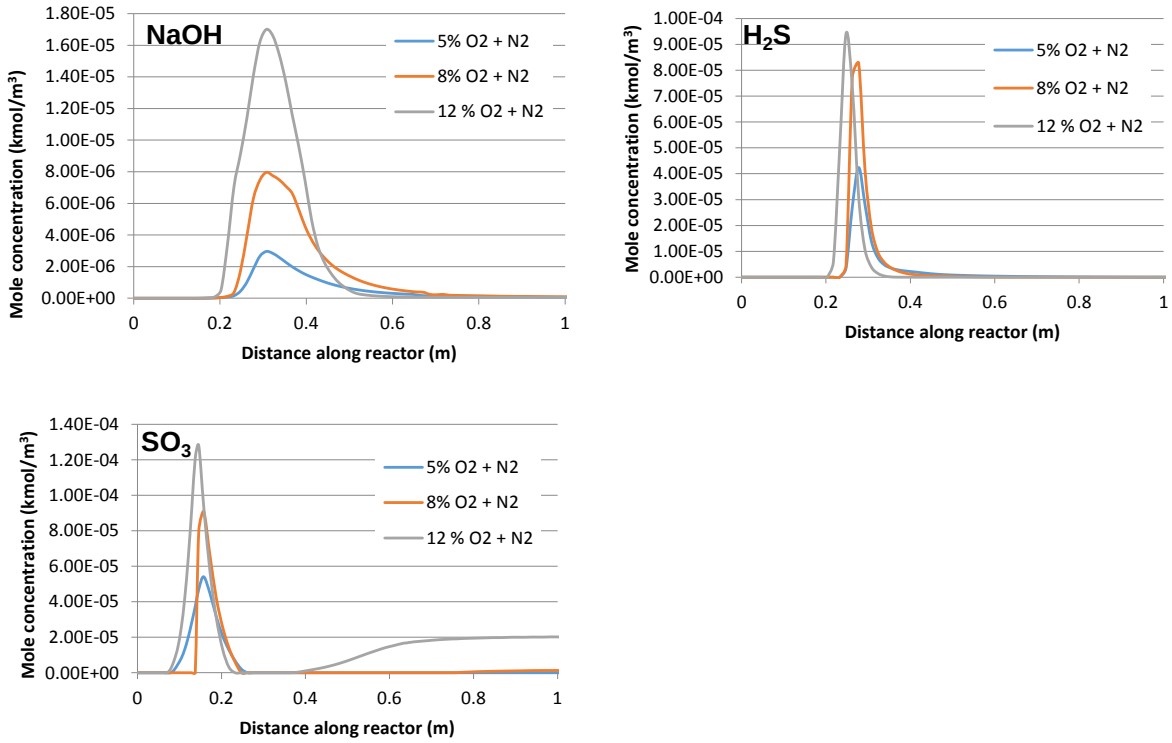

Figure 2.7 Effect of oxygen concentration on the release of key compounds along the length of the DTF.

The effect of oxygen partial fraction in the furnace on the emission of gaseous sodium and sulphur were examined. As shown in ***Figure 2.7***, the emission of gaseous sodium hydroxide is peaked at a distance of around 0.3 *m* from the coal injection tip, which is the position for the coal flame formed from the combustion of the volatiles. The peak emission of NaOH vapor is increased dramatically upon the increase on the oxygen partial fraction, due to the increased flame temperature formed at the elevated oxygen concentration. The concentration of NaOH vapor also decreases quickly upon flowing downwards along the reactor. At a distance of around 0.6 *m* which refers to the char combustion regime, the NaOH disappears completely suggesting the capture of the NaOH vapor by the refractory minerals or the solidification of Na vapor into the respective oxide/sulfates.

Regarding the two gaseous S-bearing species, their emission profiles are similar with that of NaOH. However, their peak position is a bit earlier than that for NaOH. The emission of H_2S is peaked at around 0.25 *m*, whereas the emission of SO_3 is even peaked at 0.15 *m*. Both two

positions refer to the devolatilisation stage where the oxygen is lean/absent and the temperature is also not high. Both the shortage/absence of oxygen and low temperature are in favour of the formation of these two species. Once the coal devolatilisation is complete and the volatile combustion is commenced, it is clear that these two species are either oxidized (for H_2S) or decomposed (for SO_3) into SO_2. Upon the increase on the oxygen partial pressure, the peak positions for these two species move earlier, due to the accelerated rate for every step including the initial devolatilisation. Moreover, the emission of SO_3 appears again in the char combustion regime from the distance of 0.4 *m*, which shall be attributed to the homogeneous oxidation of SO_2 in the gas phase.

2.4.6 Effect of balance gas (N_2/CO_2) on sodium and sulphur compounds with 12% O_2

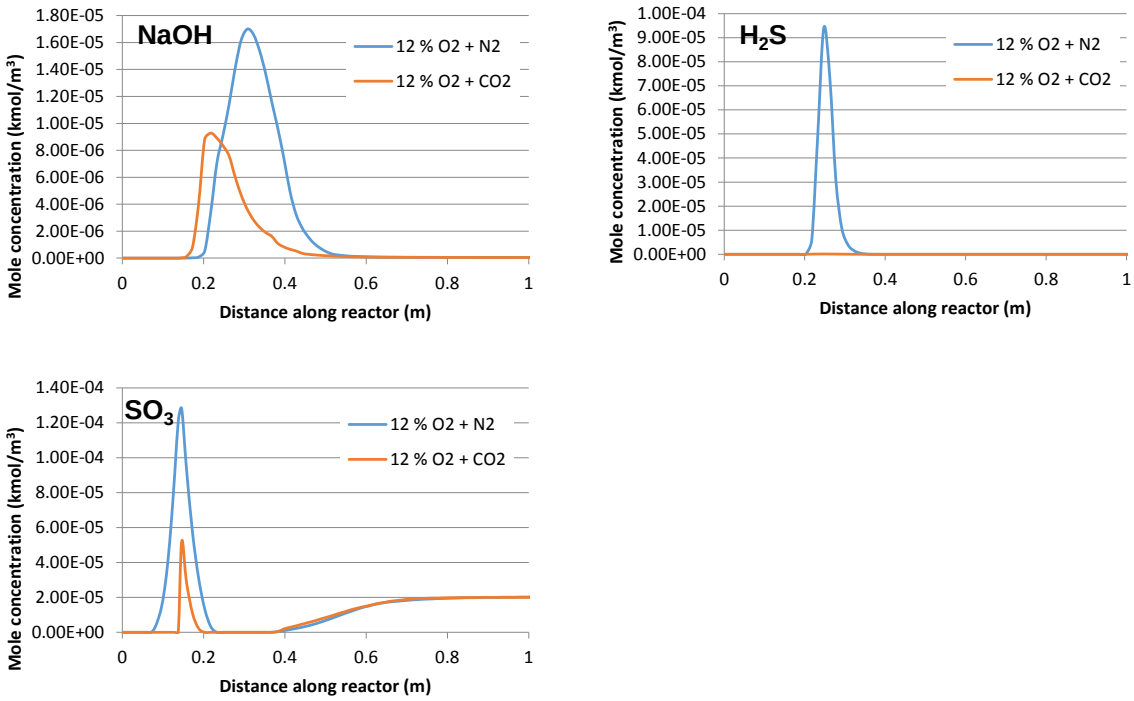

Figure 2.8 Effect of the balance gas (N_2/CO_2) on the release of key compounds along the length of the DTF.

Figure 2.8 further depicts the release of three key compounds between the two balance gases, N_2 versus CO_2. It is clear that the replacement of N_2 by CO_2 depreciates the formation of three troublesome species. This is desirable since these three species can either cause the severe fouling in the boiler or the emission of air pollutants in the flue gas. Regarding the emission of NaOH and SO_3, their peak magnitudes were reduced remarkably under the O_2/CO_2 mode, which shall be partially attributed to a lower peak temperature caused by the larger specific

heat capacity of CO_2 than N_2. The emission of H_2S is even fully disappeared under the oxy-firing mode, which shall be caused by the reaction between H_2S and/or its precursor with CO_2 to form COS. CO_2 is not inert and actively reacts with a variety of intermediate compounds that are either present in the raw coal or formed during the devolatilisation stage.

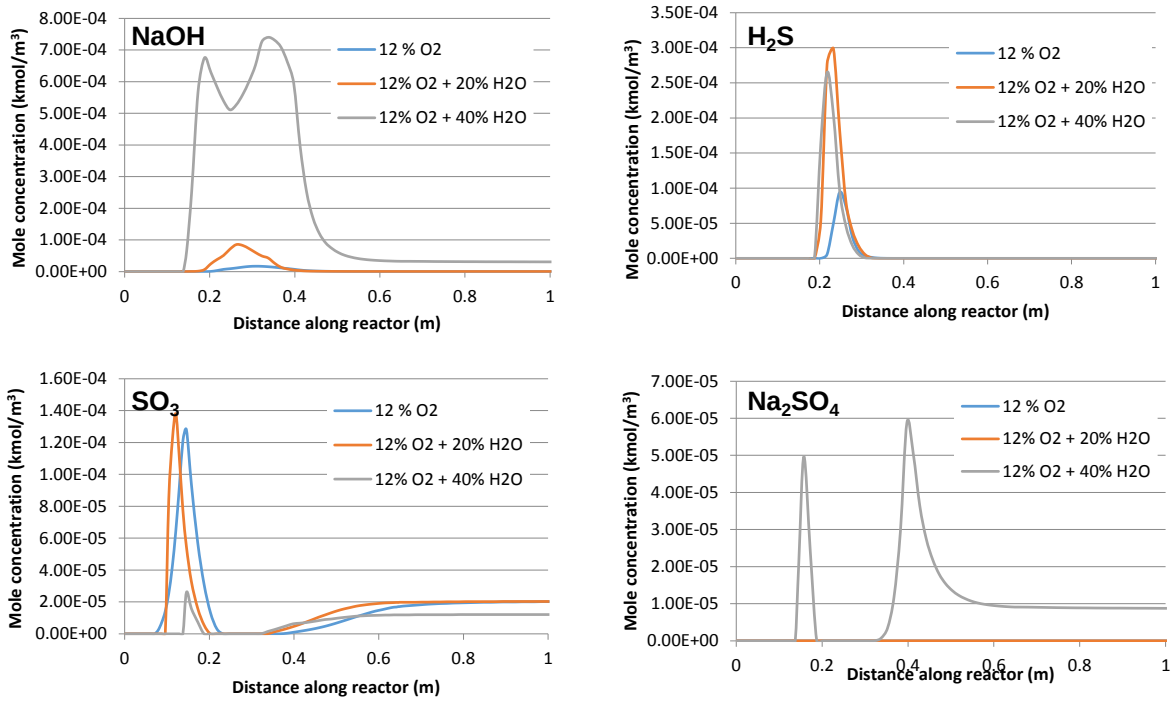

Figure 2.9 Effect of steam concentration on the release of key compounds along the length of the DTF.

2.4.7 Effect of steam on sodium and sulphur compounds with balance gas N_2

Figure 2.9 shows the emission of four key compounds including the three listed in above two figures and Na_2SO_4 as a function of steam concentration in the 12% O_2/CO_2. This is to reveal if the recirculation of wet flue gas causes the changes on the concentration profile of these four troublesome species. It is clear that the two Na-bearing species including NaOH and Na2SO4 can be improved remarkably upon the use of wet flue gas in the boiler. In particular, the latter species are released in two stages, the initial devolatilisation stage and the final char burnout regime. The former stage is responsible for the slagging near the burner vicinity, whereas the latter stage causes the fouling in the heat exchange zones in a boiler. Clearly, the use of dried flue gas is more favorable in minimising the Na – related problems in a boiler. The emission

of H_2S is also potentially increased upon the use of wet flue gas. This shall be due to the chemical reactions between steam and the S-bearing precursors in the raw coal. In contrast, the emission of SO_3 can be potentially reduced upon the use of excessive wet flue gas, which may be due to the reaction between SO_3 and excessive steam in the flame zone.

2.4.8 Concentration contours for sodium emission and ash formation

Efforts were further made to draw the overall concentration contours for the emission of sodium and the formation of key ashes upon the combustion of Victorian brown coal in the DTF. The 3 MW_{th} boiler was not simulated here, due to that the computing time is extremely long and in some cases the calculation even failed to converge. The results discussed in this section are complementary to those reported above, but are expected to provide an overall picture regarding the ash distribution in an oxy-firing environment. In particular, the distribution of slag and sulfates is explored in detail in this section.

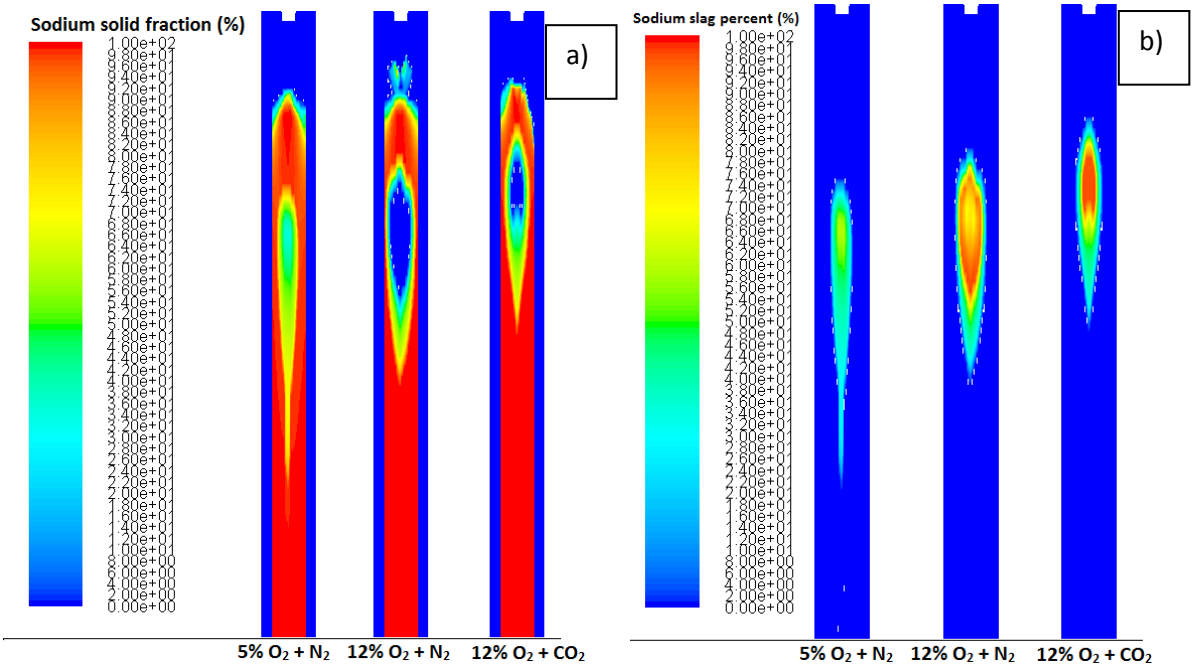

Figure 2.10 Proportion of Na in solid (a) and slag (b) for three conditions.

Figure 2.10 illustrates the distribution contour of Na in both solid and liquid slag along the length of the whole DTF. One can see that the Na_2SO_4 (l) is preferentially formed in the flame zone, both the length and position of which vary remarkably between the two combustion modes. In contrast, the solid Na-bearing species are preferentially formed in the post-flame

char combustion stage, irrespective of the combustion mode. With regarding the difference between the two combustion modes, the solid Na-bearing species are formed earlier under the oxy-fuel combustion mode, suggestive of a quicker start on the char combustion in the CO_2. This can be attributed to the CO_2 - gasification reaction that occurs in the flame-zone. This is indeed a good outcome, since the formation of Na-bearing liquidus is decreased under the oxy-fuel combustion mode, as evident in the panel b.

The distribution of Na is further verified in ***Figures 2.11*** and ***2.12*** for the concentrations of individual Na-bearing species as a function of reactor length (*i.e.* residence time). For the gaseous species including Na (g), NaOH (g), SO_2 (g), Na_2SO_4 (g) and H_2S (g), their formation is faster and the final concentrations for these species are also higher in CO_2 than in N_2. Again, this can be attributed to the difference in char particle temperature and char consumption rate in the two different balance gases. In contrast, the formation of SO_3 (g) is inhibited in CO_2, since the majority of it is preferentially converted into Na_2SO_4 (l) in CO_2. This is interesting, as it suggests that oxy-fuel combustion is able to inhibit the formation of SO_3 (g). Such a 'finding' is contradictory to the literature data, which is further validated by the experiments for ash sulphation and existing results of ours in the next chapter.

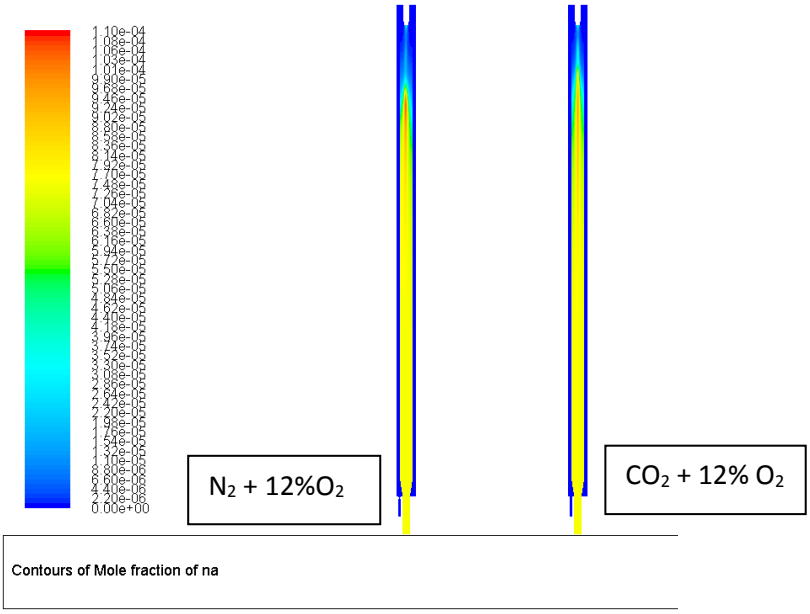

Figure 2.11 Na mole fraction distribution along furnace height.

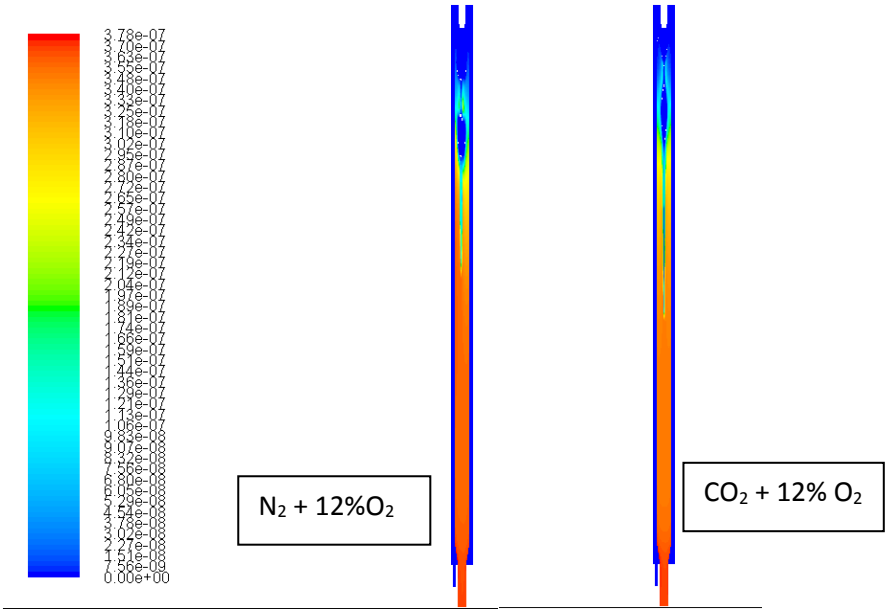

Figure 2.12 Graph of concentrations of liquid Na_2SO_4

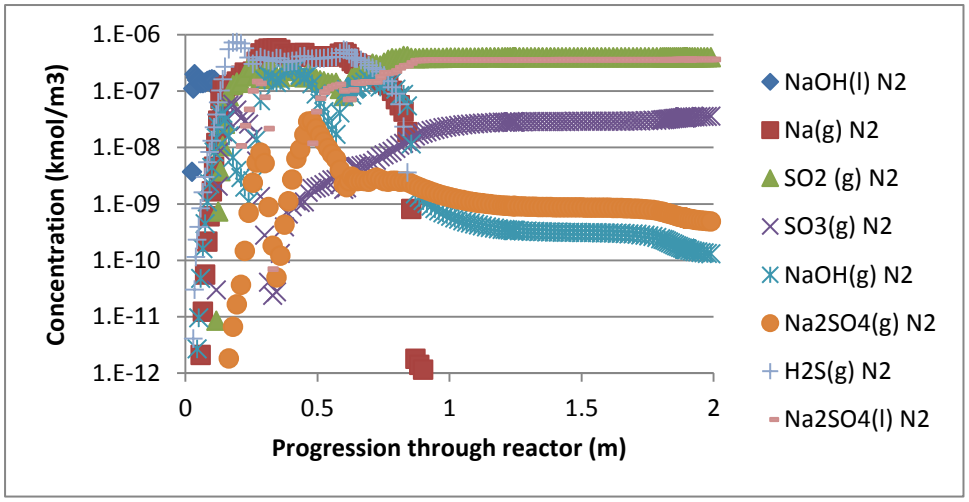

(a)

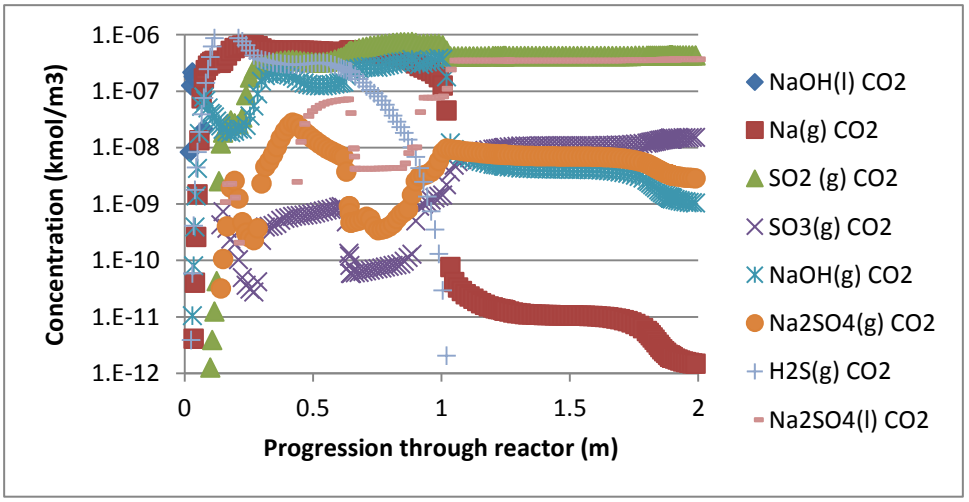

(b)

Figure 2.13 Gas concentration profiles along furnace height. (a)12 O_2 in N_2, (b)12% O_2 in CO_2

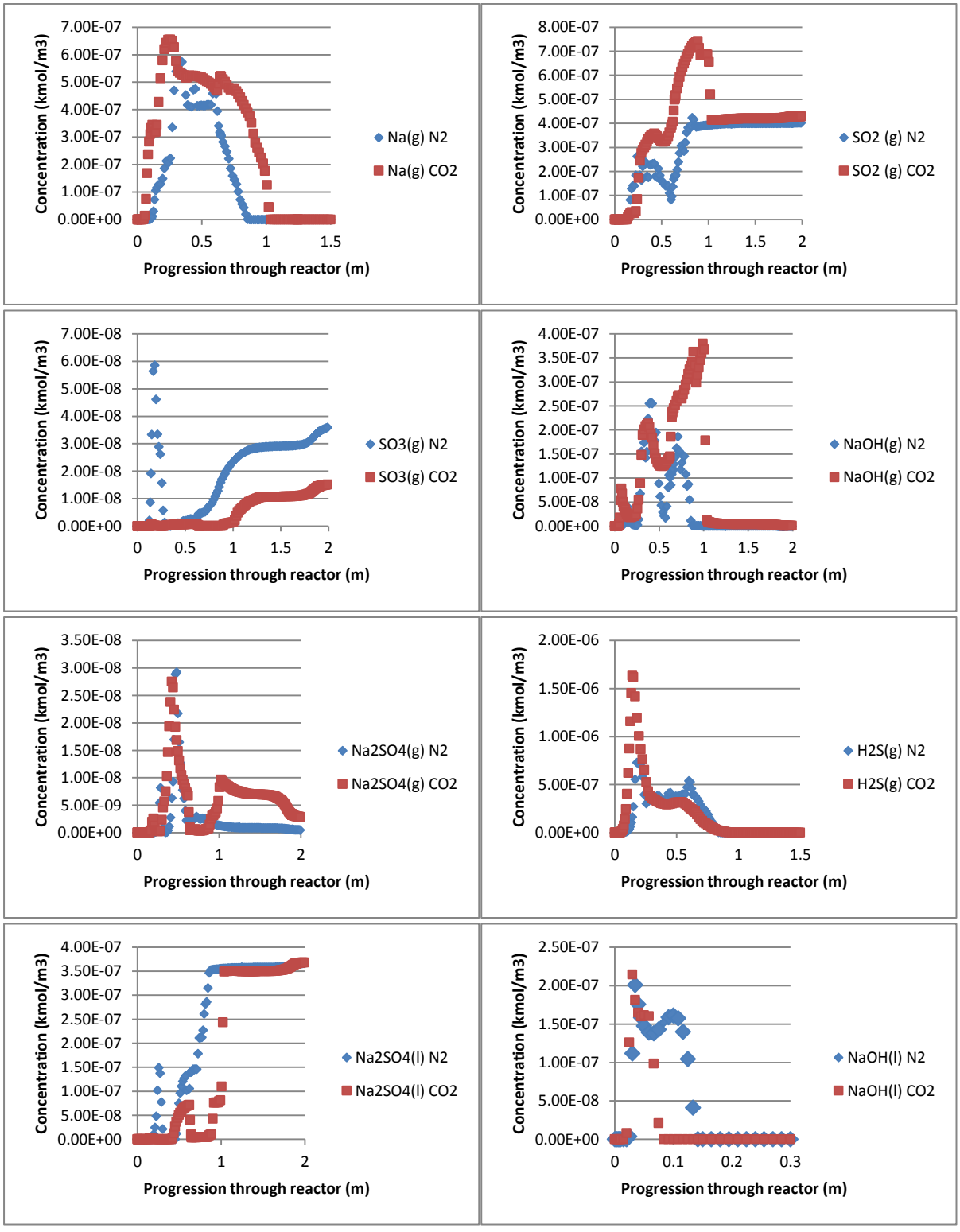

Figure 2.14 Gas concentrations along centre line of reactor. (a)12 O_2 in N_2, (b)12% O_2 in CO

Detailed results for the concentration profiles of individual species are further depicted in both ***Figures 2.13*** and ***2.14***. In Figure 2.13 are the two panels comparing the results for the two combustion modes. One can see the considerable changes in terms of the emission profile when the combustion mode shifts from the air-firing to the oxy-fuel mode. For instance, the gaseous Na (g) has a much narrower span in the air-firing mode, disappearing at the distance before 1 m. However, it lasts continuously from 1 m till the end of the reactor, suggestive of a slow emission of this troublesome elements due to a slower conversion of char in the CO_2-rich environment. The similar difference can be observed for the other species as well.

The details are given for the individual species separately in ***Figure 2.14***. Regarding the emission of Na-bearing species, again one can see a slow and longer duration for the profiles of Na (g), NaOH (g) and even Na_2SO_4 (g). In contrast, the other two Na-bearing species including NaOH (l) and Na_2SO_4 (l) show the opposite trends, suggestive of a suppression on their formation under the oxy-fuel combustion mode. Due to this, the ash deposition and slagging/fouling propensity shall be changed considerably under the oxy-fuel combustion mode.

2.5 Ash formation and deposition modelling

The ash formation and deposit modelling was further conducted via the combination of computational fluid dynamics (CFD) modelling and FactSage thermodynamic database. The flue gas temperature profile in the $3MW_{th}$ pilot scale boiler was first predicted by the CFD Fluent. Afterwards, the boiler was segregated into ten zones assuming the temperature in each zone is constant, and the two zones next to each other are connected for the flow of the solid ash powders, whereas the slag phase is assumed to deposit in the zone where it is formed. In addition, a portion of the solid particles is assumed to deposit with slag together in the zone where it is formed. This portion was determined by the experimentally measured deposit inside the boiler. The un-deposited solid powder is termed as the bypass stream to move into the next zone.

The schematic for the ash formation simulation flow is shown in ***Figure 2.15*** below. The program code was written in Fortran and is shown as appendix in the end of this report.

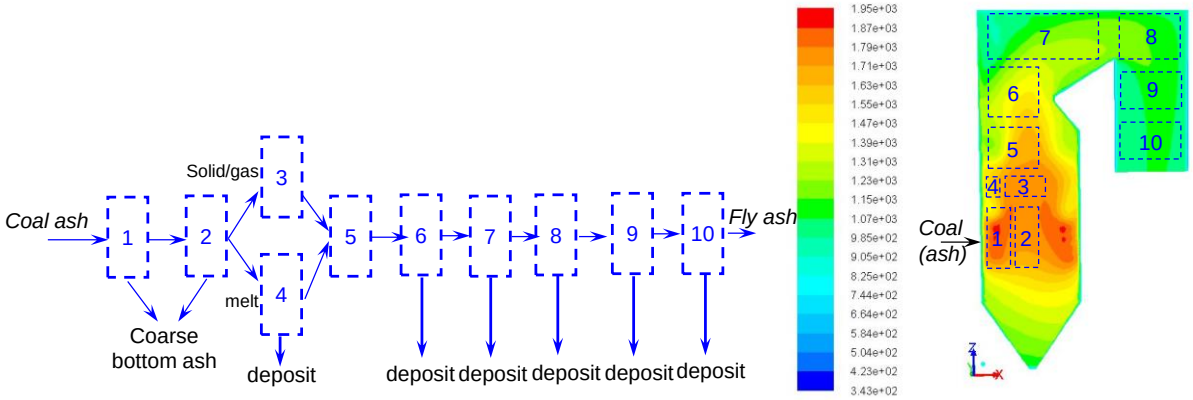

Figure 2.15 Ash formation and deposition modelling scheme

With regarding the flue gas temperature profile shown in ***Figure 2.16***, it is clear that the temperature for flue gas is quite the same between the two combustion modes, air-firing and oxy-fuel mode except the initial coal feeding stage where the cold recycled flue gas is not warmed up. However, this is not expected to affect the ash formation since ash formation only takes place once the temperature of flue gas rises to above 600^{o}C after the initial de-volatilisation stage. As shown in ***Figure 2.17***, the ash deposition ratio is the highest for Hazelwood ash at 1250^{o}C which is the burner zone and even at 771^{o}C for the super-heater zone. This is because of the abundance of alkali and alkaline earth metals in this coal, which are easily to melt and to form sulphate that can deposit on the super-heater surface. Change on the combustion mode from air-firing to oxy-fuel results in a considerable alteration on the ash deposition ratio. As shown in ***Figure 2.18***, Loy Yang ash has the largest deposition rate at the burner zone which is still shifted to around 1250^{o}C. This is because of the use of higher oxygen content, 27-30% and thus the slower flue gas flow rate in the boiler. With regarding the other two coals, their ash deposition rate in the oxy-fuel combustion was also increased compared to the air-firing result. This is because the ash fusion temperature in brown coal is very sensitive. Any increase on the flue gas temperature will enhance the ash melting and deposition propensity. A slower flue gas rate under the oxy-firing mode is also in favour of the promoting the residence time for ash particles inside the boiler. Moreover, based on the thermodynamic equilibrium prediction results in Figures 2.13 and 2.14, the preferential formation of abundant Na_2SO_4 (g) under the oxy-fuel combustion mode is also in favour of the ash deposition, because the gaseous species easily touch and even penetrate inside the fresh tube surface, thereby

assisting in building up the initial deposition layer which is sticky enough to capture more solid particles.

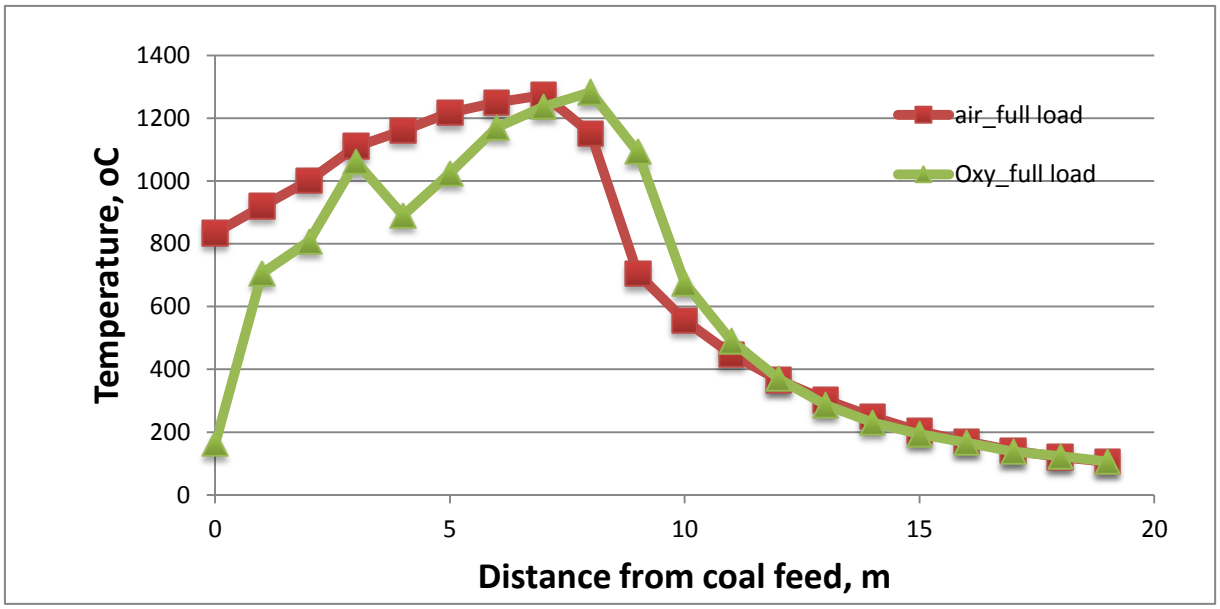

Figure 2.16 Temperature profile of flue gas along the furnace height

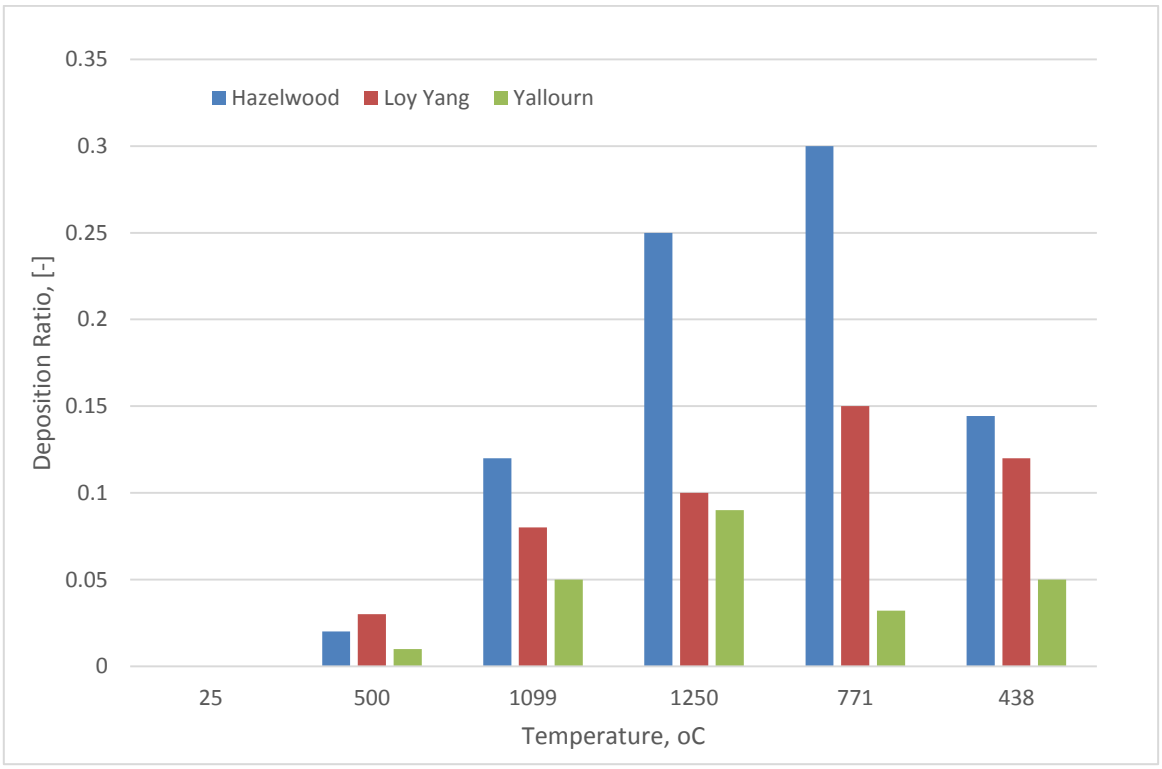

Figure 2.17 Deposition ratio for the ash in three Victorian brown coals during the air-firing.

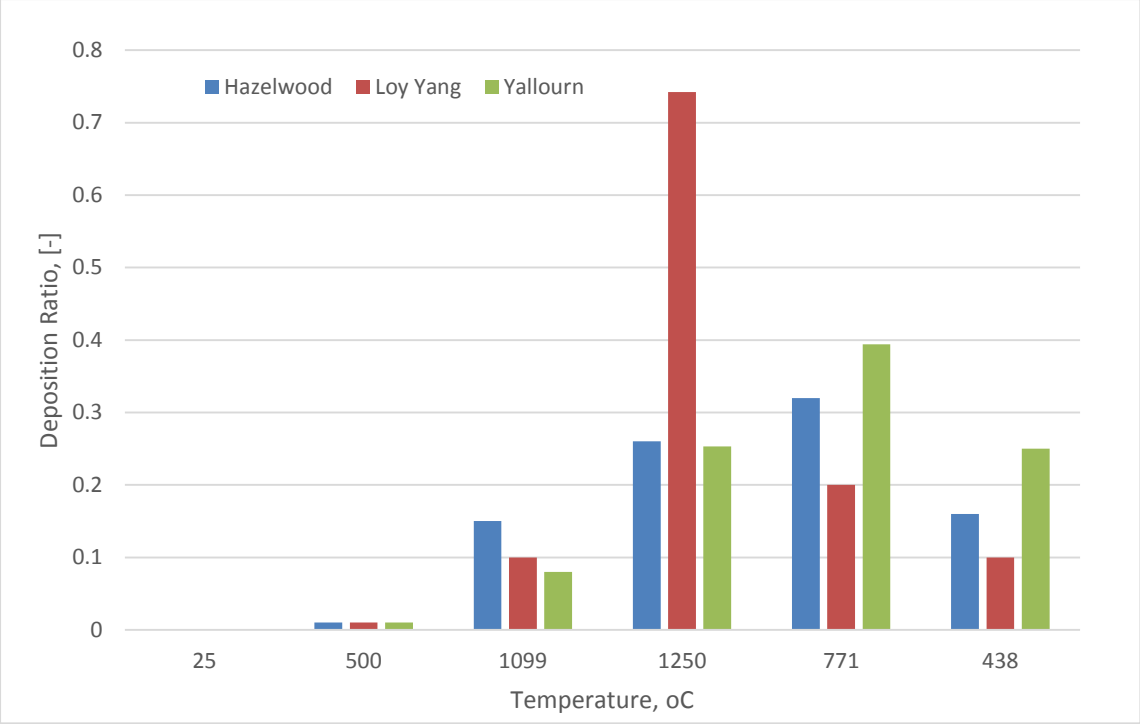

Figure 2.18 Deposition ratio for the ash in three Victorian brown coals during the oxy-firing mode.

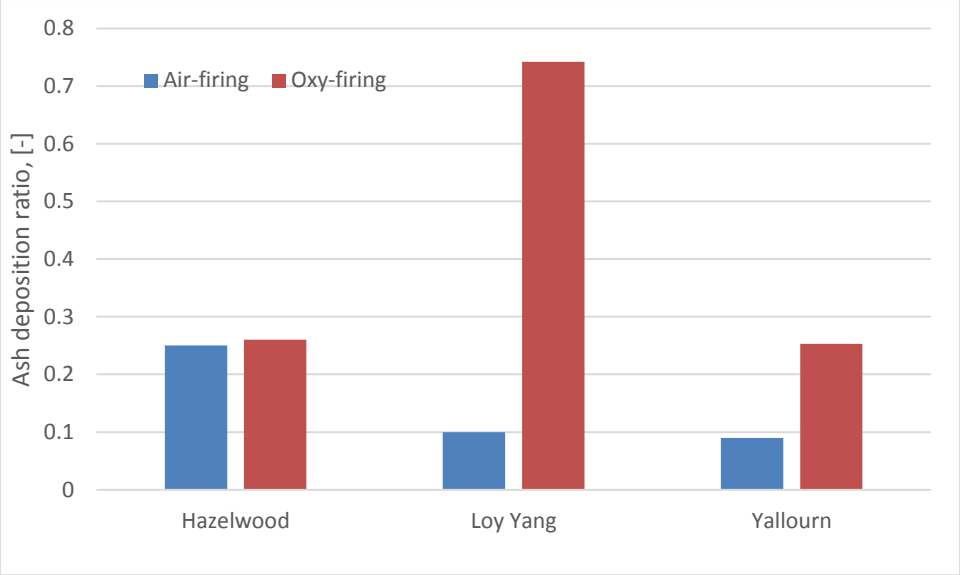

Figure 2.19 Ash deposition ratio between the combustion modes in the burner zone

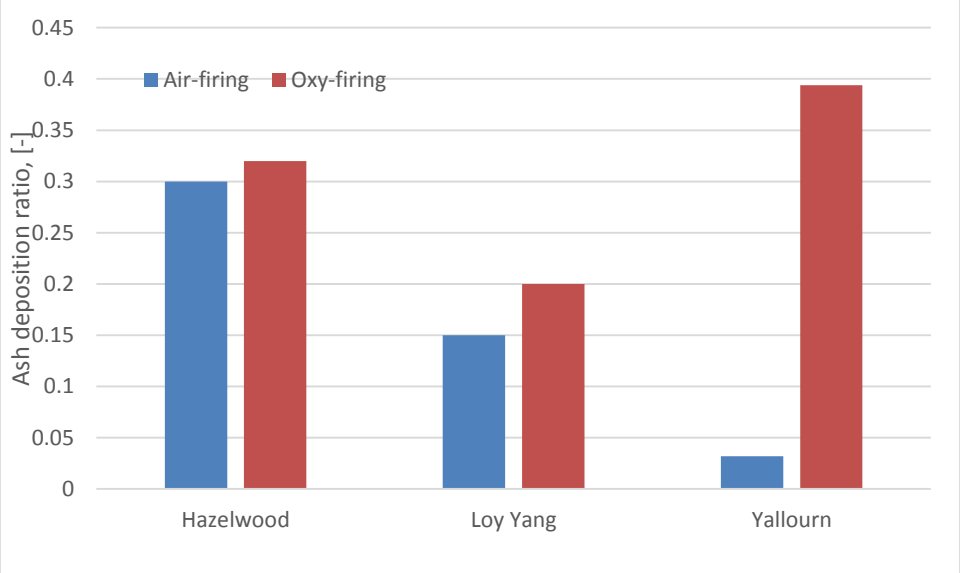

Figure 2.20 Ash deposition ratio between the combustion modes in the super-heater zone

As further shown in ***Figures 2.19*** and ***2.20*** for the comparison between the two combustion modes, the Hazelwood ash has no change in the burner zone when the combustion shifts from air-firing to oxy-fuel combustion. However, Loy Yang and Yallourn ashes are changed dramatically. This means the flue gas in the oxy-firing burner zone is too hot for these two ashes to withstand. Interestingly, for the super-heater zone where the sulfation of ash is favoured, the Hazelwood ash and Loy Yang ashes have little change on their deposition ratio. However, the iron-rich Yallourn ash has more deposited on the super-heater surface. This could be due to the recycling of the sulphur-rich flue gas causing the sulfidation and sulphation of

iron in the super-heater zone. The resultant iron sulphide and sulphates easily melts compared to iron oxide and magnesium ferrite that are preferentially formed under the conventional air-firing mode.

2.6 Conclusion

Both thermodynamic equilibrium prediction and experiments have been conducted to evaluate the ash formation and deposition rates for the Victorian brown coal ashes under the oxy-fuel combustion mode. The major results achieved are as follows:

- Oxy-fuel environment promotes the release of Na to the slag phase, which in turn contributes to an easier deposition and slightly enhanced slagging in the burner zone.
- Considerably less H_2S is formed under the oxy-fuel condition, and SO_3 will be slightly lower.
- Steam present in the furnace will significantly raise the concentration of H_2S and Na_2SO_4 and lower SO_3 only in high concentrations.
- For the ash formation under the oxy-fuel conditions, the sulfation and even carbonation are critical in super-heater zone and afterwards. In the combustion zone where coal flame is formed, the ash formation is thermodynamically controlled. However, upon the decrease in the flue gas when it flows downwards, the reaction rate control turns important. A simply ash formation model was developed by coupling FactSage and ChemSage together. The model has been fully validated, in particular for the high-temperature combustion zone where the ash formation is thermodynamically controlled.
- The ash deposition rate varies greatly with the type of brown coal. For the three coals tested in a 3MWth pilot-scale furnace, Yallourn ash is most sensible. Although its deposition rate for slagging is least in the burner zone, a large deposition rate was observed for this ash in the super-heater zone. This shall be due to the recirculation of flue gas that is made up of steam and SO_2.

2.7 Reference

[1] Amir Attar. Chemistry, thermodynamics and kinetics of reactions of sulphur in coal-gas reactions: a review. Fuel, 1978, 57: 201-212.

[2] Thmpson FC, Tilling N. J Soc Chem Ind. 1924, 49(3): 37.

[3] *Khundkar MH. Indian J Chem. 1947, 24: 407.*

[4] G Hu, KD Johansen, S Wedel, JP Hansen. Decomposition and oxidation of pyrite. Pro. Energy Combust. Sci. 2006, 32: 295-314.

[5] Esam Jassim, Steven A Benson, F M Bowman, W S Seames. The influence of fragmentation on the behaviour of pyrite particles during pulverized coal combustion. Fuel Processing Technology. 2011, 92: 970-976.

[6] S Srinivasachar, A Boni. A kinetic model for pyrite transfrmations in a combustion environment. Fuel. 1989, 68: 829-836.

[7] S Srinivasachar, JJ Helble, A Boni, N Shah, G Huffman, F Huggins, Mineral behaviour during coal combustion. 1. Pyrite transformations. Prog. Energy Combust. Sci. 1990, 16: 293-302.

[8] Asaki Z, Mori S, Ikeda M and Kondo Y. Met. Trans. B. 1985, 16B:627-638.

[9] AR Mclennan, GW Bryant, CW Bailey, BR Stanmore, TF Wall. An experimental comparison of the ash formed from coals containing pyrite and siderite mineral in oxidizing and reducing conditions. Energy & Fuels 2000; 14: 308-315.

[10] H U R Memon, A. William, P T Williams. Shock tube pyrite of thiophene. International journal of energy research. 2003; 27: 225-239.

[11] Hurley CD. Ph D Thesis, the University of Surrey. 1979.

[12] J. C. Kramlich. "The Fate and Behavior of Fuel-Sulfur in Combustion Systems". PhD thesis. Washington State University, Washington, USA. 1980

[13] S. C. Hunter. Formation of so3 in gas turbines. Transactions of the ASME. 104. 44–51. 1982.

[14] X Han. Modeling and simulation of SOx and NOx reduction processes on pulverized coal furnaces. Cuvillier Verlag Gottingen, 2003.

[15] G. Offen. Modelling of SO3 formation process in coal-fired boilers. EPRI report, 2007.

[16] W Weiseiler, GK Roy. Kinetics of lime-limestone sulfation: review of lime reactivity and sulfation kinetics in the dry limestone desulfurization processes. High Temperature High Pressures, 1981, 13: 333-345.

[17] Michael Muller, U Schnell, G Scheffknecht. Modelling the fate of sulphur during pulverized coal combustion under conventional and oxy-fuel conditions. Energy Procedia, 2013, 37: 1377-1388.

Chapter 3 Characteristics of SO_3 formation rate of Victorian brown coal during air- versus oxy-firing

3.1 Preliminary results of SO_2 and SO_3 emission in pilot-scale oxy-fuel experiments of Victorian brown coal

Regarding air-firing and oxy-fuel combustion of Victorian brown coal, flame stability and combustion characteristics have been comprehensively investigated in the 3 MWth pilot-scale furnace in Shanghai Boiler Works Co Ltd through the previous ANLEC/BCIA project. Meanwhile, preliminary data of SO_2 and SO_3 emission were also collected on site, as shown in ***Table 3.1***. In comparison to the conventional air-firing result for 265 ppm SO_2, the SO_2 emission of Victorian brown coal oxy-firing is dramatically increased to approximate 81 5ppm. The similar enhancement of SO_2 emission during oxy-firing was reported in other pilot-scale experiments, shown in ***Table 3.1***, in which the SO_2 emission from oxy-firing is generally 2.7-5.3 times than the conventional air-firing.

Regarding SO_3 emission in air combustion, the reported SO_3 emission in the literature is about 7-65 ppm, which varies randomly with literature. However, the SO_3 emission during Victorian brown coal air-firing, as conducted by us, is very low, reaching 0.08 ppm n flue gas. The SO_3 from oxy-firing case is even below the detection limit. Therefore, our investigation would focus on the difference of SO_3 emission, which was conducted through a series of lab-scale experiments.

Table 3.1 Comparison of SO_2 and SO_3 emissions tested in pilot-scale investigation of Coal oxy-fuel combustion

Facility	coal	FGR	O_2, %	Air-firing, ppm		Oxy-firing, ppm		Reference
				SO_2	SO_3	SO_2	SO_3	
Our 3MWth facility	**Vic brown coal**	**wet**	**5.0**	**265**	**0.08**	**~815**	**N/A**	
Chalmers 100KWth furnace	lignite	dry	5.5	885	19-22	2438	42-54	*3rd combust. Conf., 2013*
Vattenfall 30MWth oxyfuel plant	Bitu.		4.5	525	-	2800	-	*Energy procedia, 2011, 4: 941-950*
IHI tests	Bitu.	dry	5.0	~200	~2	~600	~7	*Pro in energy and combust sci, 2011, 37:69-88*

1MWt, EON Facility, UK				600		~1750-2300		*www.captureandstorage.info/networks/oxyfuel3rd2.htm,*
Burner flow reactor at Brigham Young Univ	lignite	wet	3.0	834	9	-	-	*Combust flame. 2013, 160: 2529-2539.*
	Sub. Bitu		3.0	262	8	800	-	
	Bitu		3.0	2583	53	7348	65	

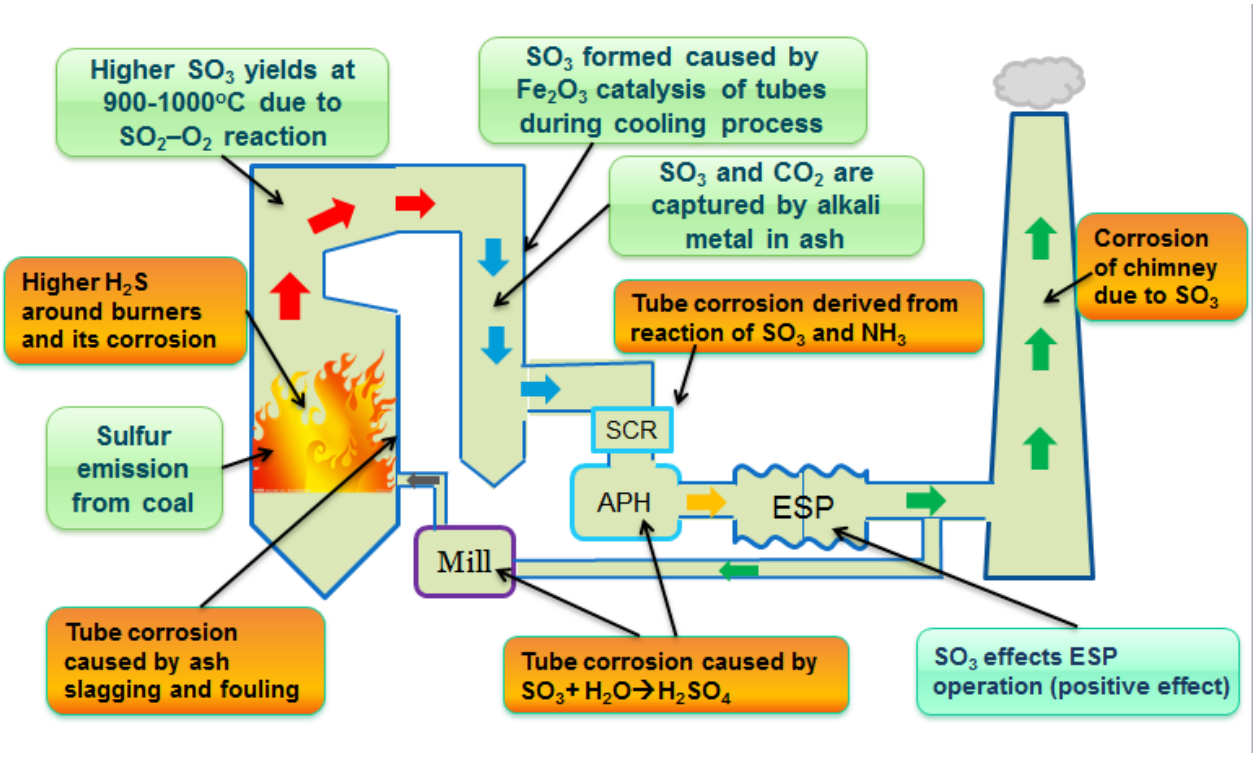

Figure 3.1 SO_3 formation mechanism and its influence on tube corrosion

Figure 3.1 outlines the SO_3 formation mechanism during coal combustion and its problems related to tube corrosion. Sulphur releasing from coal particle generally occurs within coal flame zone where the temperature is the highest in a boiler. As has been confirmed by our previous test, ~80wt% sulphur is released as gaseous hydrogen sulphide (H_2S) during the initial thermal pyrolysis of Victorian brown coal. The remaining sulphur is released during the char oxidation period. If oxygen supply is enough, sulphur oxide is generated through the oxidation of H_2S. Otherwise, a portion of H_2S remains around the burner where oxygen is insufficient, causing the corrosion of water tube surface.

The formation of SO_3 mainly happens in 900-1000oC due to the oxidation reaction of SO_2 by $SO_2+0.5O_2=SO_3$.Such a temperature range is for the super-heater and reheater zones of a

pulverised coal-fired boiler. In addition, the catalytic influences of metal oxides are notable towards SO_3 formation. A variety of oxides including alfa-Fe_2O_3, gama-Fe_2O_3, Fe_3O_4, and Al_2O_3 have been reported to promote the oxidation of SO_2 into gaseous SO_3. Another significant influence of ash on SO_3 emission is the sulphation behaviour of alkali and alkaline metals in coal ash (Ca, Mg, Na), which can react with SO_3 so as to inhibit the SO_3 emission in flue gas. These two behaviours could co-exist in a boiler and affect each other, which in turn brings up the complexity of SO_3 emission. In the orange boxes in Figure 3-1, the hazards derived from SO_3 in flue gas are further illustrated in detail. Most of the key parts of a boiler facility including mill, SCR, APH, ESP and chimney are at risk for the potential corrosion caused by SO_3, if its concentration is too high. Therefore, SO_3 emission characteristic was investigated in detail in the second milestone of this project.

3.2 Experiments for SO_3 formation of Victorian brown coal

A lab-scale fixed-bed reactor (FBR) was used to measure the SO_3 emission as a function of fly ash composition. The schematics of FBR are illustrated in ***Figure 3.2***. A coal ash sample was first loaded through a side pipe into the FBR. Subsequently, the side pipe is sealed and the reactant gases were introduced into reactor to simulate the typical flue gas compositions for both air- or oxy-firing cases. The SO_3 and SO_2 collection impinge trains were installed downstream the furnace. The collection impinges were designed to trap SO_2 and SO_3 separately based on the difference of their dew points. Hereby, 75-85oC water bath was used for separating and collecting SO_3. All the liquid samples and coal ash residue are tested by ICP-OES, XRF and XRD.

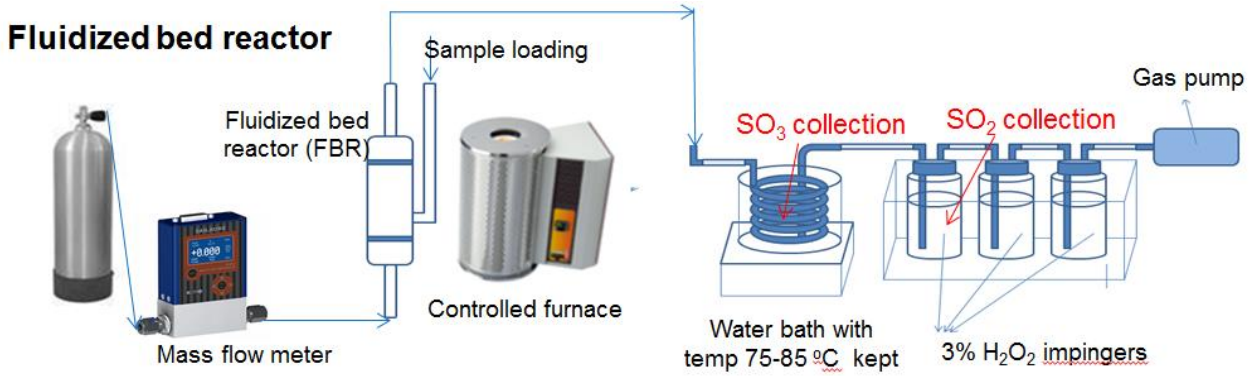

Figure 3.2 Schematic diagram of fluidized bed reactor

Table 3.2 Experimental conditions

Particle samples	Nine ash samples collected from different power plants; α-Fe_2O_3, γ-Fe_2O_3, Fe_3O_4, Al_2O_3
Temperature	650^{o}C, 750^{o}C, 900^{o}C
Fly ash mass in FBR	1 g
Gas composition and rate	3000 ppm SO_2, 4% O_2 in CO_2; 1 L/min
Gas residence time	0.1 *s*
Sampling time per run	10 *min*

All experimental conditions are tabulated in ***Table 3.2***. The fly ash samples were obtained from nine power plants including Yallourn Power Plant and Loy Yang B burning Hazelwood coal. The fly ash samples have >80% less than 40 μm in diameter. The ash composition of fly ash samples are tested by X-ray Fluorescence (XRF), as shown in ***Table 3.3***. ***Table 3.4*** lists the mineralogical properties of the fly ash samples quantified by X-ray diffraction (XRD).

The reagent-grade pure compounds, including α-Fe_2O_3, γ-Fe_2O_3, Fe_3O_4 and Al_2O_3, were applied in the experiments to clarify the foundational catalytic influence on SO3. All the pure compounds were ground to less than 40 μm in diameter prior to being used. The flue gas temperature is controlled at 650, 750 and 900 ^{o}C with 3000 ppmV SO_2 and 4vol% O_2 included within it. The gas residence time is set at 0.1 s for a mass flow rate of 1 L/min.

Table 3.3 Elemental compositions of ash samples tested

Ash samples	Yallourn ash	Hazelwood ash	XJ (without clay)	XJ (with clay)	PDS	HS	HLH	YQ	SH
Coal type	brown	brown	sub-bitu	sub-bitu	bitu	bitu	bitu	bitu	bitu
Fe_2O_3	49	19.09	2.077	7.17	7.395	1.15	3.753	4.479	10.92
Al_2O_3	3.031	3.74	7.117	10.56	25.24	28.88	12.81	30.75	13.32
MgO	23.95	31.03	14.46	11.81	2.232	0.1282	9.26	0.017	9.88
Na_2O	3.12	0.21	8.2	6.08	0.28	1.17	0.68	0.91	0.2
CaO	9.667	29.42	41.93	28.29	14.84	13.66	15.24	9.108	24.26

K_2O	0.1547	0.149	0.4025	0.8142	1.095	1.402	0.802	0.4489	0.5009
SO_3	6.253	10.12	9.809	6.396	5.095	2.678	5.162	2.617	11.39
SiO_2	2.91	3.89	13.37	26.81	42.06	48.73	50.65	49.21	27.09
other	1.9143	2.351	2.6345	2.0698	1.763	2.202	1.643	2.460	2.439

XJ=Xinjiang; PDS=Pingdingshan; HS=Heshan; HLH=Huolinhe ; YQ=Yangquan; SH=Shenhua.

Table 3.4 XRD analysis for ash samples used in SO_3 experiments

	Hazelwood	**Yallourn**	XJ, no clay	XJ, with clay	HS	HLH	YQ	PDS	SH
Quartz, SiO_2	17.2	1.46	0	2.2	38.6	48.7	66.5	40.9	25.9
Cristobalite, SiO_2	0.2	0	0	0	0	0.2	0.7	0.1	0.6
Keatite, SiO_2	0	0	0.5	0.4					
Lime, CaO	0	0	3.4	0.5					
Calcite, $CaCO_3$	10.1	3.08	3.1	1					
Gypsum, $CaSO_4 \cdot 2H_2O$	0.6	0	0	0	1.1	0	0	0	2.2
Bassanite, $CaSO_4 \cdot 0.5(H_2O)$					0	0.9	1.6	1.3	2.7
Anhydrite, $CaSO_4$	18.2	0	2.2	3.1	12.7	7.8	10.8	24.1	35.1
Bassanite, (super) $CaSO_4 \cdot 0.5(H_2O)$	0.6	0	0	0	1.9	0	0.4	0	0
C_4AF					0.3	0.7	0.3	0.2	0.3
C_2F (Ca_2Fe_2O5)	14.3	0	0	0	0	4.8	1.2	1.7	1.1
C_4AF ($Ca_2Fe_{0.28}Al_{1.72}O_5$)	4.6	0	0	0					
marialite (Na_2SO_4 $10H_2O$)			1.9	0					
Glauberite, $Na_2Ca(SO_4)_2$	1.6	0	3.4	2.6	0.9	2.9	1.5	1.1	3.8
Thenardite,Na_2SO_4	2	0.385	4	1.5	0	0.4	0.7	0	0.2

Periclase (MgO)	23.2	2.77	3.4	1					
Magnesioferrite ($MgFe_2O_4$)	1.5	49.51	0	0					
Hematite, α-Fe_2O_3	**0**	**0**	**1.4**	**1.2**	**5.6**	**14.7**	**4.4**	**17.2**	**16.7**
maghemite (γ-Fe_2O_3)	**0**	**12.86**	**0**	**0**					
Magnetite, Fe_3O_4	**0**	**0**	**0**	**0.8**	**1.3**	**3.2**	**2.1**	**0**	**3.8**
merwinite	0	0	3.2	2.4					
Mullite (Al_2O_3:SiO_2)					29	12.9	7.4	13	4.5
Alumina, beta,alkali-free, Al_2O_3					0.1	0.4	0.3	0.3	0.4
Alumina, delta-					8.5	0.4	0	0	2.8
Alumina, eta- 1					0	0.2	0.7	0.1	0
Alumina, gamma					0	1.8	1.5	0	0
Mullite ($3Al_2O_3$.$2SiO_2$)	1.9		0	0					
Gehlenite ($Ca_2(Al(Si,Al)_2O_7$)			3.5	1.3					
Amorphous amount	3.8	23	70	82					

Note: XJ=Xinjiang; PDS=Pingdingshan; HS=Heshan; HLH=Huolinhe ; YQ=Yangquan; SH=Shenhua.

3.3 Experimental results: Catalytic behavior of iron oxide and aluminum oxide in ash on SO_3 formation

Figure 3.3 shows the accumulated SO_3 formation ratio, the percentage of SO_3 volume in total S-based gas volume, as a function of flue gas temperature. It is evident that, the reaction temperature is most critical for SO_3 formation. In ***Figure 3.3***, the black line (blank case) denotes the homogenous SO_3 formation rate derived from the reaction of $SO_2 + 0.5O_2 = SO_3$, in which no any ash or solid samples was used. The homogenous formation rate of SO3 is favoured from 700^{o}C onwards. This result agrees well with the optimum temperature range of

700-1200ºC for SO_3 formation in I&EC research 2011, 50: 8505-14, as replicated in ***Figure 3.4.***

The catalytic influences of pure metal oxide on SO_3 formation have been further confirmed in ***Figure 3.3***. In the case using α-Fe2O_3, the SO_3 emission reaches its peak at 700ºC, the magnitude of which is eight times higher than the blank case for the homogenous formation of SO_3. The pure oxide γ-Fe_2O_3 is second important in SO_3 formation at the same peak having a magnitude which is only half of α-Fe_2O_3. Fe_3O_4 has less SO_3 formed and its optimum temperature slightly shifts to 750 oC. Regarding the last oxide Al2O_3, the SO_3 formation upon its existence commences at 600 ºC and remains stable after 900 ºC. In light of this,

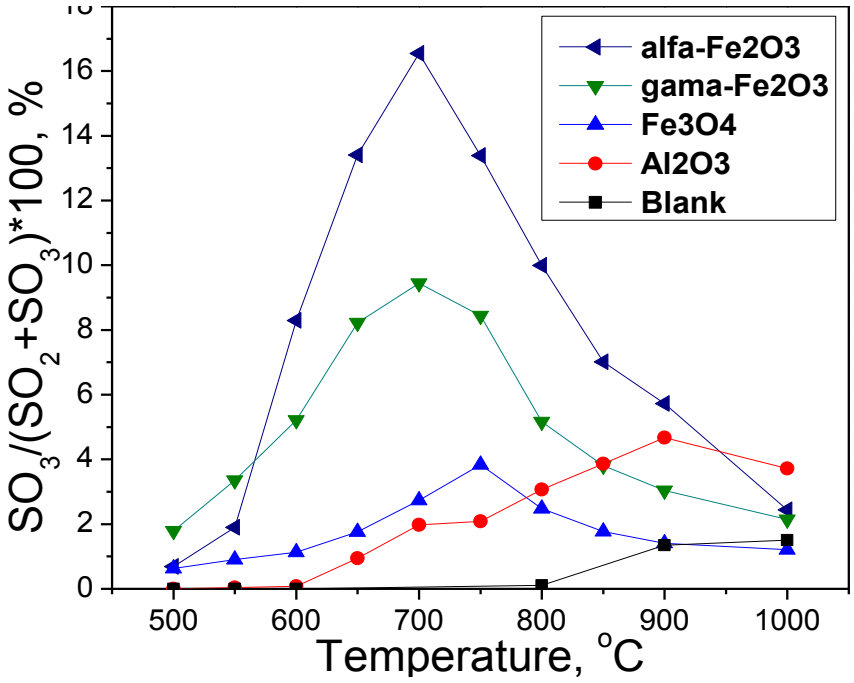

Figure 3.3 Accumulated SO_3 formation rate for the cases that catalytic metal oxides were exposed in 3000 ppm SO_2 in CO_2

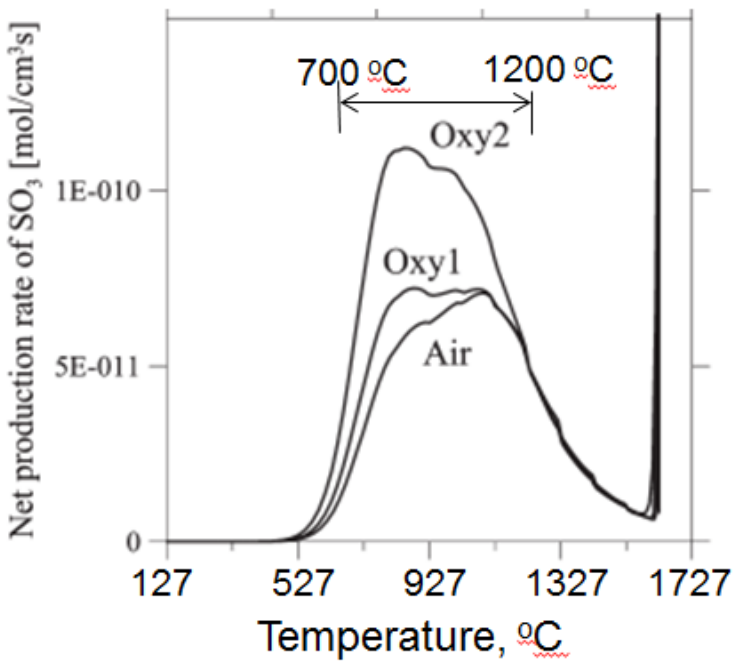

Figure 3.4 Homogenous formation rate of $SO_2+0.5O_2 \rightarrow SO_3$ as a function of temperature, stated in *I&EC research, 2011, 50: 8505-14*

3.4 Experimental results: SO_3 formation upon the existence of fly ash in flue gas

Regarding the loading of coal fly ash in flue gas, the SO_3 formation ratio is shown in ***Figure 3.5***, where the homogenous SO_3 formation levels were also included for comparison.

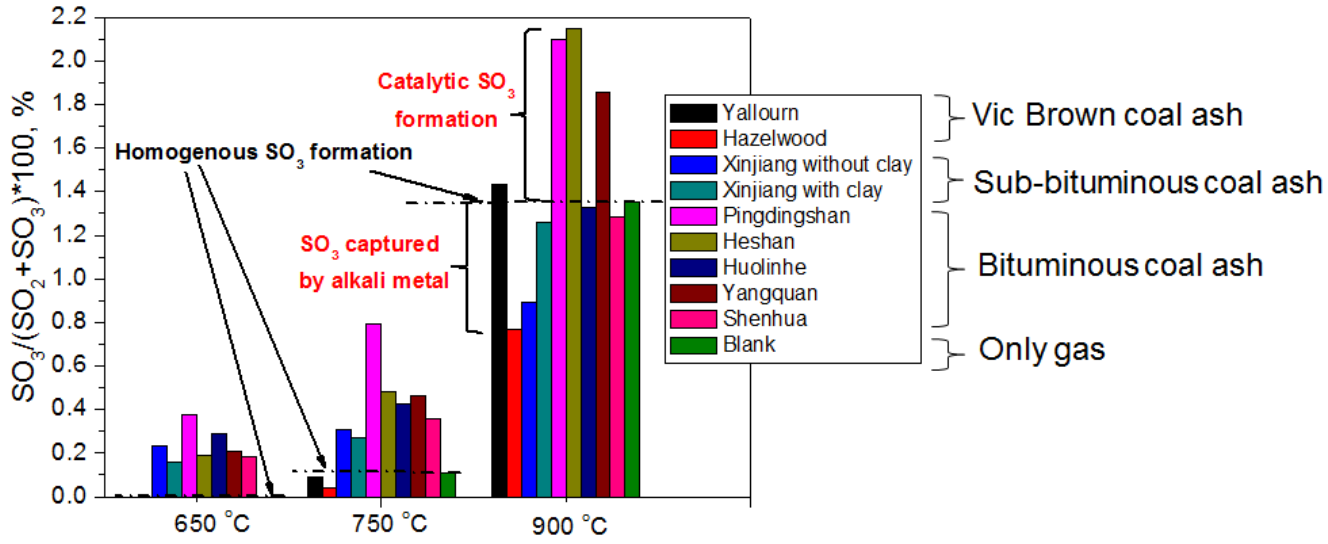

Figure 3.5 SO_3 formation ratio for various coal fly ashes exposed in 3000 ppmV SO_2 diluted in CO_2

The SO_3 emission is highest at 900°C, regardless of fly ash type. Compared with homogenous formation levels, the SO_3 emission upon the existence of fly ash in flue gas varies significantly with fly ash type. For the two Victorian brown coal fly ash samples with high alkali metals and alkaline earth metals, MgO (23.95 wt% for Yallourn ash, 31.03 wt% for Hazelwood ash), CaO (9.67 wt% for Yallourn ash and 29.42 wt% for Hazelwood ash), their SO_3 emissions are near zero at 650oC. At 750oC, their SO_3 emissions were both less than the reference baseline, implying the capture of SO3 by heterogeneous sulphation reaction. At 900oC, the SO_3 emission of Hazelwood ash is still less than the homogenous formation level. However, the SO_3 emission of Yallourn ash is above the homogenous formation level, which should be due to the abundance of Fe_2O_3 (49 wt %) within this unique fly ash sample. Back to Table 3-4 for the quantitative XRD results regarding above coal ashes tested. Yallourn ash has 12.86% gama-Fe2O3, compared with Hazelwood ash, in which no gama-Fe_2O_3 found.

Figure 3.5 also indicates that the SO_3 emission is generally less upon the existence of Victorian brown coal ash than the other bituminous coal and sub-bituminous coal ashes. For each fly ash sample, the exceeding value of SO_3 formed upon its existence can be interpreted as the catalytic formation of SO_3 caused by the catalysts in ash (e.g. Fe_2O_3 and Al_2O_3). On the other hand, the reduced value relative to the baseline for homogeneous oxidation of SO_2 can be attributed to the sulphation behavior of alkali and alkaline earth metals including Na, K, Ca and Mg in ash according to the following heterogeneous reactions where M stands for Ca/Mg or Na_2/K_2:

$$MO + SO_2 + 1/2\ O_2 = MSO_4$$
$$MO + SO_3 = MSO_4$$

Based on above understandings, an empirical factor, namely SO_3 catalytic parameter (rso3), was developed to interpret the competition between catalytic formation of SO_3 (positive) and sulphation reaction for the consumption/capture of SO_3 (negative). The SO_3 catalytic parameter is expressed as a linear function of the concentration of individual metal oxides in Equation 3-1. The value of rso3 greater than zero indicates a positive formation of SO_3 upon the catalysis of ash-forming metal oxide. In contrast, a value of rso3 less than zero is a sign of the heterogeneous capture of SO_3 by alkali and alkaline earth metals within the ash.

$$r_{SO_3} = k_1[Fe_2O_3] + k_2[Al_2O_3] - k_3([CaO] + [MgO] + [Na_2O] - [SO_3])$$
$$= \begin{cases} > 0, & SO_3 \text{ emission is higher than homogenous formation.} \\ < 0, & SO_3 \text{ captured by alkali metals in ash} \end{cases} \quad \text{(Equation 3-1)}$$

Where, [Fe_2O_3], [Al_2O_3], [CaO], [MgO], [Na_2O], and [SO_3] are the mass fractions of metal oxides in ash samples. The empirical coefficients k1, k2 can be obtained from ***Figure 3-3***, whereas another coefficient k3 can be empirically achieved from ***Figure 3-5***. They are given as below.

$$k_1 = \begin{cases} 2.08 & (600 - 800^{o}\mathrm{C}) \\ 1.76 & (800 - 900^{o}\mathrm{C}) \\ 1.50 & (900 - 1000^{o}\mathrm{C}) \end{cases} \quad k_2 = \begin{cases} 2.28 & (600 - 800^{o}\mathrm{C}) \\ 2.40 & (800 - 900^{o}\mathrm{C}) \\ 2.00 & (900 - 1000^{o}\mathrm{C}) \end{cases} \quad k_3 = 0.7$$

Upon the insertion of ash properties (***Table 1.3***) into Equation 1-1, one can then resolve the SO_3 catalytic parameters for individual ashes and establish the correlation between this parameter and SO_3 formation ratio, as demonstrated in ***Figure 3-6***. The positive correlation between these two variables proves that the establishment of SO_3 catalytic parameter is a useful way to predict the SO_3 formation ratio in flue gas.

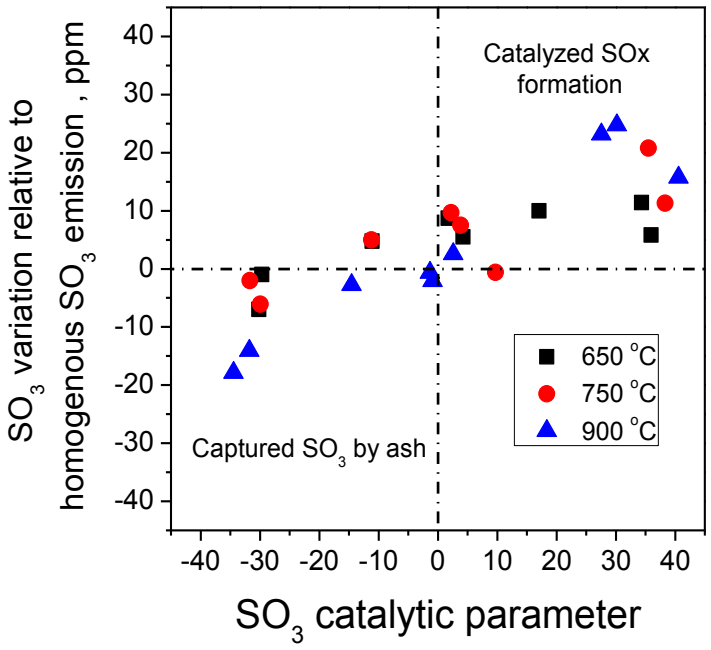

Figure 3-6 Empirical SO_3 catalytic parameter versus SO_3 formation ratio

3.5 Conclusion

The main conclusions for SO_3 formation upon the existence of Victorian brown coal fly ash in flue gas can be drawn as follows:

1) The tests clarified the catalytic impacts of metal oxides in ash on SO_3 formation, including α-Fe_2O_3, γ-Fe_2O_3, Fe_3O_4 and Al_2O_3. The reaction temperature was also critical, varying remarkably with oxide type.

2) The SO_2 concentration in flue gas reaches ~265 ppmV in conventional air-firing of Victorian brown coal. The SO_3 emission is less than 1 ppmV, which is much lower than the results reported for bituminous coal and sub-bituminous coals in the literature. This phenomenon is caused by the sulfation of abundant alkali and alkaline earth metals in Victorian brown coal ash.

3) An empirical catalytic parameter formula was proposed to correlate the emission of gaseous SO_3 and ash composition, which successfully describes the competition between catalytic effect of Fe_2O_3 and Al_2O_3 and sulphation reaction of alkali and

alkaline earth metals (Na_2O, K_2O, CaO and MgO). The combustion of yallourn coal resulted in the formation of 1.4% of SO_3 in total of S-bearing gases in flue gas at 900oC, which is slightly higher than the homogeneous formation rate for SO_3 due to the abundance of α-Fe_2O_3 in this fly ash. In contrast, the combustion of Hazelwood fly ash yielded approximately 0.8 vol% of SO_3 relative to ~1.3 % formed in blank case. This is due to the capture of a portion of SO_3 by the abundant CaO within Hazelwood fly ash.

Chapter 4 Experimental investigations on sulphation characteristics of Victorian brown coal ash

4.1 Experimental cases

A series of lab experiments were performed to further confirm the sulfation rate of Victorian brown coal ashes, including Hazelwood ash, Yallourn ash and referenced Xinjiang coal ash (typical sub-bituminous coal), as shown in the case lists in ***Table 4-1***. The lab-scale drop tube furnace was employed for the experiments to achieve oxy-firing flue gas atmosphere for 5%O_2 in CO_2 with the concentrations of SO_2 varying from blank (0 ppmV) to 1500 ppmV. Ash particle feeding rate was fixed at 0.4 g/min, and particle residence time was fixed at around 6 second in the furnace. The furnace temperature was set as 400, 600, 800 and 1000ºC. The volume rate of mixed gas was fixed at 10.0 L/min.

Table 4-1 Experimental cases in drop-tube furnace (DTF)

Fly ash samples	Hazelwood ash, Yallourn ash and Xinjiang coal ash (sub-bituminous), as obtained from power plants
Furnace temperature	400°C, 600°C, 800°C, 1000°C
Particle feeding rate	0.4 g/min
Gas composition	5% O_2 in CO_2; 0 / 500 / 1000 / 1500 ppm SO_2 ; 0 / 10% water vapour
Gas feeding rate	10 L/min
Particle residential time	~6 *s*
Particle size	<45 μm

4.2 Sulphation characteristics of Victorian brown coal ashes

Figure 4.1 shows the comparison of ash compositions amongst different flue gas conditions of combustion, *e.g.* air-firing vs oxy-firing at 800ºC and 1000ºC. The results for 400ºC and 600ºC were not shown here, because these two temperatures were found too low to cause any sulfation reactions. The SO_3 component in two Victorian brown coal ashes were both enhanced in oxy-firing, compared with the air-firing reference. The sulfation level of Hazelwood ash was also found higher than Yallourn ash, due to higher alkali metal in Hazelwood ash (as shown in ***Table 4.2***).

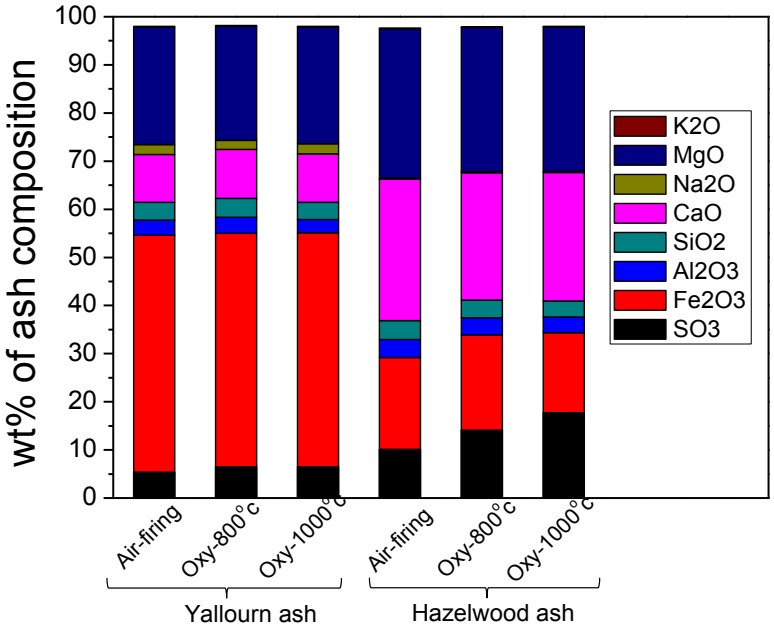

Figure 4.1 Influence of oxy-firing conditions on ash composition of Victorian brown coal ash, tested by XRF. The oxy-firing flue gas has 1500 ppm SO_2 and 5% O_2 diluted by CO_2.

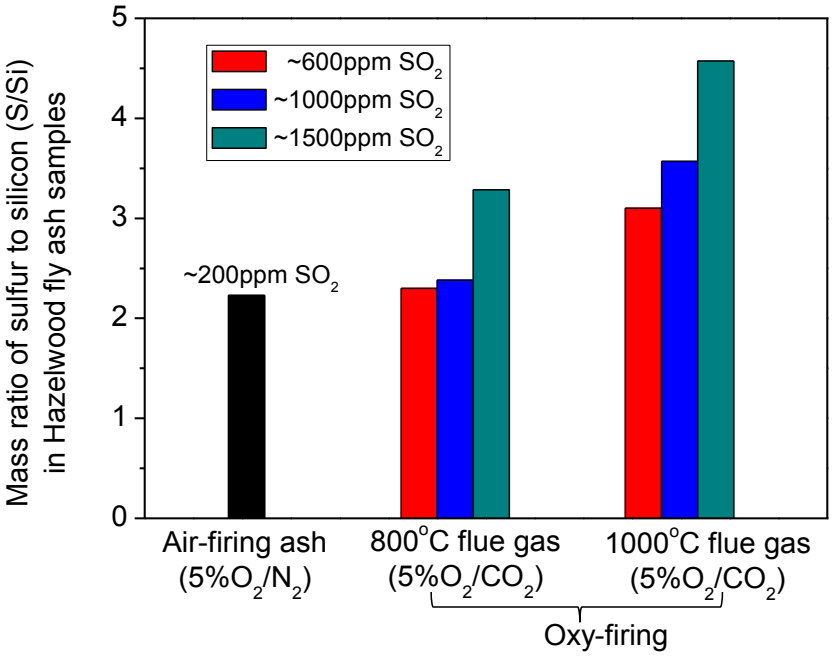

Figure 4.2 Influence of SO_2 concentration on the mass ratio of sulfur to silicon (S/Si) of Hazelwood fly ashes

The experimental conditions follow the flue gas composition found in the $3MW_{th}$ pilot-scale experiments, in which SO_2 concentration was found to be ~200 ppmV in air firing mode, whereas ~800 ppm SO_2 confirmed in the oxy-firing flue gas. Therefore, different SO_2 concentrations (600, 1000, 1500 ppm) were set in DTF oxy-firing experiments. The results of Hazelwood ash are shown in ***Figure 4.2***, showing the remarkable impacts of temperature and SO2 level on the sulfation extent of this fly ash. The mass ratio of sulphur to silicon (S/Si) was used in the figure, considering the fact that the silicon content in ash remains constant. In 800ºC flue gas with 600 ppm and 1000 ppm SO_2, the S/Si ratio in the resulting ash is trivial and similar with air-firing case where the SO_2 concentration is only 200 ppm. The sulfation of ash is not obvious. However, with the increase of SO_2 concentration to 1500 ppm, the mass content of S/Si is increased by ~1%. Regarding the oxy-fuel conditions at 1000ºC, the S/Si ratio was increased by 0.8, 1.2, 1.8% respectively, corresponding to 600, 1000, 1500 ppm SO_2 in flue gas. The S captured in ash at 1000ºC is higher than that at 800ºC. The reason lies in higher homogeneous SO_3 yielded at 1000ºC, which promote the sulfation reactions, $M+SO_3=MSO_3$ (M: Na, Mg, Ca).

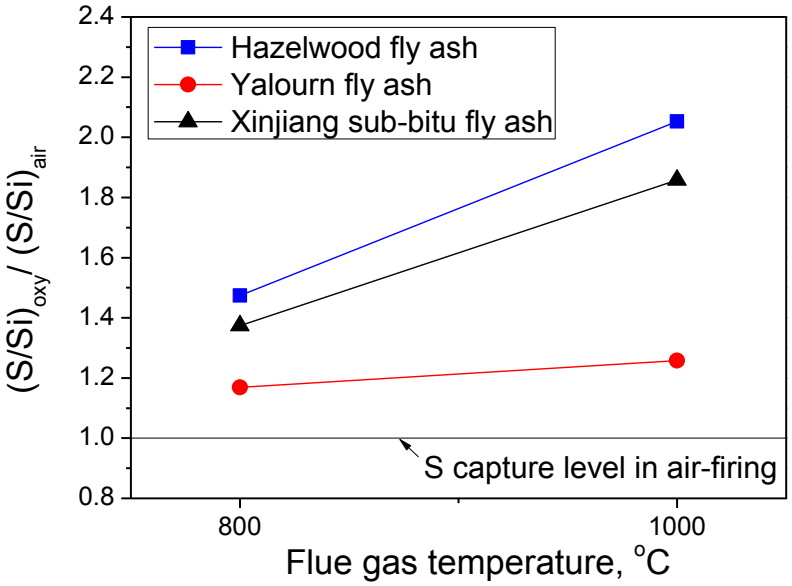

Figure 4.3 Mass ratio of S/Si contents of oxy-firing to air-firing regarding three coal fly ashes in 5%$O_{2,}$ ~1500 ppm SO_2 diluted in CO_2

Table 4.2 Total mol% of alkali metal oxides in ash

	MgO	Na_2O	CaO	K_2O	**Total alkali metal oxides**
Hazelwood ash	46.92	0.20	31.77	0.10	78.99
Xinjiang ash (no clay added)	21.58	7.90	44.70	0.26	74.43
Yallourn ash	46.56	3.91	13.42	0.13	64.03

Figure 4.3 illustrates the comparison of sulphuration level amongst Hazelwood ash, Yallourn ash and Xinjiang coal ash, as tested by XRF. The mass ratio of (S/Si) at oxy-firing to that at air-firing is used to clarify the difference between these two combustion modes. The reference line of $(S/Si)_{oxy}/(S/Si)_{air}=1$ denotes the S capture level in air-firing mode. The experimental dots in ***Figure 4.3*** show higher S level in oxy-firing when compared with air-firing. Hazelwood ash has highest sulphation capability, whereas Yallourn ash has the lowest sulfation extent, as conducted at 800ºC and 1000ºC in DTF.

Table 4.2 interpret the reason for the different sulfation extent. The total mole percentages are shown in ***Table 4.2***, summarizing the mole quantities of MgO, Na_2O, CaO and K_2O in original ashes. The highest contents of these metal oxides in Hazelwood clearly favoured its sulfation reaction.

The sulphated ash samples were further characterised by XRD to quantify the sulphate compositions within them. The mass fractions of sulphates in ash are shown in ***Figure 4.4***, regarding Hazelwood ash, Yallourn ash and one Xinjiang (sub-bituminous coal) ash for comparison. Note that, the original and fitted XRD patterns for these samples are summarised in ***Tables 4.3*** to ***4.6***. It duplicates the facts that higher SO_2 concentration and higher temperature can both increase the sulfation of coal ash. The total sulphate level of Hazelwood is much higher, 27-44 *wt%* than those of Yallourn ash 7-14 *wt%* and Xinjiang coal, 19-23 *wt%*. For Hazelwood fly ash, $CaSO_4$ is the major sulphate formed, regardless of experimental conditions. Moreover, compared to fly ash in air-firing mode, the sulphate species including $Na_2SO_4{\cdot}10H_2O$ and $Na_2Ca\ (SO_4)_2$ were formed under the oxy-firing mode. Apparently, the formation of these two species was favoured by the high SO_2 concentration in flue gas. The formation of these two species is even more obvious for the other two fly ashes. This is due to the abundance of Na_2O in them, as evident in ***Table 4.2***. Another interesting observation is related to the amount of other Ca-bearing species which differs between air-firing and oxy-fuel mode. As evident in ***Figure 4.5*** for the quantities of calcite ($CaCO_3$), C4AF ($Ca_2Fe_{0.28}Al_{1.72}O_5$) and C2F ($Ca_2Fe_2O_5$), calcite in the air-firing Hazelwood fly ash accounts for only 12 *wt%* in the total species, which is even lower than 15 *wt%* of CaSO4 formed under air-firing mode (see ***Figure 4.4 a***). The quantity of CaF is comparable to calcite and $CaSO_4$, suggestive of an easy interaction between the inherent Ca and Fe forming spinel during the air-firing of Hazelwood coal. The oxy-firing condition of 800ºC and 1000 ppm SO_2 led to the formation of ~22 *wt%* calcite, whereas the amount of $CaSO_4$ only increased to ~ 17 wt%. Clearly, the carbonation reaction is favoured at 800 ºC under the oxy-fuel mode. Increasing the SO_2 concentration to 1500 ppm in oxy-firing flue gas slightly reduced the amount of calcite, but its reduction is rather marginal. The amount of $CaSO_4$ was increased to 22 %, suggesting that sulfation reaction is superior over carbonation reaction at such a high SO_2 concentration in flue gas. Increasing the reaction temperature to 1000ºC depreciated the carbonation reaction, regardless of the concentration of SO_2 in flue gas. Instead, the sulfation reaction is further enhanced, so is the reaction between Ca and Fe for the formation of Ca-bearing spinel in fly ash.

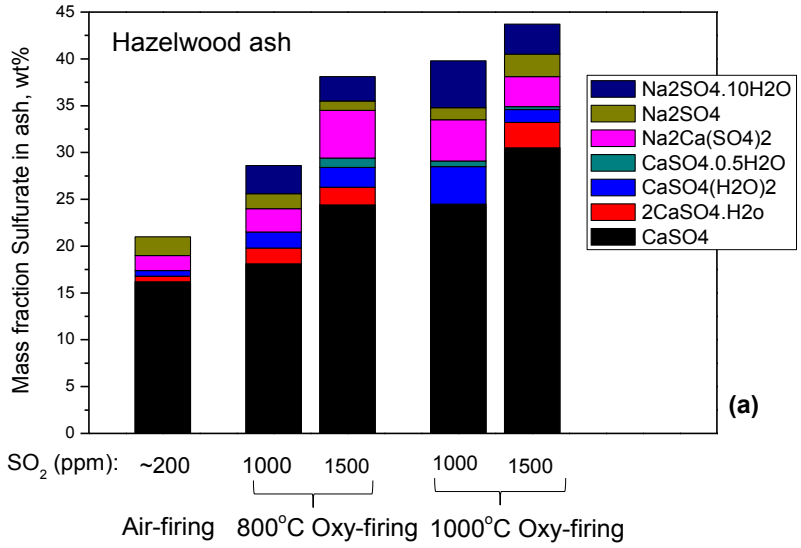
Hazelwood ash
Mass fraction Sulfurate in ash, wt%
Na2SO4.10H2O
Na2SO4
Na2Ca(SO4)2
CaSO4.0.5H2O
CaSO4(H2O)2
2CaSO4.H2o
CaSO4
(a)
SO2 (ppm): ~200 1000 1500 1000 1500
Air-firing
800°C Oxy-firing
1000°C Oxy-firing

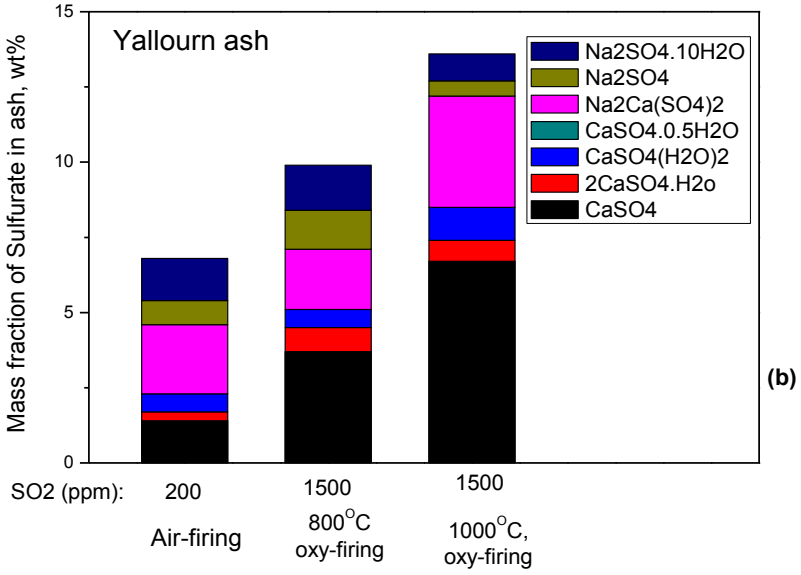
Yallourn ash
Mass fraction of Sulfurate in ash, wt%
Na2SO4.10H2O
Na2SO4
Na2Ca(SO4)2
CaSO4.0.5H2O
CaSO4(H2O)2
2CaSO4.H2o
CaSO4
(b)
SO2 (ppm): 200 1500 1500
Air-firing
800°C oxy-firing
1000°C, oxy-firing

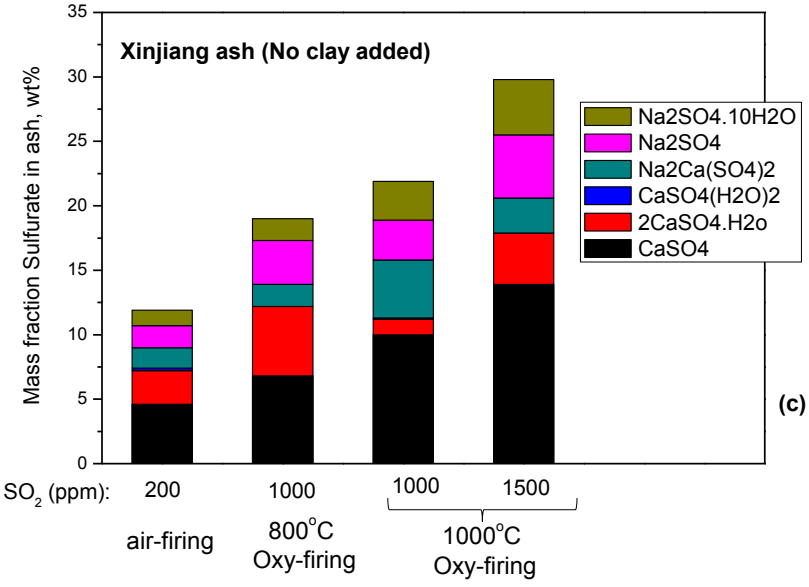
Xinjiang ash (No clay added)
Mass fraction Sulfurate in ash, wt%
Na2SO4.10H2O
Na2SO4
Na2Ca(SO4)2
CaSO4(H2O)2
2CaSO4.H2o
CaSO4
(c)
SO2 (ppm): 200 1000 1000 1500
air-firing
800°C Oxy-firing
1000°C Oxy-firing

Figure 4.4 Comparison of sulphate compositions in ash samples achieved from both air-firing and oxy-firing, as tested via quantitative XRD. (a) Hazelwood ash, (b) Yallourn ash, (c) Xinjiang ash (without clay).

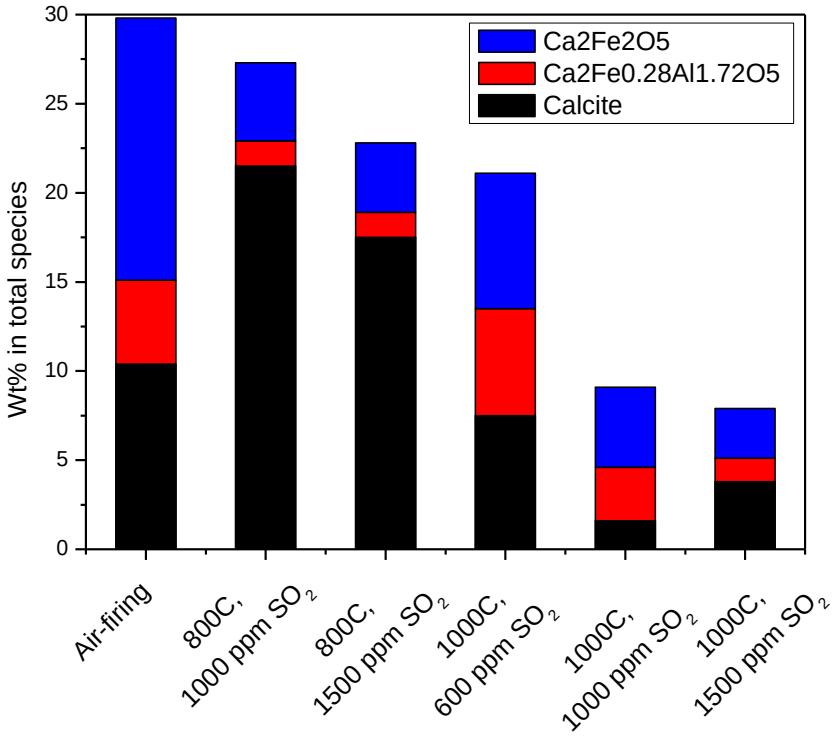

Figure 4.5 Quantifies of Ca-bearing species except Ca sulphates formed during the air-firing and oxy-fuel combustion of Hazelwood coal

Table 4.3 Species in the air-firing Hazelwood fly ash and its oxy-fuel combustion counterparts

	Hazelwood fly ash (air-firing)	800 C		1000 C		
Phase		1000 ppm SO2	1500 ppm SO2	600 ppm SO2	1000 ppm SO2	1500 ppm SO2
Quartz (SiO2)	17.7	1.3	1.1	0.3	0.7	1.8
Periclase (MgO)	23.9	18.2	20.3	27.4	24.1	14.1
Gypsum (CaSO4 H2O)	0.6	4	2.1	1.7	1.4	2.6
Bassanite (2CaSO4 H2O)	0.6	0.1	1.9	1.7	2.7	4.2
Anhydrite (CaSO4)	18.8	24.4	24.4	18.1	30.5	39.5
Bassanite, (super)	0.0	0.6	1	0	0.3	0
Calcite 1	0.0	0	0	3	0.3	0.2
Calcite 2 (CaSO3)	10.4	21.5	17.6	7.5	1.6	3.8
C4AF	4.7	1.4	1.4	6	3	1.3
C2F	14.7	4.4	3.9	7.6	4.5	2.8
Cristobalite	0.2	0.6	0.7	0.4	0.5	0.7
Glauberite (Na2Ca(SO4)2)	1.6	4.4	5.1	2.5	3.2	5.7
Thenardite (Na2SO4)	2.1	1.3	1	1.6	2.4	2.6
Mullite (Al2O3:SiO2 1.56)	2.0	5.5	6.2	4.7	7	6.8
Marialite	0.0	5	2.6	3	3.2	0
Lime (CaO)	0.0	0	0	0.1	0.6	0.3
Hematite	1.2	0	0.6	4.4	2.5	3.2
Maghemite	0.0	7.5	10.4	10	11.6	10.6

Table 4.4 Species in the air-firing Yallourn fly ash and its oxy-fuel combustion counterparts

	Air-firing of Yallourn fly ash	800C, 1500 ppm SO2	1000 C, 1500 ppm SO2
Quartz (SiO2)	1.1	1.3	1.2
Periclase (MgO)	6.8	0.6	0.7
Gypsum (CaSO4 H2O)	0.6	0.6	1.1
Bassanite (2CaSO4 H2O)	0.3	0.8	0.7
Anhydrite (CaSO4)	1.4	3.7	0.7
Calcite 2 (CaCO3)	1.1	1.2	1.1
C4AF	2	0	0
C2F	0	3	11.8
Cristobalite	0.6	0.5	0.6
Glauberite (Na2Ca(SO4)2)	2.3	26.1	21.9
Thenardite (Na2SO4)	0.8	1.3	0.5
Mullite (Al2O3:SiO2 1.56)	0	3.1	7.6
Marialite	3.4	1.5	0.9
Lime (CaO)	0	0	0
Hematite	6.9	3.2	6.7
Maghemite	30.5	3	3.7
Magnetite	34.6	35.2	22.1
Merwinite	6.2	2	14.9
Gehlenite	0	9.3	2.4

Table 4.5 Species in the air-firing Xinjiang (without clay) fly ash and its oxy-fuel combustion counterparts

	Raw XJ without clay	800 C 1000 ppm SO2	1000 C, 1000 pm SO2	1000 C, 1500 ppm SO2
Mullite	0	0	0	0
Omphacite	0.5	0	1.4	2.2
Merwinite	2.4	3.3	4	5
Magnesioferrite	2.2	0	3.5	
Magnetite	0	10.8	0	0
Glauberite	7.8	1.6	2.7	6.4
Marialite	3.2	15.2	4.3	2.6
Thenardite	7.3	3.3	4.9	2.3
C4AF	8.9	1.8	3.4	5.2
C2F	6	1.4	8.4	6.5
Periclase	10.5	4.7	6.6	6.7
Gehlenite	7.2	5.5	11.6	13.9
Calcite 1	10.3	1.3	20.4	2.9
Bassanite	1.7	5.3	4	2.4
Gypsum	0.3	0	0	0.6
Anhydrite	10.3	7.6	13.9	24.1
Hematite	9.1	4.8	5.9	8.2
Brucite	1.4	1.1	0	0.1
Keatite	1.1	2.3	1.7	1.4
Maghemite	0	26.8	0	0
Lime	7.6	1.8	1.3	4.5
Quartz	1.2	0.6	2	1.3
Pyroaurite	1	0.3	0.2	0.2
Cristobalite	0	0.6	0.1	0

Table 4.6 Species in the air-firing Xinjiang (with clay) fly ash and its oxy-fuel combustion counterparts

	Raw XJ with clay	800 C, 1500 ppm SO2	1000 C, 1500 ppm SO2
Mullite	1.2	0.7	0.8
Magnesioferrite	0	0	3.9
Omphacite	0.8	1.1	5.3
Merwinite	4.5	1.3	5.8
Glauberite	4.7	0.9	2.4
Magnetite	5	2.8	0
Anhydrite	22.4	39.6	27.3
Marialite	2.2	4	4
Thenardite	1.5	0.8	2.3
C4AF	5.5	2.8	1.3
C2F	4.8	4.8	1.7
Gehlenite	1.5	0.8	16.1
Bassanite	1.1	1.9	2.5
Periclase	6.5	6.5	3.4
Hematite	11.4	7	9.6
Gypsum	1.7	1.2	0.6
Calcite 1	8.7	11.1	1.7
Quartz	12.2	7.9	6.2
Brucite	0.4	0	0
Keatite	0	0.1	0.8
Maghemite	0	3	3.9
Pyroaurite	0.7	0.1	0.1
Lime	3.3	1.6	0
Cristobalite	0	0.2	0.4

4.3 Experimental studies on carbonation characteristics of Victorian brown coal ash

4.3.1 Test approach for carbonate in ash

As mentioned above, the carbonation of Victorian brown coal fly ash takes place simultaneously with the sulfation reaction. The oxy-fuel combustion can enhance the carbonation reaction due to the high CO_2 content in flue gas. To further confirm the carbonation reaction rate of Victorian brown coal fly ash samples, extra experiments were conducted through the use of drop-tube furnace at 400°C - 1000°C and the feeding of 10 L/min 5% O_2 balanced by CO_2 into the DTF. Regarding the residue ash samples collected in carbonation experiments, the carbonation extent in ash was tested by TGA (thermal gravimetric analyser). The non-isothermal heating programs were run in TGA at a constant heating rate of 20 °C/min from room temperature to 1000°C. During initial stage of heating up, 100°C of particle temperature has been kept for thirty minutes to remove the moisture in ash. The ash sample is expected to undergo decomposition reactions during the heating period, including:

$$CaCO_3 \rightarrow CaO+CO_2$$
$$MgCO_3 \rightarrow MgO+CO_2$$

4.3.2 Experimental results

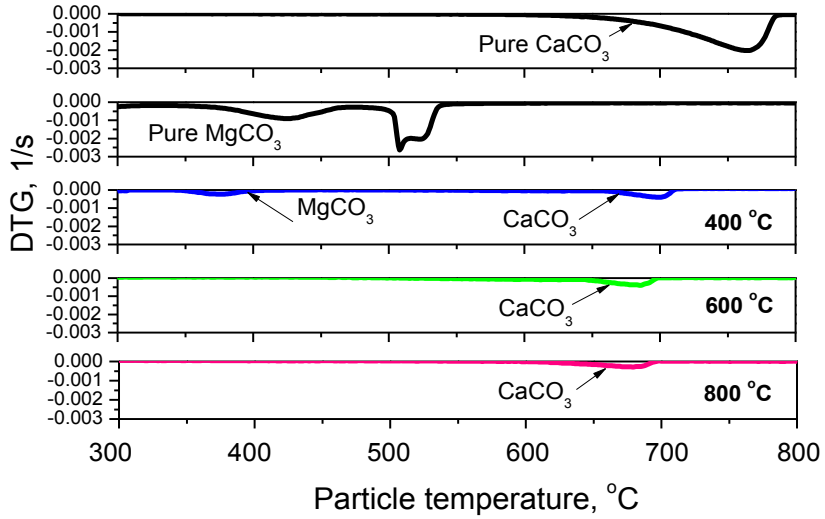

Figure 4.6 DTG curve measured on TGA to quantify $MgCO_3$ and $CaCO_3$.

Figure 4.6 and ***Figure 4.7*** show the pure $CaCO_3$ and $MgCO_3$ decomposition processes in TGA. ***Figure 4.6*** shows the DTG curves, and ***Figure 4.7*** shows weight loss curves. In these two figures, the decomposition of $MgCO_3$ occurs at 300-580^{o}C, whereas the temperature of 600-800^{o}C is the decomposition temperature range for $CaCO_3$. Considering above decomposition temperature range, the CO_2 releasing values from $CaCO_3$ and $MgCO_3$ can be determined based on ***Figure 4.7***, which also helps quantify the contents of $CaCO_3$ and $MgCO_3$ in the ash samples collected in the experiments of 400^{o}C, 600^{o}C, 800^{o}C and 1000^{o}C, respectively. The results are summarized in ***Figure 4.8***.

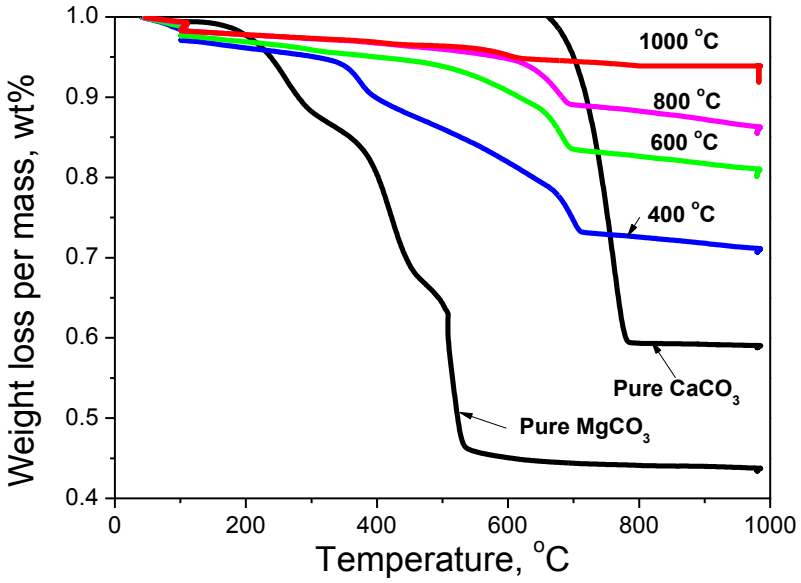

Figure 4.7 Weight lost curve measured on TGA to quantify $MgCO_3$ and $CaCO_3$.

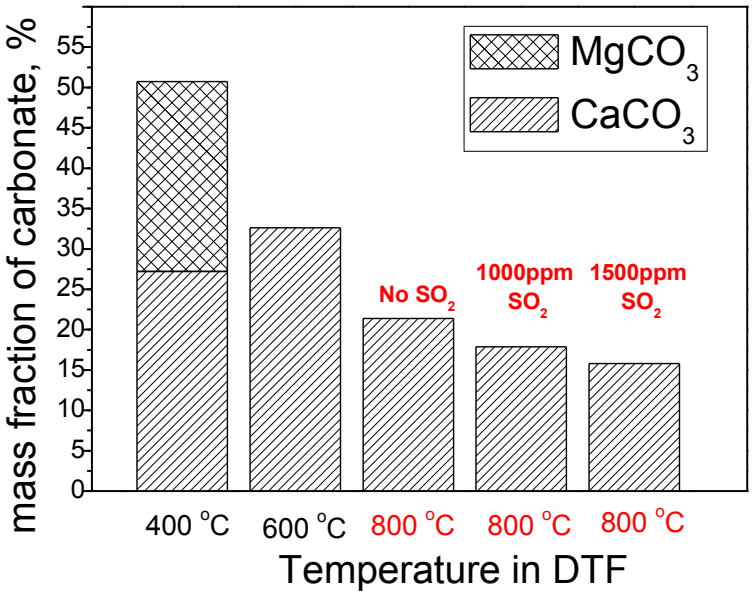

Figure 4.8 Contents of $CaCO_3$ and $MgCO_3$ measured through TGA.

The carbonation behaviour of Victorian brown coal mainly takes place at the temperature less than 1000°C. The carbonation extent of Victorian brown coal ash also increases upon the decrease of reaction temperature, as evident shown in ***Figure 4.8***. Especially a high extent of $MgCO_3$ was found in the ash at 400°C. Therefore, it can be understood that carbonation behaviour in ash only takes place inside the rear flue gas pipeline of furnace. The quantitative

XRD analysis results shown in ***Table 4.3*** also confirmed the abundance of calcite in the ash residue after 800^{o}C. Moreover, the carbonation experiments were expanded to the cases with flue gas with SO_2 mixed.

Figure 4.8 illustrates the influence of SO_2 concentration on carbonation level in ash. The total mass fraction of $MgCO_3$ and $CaCO_3$ is 24% in flue gas without SO_2 at 800^{o}C. However, with the concentration of SO_2 in flue gas increases to 1000 ppm and 1500 ppm, the total carbonate mass fraction is decreased to 17% and 13%, respectively. It witnesses that SO_2 gas can inhibit the carbonation process of CaO in ash during oxy-fuel combustion. Moreover, ***Table 4.3*** suggests that the interaction between CaO and Fe_2O_3 took place over the carbonation reaction at the temperatures above 800 ^{o}C, resulting in the formation of 11.1 *wt%* and 12.6 *wt%* C2F ($Ca_2Fe_2O_4$) at 1000 ^{o}C with and without steam in flue gas, respectively. This is much higher than only ~2 *wt%* calcite formed under the same conditions.

Table 4.3 Quantitative – XRD results for ash residues after carbonation reaction in DTF

		Oxy-firing		
Phase	Air-firing	800 C	1000 C	1000 C, 10 %Steam
Quartz	17.7	3.1	1	0.5
Periclase	23.9	16.3	22.9	24.6
Gypsum	0.6	1.3	1.3	0.9
Bassanite	0.6	1.6	1	0
Anhydrite	18.8	25.6	28.3	32.4
Bassanite, (super)	0	0.7	0	0
Calcite 1	0	0	0	0
Calcite 2	10.4	24.9	2.6	2.1
C4AF	4.7	1.8	5.6	7
C2F	14.7	4.6	11.1	12.6
Cristobalite	0.2	0.4	0.1	0
Glauberite	1.6	2.6	3.6	2.3
Thenardite	2.1	0.4	0.9	0.1
Mullite (Al2O3:SiO2 1.56)	2	3	3.2	1.9
Marialite	0	4.2	0.6	1.3
Lime	0	0	2.8	3.4
Hematite	1.2	1.3	7	7.5
Maghemite	0	8.1	7.8	3.6

4.4 Thermodynamic modelling of ash formation of Victorian brown coal through FactSage Software

FactSage is a good software to predict the ash formation and properties, as used to model the sulphuration level of ash samples tested here. This modelling belongs to thermodynamic modelling based on the chemical equilibrium states, and the results show the ultimate chemical state with an infinite reaction time. ***Figure 4.9*** is the comparison between the experimental data and prediction results through FactSage, which shows a rather good agreement. It also shows the ash properties are close to the chemical equilibrium at 1000^{o}C furnace temperature. Clearly, the reaction is quite fast for the fly ash samples tested here, probably due to their fine/ultrafine particle size.

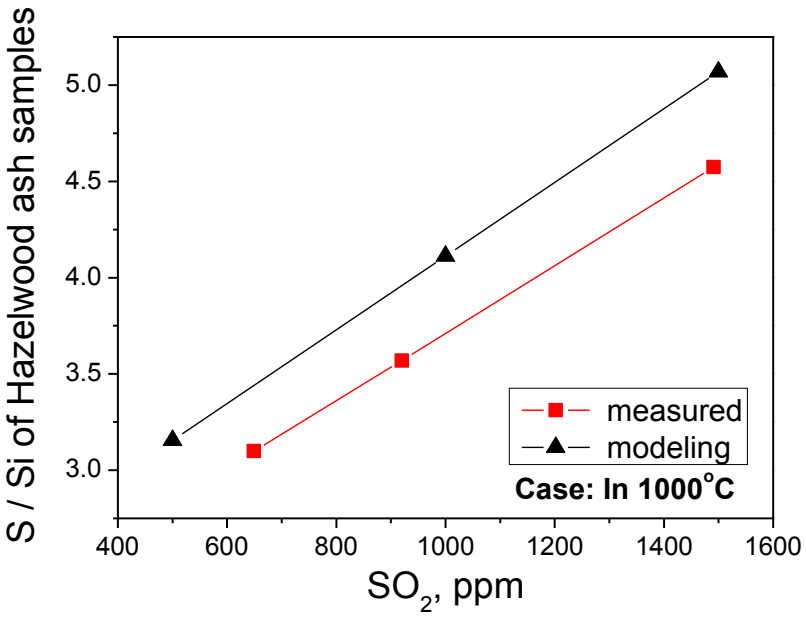

Figure 4.9 Predicted sulfur content (S/Si) in Hazelwood ash under chemical equilibrium state

4.5 Conclusion

Sulfation behaviour of Victorian brown coal ash was investigated. The main conclusions are

1) Sulfation behaviour of Hazelwood coal ash is serious because of the large amount of alkali metal in ash. Relatively, the sulfation behaviour of Yallourn coal ash is less since much Fe content in ash, which triggers the higher catalytic SO_3 formation.

2) The sulfation capability of ash is proportional to the mole fraction of total alkali metal in ash. Furthermore, the sulfation behaviour of fly ash at 1000C is higher than that at 800C, which is resulted by higher SO_3 homogeneous formation.

3) The contents of $MgCO_3$ and $CaCO_3$ can be measured through heating operation of TGA, which beyond the test capability of XRF.

4) The $CaCO_3$ quantity in ash increases with the decrease of reaction temperature. $MgCO_3$ exists in ash collected at 400^oC condition. Above 600^oC, there is no $MgCO_3$ found in ash.

5) SO_2 in flue gas can restrain the carbonation process of ash at the temperatures above 800^oC.

6) FactSage software is reliable to predict the sulfation level of ash samples in chemical equilibrium state, as well verified through the comparison with experimental measured data. FactSage will be applied in foreseeable CFD modelling to predict the ash-related problem in industrial furnace.

Chapter 5 Pilot-scale experiment on ash deposition behaviour during Hazelwood coal combustion in air – and oxy-firing modes

5.1 Pilot-scale experiment

The pilot-scale experiment of ash deposition tests was conducted in a 3 MW_{th} furnace, the schematic of which was drawn in ***Figure 5.1***. For oxy-fuel combustion, the flue gas after the bag-filter was recirculated, mixed with high-purity oxygen from the air-separation unit (ASU), and then passed through a pre-heater and split into both primary and secondary gas. The temperature of the recirculated flue gas is around 200^{o}C, which is the same as the pre-heated air used for the air-firing combustion. The air-dried Hazelwood coal with a moisture content of ~ 15 *wt%* was burnt. Three cases were studied for its ash deposition, air_low load referring to a low load under the air-firing mode; air_full load denoting a full load of the furnace under the air-firing mode; whereas oxy_full load referring to the full load of the furnace under the oxy-fuel condition. The coal feeding rates for the three cases are depicted in ***Figure 5.2***. The data for the low-load air-firing mode are missing, which is estimated to be around 180 kg/h. For the two full-load cases, the averaged coal feeding rate is 250 kg/h and 331 kg/h for air-firing and oxy-firing mode, respectively.

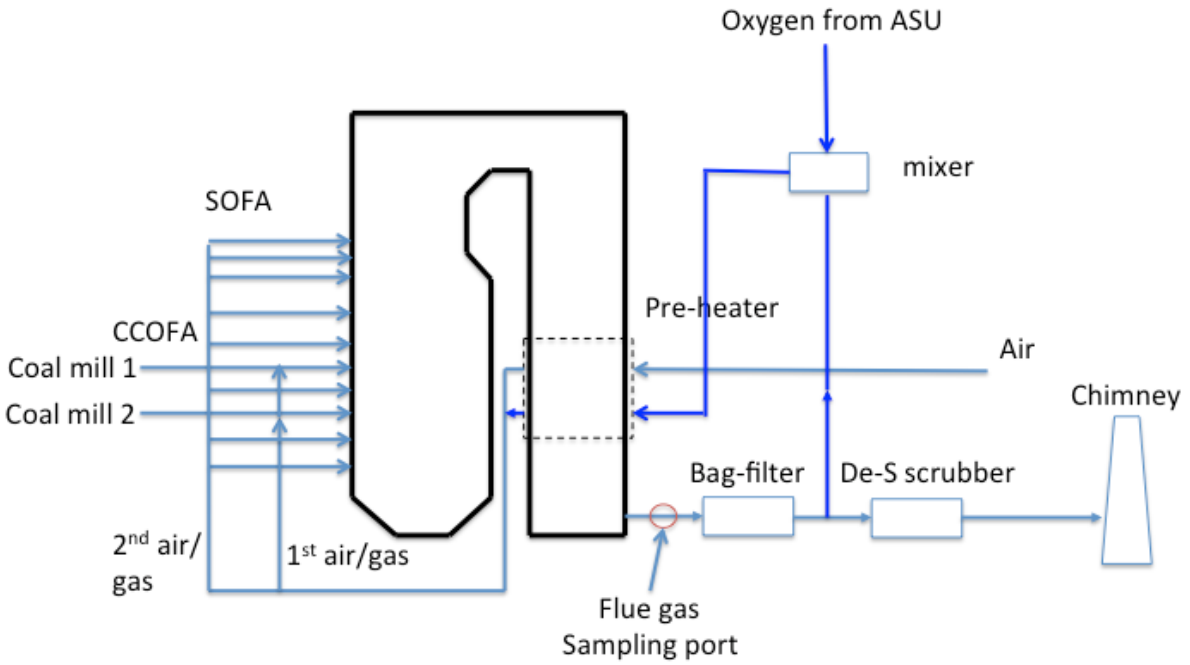

Figure 5.1 Schematic of the 3 MW_{th} pilot-scale boiler system used for oxy-fuel combustion ash test in this study

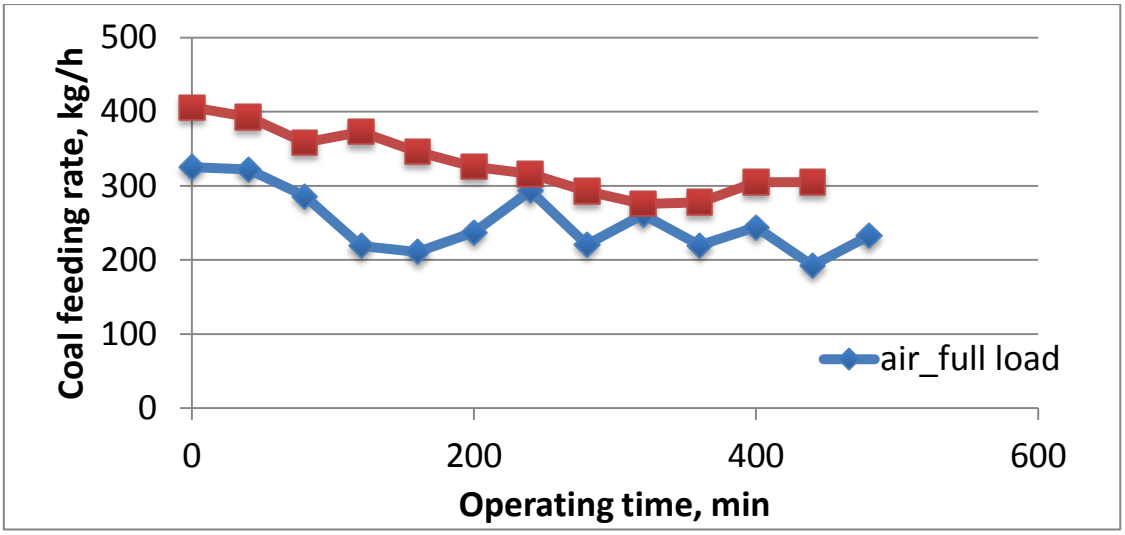

Figure 5.2 Coal feeding rate profile for the two full-load modes combustion in the pilot-scale facility

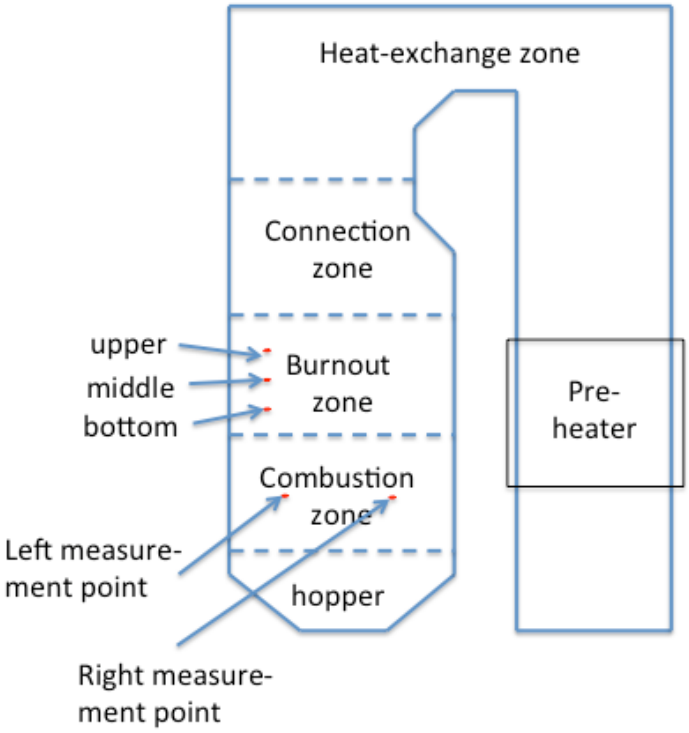

Figure 5.3 Temperature measurement locations in the pilot-scale furnace

The temperature profile in the furnace was measured in three major zones, combustion zone (two thermocouples, left and right), burnout zone (three thermocouples located in three layers, bottom, middle and upper) and connection zone between the burnout zone and superheater, as shown in ***Figure 5.3***. The measured temperature profile in the combustion zones is depicted in

Figure 5.4 and ***Figure 5.5***. For both two thermocouples installed on the left and right sides, the full-load combustion in air resulted in a quicker ignition and thus a quicker temperature rise. Instead, for both low-load in air and full-load in oxy-fuel mode, the temperature rise is rather slow. This is due to the ignition delay. Moreover, compared to the case of low-load in air having its highest temperature delayed, the full-load in oxy-fuel did not show such a phenomena, indicating that coal combustion rate was accelerated by the high-oxygen concentration in the furnace. For the temperature profiles in burnout zone and the connection zone in ***Figures 5.6*** to ***5.9***, one can see that the oxy-fuel combustion flue gas is generally slightly cooler than the full air-firing mode. The temperature gap between these two modes is maximum 100^{o}C. This should be attributed to the difference in flue gas composition and its thermal properties such as the specific heat capacity.

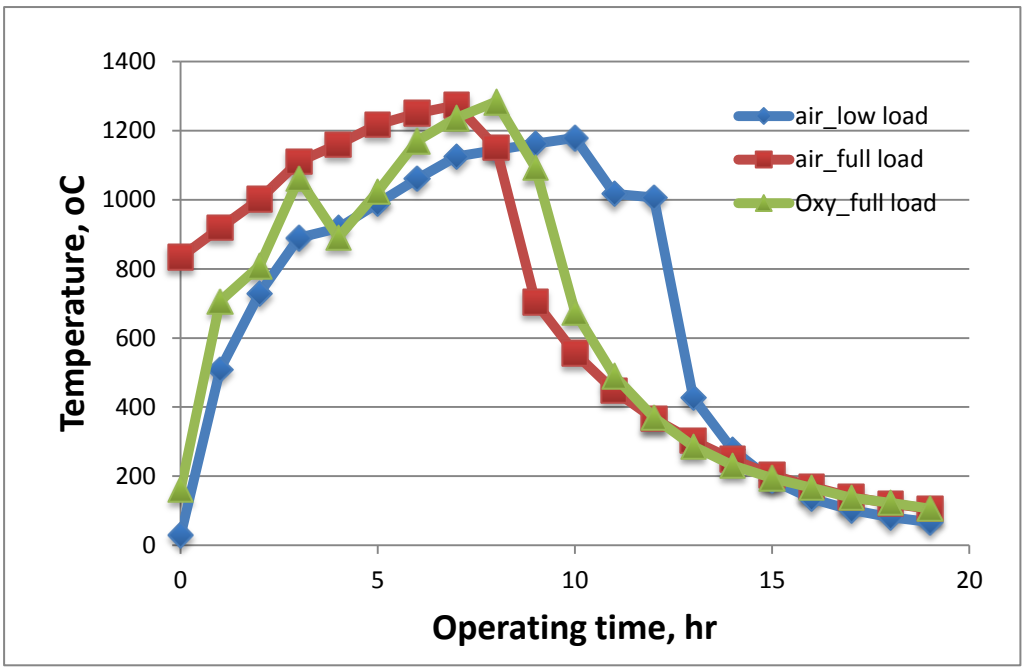

Figure 5.4 Temperature profile in the left side of the combustion zone

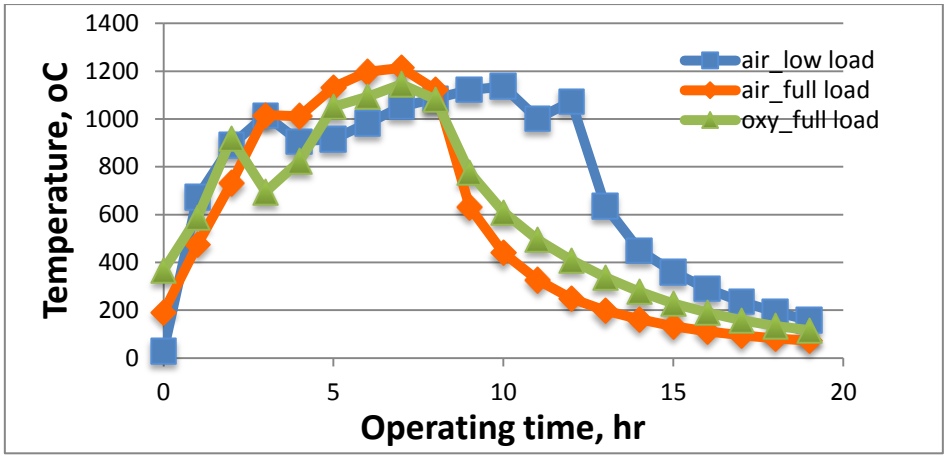

Figure 5.5 Temperature profile in the right side of the combustion zone

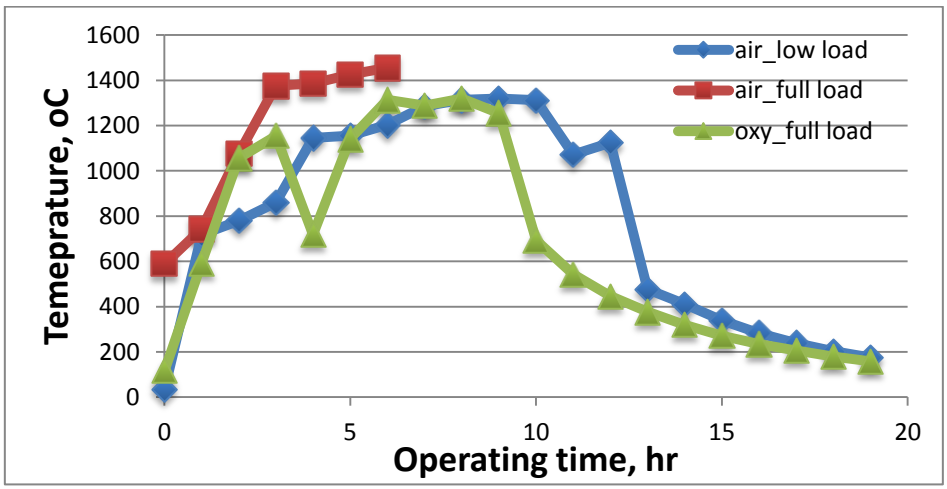

Figure 5.6 Temperature profile in the bottom layer of the combustion zone

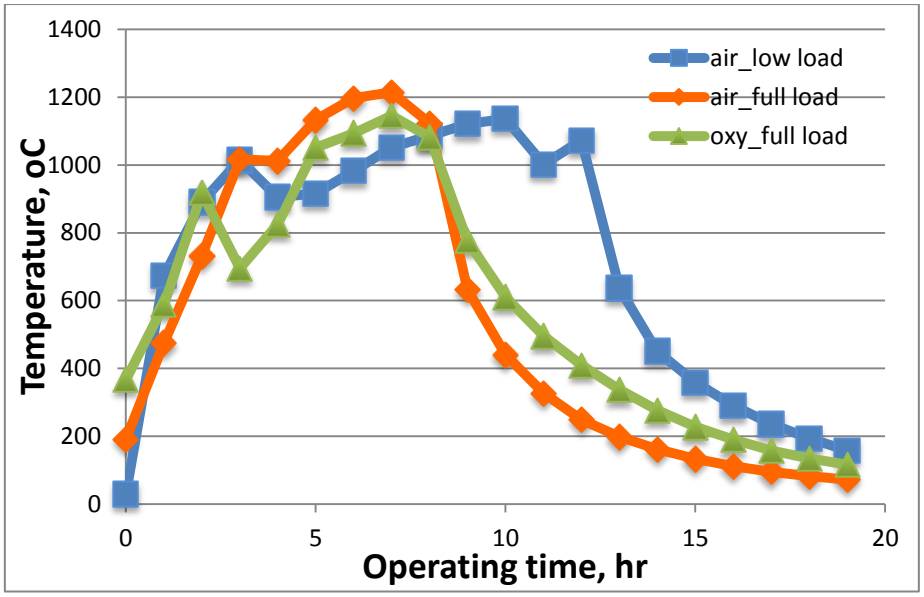

Figure 5.7 Temperature profile in the middle layer of the combustion zone

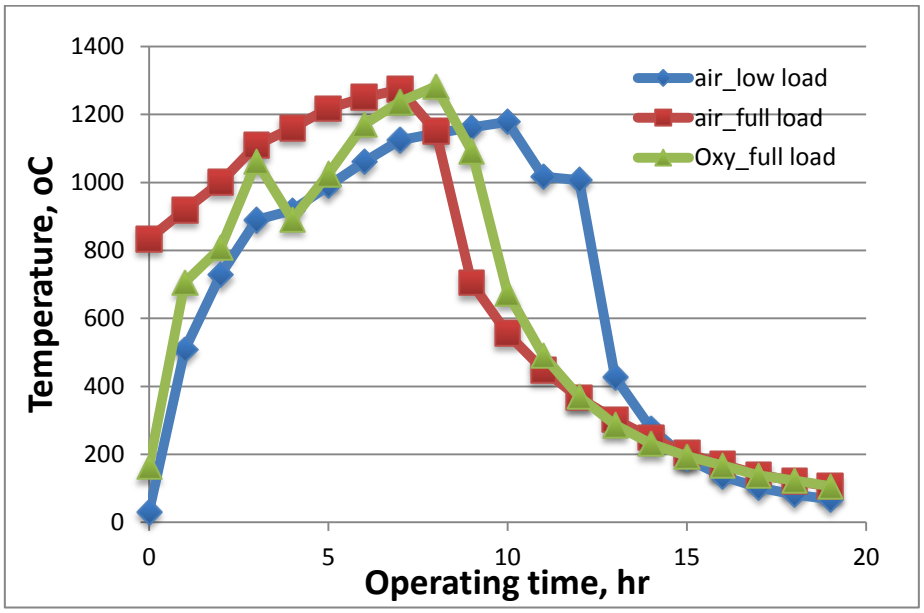

Figure 5.8 Temperature profile in the upper layer of the combustion zone

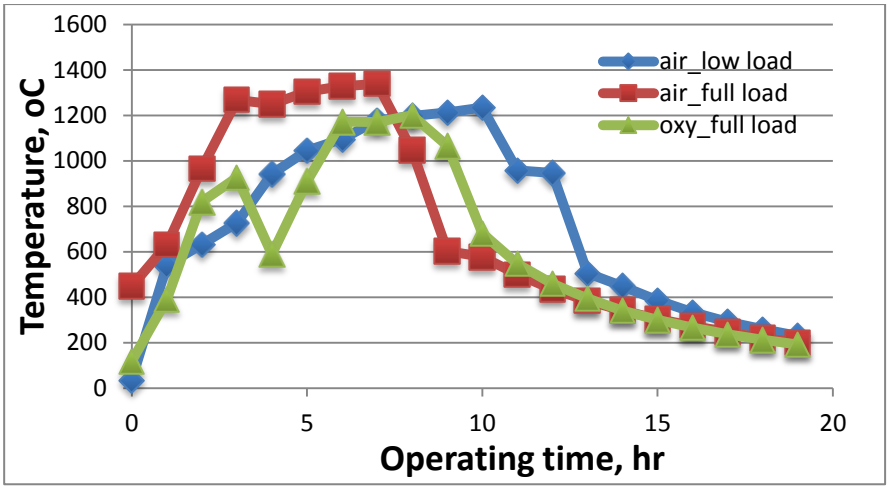

Figure 5.9 Temperature profile in the connection zone in the furnace

The flue gas composition was measured at the exit of the furnace. As shown in ***Figure 5.10***, compared to the two air-firing cases creating around 12% CO_2 in the flue gas, the oxy-fuel mode resulted in a purity of ~80% in the flue gas. The remaining unreacted oxygen in flue gas shown in ***Figure 5.11*** accounts for around 5 %, with no obvious difference observed between the three cases. The concentration of carbon monoxide (CO) shown in ***Figure 5.12*** indicates that CO was burnt quickly in the air-firing mode. In contrast, the CO consumption was a bit slow in the oxy-fuel mode, and therefore, the CO concentration in the boiler is higher than the air-firing mode even after four hours.

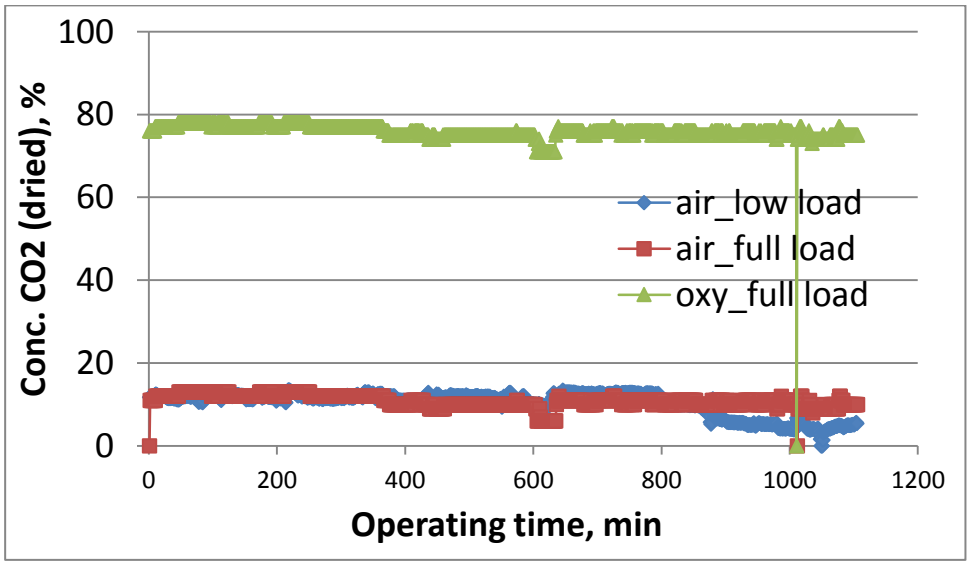

Figure 5.10 Concentration of CO_2 in flue gas (dried)

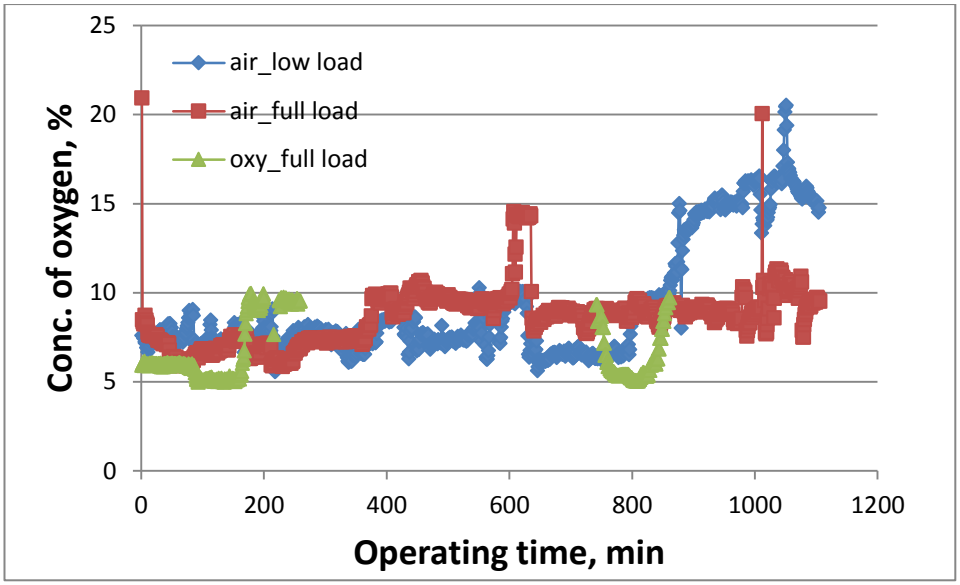

Figure 5.11 Concentration of O_2 in flue gas (dried)

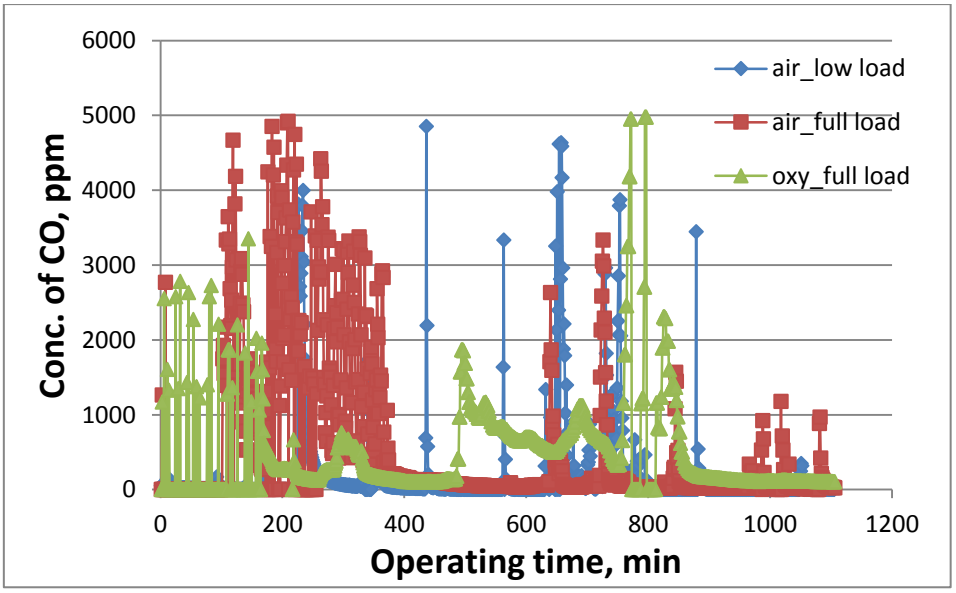

Figure 5.12 Concentration of CO in flue gas (dried)

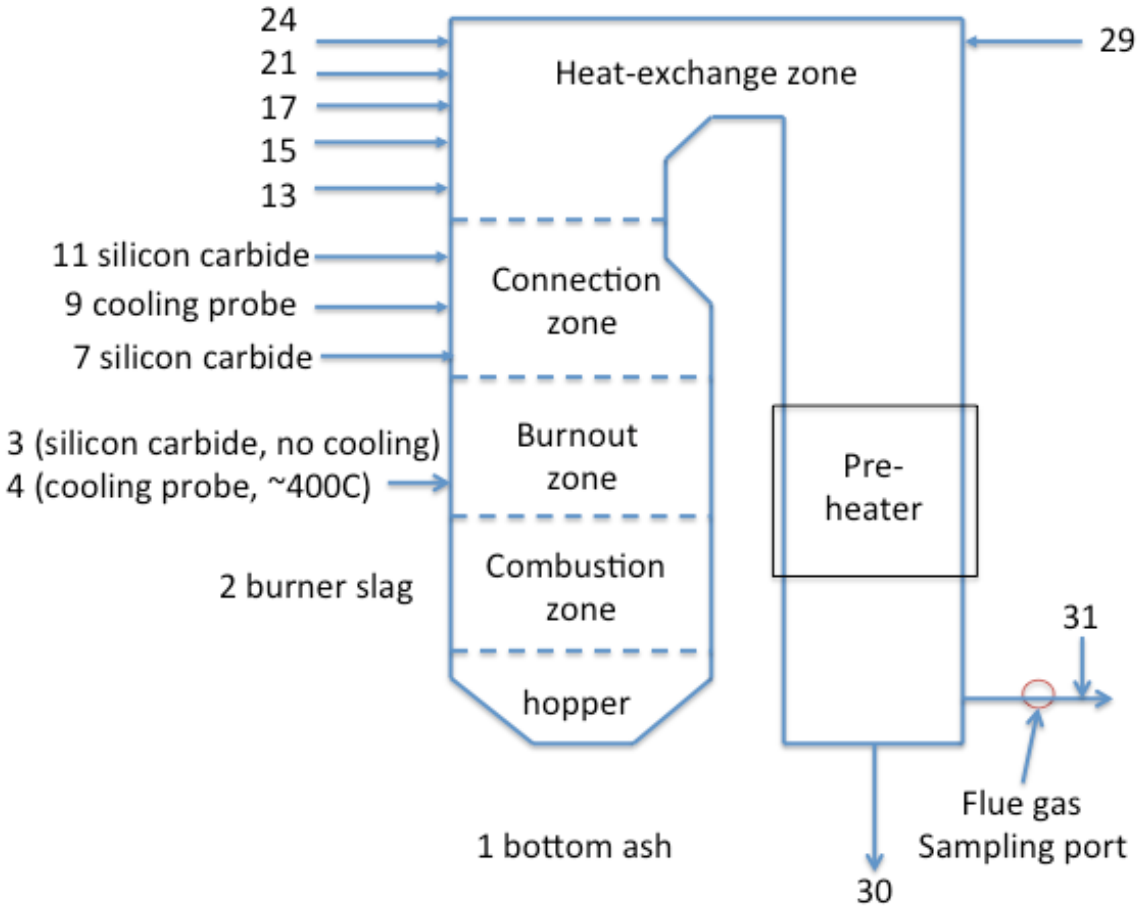

Figure 5.13 Ash deposition locations along the pilot-scale furnace

The ash deposits along the furnace were collected at various locations, as visualised in ***Figure 5.13***. The silicon carbide tubes were used for ash deposition, as shown in ***Figure 5.14*** for the probe locations for the combustion zone and burnout zone. The typical deposits on the silicon carbide tube in the combustion zone are also demonstrated in ***Figure 5.14***. One can see a tough deposition of the molten ash for the dried Hazelwood coal ash, due to the high-temperature from the coal flame. The elemental compositions of ash deposits were quantified by X-ray fluorescence (XRF) spectroscopy. The bulk chemical compositions were determined by X-ray diffraction (XRD). The resulting XRD patterns were processed by Siroquant to quantify the contents of amorphous species and individual crystals. The optical microscopy (OM) and scanning electron microscopy (SEM) will be used to observe the microstructures of ash deposits in next step.

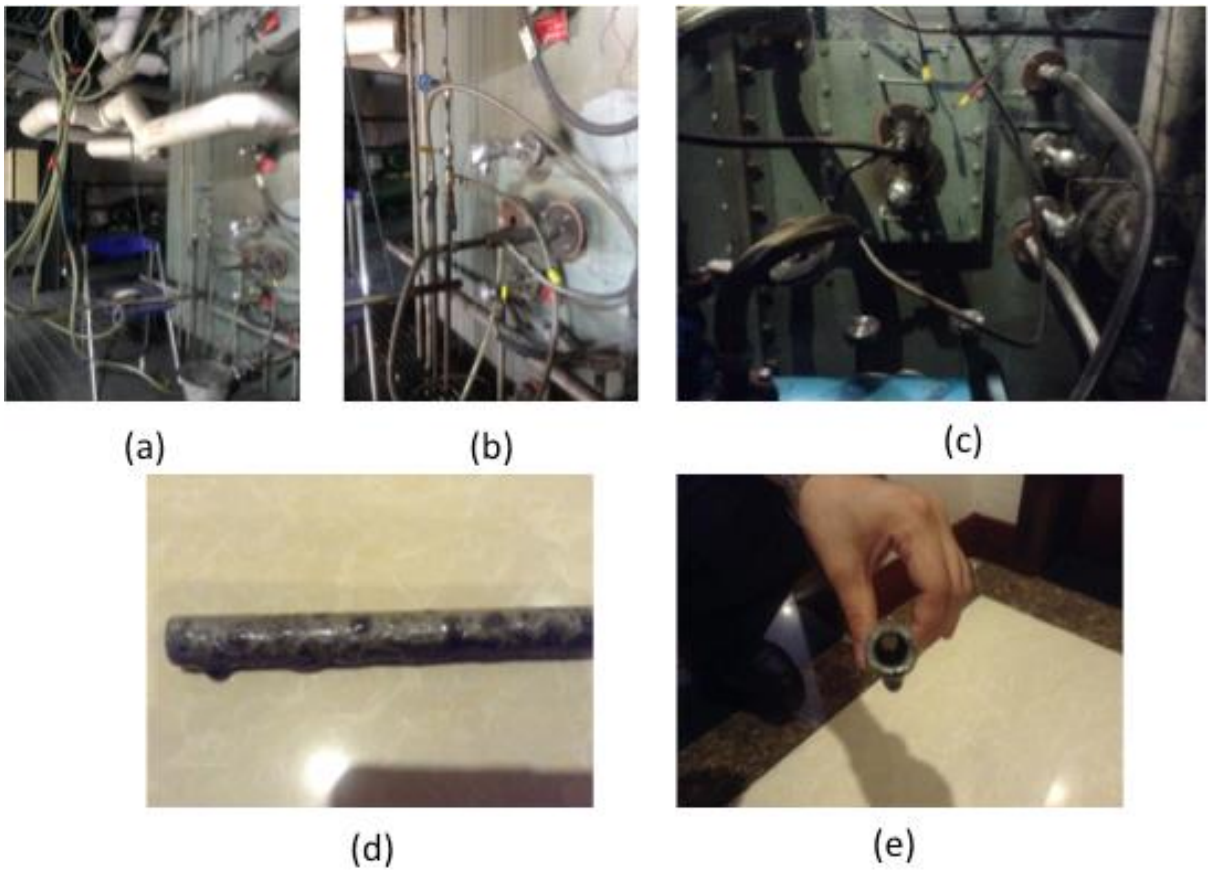

Figure 5.14 The ash deposit sampling position in the combustion zone (a, b), burnout zone (c), and the typical oxy-fuel slag deposit on silicon carbide (d, e)

Figures 5.15 to ***5.16*** demonstrate the comparison of the contents of four major elements, Na, Ca, Fe and S in their most stable oxide form in the ash depositions between full-load air-firing and oxy-fuel mode. Interestingly, Na_2O is abundant in the oxy-fuel ash deposits, particularly in the ash deposits formed in the combustion zone (numbered 5 in ***Figure 5.15***). Since the coal used is the same, the enhanced Na_2O in oxy-fuel ash deposits should be caused by the recirculation of the fine/ultra-fine Na_2O-bearing particles that escaped the bag-filter. Fe (in ***Figure 5.16***) in the oxy-fuel ash deposits has a rather even distribution, and a lower content in the high-temperature deposits than in the respective air-firing high-temperature deposits. This should be due to a lower flue gas temperature in the oxy-fuel mode. With respect to Ca in ash deposits in ***Figure 5.17***, its profile is rather similar between the two combustion modes, indicating the stable behaviour of this metal and its insensitive change against flue gas temperature. The largest discrepancy between the two combustion modes was found for the distribution of S in the ash deposits. As can be found from ***Figure 5.18***, although the content

of S in the high-temp ash deposits (No 5) from oxy-fuel is higher than in the respective ash deposit from the air-firing mode, the contents of S in other ash deposits from oxy-firing are much lower than in the respective air-firing deposits. This implies the weaker sulfation reaction for ash particles under the oxy-fuel mode, although its flue gas temperature is about 100 C lower than in the air-firing mode. Apparently, the other parameters such as the existence of abundance CO_2 and even the formation of local reducing environment may have affected the ash formation mechanism. The enhanced sodium caused by the recirculation of flue gas into the furnace may have been largely captured by the refractory metals such as aluminium and silicon, thereby losing its sulfation propensity in the heat-exchange zone in the furnace.

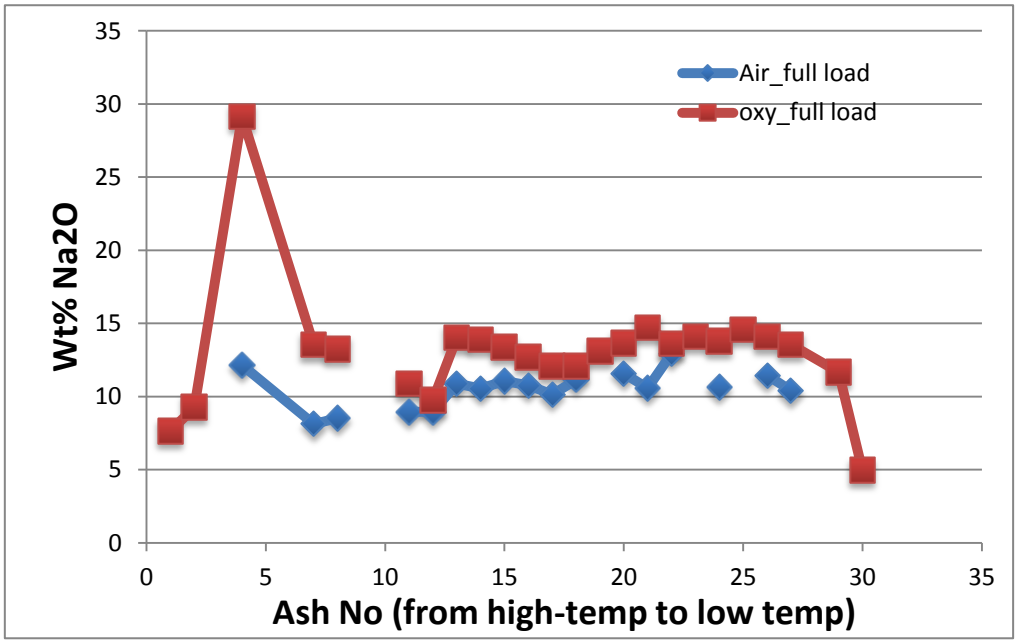

Figure 5.15 Content of Na_2O in ash deposits collected from two full-load combustion modes

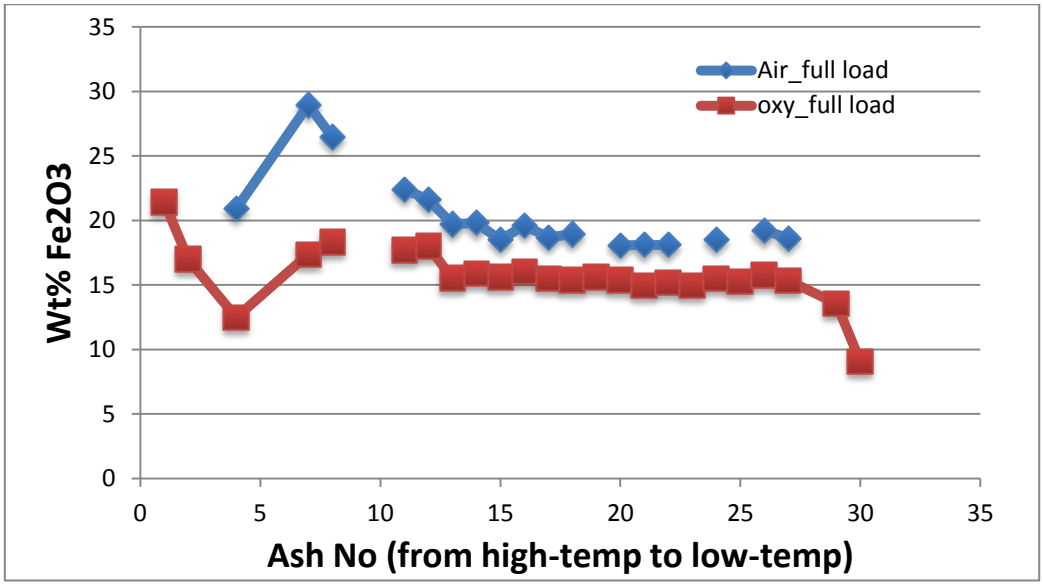

Figure 5.16 Content of Fe_2O_3 in ash deposits collected from two full-load combustion modes

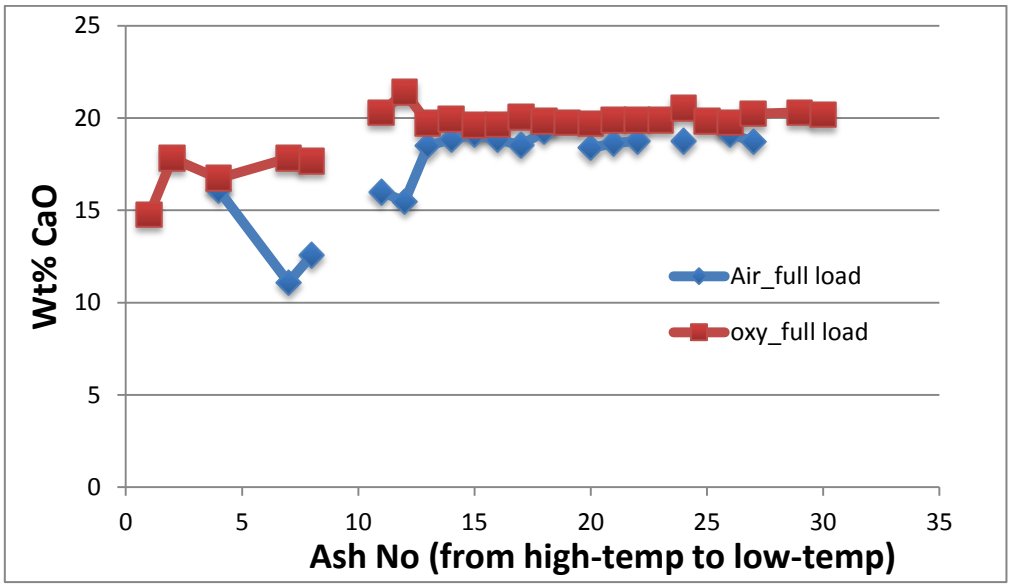

Figure 5.17 Content of CaO in ash deposits collected from two full-load combustion modes

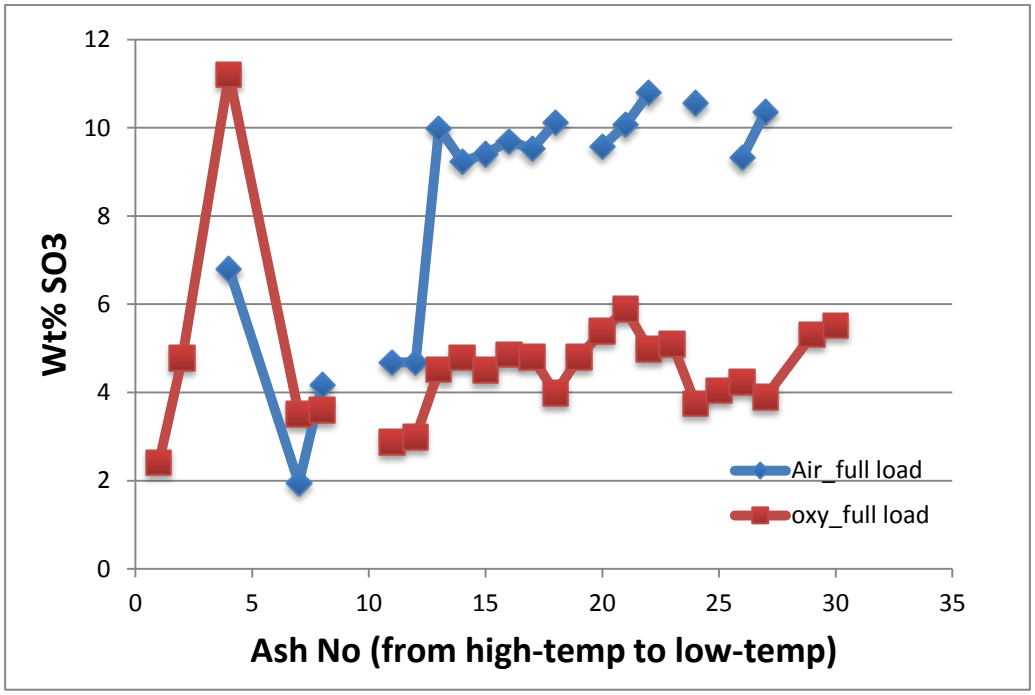

Figure 5.18 Content of SO_3 in ash deposits collected from two full-load combustion modes

XRD analysis for the ash deposits from the full-load air-firing mode are summarised in ***Figures 5.19*** to ***5.21*** for the contents of alumina-silicates, oxides, and sulphates/carbonates, respectively.

The results are in broad agreement with the fly ash sample collected from the Hazelwood power plant in the Latrobe Valley. As can be seen, the free oxides, sulphates and carbonates are rich in the ash deposits. Anhydrite ($CaSO_4$) is the most abundant sulphate, echoing the abundance of Ca and its quick sulfation for Hazelwood coal. Glauberite ($Na_2Ca(SO_4)_2$) and thernerdite (Na_2SO_4) are the two major sulphates for Na with comparable contents in the ash deposits. These species cause the tube corrosion in the heat-exchange zone. Characterisation of the oxy-fuel fly ashes is underway, which will be added in next report to compare with air-firing results.

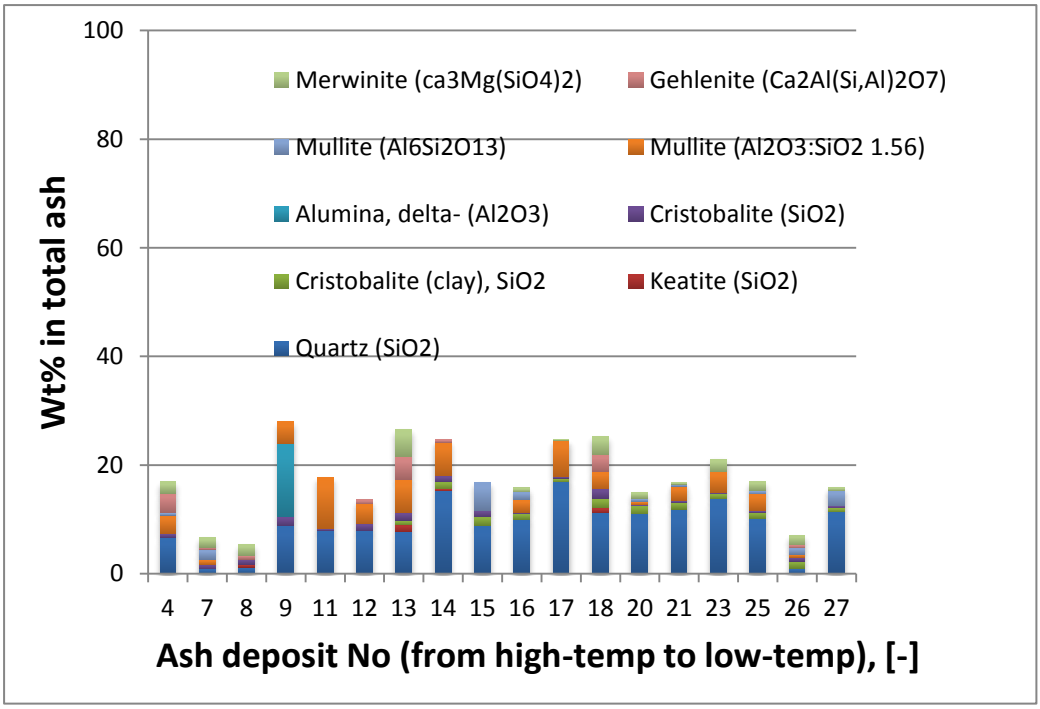

Figure 5.19 Quantified contents of alumina-silicates in air ash deposits (full-load)

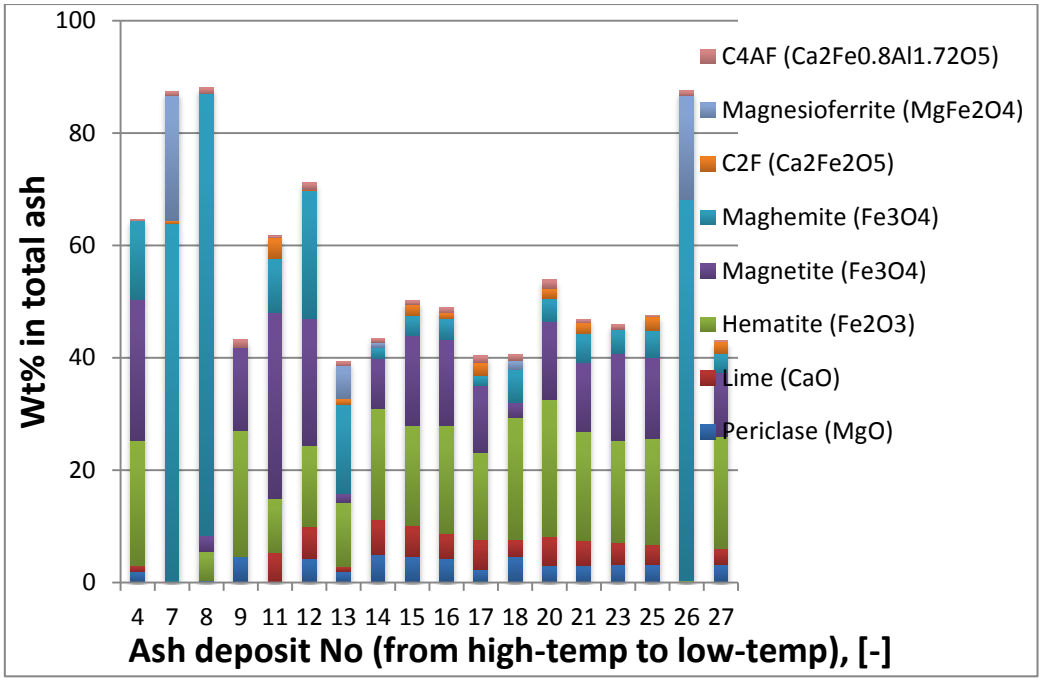

Figure 5.20 Quantified contents of oxides in air ash deposits (full-load)

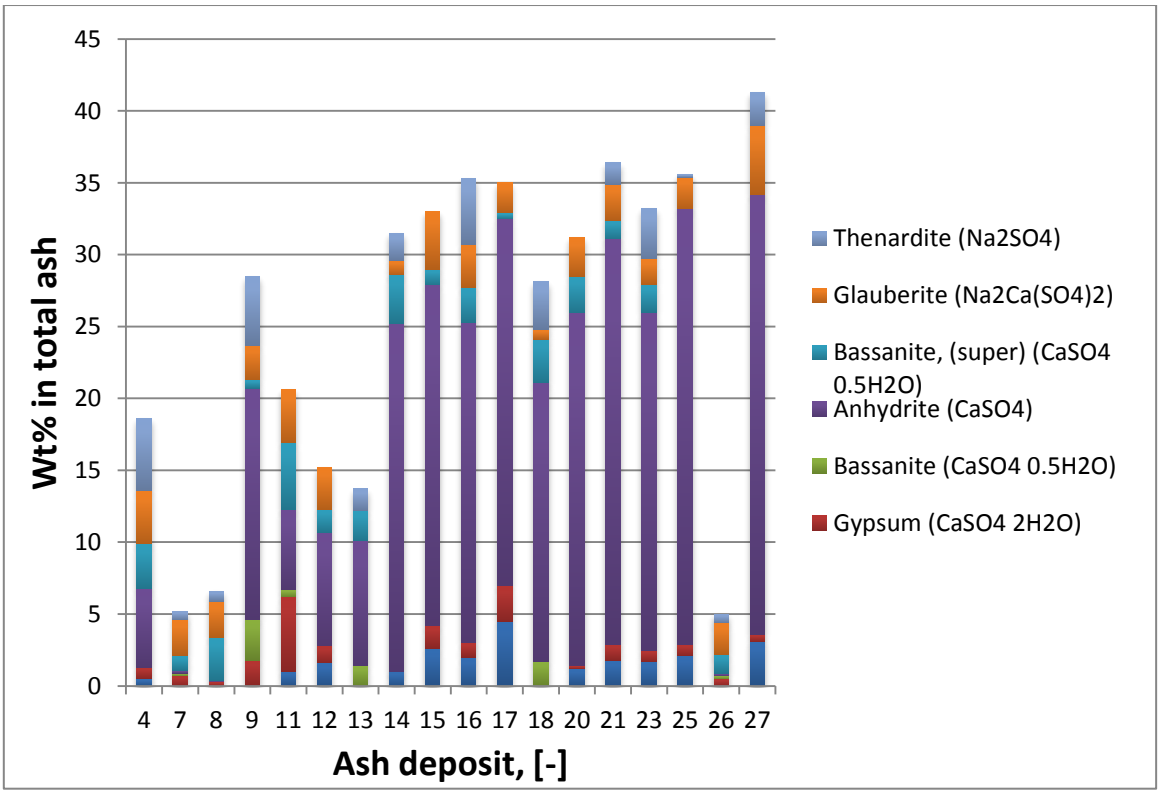

Figure 5.21 Quantified contents of sulphates/carbonates in air ash deposits (full-load)

Chapter 6 Investigations of water tube corrosion caused by Victorian brown coal ash at 650ºC

Deposits and corrosion on heat transfer tube surfaces play a major role on coal fired boiler performance. Understanding tube corrosion mechanisms allows the deployment or retrofit of advanced tube materials and maintain a long lifetime for a boiler. In this section, the tube corrosion experiments of Victorian brown coal ash are introduced. This work is to help the future pilot-scale test in understanding the corrosion effects of deposited Victorian brown coal ash on tube hot corrosion during air-firing versus oxy-fuel combustion, regarding various water tubes made of different steel materials.

6.1 Tube corrosion test set – up and conditions

A horizontal test furnace was used and its schematic diagram is shown in ***Figure 6.1***. The temperature in furnace is fixed to mimic post-combustion flue gas temperature with a range of 500-800ºC, which is similar with the conditions near super-heater and re-heaters in an industrial furnace. For each run, the ash sample were placed on the square specimen (plate) made of typical steels to mimic the ash deposition on a real steam tube surface. The ash specimens are located on a quartz-made sample holder inside the corrosion furnace, shown in ***panel (a)***. ***Panel (b)*** illustrates the gas control system (at furnace entry) and flue-gas analyzer system (at furnace rear) connected with furnace. There is a thermocouple to record the on-line temperature for the specimen. All ash specimens were tested under 50 -100 hr exposure for the tube surface corrosion.

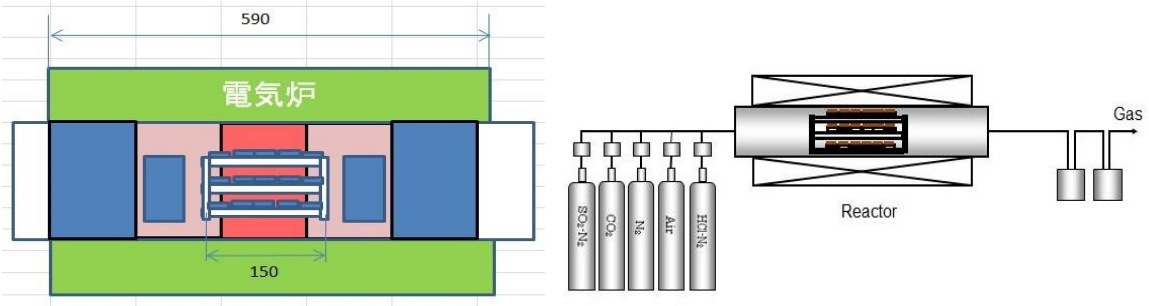

(a) (b)

Figure 6.1 Schematic diagrams of the hot corrosion furnace (a) Samples and sampler holder inside the furnace; (b) Gas pipelines linked with the furnace.

Table 6.1 Gas compositions used in air-firing vs oxy-firing

Gas composition	Air-firing	Oxy-firing
O_2 [vol%]	4.0	4.0
CO_2 [vol%]	15.0	Bal.
SO_2 [ppm]	300	3000
HCl [ppm]	260	1000
H_2O [vol%]	8.0	30
N_2 [vol%]	Bal.	10

The gas compositions are fixed and shown in ***Table 6.1*** to mimic the typical air-firing and oxy-firing conditions. The gas flow rate is 300 mL/min. The furnace was kept in 650^{o}C since it is the most critical temperature for tube surface corrosion. Furthermore, the elemental compositions of the five fly ash samples including Yallourn one were determined by XRF, shown in ***Table 6.2***, including two Xinjiang ash (sub-bituminous coal), Hazelwood fly ash, modified Hazelwood ash through adding Na_2SO_4 (10 *wt%*) and K_2SO_4 (10 *wt%*), and Yallourn fly ash. XRD results shown in the 2nd report indicate that, the concentration of Na2SO4 decreases in a sequence of HW < XJ_C < YL < XJ < HW_NaK. Six steel specimens were tested, whose properties are shown in ***Table 6.3***, including SS400, SUS304, SUS347, T23, T91, 12Cr1MoVG. The specimens' photographs are shown in ***Figure 6.2***.

.

Table 6.2 Ash composition of samples tested

	Ash composition [*wt%*]								
Ash samples	Na_2O	MgO	Al_2O_3	SiO_2	P_2O_5	SO_3	K_2O	CaO	Fe_2O_3
XJ (Ash 1)	10.4	12.46	8.27	16.24	0.45	10.58	0.45	38.82	0.38
XJC (Ash 2)	6.62	9.1	12.11	34.83	0.27	6.49	0.87	24.55	3.75
HW (Ash 3)	0.2	29.3	3.01	5.82	0.0	12.8	0.17	32.4	14.0
HWNaK (Ash 4)	4.53	23.4	2.4	4.6	0.0	12.8	5.6	25.9	11.2
YL (Ash 5)	3.12	23.95	3.03	2.91	0.0	6.25	0.15	9.67	49.0

Where, XJ= Xinjiang fly ash (no clay added), XJC=Xinjiang ash mixed with clay, HW=Hazelwood fly ash, obtained from power plant, HWNaK=Hazelwood fly ash (80 *wt%*)+Na_2SO_4(10 *wt%*)+K_2SO_4(10 *wt%*), and YL for Yallourn fly ash.

Table 6.3 Specimen materials

Specimen	Steel grade	Composition
SS400	*Carbon steel (JIS SS400-ASTM A283)*	
SUS304	*Austenite stainless steel (JIS SUS304-ASTM S30400)*	18Cr-8Ni
SUS347	*Austenite stainless steel*	18Cr-8Ni-Nb
T23	*Low-alloy steel*	2.25Cr-1.6W-V-Nb
T91	*High chrome ferritic steel*	9Cr-1Mo-V-Nb
12Cr1MoVG	*High chrome ferritic steel*	12Cr-1Mo-V

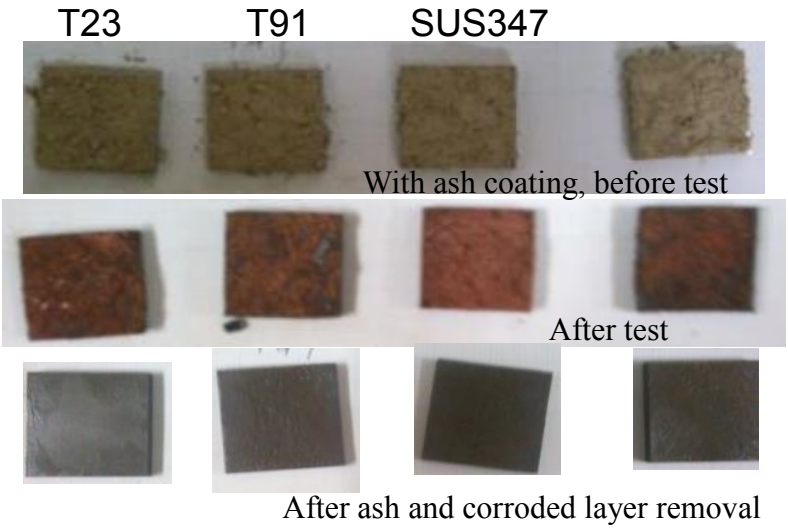

Figure 6.2 Specimens photographs before test, after test and after cleaning ash residue.

6.2 Comparison of tube corrosion between air-firing and oxy-firing conditions

Figure 6.3 depicts the results for tube corrosion upon the exposure to Yallourn fly ash and ash-free flue gas in air-firing case. For comparison, the results for the other fly ash samples were also included. As can be seen, the flue gas without the loading of fly ash caused the minimum corrosion for all the tubes except 12Cr1MoVG. However, once fly ash is deposited on the tube furnace, the corrosion was enhanced at varying extents for different materials. Upon the use of the normal carbon steel tube SS400, Yallourn fly ash resulted in the least mass loss, whereas XJ raw fly ash is the worst. However, for the other three high-Cr tubes from T23 to T91 and12

Cr1MoV, Yallourn fly ash led to the worst corrosion, whereas the use of XJC ash caused least corrosion. Since the content of Na_2SO_4 in Yallourn fly ash is not the highest, it is apparent that another element except Na_2SO_4 in fly ash is also crucial in affecting the tube corrosion. Regarding the different tubes tested, SUS304 is obviously the best one, although its Cr content is not the highest. The similar results were observed under the oxy-fuel condition. As demonstrated in ***Figure 6.4***, except the carbon steel tube SS400 for which Yallourn fly ash shows the least tube corrosion, the other tubes were corroded quite intensively upon the exposure to Yallourn fly ash.

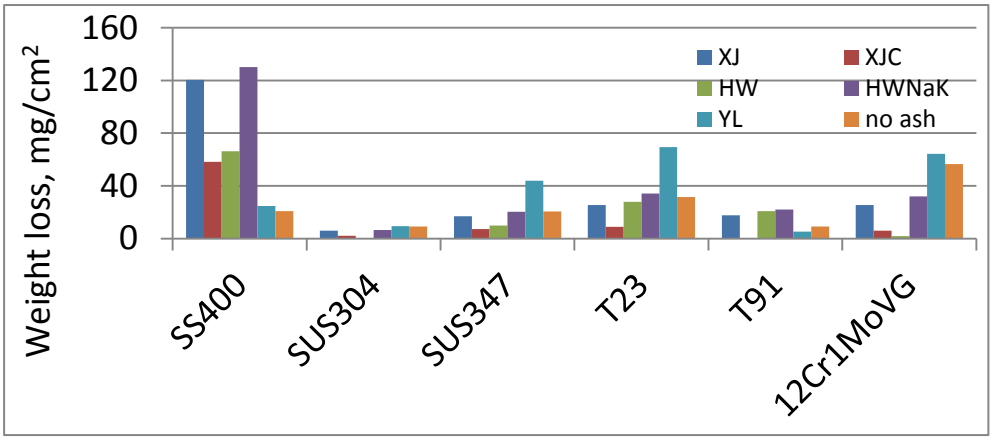

Figure 6.3 Mass loss for different tubes exposed to six different fly ash samples and flue gas only under the air-firing condition.

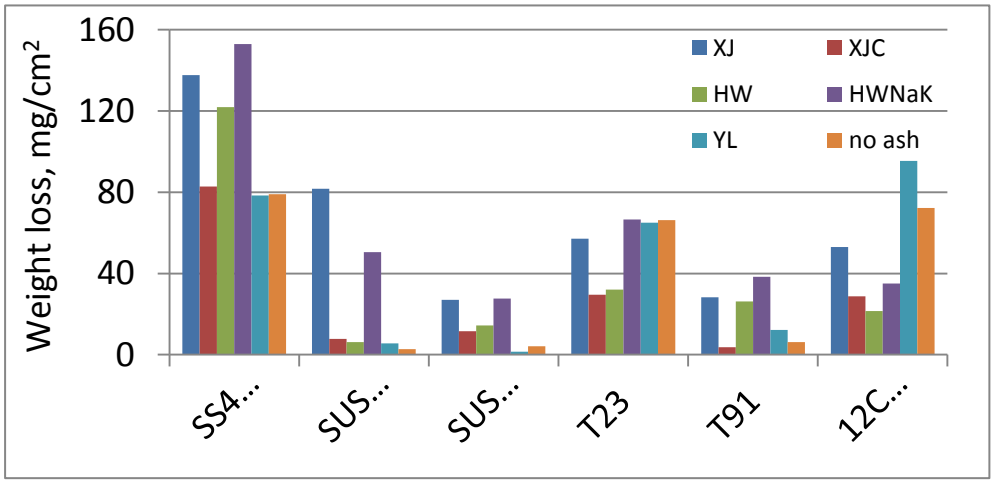

Figure 6.4 Mass loss for different tubes exposed to six different fly ash samples and flue gas only under the oxy-firing condition.

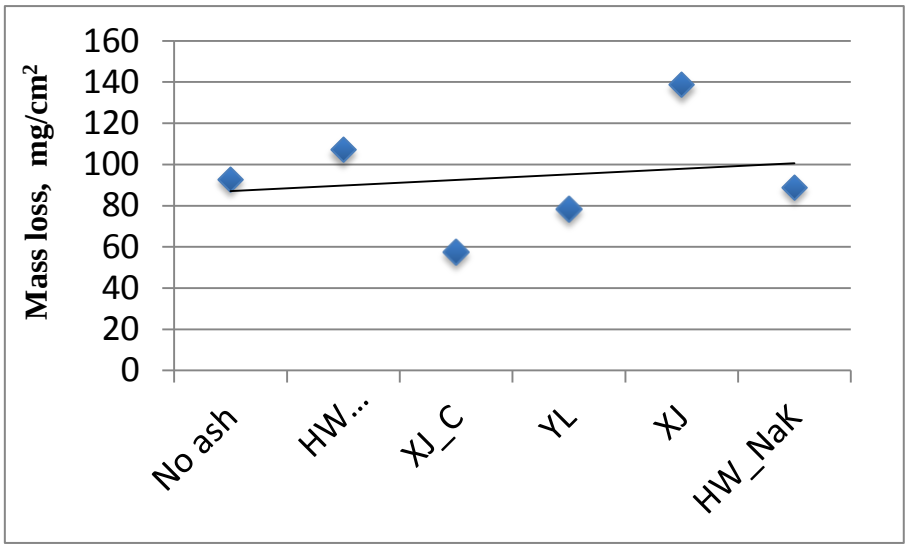

Figure 6.5 SS 400 tube corrosion as a function of fly ash sample under oxy-firing mode

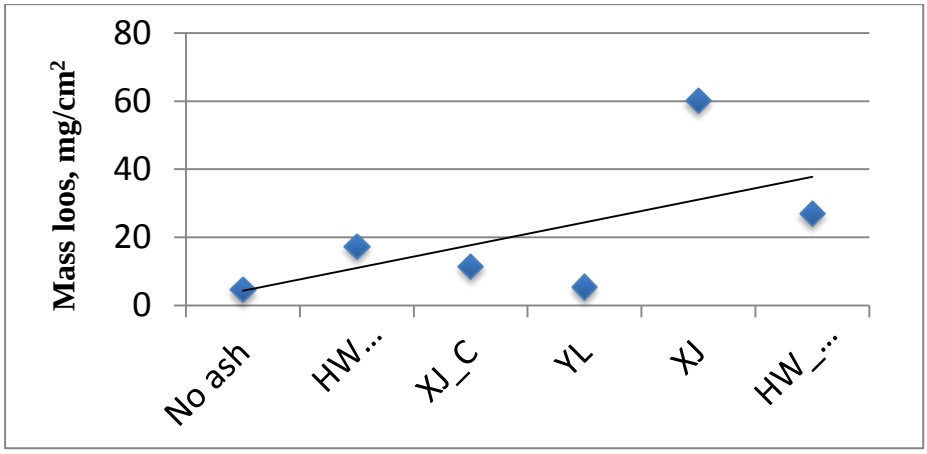

Figure 6.6 SUS 304 tube corrosion as a function of fly ash sample under oxy-firing mode

The effect of fly ash type on the tube corrosion was plotted in ***Figures 6.5*** and ***6.6*** for the tube SS400 and SUS304, respectively. The x-axis refers to ash-free flue gas and six fly ashes as an ascending sequence in terms of the concentration of Na_2SO_4. As demonstrated in both two figures, the correlation between the content of Na_2SO_4 in fly ash and tube corrosion is not strong. For the normal carbon steel SS400 used, its mass loss upon the exposure to ash-free flue gas is even comparable to the results achieved with the adhesion of fly ash on its surface. Clearly, the flue gas corrosion is more significant for this tube material. With regard to the advanced tube SUS304, a relatively clear correlation was confirmed, which also possesses a large slope. Compared to flue gas alone, the adhesion (thus, deposition) of fly ash on the tube

surface obviously enhanced the mass loss. Increasing the content of Na_2SO_4 in fly ash worsened the corrosion of SUS304. Except this variable, there should be another one affecting the tube corrosion as well, as hinted by the outline point for XJ coal ash in ***Figure 6.7.***

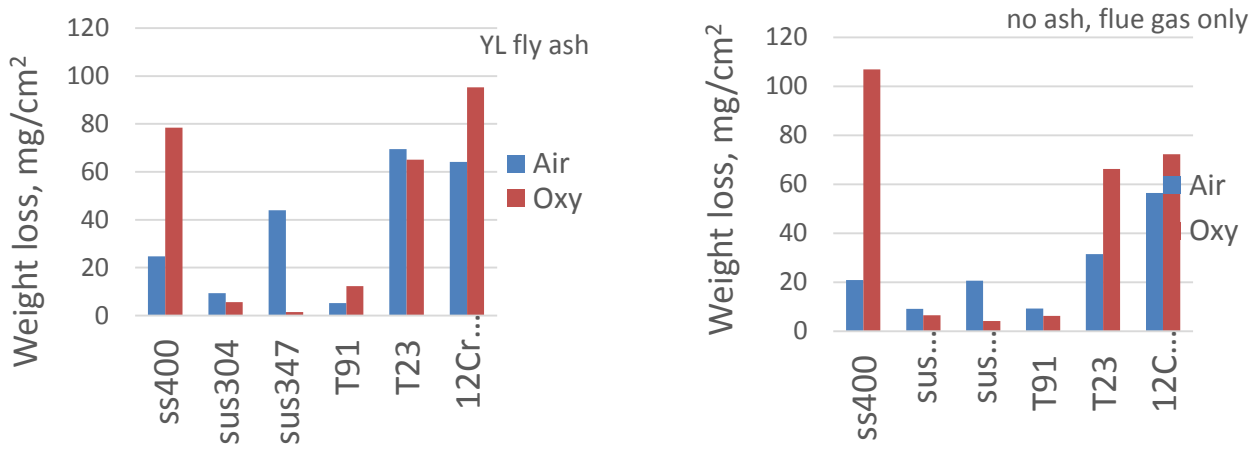

Figure 6.7 Comparison of tube corrosion between air-firing and oxy-fuel combustion modes for Yallourn fly ash and flue gas

Figure 6.7 further plots the comparison of tube corrosion between air-firing and oxy-fuel modes for Yallourn fly ash and flue gas. For Yallourn fly ash, the tubes including SS400, T91 and 12Cr1Mov were corroded with a larger mass loss under the oxy-fuel mode than the air-firing mode. However, for the other tubes, their corrosion under oxy-fuel mode is lower than or comparable to the air-firing result. The similar observation was confirmed for the ash-free flue gas only case. This implies that mass loss is not the only criteria that should be employed to assess the tube corrosion. Although the vaporisation of iron upon chlorination results in mass loss for a tube surface, the sulfation and oxidation reaction can increase the mass of the tube surface. As a result, the net mass of a tube specimen does not necessarily decrease upon its interaction with fly ash and/or flue gas. This will be further explained in next subsection.

6.3. Characterisation of the cross-section of corroded tubes

6.3.1 Structures and Microstructures for Corroded Tubes Caused by the Interaction with Hazelwood and Yallourn Fly ash

The structures for the cross-section of corroded tubes were observed by the use of an optimal microscopy (Nikon). Prior to the analysis, the corroded tube was mounted in epoxy resin, which was then cut by wire meshing to achieve its cross-section. The resulting cross-section was further polished by the use of silicon carbide papers. The same cross-section was also observed by scanning electron microscope (SEM, JEOL 7100) to observe its microstructure. The SEM was coupled with EDS that allows for both spot and line analysis.

The structures for the corroded tubes upon the interaction with Hazelwood fly ash in air-firing mode are illustrated in ***Figure 6.8***. For each tube cross-section picture, the bottom bright part refers to the bulk tube, whereas the top yellowish part denotes the epoxy resin used to mount the tube. The middle zone includes fly ash particles and the interface caused by the corrosion of tube. Such a zone especially the interface is unclear and even invisible for some tubes such as SUS304 and SUS347. However, it is clearly shown for the tubes exposed to Hazelwood fly ash in the oxy-firing mode in ***Figure 6.9***. Taking the SS400 tube as an example, an interface in dark brownish colour was formed on its surface, which refers to the corroded surface for this tube material. With regard to the other tubes including 12CrMoVG, T23 and even SUS347, a peeled-off layer was even observed, which sticks to the ash layer and shows in dark greyish colour. Clearly, all the tubes have been corroded significantly under the oxy-fuel case.

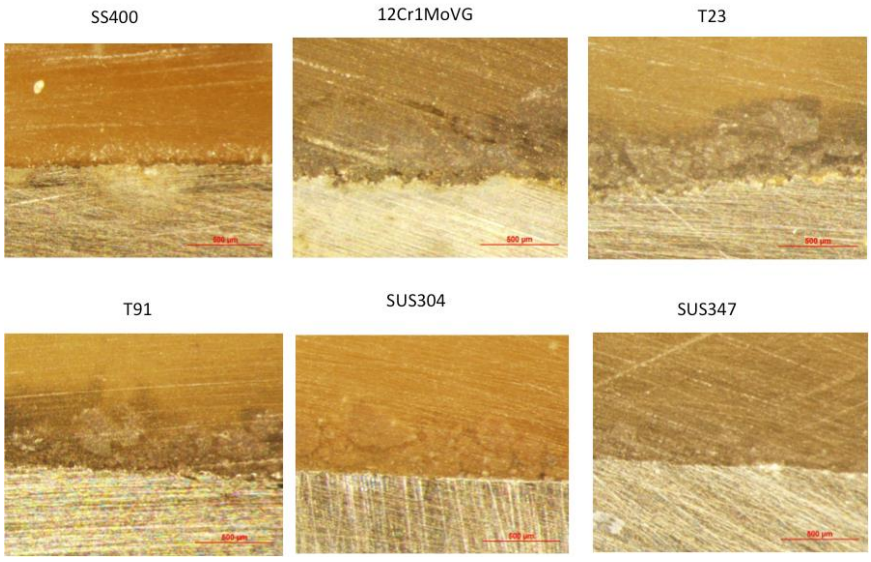

Figure 6.8 Structures for the cross-section of corroded tubes upon the adhesion of Hazelwood fly ash under the air-firing mode

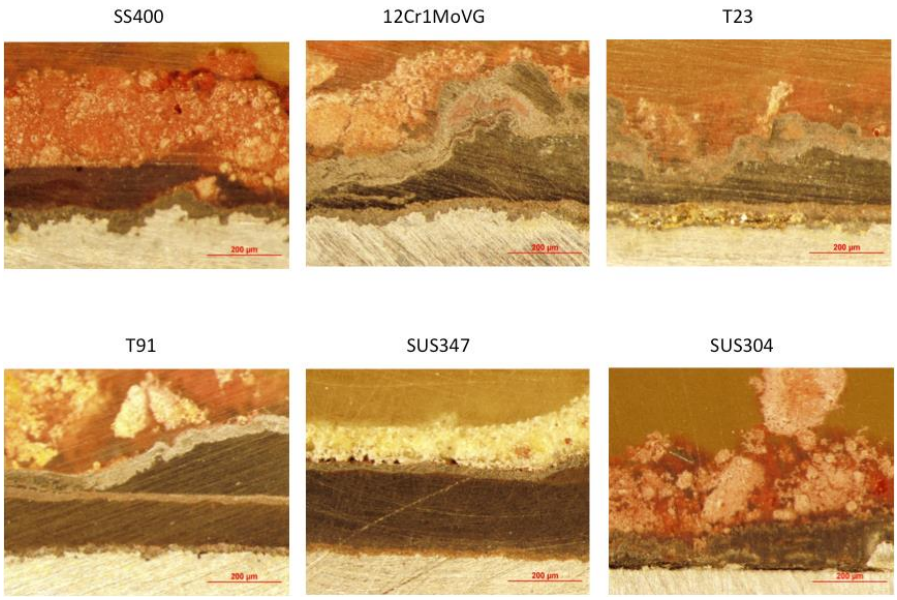

Figure 6.9 Structures for the cross-section of corroded tubes upon the adhesion of Hazelwood fly ash under the oxy-firing mode

A statistical analysis was conducted to quantify the depth of the corrosion interface for each tube under the oxy-fuel mode. Based on the interface depth, the corrosion rate or interface growth rate was further calculated by dividing the interface depth by the exposure time, 50 h employed in this study. The results are depicted in ***Figure 6.10***. The X-axis refers to the tube materials as an ascending sequence of the content of chromium (Cr) within them. Clearly, expect the tube T23, the content of Cr has a good correlation with the tube corrosion depth and its growth rate as well. Compared to SS400 having a depth of 40 μm and a growth rate of 0.7 μm/h, the use of SUS347 decreased the tube corrosion depth to only 10 μm, whereas its tube corrosion rate was decreased below 0.2 μm/h.

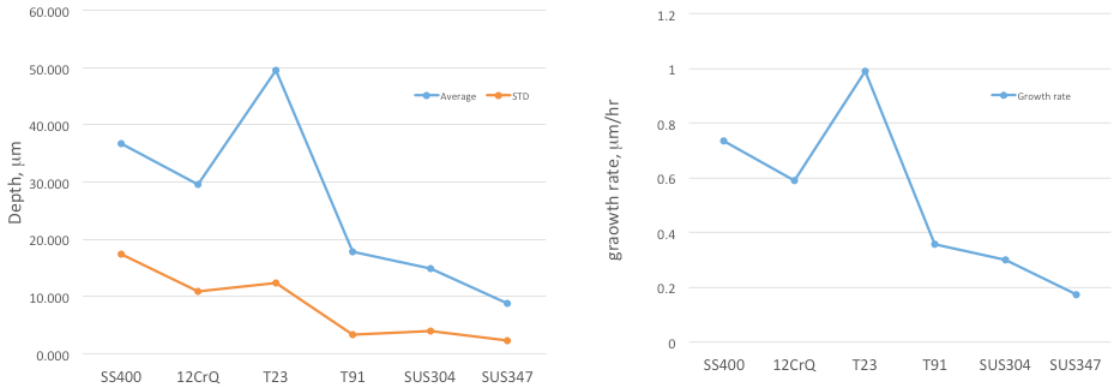

Figure 6.10 The interface depth and growth rate for the tubes exposed to Hazelwood fly ash in the oxy-firing mode.

6.3.2 Micro-Structure for the Cross-Section of Corroded Tubes

Figure 6.11 demonstrates the distributions of individual elements along the tube SS347 cross-section, upon the exposure to flue gas without *(a)* and with fly ash loading *(b)* under the oxy-fuel mode. Clearly, the flue gas only resulted in the oxidation of Cr and Fe. The resultant oxides should break down and thus failed to form a protective layer. This could be due to the formation of chloride eutectics, as suggested in ***Fig 6.8*** and ***6.9***. Therefore, oxygen (O) penetrated deeply into the Fe metal matrix. Such a phenomena was not confirmed for the air-firing flue gas only (data not shown), reflecting the high concentrations of corrosive gases, CO_2, H_2O, SO_2 and HCl within the oxy-fuel flue gas. For the fly ash-laden case, a Cr-rich protective layer was observed on the top of the interface, implying the resistance of fly ash layer against the attack of corrosive gases particularly HCl in flue gas. This could be due to the preferential chlorination of alkali and alkaline earth metals in the ash layer, and therefore, the molten chlorides were not formed on tube surface. Instead, both O and S permeated through the interface, suggestive of their overwhelming role on the ash-related tube corrosion, causing oxidation, sulfation and/or sulfidation of iron and other metals. In addition, since the creeping of S was not observed in the flue gas only case, the S in fly ash was apparently the major source accounting for the sulfation/sulfidation across the interface. Its interaction with iron metal could be due to the direct reaction between alkali sulphates and iron metal, as depicted in *equation (6-1)*, or the combined reaction between alkali sulphates, SO_3 (derived from SO_2 and O_2 in flue gas) and iron oxide (Fe_2O_3), as shown in *equation (6-2)*.

$$2\ (Na,K)_3Fe(SO_4)_3 + 17\ Fe = 8\ Fe_2O_3 + 3\ FeS + 3\ (Na,K)_2S \qquad (6\text{-}1)$$

$$m\ Na_2SO_4 + n\ K_2SO_4 + 0.5\ Fe_2O_3 + 1.5\ SO_3 = (Na,K)_3Fe(SO_4)_3,\ m+n = 1.5 \qquad (6\text{-}2)$$

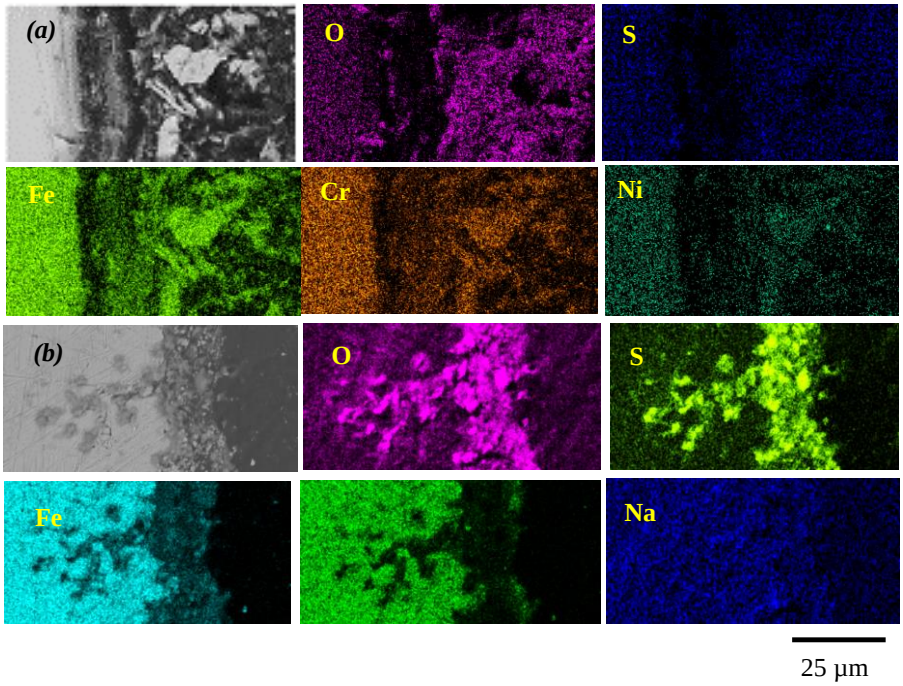

Figure 6.11 Elemental mapping for the cross-section of SUS347 exposed to flue gas only *(a)* and HW ash *(b)* in the oxy-firing mode

6.3.3 Characteristics of Fe-Bearing Species by XRD

Table 6.4 list the crystal species on the *bulk surfaces* of the corroded tubes upon the exposure to HW fly ash. The corresponding XRD patterns are shown in ***Figures 6.12*** and ***6.13***. Hematite/maghemite (Fe_2O_3) is the sole major species detected for all of the tubes under the oxy-fuel mode, whereas magnetite (Fe_3O_4) and wustite (FeO) are dominant for the air-firing tube surfaces. Clearly, apart from bulk O_2, the other gases including CO_2 and H_2O in oxy-firing flue gas are also the sources causing the full oxidation of tube surfaces under the oxy-firing mode. In addition, compared to 12Cr1MoVG being the only tube with eskolaite (Cr_2O_3) on its surface under the oxy-fuel mode, Cr_2O_3 was found for the high-Cr tubes from T91 through to

SUS347 in the air-firing mode, corresponding to the probable formation of Cr oxide-rich protective layer under the mild environment (e.g. low HCl, low steam and low SO_2 in the air-firing mode). Such a protective layer was either too thin to be detected (as shown in ***Figure 6.12***), or fully broke down under the oxy-fuel mode, due to the higher content of HCl that can permeate through the oxide scale once defects or cracks develop in it. In addition, pyrrhotite (FeS) was the only crystal detected by XRD on the SS400 tube exposed in the air-firing mode, which supports the equation (6.1).

Table 6.4 XRD results for the corroded tube surface exposed to HW ash

Tube	Mode	Major	Minor
SS400	Air	Hematite(Fe_2O_3)	Pyrrhotite (FeS)
	Oxy	Hematite (Fe_2O_3)	Magnetite (Fe_3O_4)
12Cr1MoVG	Air	Wustite (FeO)	Maghemite (Fe_2O_3)
	Oxy	Maghemite (Fe_2O_3)	Eskolaite (Cr_2O_3)
T23	Air	Magnetite (Fe_3O_4)	Ferric tungstate (Fe_2WO_6)
	Oxy	Hematite(Fe_2O_3)	Magnetite (Fe_3O_4)
T91	Air	Magnetite (Fe_2O_4)	Eskolaite (Cr_2O_3)
	Oxy	Hematite(Fe_2O_3)	Maghemite (Fe_2O_3)
SUS304	Air	Hematite(Fe_2O_3)	Eskolaite(Cr_2O_3)
	Oxy	Hematite(Fe_2O_3)	Maghemite (Fe_2O_3)
SUS347	Air	Maghemite (Fe_2O_3)	Eskolaite (Cr_2O_3)
	Oxy	Hematite(Fe_2O_3)	Maghemite (Fe_2O_3)

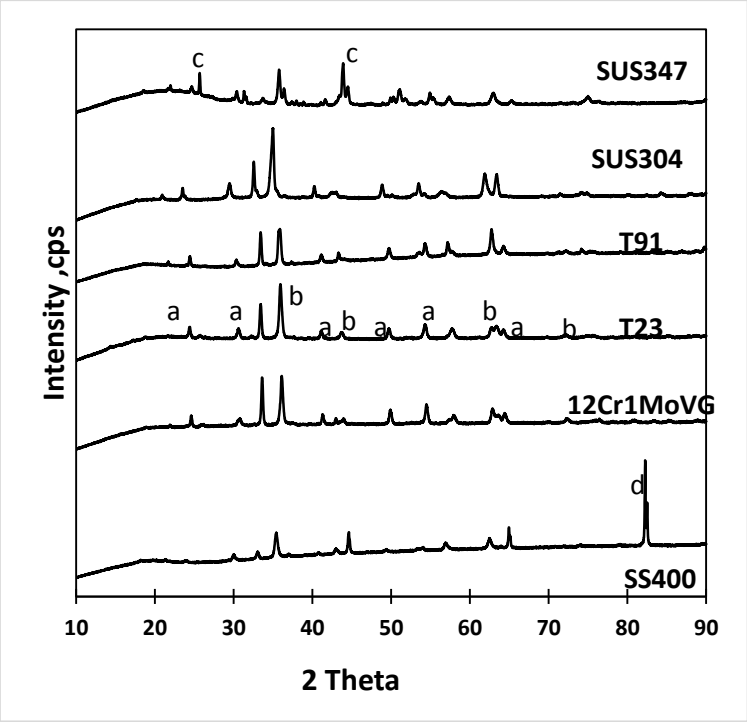

Figure 6.12 XRD Spectra for the corroded tubes exposed to Hazelwood fly ash under oxy-fuel combustion (a: Hematite (Fe_2O_3); b: Magnetite (Fe_2O_4); c: Maghemite (Fe_2O_3); d: Eskolaite (Cr_2O_3)).

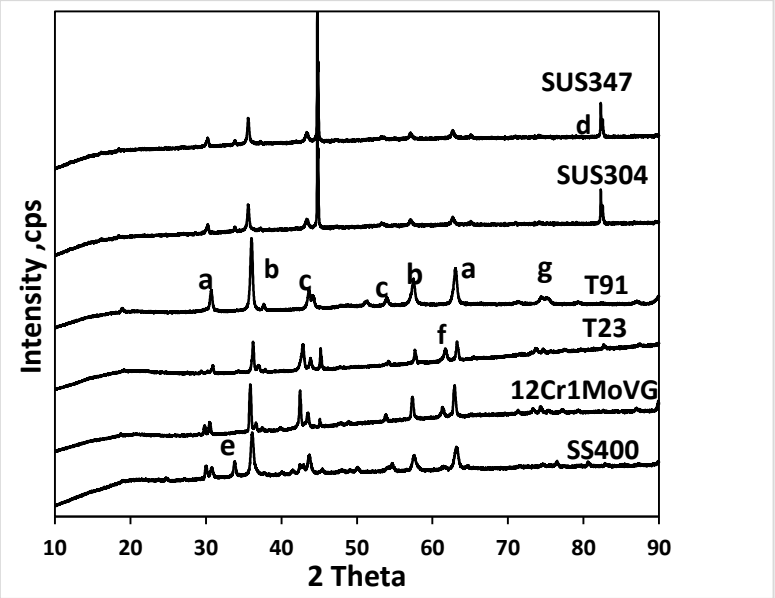

Figure 6.13 XRD Spectra for the corroded tubes exposed to Hazelwood fly ash under air-firing combustion (a: Hematite (Fe_2O_3); b: Magnetite (Fe_2O_4); c: Maghemite (Fe_2O_3); d: Eskolaite (Cr_2O_3); e Pyrrhotite (FeS); f: Wustite (FeO); g: Ferric tungstate (Fe_2WO_6))

6.3.4 Synchrotron X-ray absorption spectroscopy (XAS) speciation of iron on the cross-section of corroded tubes

6.3.4.1 Experimental set-up and the XANES spectra for blank tubes

The K-edge XANES spectra of Fe the cross-section of tube surface were obtained from beam line BL16A1 at the National Synchrotron Radiation Research Centre (NSRRC). The resin-mounted tube specimen holder, chamber and the insertion of tube specimen into the sample chamber are depicted in ***Figure 6.14***. With respect to the XANES analysis, a fixed exit double crystal Si (111) monochromator was used for the diffraction of the X-ray beam. For the analysis of Fe, pure elemental Fe was used for the calibration at a K-edge absorption energy of 7112 eV. The peak energy absorption (white-line) position was taken as the base (0 eV), with all

subsequent spectra recorded 200 eV below and 800 eV above this point in fluorescence mode. The pre-edge scan was conducted from -200 eV to -20 eV, at a step of 2 eV and 1 s per step. Following it is the scan from -20 eV to 40 eV at a step of 0.25 eV and 2 s per step. The final step spanned from 40 eV to 800 eV, with a step of 0.06 eV and 4 s per step.

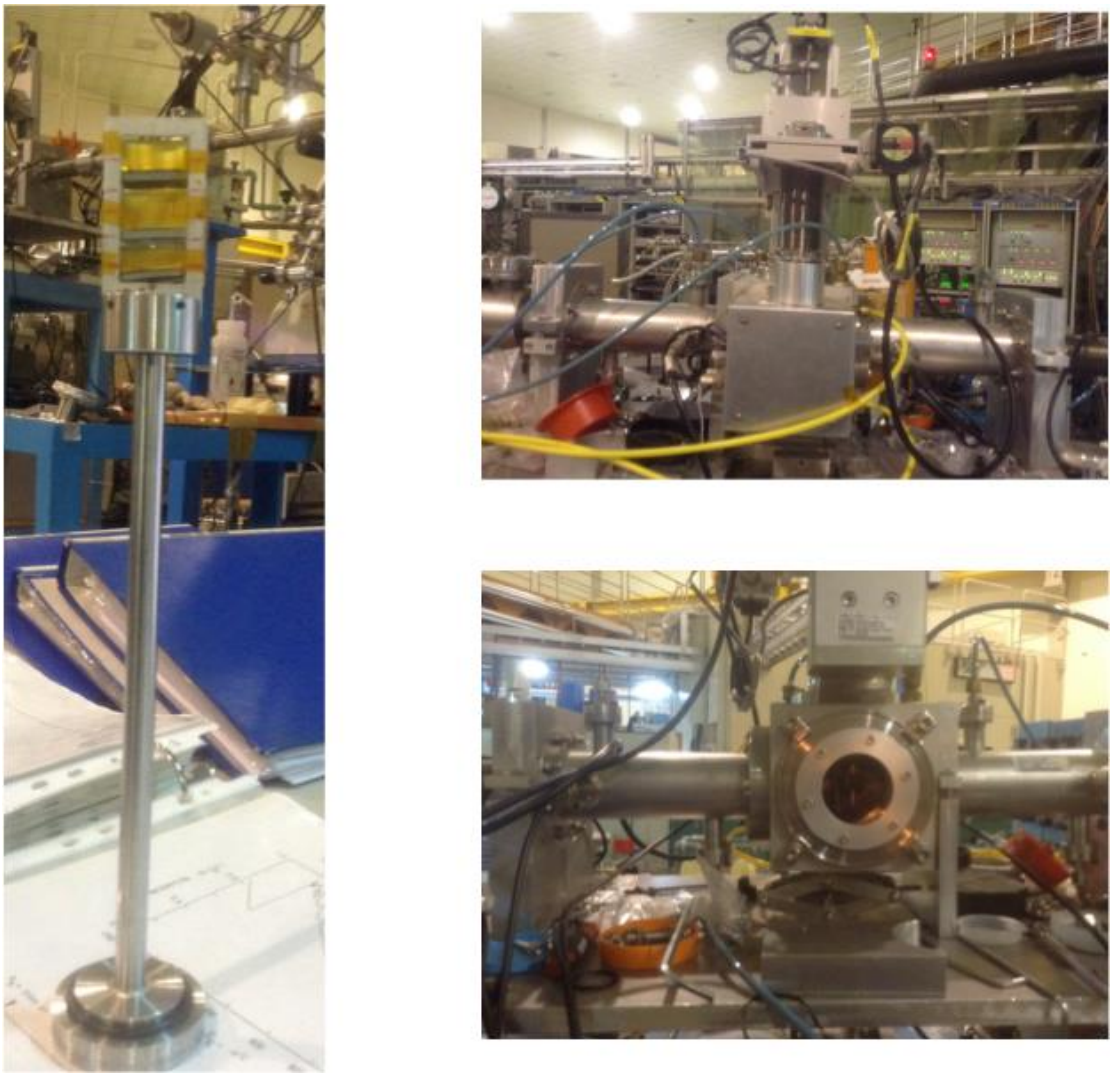

Figure 6.14 Sample holder and chamber for XANES analysis of the cross-section of tube surface in the beamline BL16 A, NSRRC, Taiwan, on June 2-8, 2015

For the XANES analysis of the cross-section of a tube surface, 3-5 spots along its cross-section were tested. As visualised in ***Figure 6.15***, five spots examined for a tube cross-section include, bulk material (the centreline of the tube), bottom (interfacial surface caused by corrosion between ash and tube), middle (between interface and the centre of the tube), bottom opposite

(the surface exposed to flue gas side), and middle opposite (between flue gas side interface and tube centre). The samples analysed for Fe K-edge XANES spectra are listed in **Table 6.6**.

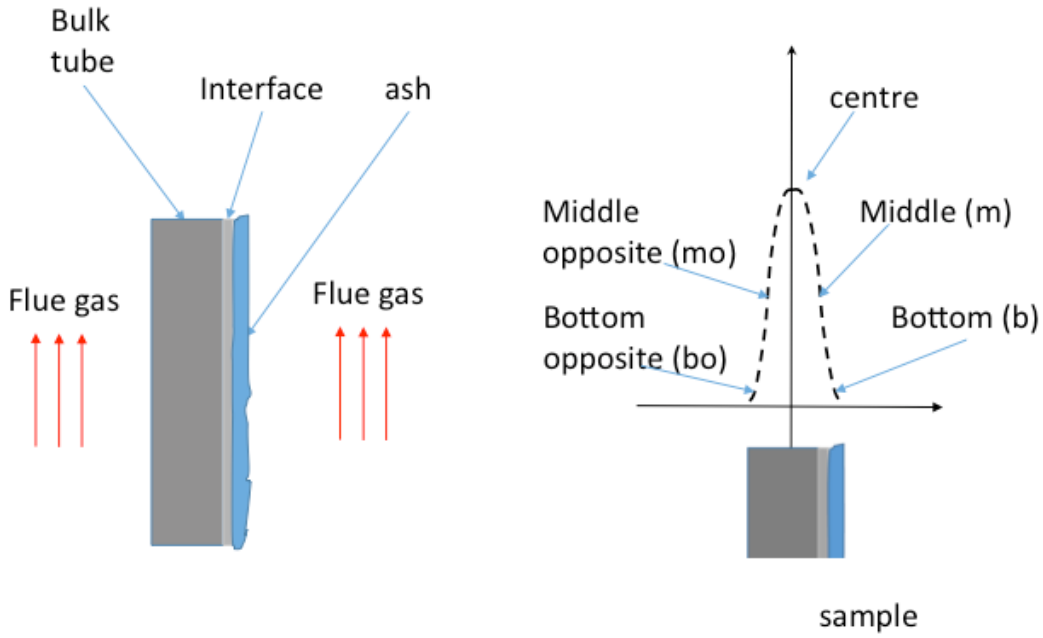

Figure 6.15 Visualised locations for the five spots examined along the cross-section of the tube

Table 6.6 Sample list done by the synchrotron XANES analysis on June 2-6 2015

	No	Ash sample	Flue gas composition	Tube material	File name
Effect of tube material on ash 3 corrosion in air vs oxy	1	Hazelwood fly ash (No 3)	Oxy	SS400	C1Fe.dat, C1Fem.dat, C1Feb.dat
	2	Hazelwood fly ash (No 3)	Oxy	SUS347	C2Fe.dat, C2Fem.dat, C2Feb.dat
	3	Hazelwood fly ash (No 3)	Oxy	T23	C3Fe.dat, C3Fem.dat, C3Feb.dat
	4	Hazelwood fly ash (No 3)	Oxy	T91	C4Fe.dat, C4Fem.dat, C4Feb.dat
	5	Hazelwood fly ash (No 3)	Oxy	12Cr1MoV	C5Fe.dat, C5Fem.dat, C5Feb.dat
	6	Hazelwood fly ash (No 3)	Air	SS400	C6Fe.dat, C6Fem.dat, C6Feb.dat
	7	Hazelwood fly ash (No 3)	Air	SUS347	C7Fe.dat, C7Fem.dat, C7Feb.dat

	8	Hazelwood fly ash (No 3)	Air	SUS304	C8Fe.dat, C8Fem.dat, C8Feb.dat
	26	Hazelwood fly ash (No 3)	Air	T23	C26Fe.dat, C26Fem.dat, C26Feb.dat
	10	Hazelwood fly ash (No 3)	Air	T91	C10Fe.dat, C10Fem.dat, C10Feb.dat
	11	Hazelwood fly ash (No 3)	Air	12Cr1MoV	C11Fe.dat, C11Fem.dat, C11Feb.dat
Effect of ash composition on SS440 corrosion in air vs oxy	12	Ash No 1 (XJ)	Air	SS400	C12Fe.dat, C12Fem.dat, C12Feb.dat
	13	Ash No 2 (XJ_C)	Air	SS400	C13Fe.dat, C13Fem.dat, C13Feb.dat
	14	Ash No 4 (HW_NaK)	Air	SS400	C14Fe.dat, C14Fem.dat, C14Feb.dat
	15	Ash No 5 (YL)	Air	SS400	C15Fe.dat, C15Fem.dat, C15Feb.dat
	16	Ash No 1 (XJ)	Oxy	SS400	C16Fe.dat, C16Fem.dat, C16Feb.dat
	17	Ash No 2 (XJ_C)	Oxy	SS400	C17Fe.dat, C17Fem.dat, C17Feb.dat
	18	Ash No 4 (HW_NaK)	Oxy	SS400	C18Fe.dat, C18Fem.dat, C18Feb.dat
	19	Ash No 5 (YL)	Oxy	SS400	C19Fe.dat, C19Fem.dat, C19Feb.dat
Effect of ash composition on T23 corrosion in air vs oxy	20	Ash No 1 (XJ)	Air	T23	C20Fe.dat, C20Fem.dat, C20Feb.dat
	9	Ash No 2 (XJ_C)	Air	T23	C9Fe.dat, C9Fem.dat, C9Feb.dat
	21	Ash No 4 (HW_NaK)	Air	T23	C21Fe.dat, C21Fem.dat, C21Feb.dat
	22	Ash No 1 (XJ)	Oxy	T23	C22Fe.dat, C22Fem.dat, C22Feb.dat
	23	Ash No 2 (XJ_C)	Oxy	T23	C23Fe.dat, C23Fem.dat, C23Feb.dat

	24	Ash No 4 (HW_NaK)	Oxy	T23	C24Fe.dat, C24Fem.dat, C24Feb.dat
	25	Ash No 5 (YL)	Oxy	T23	C25Fe.dat, C25Fem.dat, C25Feb.dat

The standards used include pure iron metal (Fe), hematite (Fe_2O_3), maghemite (Fe_2O_3), magnetite (Fe_3O_4), augite ($NaFeO_2$), wusetite (FeO), siderite ($FeCO_3$), ferrous sulphate ($FeSO_4$), ferric sulphate ($Fe_2(SO_4)_2$), and ferrous chloride ($FeCl_2$). All spectra were normalised using the ATHENA software (normalization order of 2, pre-edge range normalization range of -192 eV to -30 eV and post-edge range of +77.5 eV to +281 eV). Subsequently, the linear combination fitting (LCF) feature was used on the normalized sample spectra for the quantification of iron speciation. The LCF was done from -20 eV to +50 eV with respect to the peak energy absorption (white-line) position (~7122 eV).

Table 6.7 Elemental compositions of the six tube materials used

Tube	C	Mn	Si	P	S	Cr	Ni	N	Mo
SS400	<0.17-0.20	1.4	-	0.045	0.045				
12CrMoVG	0.08-0.15		0.17-0.37	<0.03	<0.03	0.9-1.2			0.25-0.35
T23						2.25			0.2
T91						9			1
SUS304	<0.08	2	0.75	0.045	0.03	18-20	10.5	0.1	
SUS347	0.04-0.08	<2	1	0.045	0.03	17-19	13		0.5

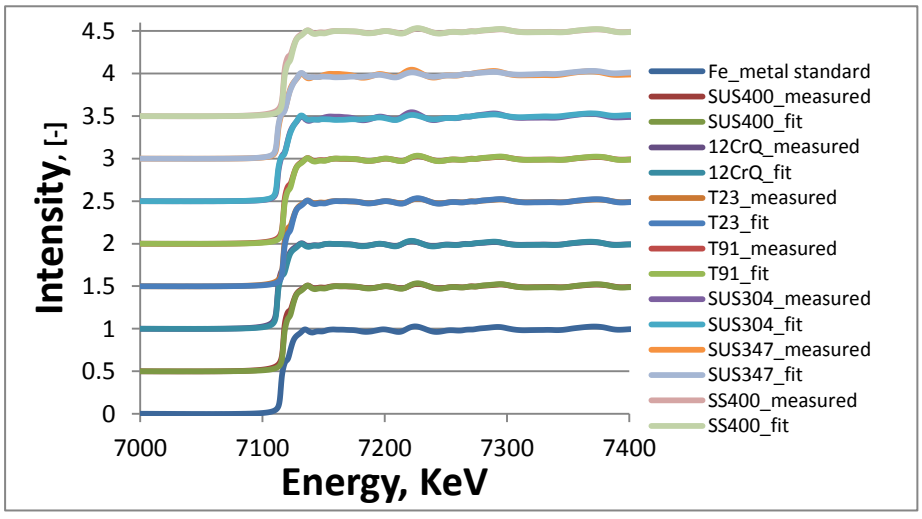

Figure 6.16 XANES spectra and respective fitted curves for the six tube materials and pure iron metal standard

Elemental compositions of the tube materials used are listed in ***Table 6.7***. Note that, the tubes were listed in an ascending sequence in terms of the content of Cr. The XANES spectra for the blank tubes are depicted in ***Figure 6.16,*** where both the originally measured spectra and the respective fitting curves were plotted. The LCF results are tabulated in ***Table 6.8***. Clearly, iron metal is the major and almost the single phase for iron in the tubes from SS400 to T91. However, apart from iron metal, some oxides are present in the other two tubes. This should be due to the oxidation of tube cross-section upon the exposure to air after the hot corrosion test.

Table 6.8 XANES LCF fitting results for the speciation of iron on the cross-section of the six tubes

	SS400	12CrMoVG	T23	T91	SUS304	SUS347
Fe_metal	0.977	0.9945	0.9751	0.9165	0.812	0.886
Augite					0.005	0.0085
FeO					0.183	0.1055
$Fe2O_3$ (hem)				0.075		
Fe_2O_3(Magh)						
Fe_3O_4						
$Fe(CO_3)$	0.023		0.0249	0.0085		
$FeCl_2$		0.0055				

6.3.4.2 Distribution of iron species along the cross-section of SS400

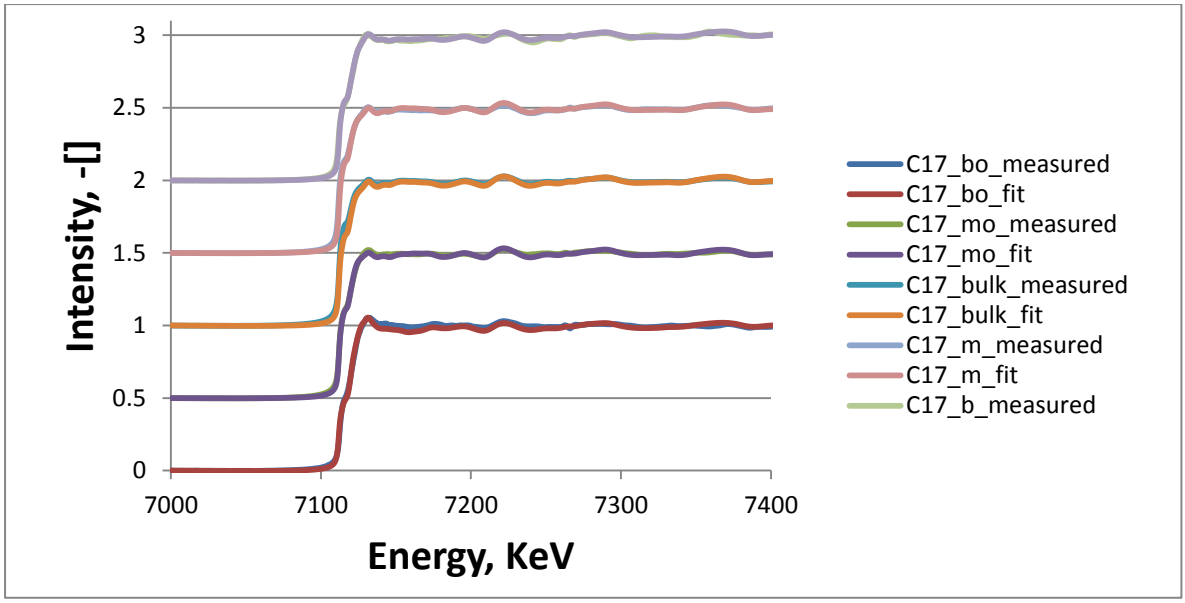

Figure 6.17 XANES spectra and fitted curves for SS400 exposed to XJ_C ash in oxy-firing mode

The distribution of iron species along the cross-section of the corroded SS400 was examined first. The tube was exposed to XJ_C ash in the oxy-firing mode. The original and fitted XANES spectra are shown in ***Figure 6.17,*** whereas the LCF results are tabulated in ***Figure 6.18***. It is clear that the iron speciation has a distribution along the cross-section of the tube. Compared to the presence of pure metal only in the centre, siderite and a tiny amount of pyrite were observed in the middle zone exposed to the flue gas side. This is a clear sign of the penetration of both oxygen (from CO_2 in this case) and sulphur into the tube. Interestingly, there is no any oxide or sulphide/sulphate in the middle zone on the fly ash side. Apparently, the presence of fly ash exerted a resistance against flue gas penetration. Regarding the two interfaces, hematite is the most abundant species on fly ash side, which is accompanied by siderite and pyrite in a descending sequence. On the other hand, siderite and hematite are comparable in amounts on the flue gas side.

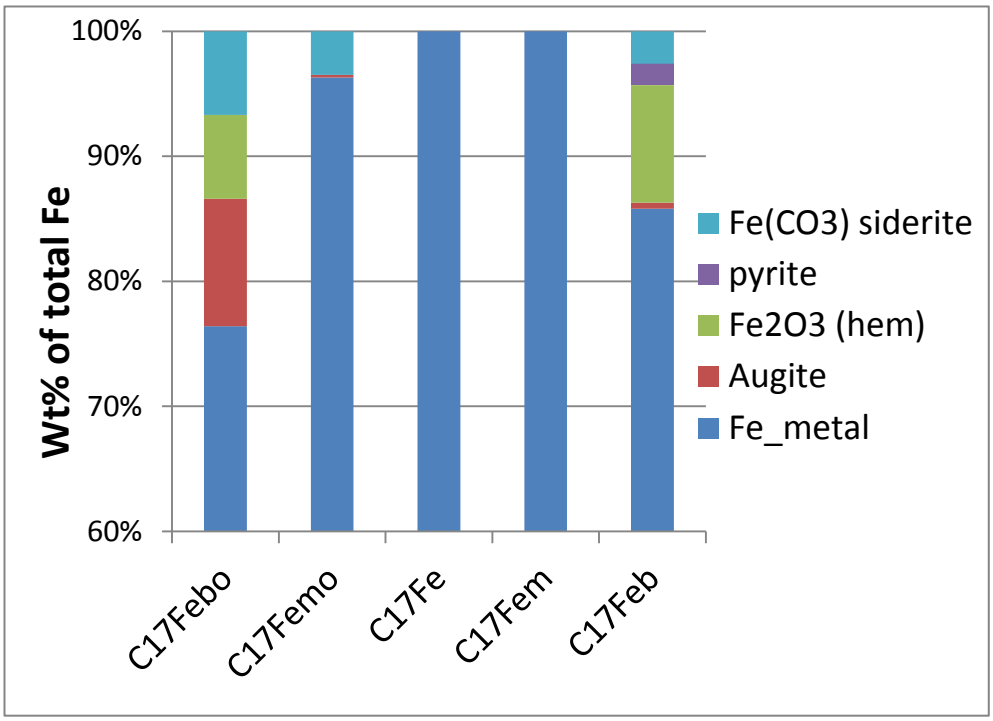

Figure 6.18 Quantified speciation for iron-bearing compounds along the cross-section of tube SS400 exposed to XJ_C ash in oxy-firing mode

6.3.4.4 Effect of tube material on the corrosion by Hazelwood fly ash

The effect of tube material on the corrosion caused by Hazelwood fly ash in air is depicted in ***Figures 6.19*** and ***6.20***. ***Figure 6.19*** demonstrates the change on the middle zone of the tubes, whereas ***Figure 6.20*** depicts the change on the interface for the tubes. Included in each figure are the original XANES spectra, fitted curve and LCF results. As can be seen, the tubes T91 and SUS304 have the most severe oxygen penetration, with the formation of wustite (FeO) and even augite in their middle zones. The other tubes were little corroded in its middle zone. The severe corrosion on the surface was further confirmed for these two tubes. That is, magnetite, hematite and augite were formed for the tube T21, whereas hematite and siderite were formed for the tube SUS304. For the SS400 with lowest Cr content, hematite is the only species formed on its corroded surface. For the medium-Cr tubes from 12Cr1MoV through to T91, the amount of magnetite (Fe_3O_4) was increased with the increase on the content of Cr. For the two high-Cr tubes SUS304 and SUS347, magnetite was not observed, whereas hematite is the major species formed. Clearly, the oxidation speciation extent of iron was affected by the content of Cr within it.

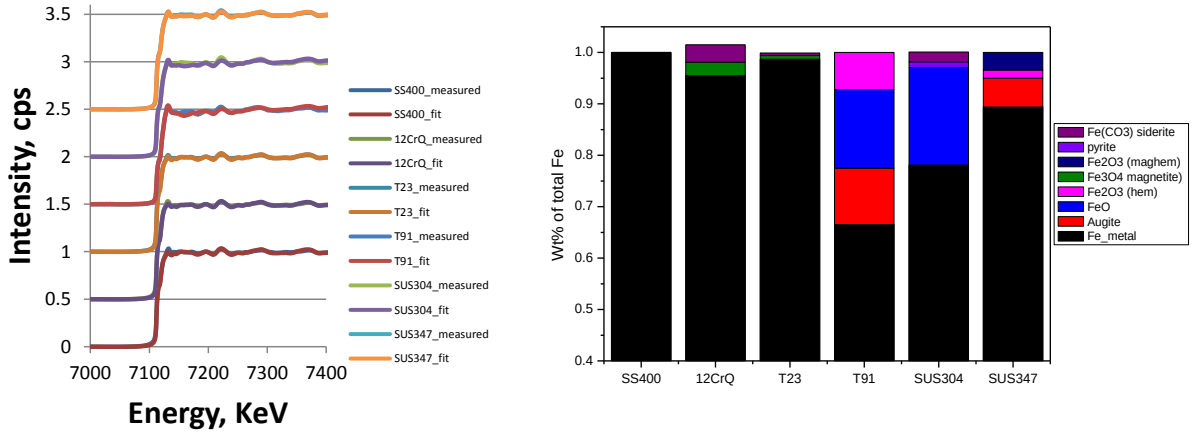

Figure 6.19 XANES spectra, fitted curve and LCF results for the middle zones of the six tubes exposed to Hazelwood fly ash in air-firing mode

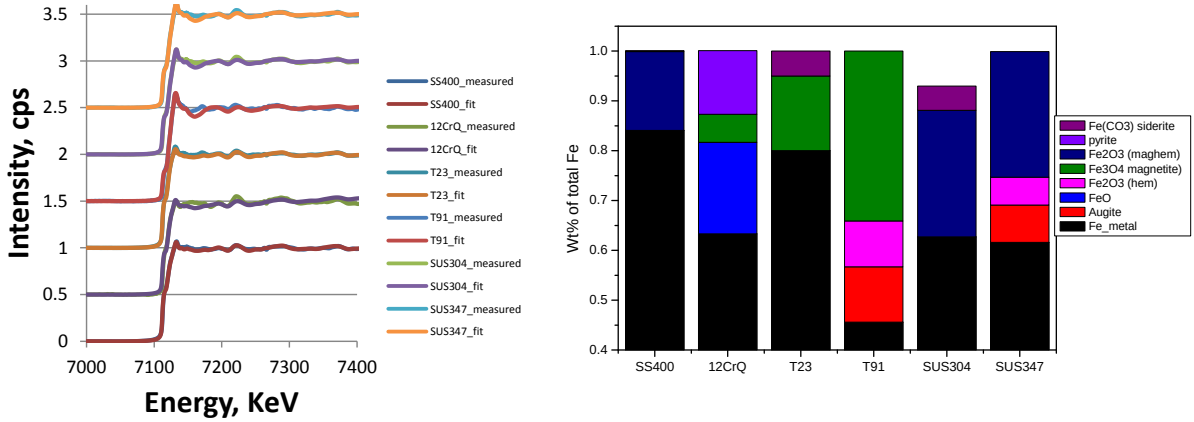

Figure 6.20 XANES spectra, fitted curve and LCF results for the interfaces of the six tubes exposed to Hazelwood fly ash in air-firing mode

Figures 6.21 and 6***.22*** depict the XANES spectra and fitting results for the middle zones and interfaces of the six tubes exposed to Hazelwood fly ash in the oxy-firing mode. Regarding the middle zone, one can see that augite is the major Fe-bearing species formed for the high-Cr tube SUS347, whereas siderite is the single compound for the two medium-Cr tubes, T23 and T91, and few of the oxidized species were found for the two low-Cr tubes. The Fe-bearing compounds on the interfacial layers of these tubes are broad. In general, the fraction of augite was increased upon increasing the content of Cr in the tubes, whereas the amount of siderite was decreased on the tubes with elevated Cr content.

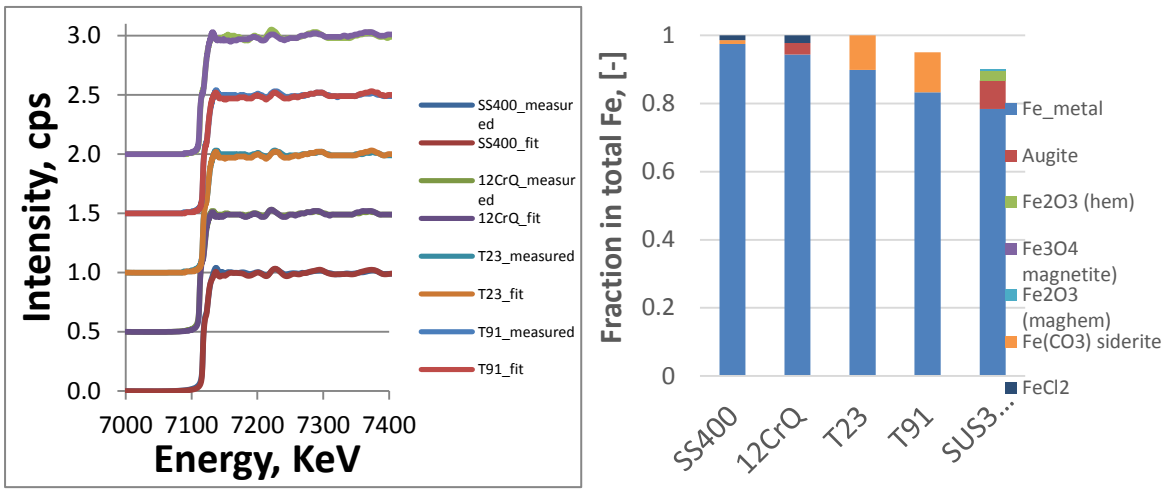

Figure 6.21 XANES spectra and fitting results for the middle zone of SUS347 exposed to Hazelwood fly ash in oxy-firing mode

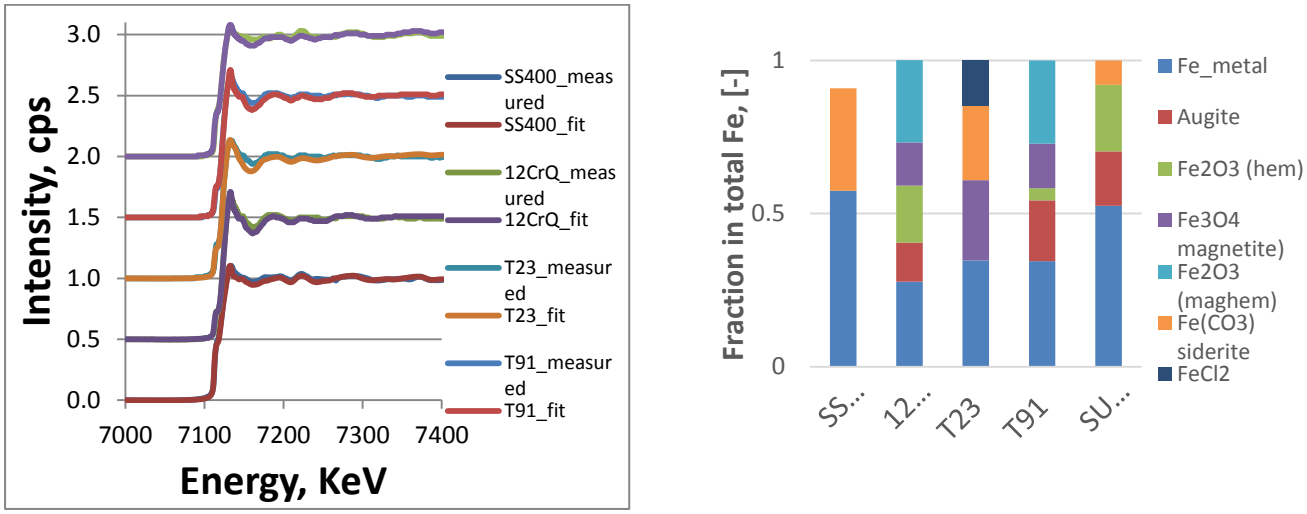

Figure 6.22 XANES spectra and fitting results for the interfacial layer of SUS347 exposed to Hazelwood fly ash in oxy-firing mode

6.3.4.5 Effect of fly ash compositions on the corrosion of tube material SS400

The effect of fly ash compositions on the corrosion of tube material SS400 in air-firing mode was demonstrated in ***Figures 6.23*** and ***6.24***. Note that, the X-axis for the LCF results in the two right panels refer to the five fly ash samples with an ascending sequence in terms of the content of sodium sulphate, ash 5 (Yallourn) < 2 (XJ_C fly ash) < 3 (Hazelwood) < 1 (XJ raw

coal fly ash) < 4 (HW_NaK, Hazelwood fly ash mixed with sodium sulphate and potassium sulphate).

With respect to the middle zone in ***Figure 6.23,*** it was rarely corroded irrespective of fly ash compositions. This is expectable, since the tube corrosion in air is very mild, and few of the corrosive components such as oxygen and sulphur was able to penetrate inside the tube. However, regarding the interfacial layer results in ***Figure 6.24***, the speciation of iron is rather random, showing unclear trend with the fly ash composition. Here again, this can be attributed to the mild corrosion in air-firing mode. The interfacial layer formed was thus thin, and its analysis is thus subject to large error that was mainly due to the difficulty for locating the interface prior to commencing the XANES analysis.

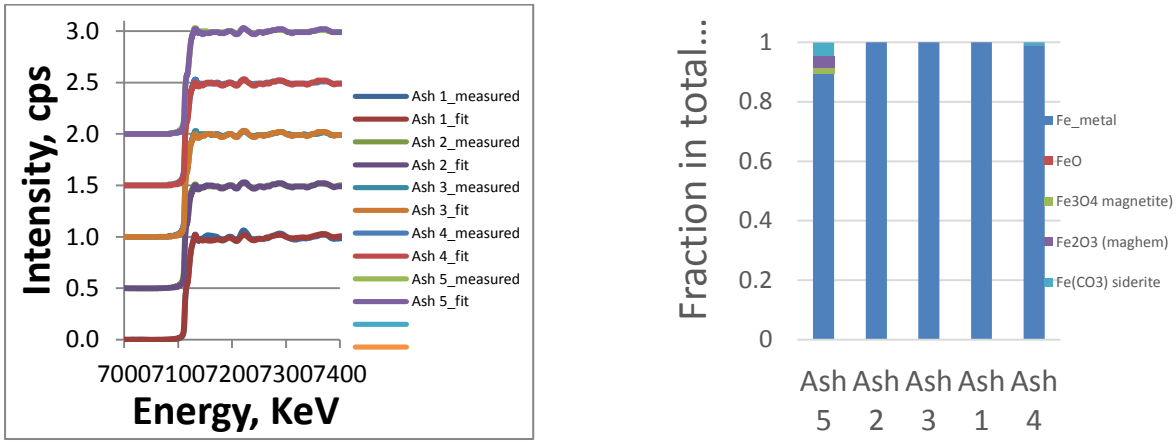

Figure 6.23 XANES spectra and LCF results for the middle zone of the tube material SS400 exposed to five different fly ashes in air-firing mode

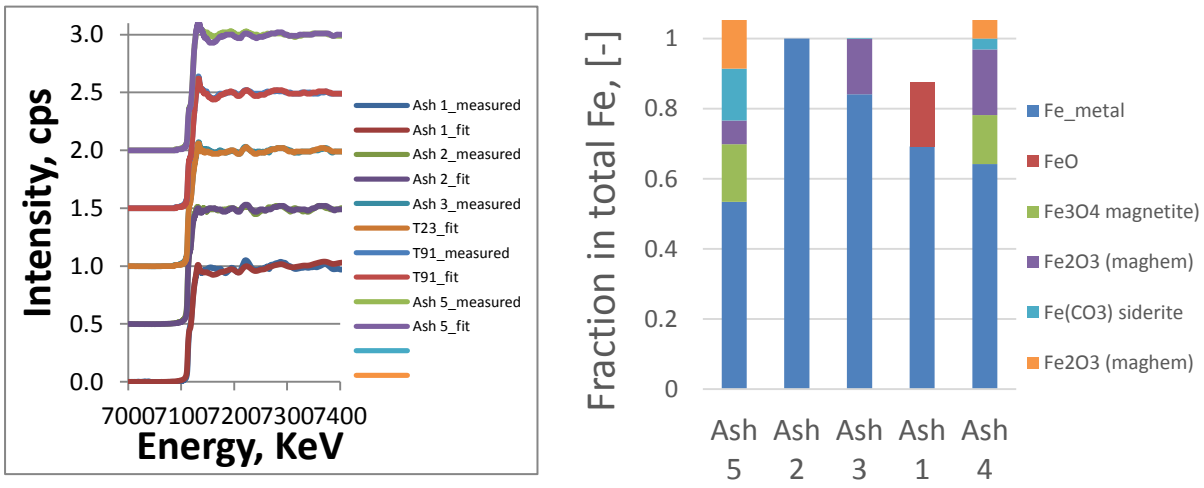

Figure 6.24 XANES spectra and LCF results for the interfacial layer of the tube material SS400 exposed to five different fly ashes in air-firing mode

Figures 6.25 and ***6.26*** depict the effect of fly ash composition on the corrosion of tube SS400 in the oxy-firing mode. Obviously, the tube corrosion was severe under the oxy-fuel mode, and hence, even the middle zone of the tube was corroded. As shown in ***Figure 6.25***, augite is rich in fly ash with the highest sodium sulphate content, whereas siderite ($FeCO_3$) is abundant in the tube middle zone corroded by the two medium-Na_2SO_4 fly ash samples. Interestingly, few of the Fe-bearing oxides were found in the middle zone corroded by the two low-Na_2SO_4 tubes. With respect to the interfacial layer shown in ***Figure 6.26***, one can see a clear decrease on the amount of oxidised Fe-bearing compounds with the increase of the Na_2SO_4 content in the fly ash. In addition, with the increase on the Na_2SO_4 content, one can see an increase on the fraction of augite, indicative of the enhance interaction between Fe metal and sodium sulphate in the fly ash.

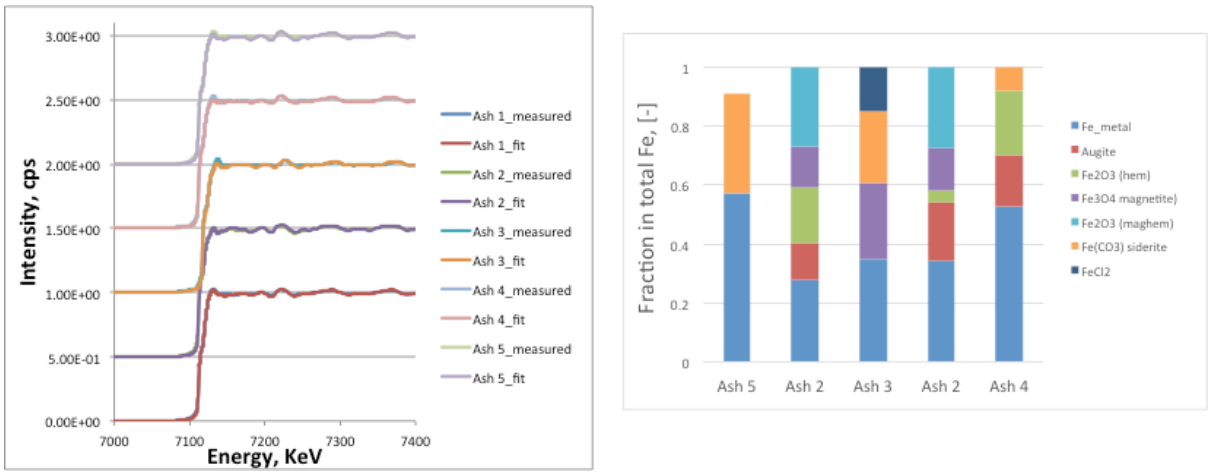

Figure 6.25 XANES spectra and LCF results for the middle zone of the tube material SS400 exposed to five different fly ashes in oxy-firing mode

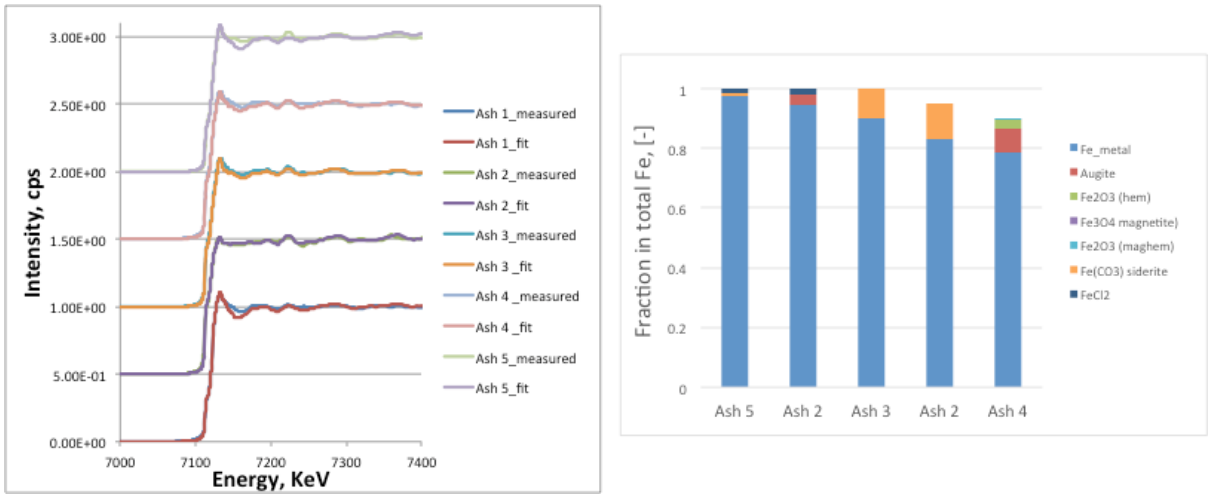

Figure 6.26 XANES spectra and LCF results for the interfacial layer of the tube material SS400 exposed to five different fly ashes in oxy-firing mode

6.3.4.6 Effect of fly ash compositions on the corrosion of tube material T23

The effect of fly ash compositions on the corrosion of tube material T23 in air-firing mode was demonstrated in ***Figures 6.27*** and ***6.28***. Here again, the X-axis for the LCF results in the two right panels refer to the five fly ash samples with an ascending sequence in terms of the content of sodium sulphate, ash 5 (Yallourn) < 2 (XJ_C fly ash) < 3 (Hazelwood) < 1 (XJ raw coal fly ash) < 4 (HW_NaK, Hazelwood fly ash mixed with sodium sulphate and potassium sulphate). With respect to the middle zone in ***Figure 6.27***, it was rarely corroded except fly ash 4 for Hazelwood fly ash mixed with 10 *wt%* Na_2SO_4 and K_2SO_4. The most abundant species was found to be hematite, suggestive of the oxygen penetration inside the tube. Regarding the interfacial layer results in ***Figure 6.28***, the similar phenomena was observed too, that is, fly ash 4 caused the most severe corrosion for T23. Apart from hematite, Fe^{3+} sulphate was also observed. This is a clear sign of the sulfation of iron metal surface.

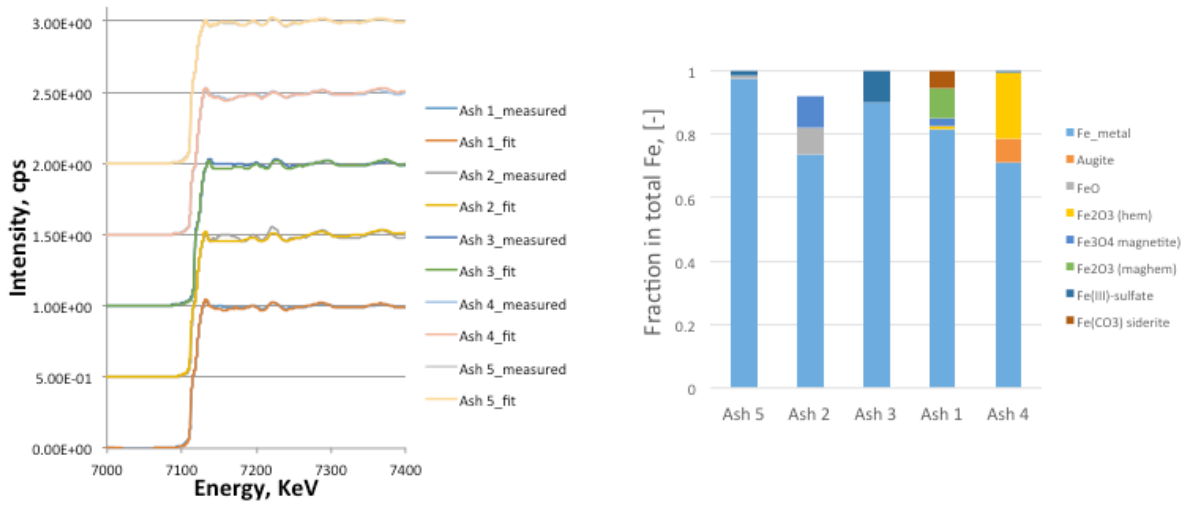

Figure 6.27 XANES spectra and LCF results for the middle zone of the tube material T23 exposed to five different fly ashes in air-firing mode

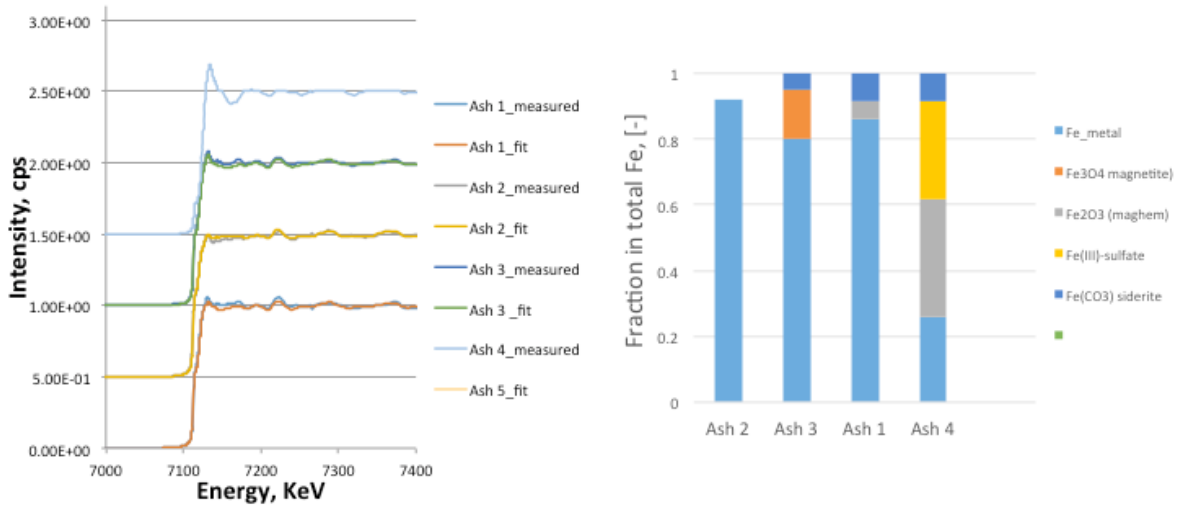

Figure 6.28 XANES spectra and LCF results for the interfacial layer of the tube material T23 exposed to five different fly ashes in air-firing mode

Figures 6.29 and ***6.30*** depict the effect of fly ash composition on the corrosion of tube T23 in the oxy-firing mode. Obviously, the tube corrosion was severe under the oxy-fuel mode, and hence, even the middle zone of the tube was corroded. As shown in ***Figure 6.29***, the fly ash No 4 with the highest Na_2SO_4 content also led to the most severe corrosion for this tube, resulting in the formation of hematite in its middle zone. With respect to the interfacial layer shown in ***Figure 6.30***, one can see a clear increase on the amount of hematite (Fe_2O_3) with the increase of the Na_2SO_4 content in the fly ash. For the low-Na_2SO_4 fly ash samples, the fraction of magnetite (Fe_3O_4) is high, implying the insufficient oxidation of iron metal surface.

Moreover, the fraction of siderite ($FeCO_3$) was found reasonably high, implying that the abundant CO_2 in oxy-firing flue gas is an oxidant to promote the oxidation of iron metal too.

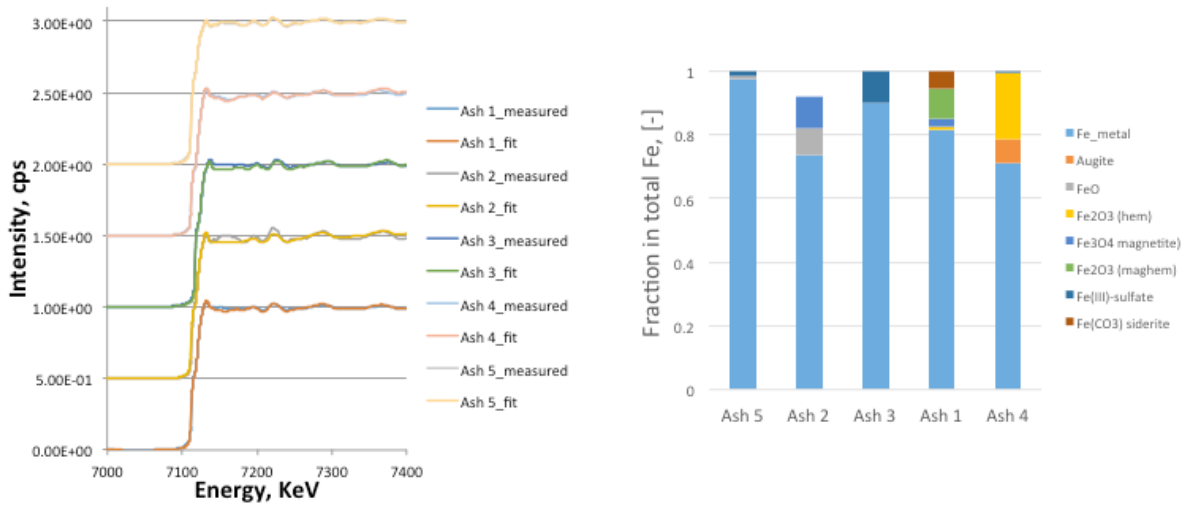

Figure 6.29 XANES spectra and LCF results for the middle zone of the tube material T23 exposed to five different fly ashes in oxy-firing mode

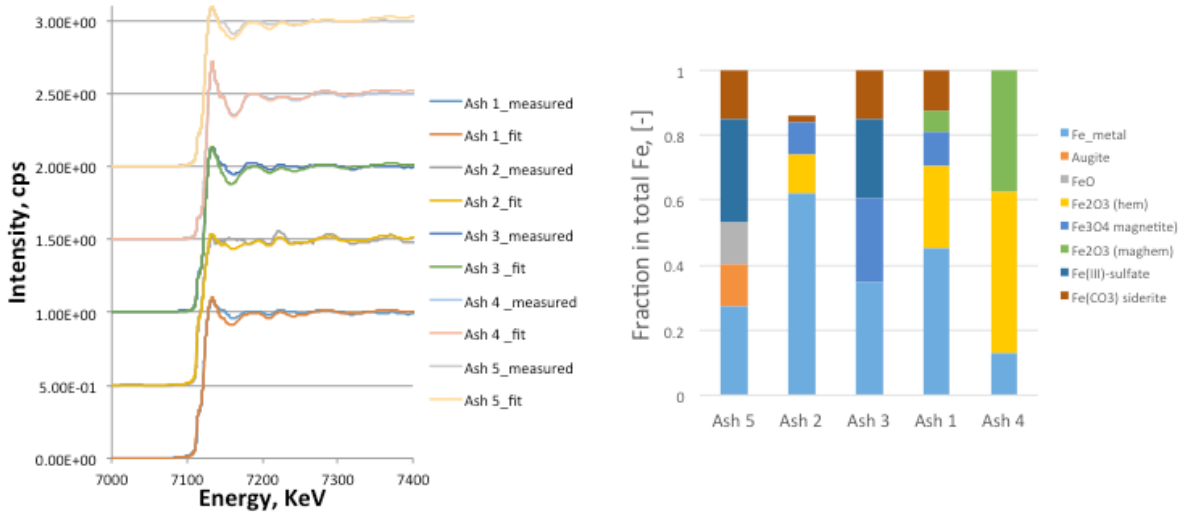

Figure 6.30 XANES spectra and LCF results for the interfacial layer of the tube material T23 exposed to five different fly ashes in oxy-firing mode

6.3.5 Characteristics of S-Bearing Species by XANES

Although XRD has detected the Fe-bearing species on the corroded tube surface, it failed to clarify the role of S. On the other hand, Table 4 for thermodynamic equilibrium prediction suggests the potential presence of sulfide upon the interaction between ash and tube surface. In

light of this, the XANES results in ***Figure 6.31*** provide complementary information that is critical in revealing the tube corrosion upon the attack of S. Under the air-firing mode, sulfate is the predominant S-bearing species on the corroded tube surface, which should denote Fe^{2+}/Fe^{3+} sulfate, and/or $(Na, K)_3Fe(SO_4)_3$ having a same energy position of ~2480 eV. Apart from it, the peak at 2470 eV for sulphide is also obvious for all the tubes expect SS400, T23 and SU347. The altitude of sulphide peak shows little dependence on the Cr content in the tubes. Upon the shift to oxy-fuel combustion mode, the relative altitude for the peak of ~2470 eV was enhanced for almost all the tubes. This should be due to the enhanced formation of $(Na, K)_3Fe(SO_4)_3$, which in turn promoted the reaction equation (6-1). ***Figure 6.32*** further proved this. Compared to flue gas only and YL ash with the least alkali sulphates, sulphide is the principal S-bearing species on the tube surface exposed to HW ash. Adding extra alkali sulphates further enhanced the altitude for the peak related to sulphide, as well as the peak for sulphates.

The formation of sulphides should also be responsible for the break-down of Cr_2O_3 layer on the tube surface, as it provides paths for rapid outward diffusion of metals such as Ni, Cr, and Fe which in turn accelerate the corrosion attack. In combination with all the results achieved, it is clear that SUS347 is the most suitable tube to be used under the oxy-fuel combustion of low-rank brown coal which is rich in alkali and alkaline earth metals.

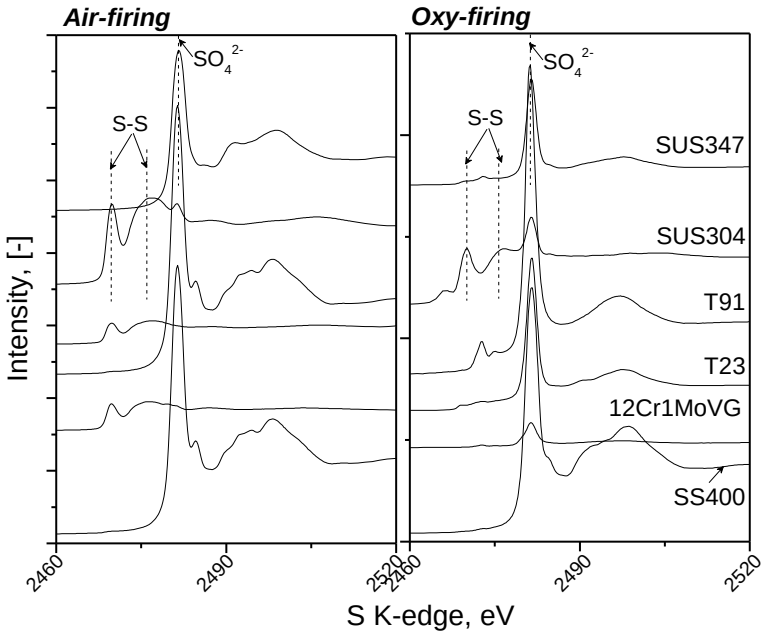

Figure 6.31 S K-edge XANES spectra for all the tubes exposed to HW fly ash

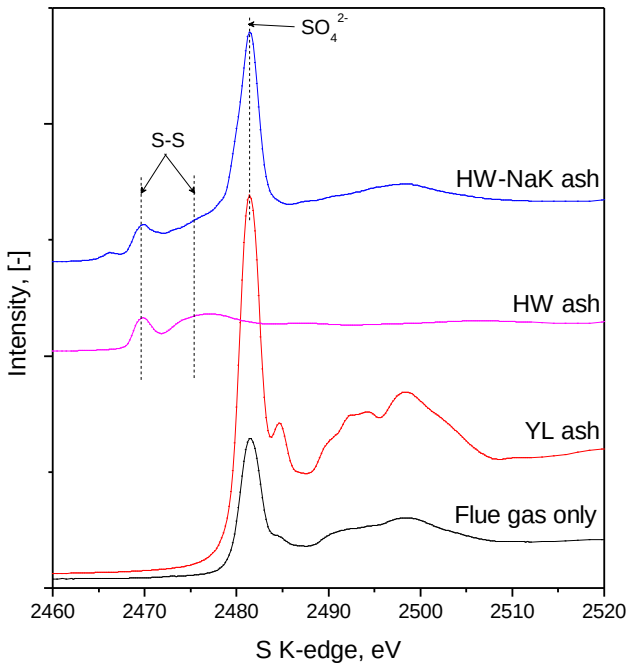

Figure 6.32 S K-edge XANES spectra for SUS347 exposed to three ashes in the oxy-fuel mode

6.4 Conclusion

(1) SS400 is not a good material of tube for oxy-fuel combustion of Victorian brown coal. However, the advanced materials including SUS347, T23, T91 and 12Cr1MoVG exhibited high corrosion resistance, which can be used in the design of water tube for the combustion of Victorian brown coal under oxy-firing mode.

(2) The aggressive gases in oxy-firing condition led to a higher corrosion rate for SS400 than under air condition.

(3) Alkali sulfates of Victorian brown coal ash (e.g. Na_2SO_4, K_2SO_4) can cause severe corrosion and high weight loss of tubes. Clay addition during coal combustion is one method to reduce the corrosion level of tubes.

Chapter 7 Evaluate the possibilities of two fuel quality control techniques on the tube corrosion rate, under both conventional air-firing and oxy-fuel combustion conditions

7.1 Effect of fly ash type and silica additive on tube corrosion

7.1.1 Mass Loss and Surface Oxidation in Pure Gases

The mass losses of tubes for pure CO_2 and the two flue gases are shown in ***Figure 7.1***. The results for pure air were found to be similar to pure CO_2, and thus are not listed here. With respect to the pure CO_2, a trivial mass gain of around -0.1 ~ -0.5 mg/cm^2 within the experimental error range was confirmed for all the tubes, which is clearly insignificant compared to the mass losses observed in the two flue gases, irrespective of the tube material. This implies that pure CO_2 has a negligible effect on the mass loss/gain of the tubes tested here, when compared with the other components in the flue gas, under the experimental conditions (*i.e.* 650^{o}C and 50 hr exposure time) tested here. For the air-firing flue gas, SS400 shows the largest mass loss rate, followed by the other tubes in an ascending sequence of Cr content. A similar trend was observed for the oxy-firing flue gas. In addition, except the tube SS400 showing a comparable mass loss between the two gases, the other tubes exhibited a much higher loss in oxy-firing than in the air-firing mode. The mass loss could be attributed to the enhanced volatilisation of metals by the abundant steam and HCl in the oxy-firing flue gas, as well as the dusting of the oxidised surface which was brushed clean after the experiment.

Figure 7.2 demonstrates the macro-structures for the cross-sections of tube T23 exposed to the four gases. For the pure air and CO_2, the interface between metal and its oxide layer is very thin compared to the two flue gases. In the oxy-firing flue gases, the interface layer is even slightly detached from the bulk metal, implying spallation of the oxidation layer due to severe corrosion. The amplified details for the corrosion interface are further evident in ***Figures 7.3*** and ***7.4*** for the tube T23. Clearly, CO_2 is not an inert gas, as it contributes to the tube corrosion. Such a finding has also been previously reported. For the results related to pure CO_2 in ***Figure 7.3***, the top surface of the tube becomes flawed and porous, implying the formation of defects and cracks that aid gaseous diffusion. The elemental mapping results confirm the abundance of O, Fe and C on the corroded surface, with the existence of trivial Cr and Si as well. Note that, due to the carbon coating prior to the SEM observation, it is unclear if the C detected here is due to the carburisation reaction cause by the Boudouard equilibrium ($CO_2 + C \leftrightarrow CO$).

Moreover, it is clear that oxidation of Cr and Si took place in the oxide layer, exerting a protective role to minimise the wastage of iron.

Figure 7.4 confirms the enhanced corrosion for the tube T23 exposed to the two flue gases. The top surface is even spalled off, particularly in the oxy-firing flue gas. This reflects the high concentrations of HCl and steam within this gas. Regarding the air-firing flue gas, the spalled layer is dominated by Fe and C, whereas the other three elements are present in low concentrations. Note that, the carburisation reaction can be ruled out here, as it is difficult to achieve the Boudouard equilibrium in the presence of steam and oxygen with CO_2 [26]. In contrast, upon exposure to the oxy-firing flue gas, oxygen is the most abundant element in the oxide layer. This should be attributed to the enhanced diffusion of O into the metal. CO_2 has been suggested to be able to increase the transport of reactants within the oxide scale, although a theory has yet to be established to confirm this. Moreover, upon the spallation of oxide layer by the attack from steam, HCl and/or SO_2, the diffusion of oxygen towards the un-oxidised metal was accelerated. Interestingly, for both flue gases, the distribution of S in the oxide layer is weak, implying little sulfation/sulfidation reaction. In other words, the occurrence of reaction equation 3 is negligible in the case of the tubes being exposed to flue gas only, for an experimental temperature of 650^{o}C and 50 *hr* only.

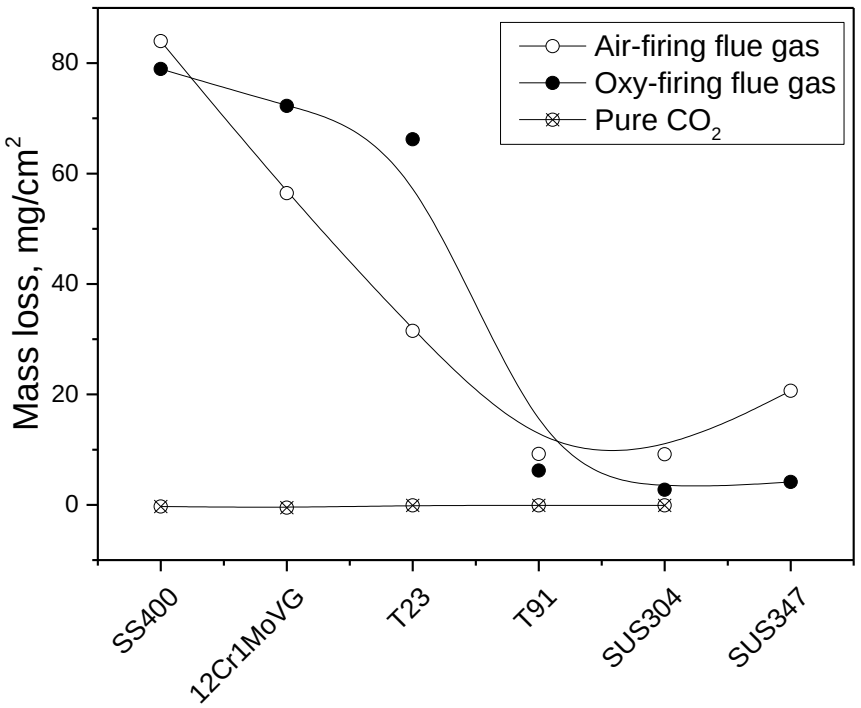

Figure 7.1 Mass losses of all the tubes exposed to three gases, pure CO_2, air-firing flue gas and oxy-firing flue gas

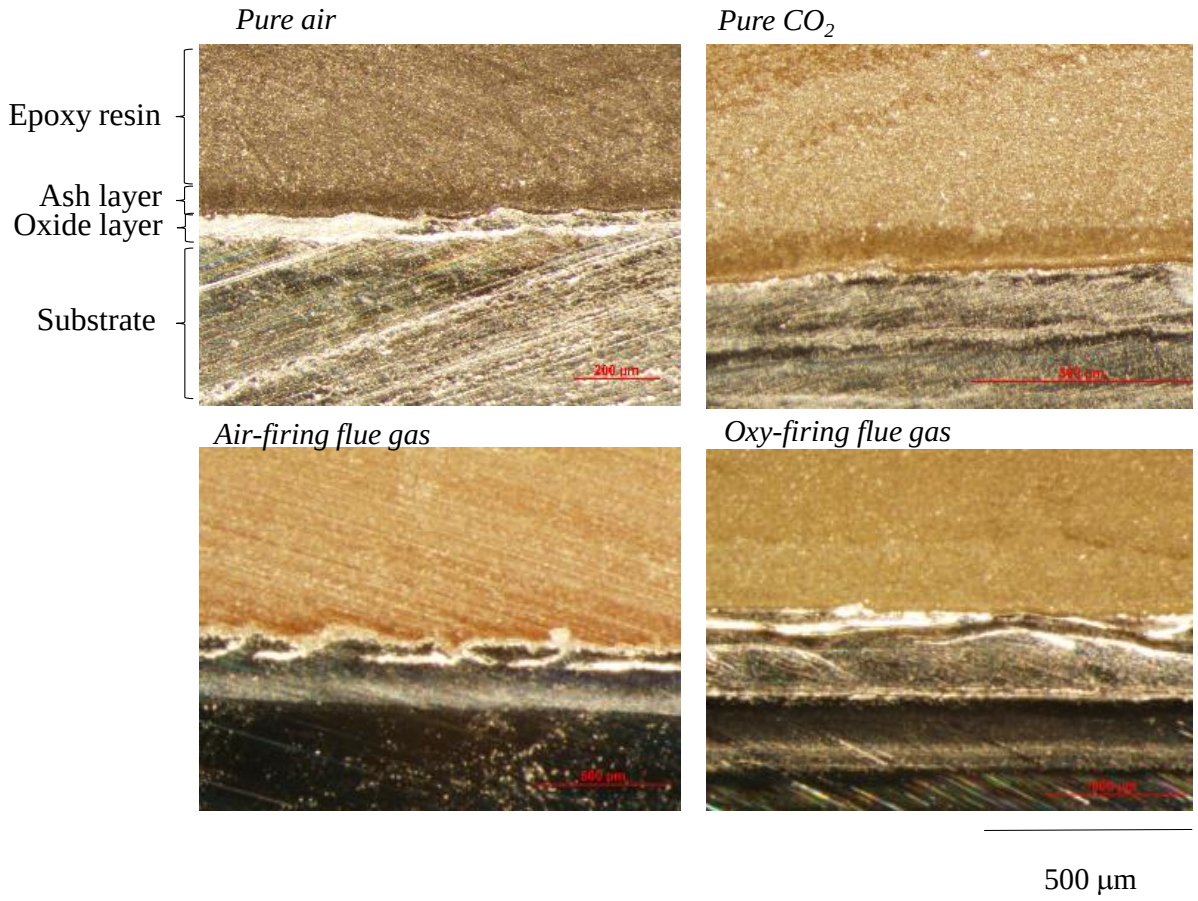

Figure 7.2 Macro-structure for the cross-section of tube T23 exposed to four gases

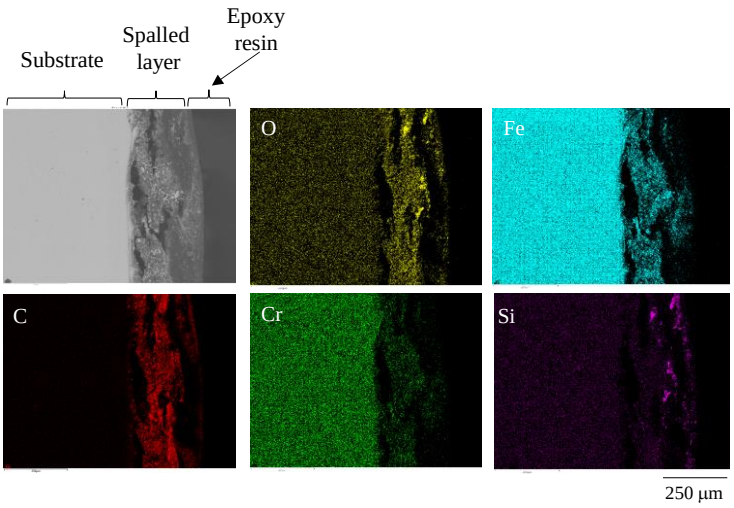

Figure 7.3 Typical micro-structure for the cross-section of T23 specimen exposed to pure CO_2

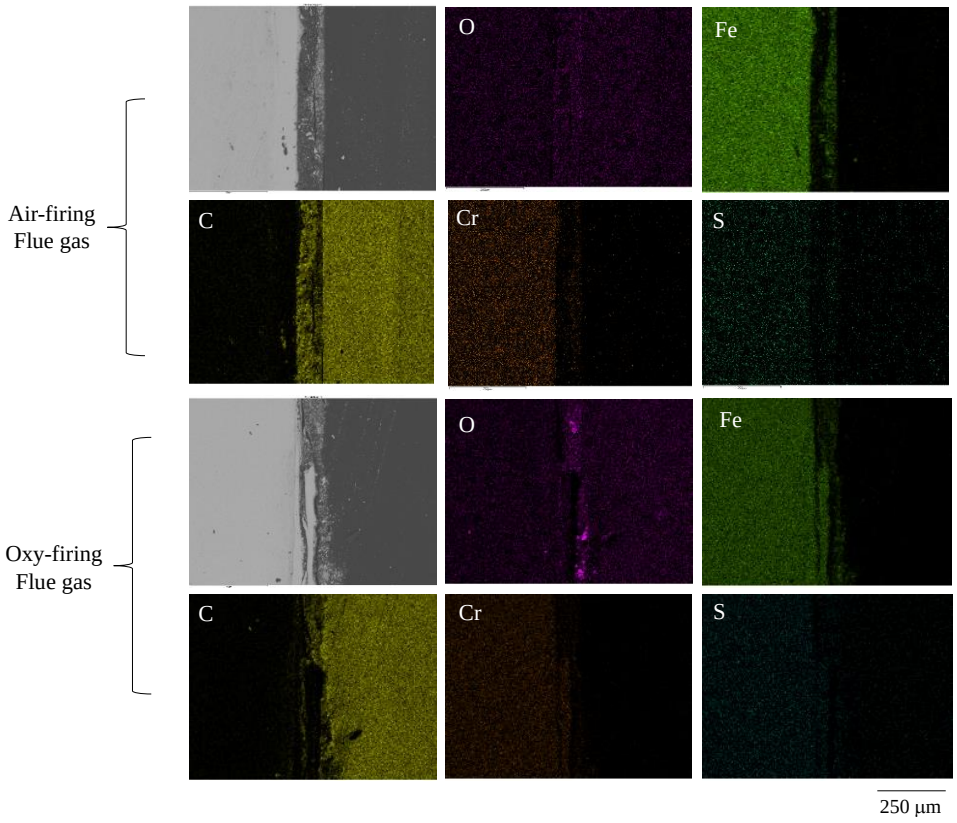

Figure 7.4 Typical micro-structure for the cross-section of T23 specimen exposed to flue gases with the absence of fly ash

7.1.2 Mass Loss and Surface Oxidation upon the Exposure to Ash Species

The mass losses of the six tubes upon the interaction with fly ashes are plotted in **Figure 7.5**, where the results for two flue gases are included for comparison. The tube specimens on the X-axis are listed with increasing Cr content. For either air-firing (in panel *a*) or oxy-firing mode (in panel *b*), the coating of XJ ash on a tube particularly SS400 accelerated the mass loss of the tube. In contrast, the coating of XJ_S ash, derived from the combustion of the same parent coal mixed with silica additive, alleviated the mass loss remarkably. Except the carbon steel tube SS400 with no Cr, the other tubes exhibited a comparable or even low mass loss for the coating of XJ_S ash when compared to the flue gas only case. Clearly, the ash-related corrosion is minimised or avoided upon the addition of silica to coal. The resultant ash deposit should thus

play a shielding role to inhibit the contact of tube to flue gas. However, the ash deposit itself may cause a different corrosion mechanism on the tube surface. With respect to the discrepancy between the two combustion modes, re-plotting of the results in panels (a) and (b), as shown in panel c of ***Figure 7.5*** confirmed that the tube corrosion in oxy-firing mode was enhanced for almost all the conditions except the high-Chrome ferritic steel T91 and the two austenite stainless steels, SUS304 and SUS347. For these advanced materials, the mass loss in oxy-firing mode is much closer to the air-firing mode, although the contents of oxidising gases are much higher in the former gas.

The macro-structures for the carbon steel SS400 upon the coating of fly ash are illustrated in ***Figure 7.6***. Taking panel (b) for the XJ ash in oxy-firing mode as the example, the top rumpled layer refers to the molten ash species, which could be formed by the melting of the ash on its own or the formation of new eutectics with the oxidised tube surface. Under the rumpled layer is a solid layer namely metal/oxide interface or scale referring to the corroded top surface of the tube. The bottom layer is the bulk tube which is dense compared to the other layers. Clearly, the interface layer is thickest under the oxy-firing mode for the XJ ash. It also attaches closely with the ash deposit, which can be referred as to the flux mechanism in which the metal can dissolve into the molten eutectics. The use of XJ_S ash in the oxy-firing mode led to a thinner layer for the interface. However, the break-down of the interface is still observed. Similar observations were found for the low-Cr tube T23 as evident in ***Figure 7.7***. The corrosion of T23 upon the coating of XJ ash even led to the spallation of the interface, as visualised in ***Figure 7.7(b)***. The coating of XJ_S ash in lieu of XJ ash inhibited the tube spallation.

Two typical microstructures were further observed for the tube T23 exposed to XJ ash in the oxy-firing mode. One microstructure is related to the corrosion and spallation of the top surface. As illustrated in ***Figure 7.8***, apart from a porous layer attaching to the bulk tube, a spalled scale was also found detaching away from the bulk tube. The top layer is dominated by oxides, as indicated by the EDS mapping results that show O is the most abundant element, followed by Cr, S, Fe and C. Clearly, both O and S diffused inwards, whereas Cr and Fe diffused outwardly for the corrosion and spallation of the tube. The faster diffusion of Cr than Fe resulted in the formation of a Cr-rich protective layer. The absence of Cl should be due to the volatilisation of chlorides from the tube surface, or the inhibition of the formation of chloride in the co-existence

of S and Cl in flue gas. More interestingly, compared to the other elements especially O distributing evenly in the whole top layer, S is preferentially present in the boundary/interface between the metal/oxide layer and the bulk tube. This should be due to a faster diffusion for S than O through the tube lattice. However, the S observed here may not be necessarily SO_2 in the bulk gas, since that the flue gas only exposure, as shown in ***Figure 7.4*** failed to confirm the presence of S inside the tube. Instead, the S in the tube/metal boundary should be formed under the assistance of the ash sample, e.g. via reaction equations 4 and 5. In other words, the alkali-metal sulphates or sulphides were formed in the tube/oxide boundary. These species should be responsible for the spallation of the tubes, as further evident by the abundance of S, Na and Ca in the spalled scale in ***Figure 7.8***. The abundance of Cr in the spalled layer suggests the break-down of the Cr protective layer and the accelerated outwards diffusion of Cr under S attack.

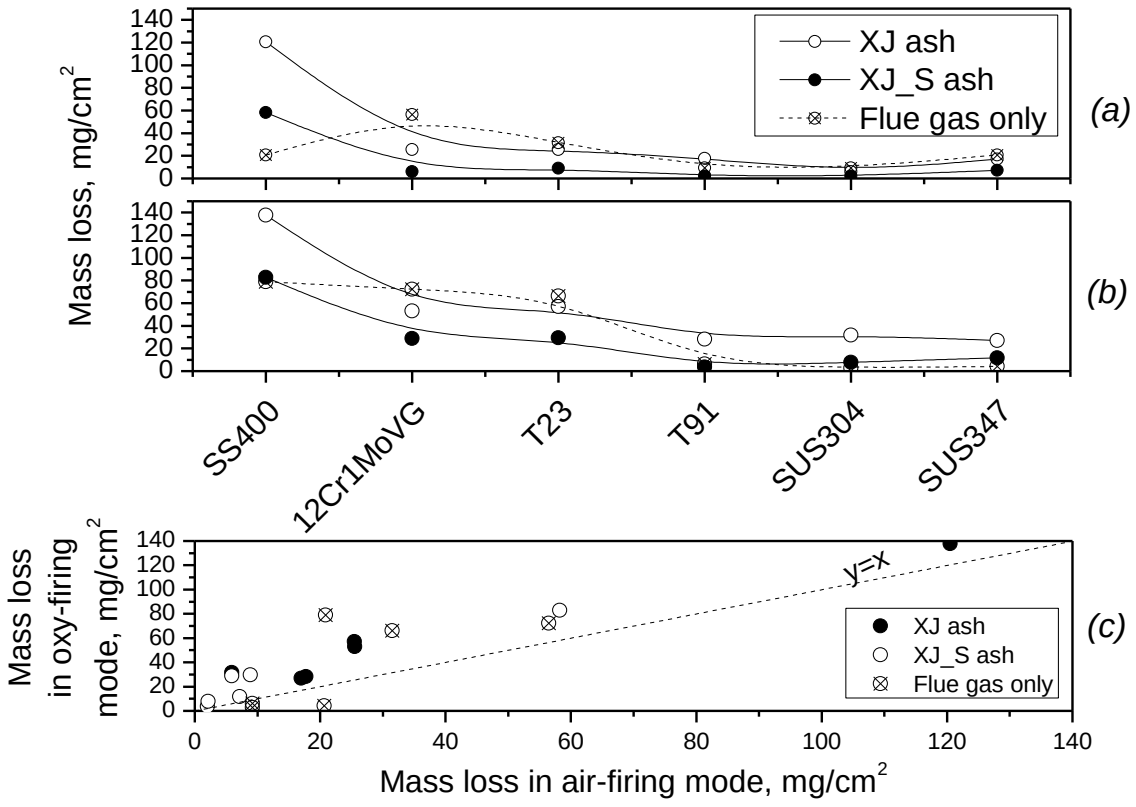

Figure 7.5 Mass loss as a function of tube material in air-firing mode (a), oxy-firing mode (b) and the comparison between the two combustion modes (c)

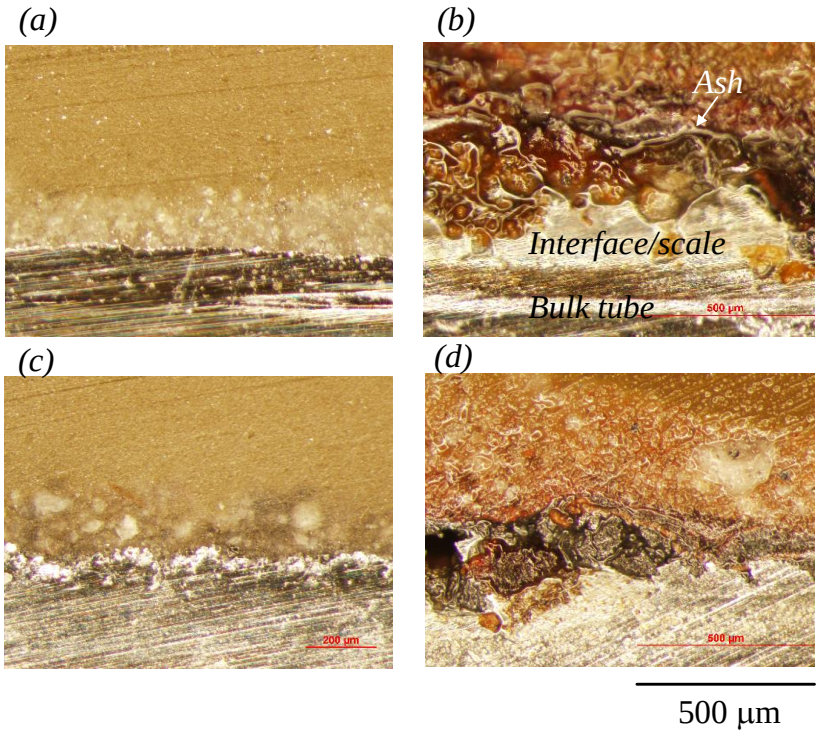

Figure 7.6 Macro-structure for the cross-section of corroded SS400. Panels (a) to (d) are for air-firing of XJ ash, oxy-firing of XJ ash, air-firing of XJ_S ash, and oxy-firing of XJ_S ash.

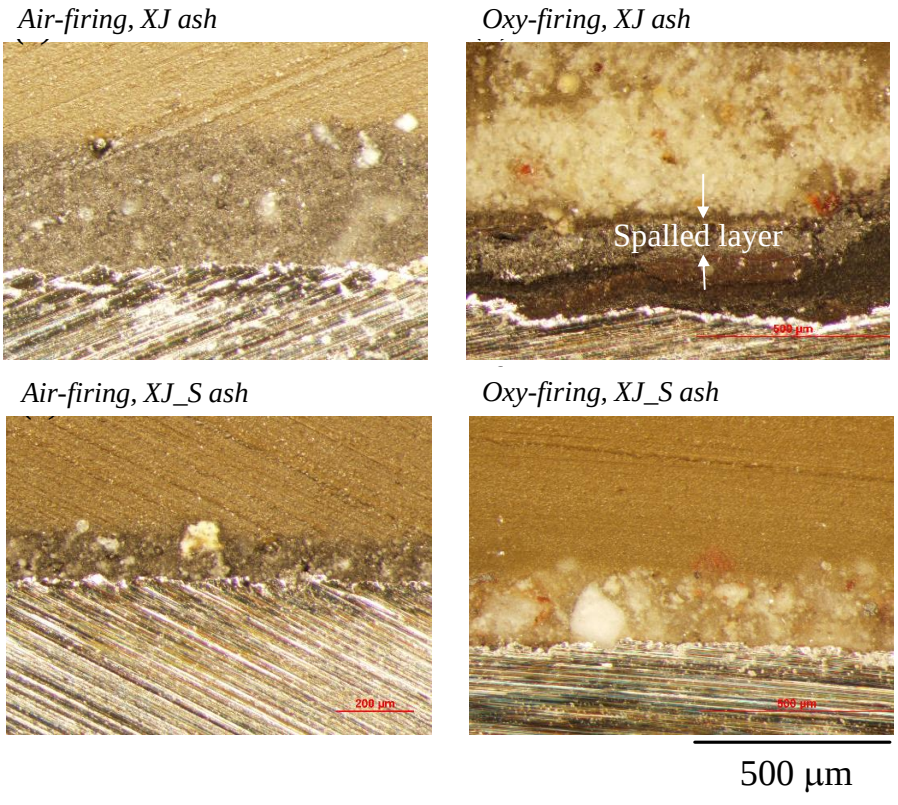

Figure 7.7 Macro-structure for the cross-section of corroded T23.

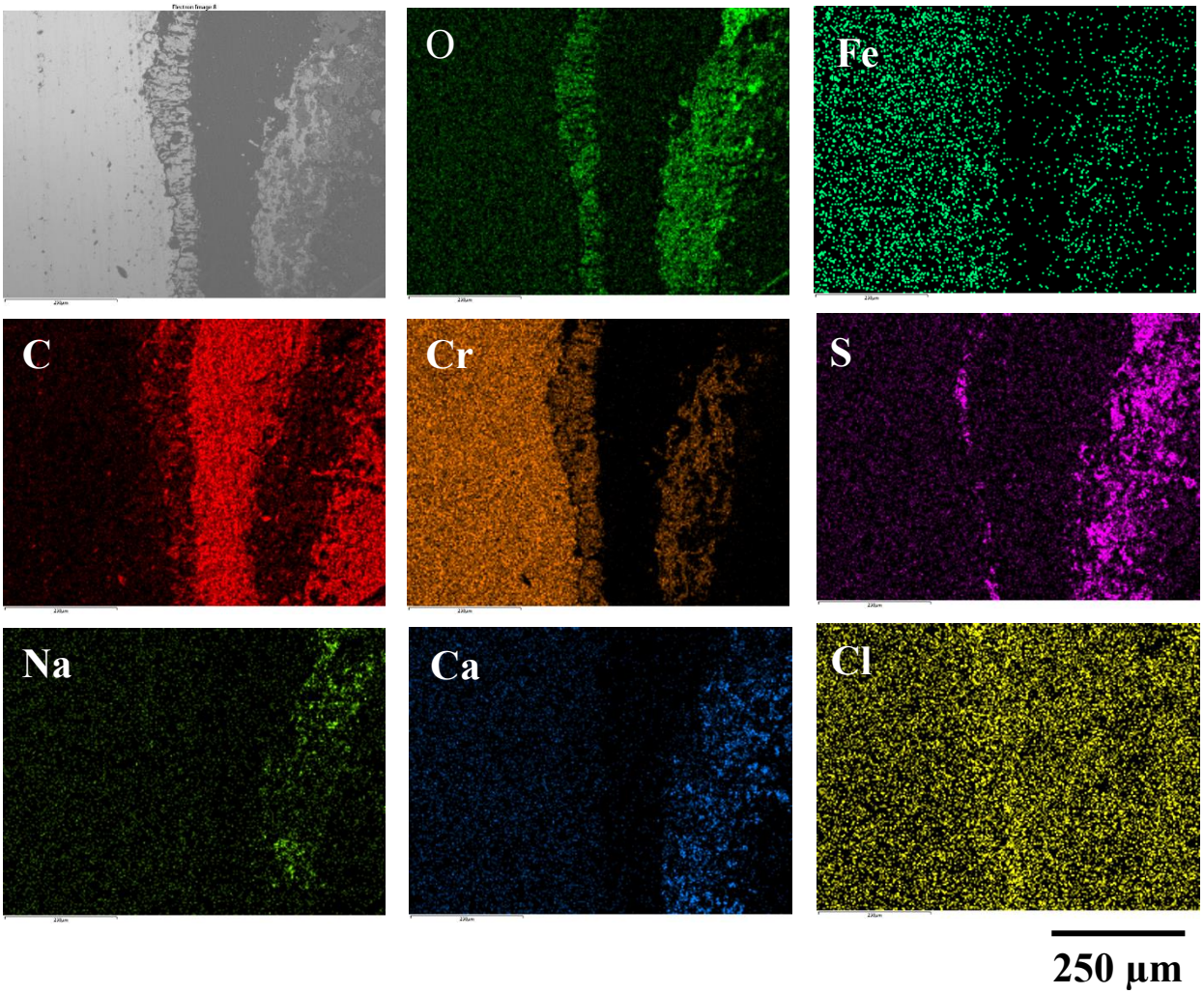

Figure 7.8 The first typical micro-structure for the cross-section of T23 specimen exposed to oxy-firing flue gas, with the coating of XJ fly ash on the surface

Figure 7.9 illustrates another typical microstructure for the tube surface corroded upon the coating of XJ ash. Compared to the first microstructure reflecting the lattice - diffusion of the oxidants through the oxide layer, the second type in this figure suggests the absence of O whilst the presence of S, Na and even C in the tube bulk, rather than on the top surface. Such a phenomenon should be caused by the grain-boundary diffusion of these elements through the spaces between individual crystal grains. The grain-boundary diffusion has proven faster than the lattice diffusion. This should hold true particularly for Na which is either in solid or liquid phase. The grain-boundary diffusion may also explain the preferential abundance of S on the metal/oxide interface in ***Figure 7.8***. That is, the S, either in gaseous or liquid phase should

preferentially traverse through the interstitial space between the top oxide layer and the bulk tube.

Only one typical microstructure was observed for the tube corroded surface upon the coating of XJ_S ash. As demonstrated in ***Figure 7.9*** multiple oxide layers were formed on the tube surface. The top layer attaches intimately to the bulk tube, mainly consisting of Fe and Cr. With respect to the middle scale, apart from the abundance of Fe and Cr, the presence of C, S and Cl was also confirmed. In particular, S is the most prevalent, which is also preferentially present on the left-hand surface of the middle scale. This further suggests that S easily traverses through the interstitial space between top layer and the middle scale. The resultant sulphates or sulphides caused the spallation of the oxide layer. However, compared to the top and spalled layers for the XJ ash in Figure 10, one can clearly see that the multiple layers formed by the coating of XJ_S ash are dense and less porous. Therefore, their protection on the bulk tube is still effective.

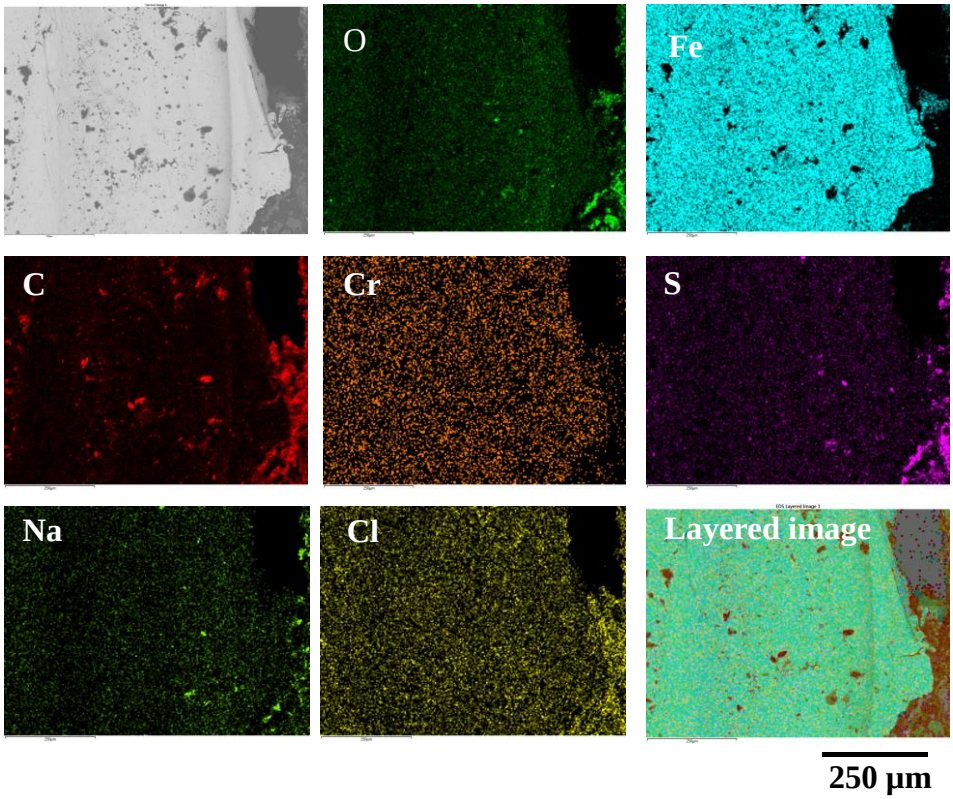

Figure 7.9 The second typical micro-structure 1 for the cross-section of T23 specimen exposed to oxy-firing flue gas, with the coating of XJ fly ash on the surface

7.1.3 Oxide Layer Growth Rate

Statistical analysis was conducted to quantify the thickness of the corrosion interface for each corroded tube, based on the macro- or micro-structures for the cross-sections observed by OM or SEM. Furthermore, based on the interface depth, the corrosion rate or interface growth rate was calculated by dividing by the exposure time, 50 *hr* employed in this study. Such an effort is expected to provide complementary results to the mass losses shown in ***Figure 7.5***. On the one hand, the oxide layer formed provides a protective layer to avoid the mass gain/loss of a tube. On the other hand, the growth of the oxide layer continuously increases the mass gain of the tube. The thicker the oxide layer is, the larger the mass gain should be. However, as evident in ***Figures 7.8*** and 7***.10***, the oxide layer was partly spalled due to the attack of S even in the case of the XJ_S ash. The spalled pieces were even mixed with ash particles due to the formation of eutectics, which in turn contributes to the mass loss of the tube. As shown in ***Figure 7.11*** with the X-axis being the increasing Cr content in the tubes, the oxide layer growth rate decreases monotonically upon the increase of Cr content in the tube, either in flue gas only or upon the coating of fly ash. Such a trend is also consistent with the mass loss change in ***Figure 7.5***. Clearly, the oxide layer formed is either fragile that can be brushed away easily, or fully dusty that was mixed/molten together with the fly ash deposit. This particularly holds true for the carbon steel SS400 and low-Cr tubes, as evident in ***Figure 7.12*** for the amplified tube surface. Upon increase of the Cr content, the oxide layer formed becomes denser, although thinner (see ***Figure 7.12***). Its inhibitive effect on the inward diffusion of O and S is thus more pronounced. The trivial mass loss for the high-Cr tubes should be attributed to the volatilisation of the oxide layer via the reaction with steam and HCl.

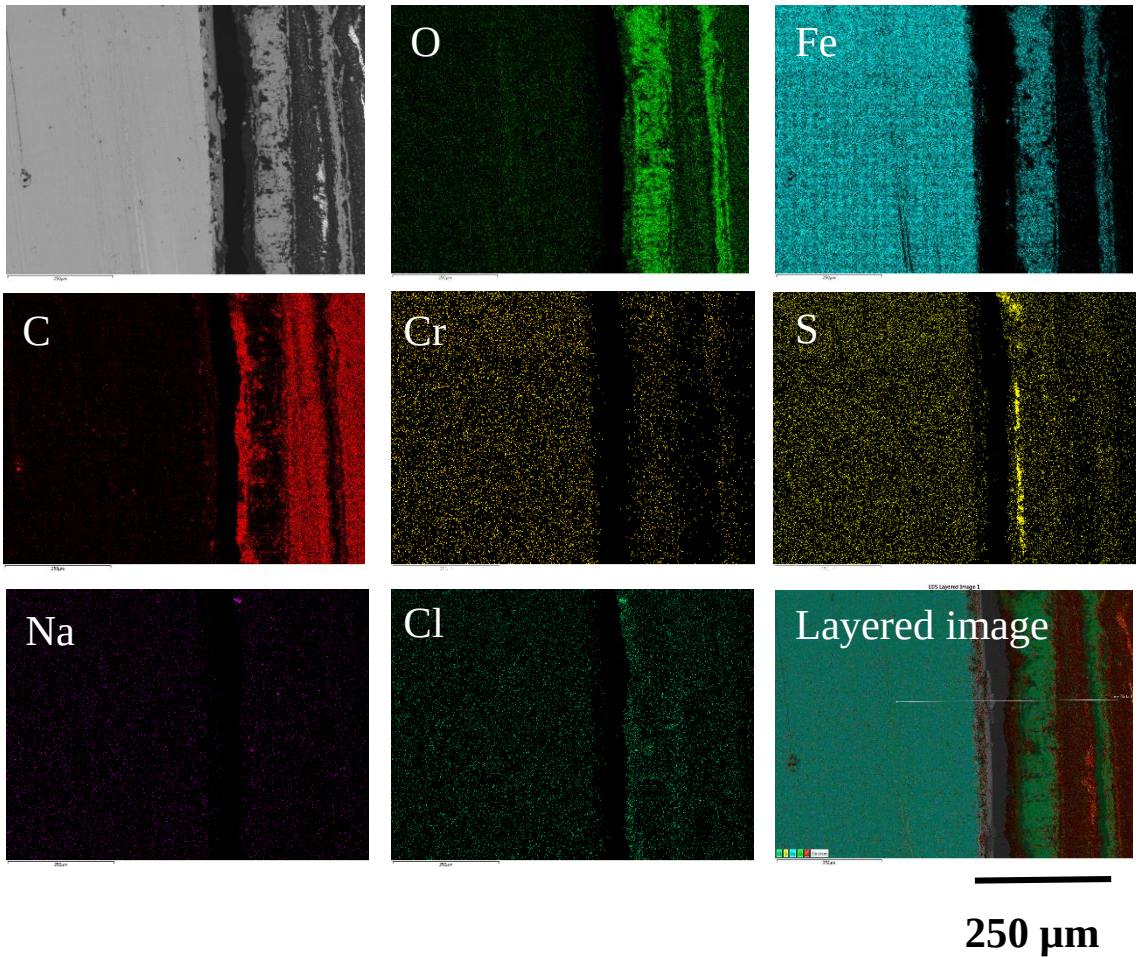

Figure 7.10 Typical micro-structure for the cross-section of T23 specimen exposed to oxy-firing flue gas, with the coating of XJ_S fly ash on its surface

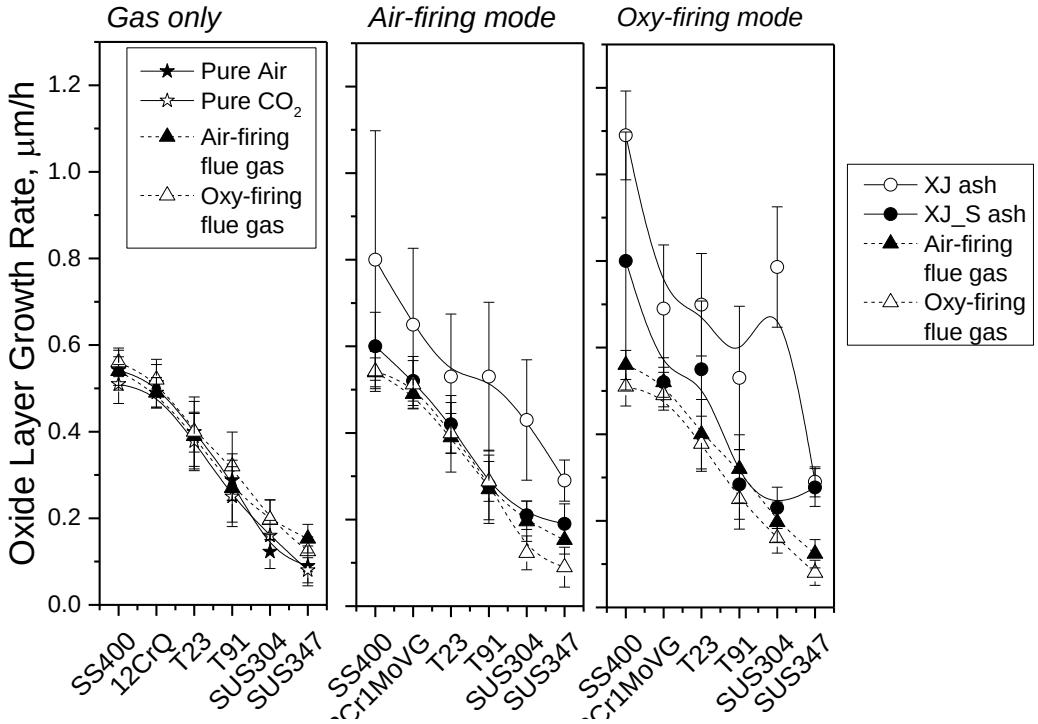

Figure 7.11 Oxide layer growth rate of the tubes

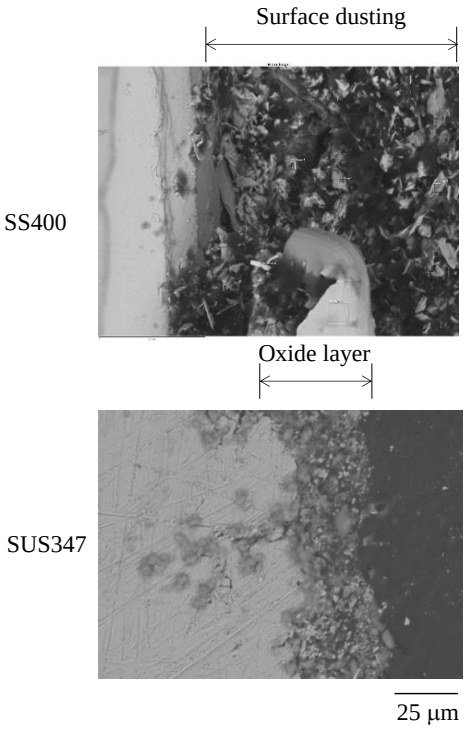

Figure 7.12 Amplified oxide layer for SS400 and SUS347 exposed to oxy-firing flue gas with the coating of XJ ash

7.1.4 Correlation of Tube Mass Loss and Ash Species

As has been confirmed by the microstructural observations, the penetration of O and/or S is the most critical factor on the growth of the oxide layer, and thus the wastage of the tubes. These two oxidants interplay rather than compete with each other, accelerating the tube wastage accordingly. The S has been confirmed to relate to the sulphates, particularly Na sulphates in the fly ash. Regarding the oxidation of metals by O, the dissociation of the bulk oxidants including O_2, CO_2 and even steam to produce the respective O radical is the initial step, and even the rate-controlling step for the overall oxidation reaction. The dissociation of bulk oxygen is generally catalysed by the alkali (Na, K) and alkaline earth (Ca, Mg) metal oxide acting as the oxygen-shuttling agent via the redox reaction swing between a metallic cation and its radical. In addition, the oxides and chlorides of Na, K and Ca have been proven to promote the oxidation of Cr^{3+} (the protective layer of the tube) to the respective chromate (Cr^{6+}), leading to the chromium depletion and thus the breakdown of the protective Cr-oxide. Regarding iron oxide, on the one hand, it is catalytic for the dissociation of steam for the reforming reactions, and also catalytic for the formation of SO_3 in the coal-fired flue gas, particularly under the oxy-firing mode. On the other hand, the spinel chromite $(Fe, Cr, Ni)_3O_4$ can be formed on the Cr-oxide protective layer, via the reaction between iron oxide and Cr_2O_3. All these can contribute to the break-down of the Cr-oxide protective layer.

Efforts were made to correlate the contents of sulphates, oxides and both of them in five fly ashes with mass loss rates of the six tubes tested. The resultant plots are illustrated in ***Figures 7.13*** and ***7.14***, whereas the respective correlation coefficients are listed in ***Table 7.1***. Note that, calcium sulphates in ***Table 7.2*** were not included for the correlation analysis, considering that its mobility is poor and thus has limited reaction with oxide layer on the tube surface. The oxides considered include periclase (MgO), lime (CaO), hematite (Fe_2O_3), magnetite (Fe_3O_4) and even calcite ($CaCO_3$). Same as K carbonate [50], calcite is supposed to decompose into lime which can either catalyse the dissociation of oxygen or react with Cr-oxide layer subsequently.

The results in ***Table 7.1*** suggest a broad variation of the correlation coefficient with the tube material, which also differs between the two combustion modes. With respect to the air-firing mode with less impure components in the flue gas, the carbon steel SS400 is the only tube showing a positive correlation with the content of Na sulphate in the fly ash. This suggests the occurrence of the reaction 4 and 5 for this Cr-free tube, in which the involvement of oxygen and chromium is not necessary. For the rest of the tubes with varying Cr contents, the content of Na sulphate is clearly insignificant, due to the fact that the reaction between Na sulphate and the Cr-oxide layer in equation 6 below is thermodynamically impossible at 650^{o}C, with a positive ΔG equal to 159,744 J/mol. On the other hand, the oxides show a positive correlation coefficient for the tubes T23 and SUS347. This should be due to the reaction between oxides (e.g. CaO) and Cr-oxide that is thermodynamically available at 650^{o}C, as shown in equation 7 below, and/or the enhanced sulfation reaction of Cr-oxide due to the formation of extra SO_3 via the catalysis of iron oxide. The sulfation of Cr-oxide is also thermodynamically available, as evident by the equation 8 below. However, the extents of these two reactions should be very limited particularly for the other three tubes in the air-firing mode. This may be due to the existence of the other metals such as Mo, V and Nb that can significantly resist the attack related to the oxides in fly ash.

$$Na_2SO_4 + \tfrac{1}{2}\, Cr_2O_3 + \tfrac{1}{4}\, O_2 = Na_2CrO_4 + SO_2 \qquad \Delta G_{650^oC} = 159744 \text{ J/mol} \qquad (6)$$

$$2CaO + Cr_2O_3 + 3/2\ O_2 = 2\ CaCrO_4$$

$$\Delta G_{650^oC} = -40101 \text{ J/mol} \qquad (7)$$

$$Cr_2O_3 + 3SO_3(g) = Cr_2(SO_4)_3$$

$$\Delta G_{650^oC} = -55292 \text{ J/mol} \qquad (8)$$

The correlation of ash speciation with the tube corrosion rate is more complicated in the oxy-firing mode. SS400 corrosion is still highly sensitive to the content of Na sulphates in fly ash, same as that observed in the air-firing mode. In addition, the tube SUS347 and even SUS304 with the largest Cr content was also readily attacked by Na sulphate. This may be due to an enhanced sulphation reaction (equation 8) for Cr for these two high-Cr austenitic steels,

resulting in the formation of Cr sulphate exerting a synergetic role with Na sulphate on the tube oxidation. As has been confirmed for the same austenitic steels coated with different sulphates at 650°C, the coating of Na_2SO_4-$Cr_2(SO_4)_3$ mixture resulted in a higher oxidation rate for the tube surface than the coating of either Na_2SO_4 or $Cr_2(SO_4)_3$ alone. It may be due to the formation of low-temperature eutectics, although the final confirmation has yet to be achieved. With respect to the other three tubes with low-/medium-Cr content, either oxide or both sulphate and oxide plays a combined role on their corrosion rates, although the correlation is not strong enough. The enhanced role of Na sulphate can still be explained by the formation of $Cr_2 (SO_4)_3$, whereas the role of oxides should be the same as in the air-firing mode, as explained before.

Table 7.1 Correlation coefficient (R^2) for the corrosion rate of individual tubes versus the content of Na sulphate and oxides (CaO, Fe_2O_3 and Fe_3O_4) in five fly ashes

	Na Sulfate	Oxide	Na Sulfate + Oxide
Air-firing condition			
SS400	**0.92027**	-0.12495	0.14139
12Cr1MoVG	-0.3067	0.48840	0.00372
T23	-0.17373	**0.91906**	-0.05307
T91	0.22864	-0.31685	0.32794
SUS304	-0.32167	0.17514	0.12943
SUS347	-0.20951	**0.69365**	-0.09446
Oxy-firing condition			
SS400	**0.71632**	-0.30401	0.35802
12Cr1MoVG	-0.12132	0.42304	-0.26069
T23	-0.13049	0.14106	**0.63580**
T91	-0.48419	-0.30806	**0.63526**
SUS304	**0.47801**	-0.27673	0.10124
SUS347	**0.85517**	-0.06285	0.03826

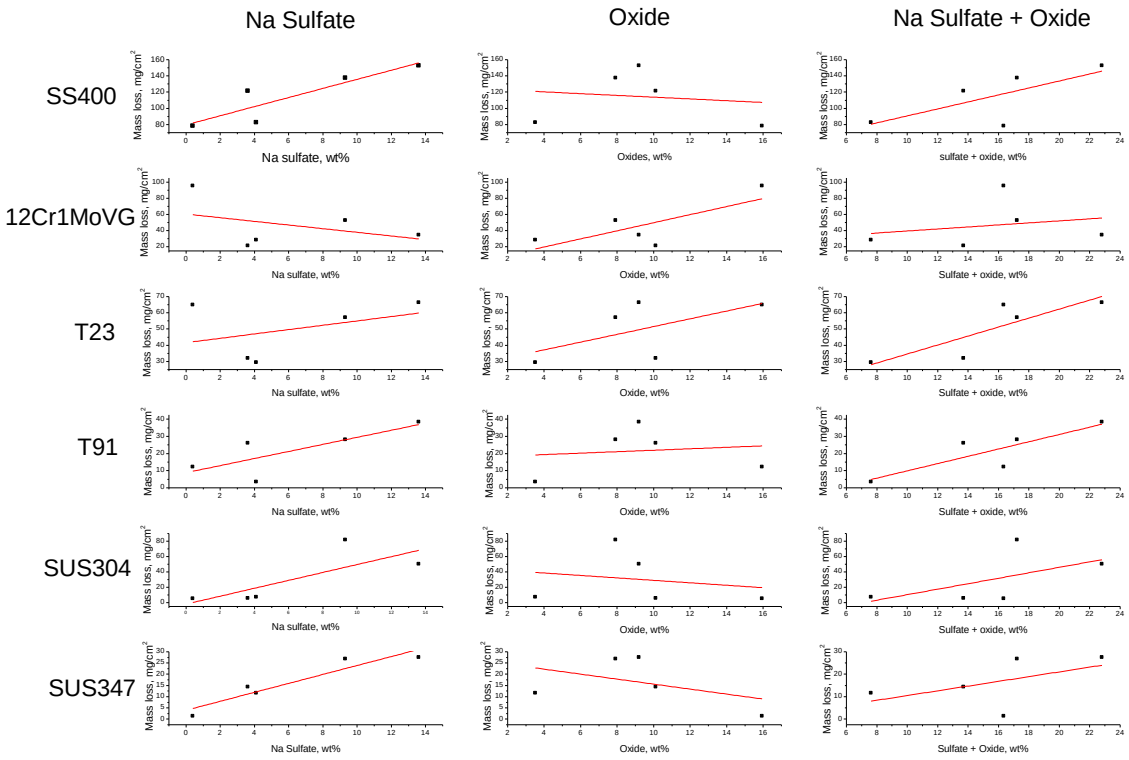

Figure 7.13 Correlation between mass loss rate of tube and two species (Na sulphates and oxides) in five ashes in the oxy-firing mode

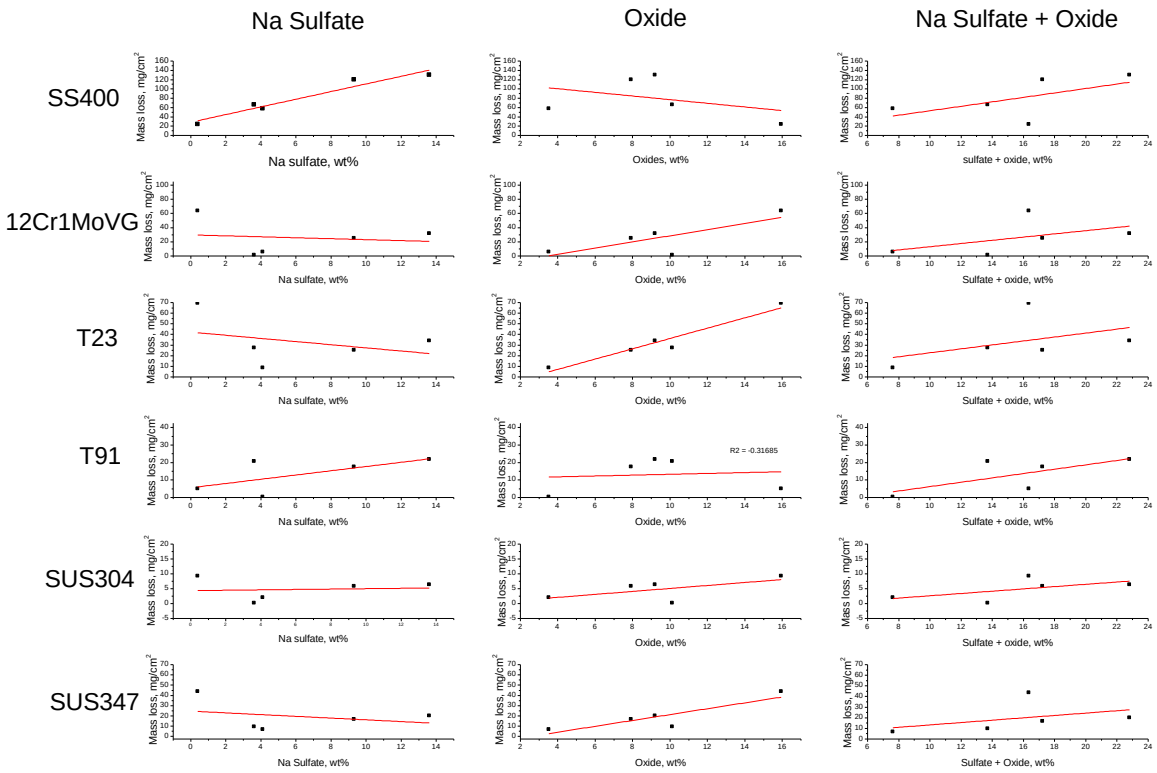

Figure 7.14 Correlation between mass loss rate of tube and two species (Na sulphates and oxides) in five ashes in the oxy-firing mode

7.1.5 Implications of This Study to the Operation of Oxy-Firing Boiler Burning Low-Rank Coal

Although only one temperature and a fixed exposure time of 50 *hr* were tested, it has been clarified in this study that the corrosion rates in oxy-firing mode are generically higher than the respective air-firing mode for carbon steel and those with low- and medium - Cr contents. The abundant oxidants in the wet flue gas including CO_2 and steam enhanced the oxidation rate of the tube surface, whereas the impure SO_2 is less responsible for the growth of the oxide layer. However, the presence of a large quantity of SO_2 in flue gas may facilitate the formation of Cr sulphate that plays a synergetic role with Na sulphate to enhance the corrosion rates for the high - Cr austenitic steels. In light of this, de-sulfurization of flue gas to reduce the SO_2 content down to a level close to the air-firing case should be considered, otherwise even the high – Cr austenitic steel would be corroded rapidly. With respect to the presence of HCl in the flue gas, its detrimental effect on the volatilisation of Cr is largely inhibited in the case that it co - exists with SO_2. Desulfurisation can reduce the risks related to these two gases simultaneously. With

respect to the ash deposit, apart from Na sulphate triggering the penetration of S inside the tube, the free oxide/carbonate is also responsible for promoting the activation and thus penetration of O. The use of the refractory silica additive is effect in eliminating the detrimental effect of both two species even in the absence of de-sufurisation unit downstream of the boiler, thereby alleviating the tube corrosion rate down to a level caused by the flue gas only. In combination with the positive results for the minimisation of ash slagging/fouling and emission of trace elements in the boiler, the results here strongly recommend the use of silica as an additive to the low-rank coal during its combustion, particularly under the oxy-firing mode.

7.2 Effect of washing prior to combustion on high temperature tube corrosion

Due to the consideration on the deposition of Victorian brown coal fly ash on the super-heater zone, in particular the iron-rich Yallourn fly ash, ash deposition and tube corrosion test were further conducted in a horizontal tube furnace to mimic the flue gas composition and temperatures in the super-heater zone. In particular, efforts in this stage were made to explore the interaction between S-bearing gas components, SO_2, and the sulfur-bearing sulphate in the ash deposits collected from the pilot-scale plant. For such a study purpose, the Hazelwood ash deposit collected from the pilot-scale was washed by water and acids to remove Na, Ca and sulphate within it. Additionally, the iron was also partially removed by the washing. The resultant new ash deposit properties are shown in ***Table 7.2*** below.

As can be seen, the original Hazelwood ash deposit is very rich in sodium, counting for 10 *wt%* in its oxide form. It is accompanied by abundant calcium (Ca) of 39.21 *wt%* and 10.86 *wt%* sulphur (S). The same coal was washed by the use of water and 1M hydrochloric acid (HCl). For water washing, a three – stage counter-current process was applied, leading to the formation of three washed coals, W1-W3. On the other hand, for the acid washing, a two – stage counter – current with acid in stage 1 and water in stage 2 was employed, yielding two samples, A1 and A2 from the two stages, respectively. Regarding the ash samples from the water-washed coals, the content of Na was reduced remarkably. The use of acid further slightly reduced the content of Ca, whereas Na has little change compared to the water-washed coal samples. This is because Na in this coal is mostly present as water-soluble species that can easily dissolve into the neutral water.

Table 7.2 Elemental compositions of the ash deposit samples tested in this study

Compositions (*wt %*)	**Samples**					
	Raw coal	*Water washed*			*Water+ Acid (1 M HCl) washed*	
	HZ	**W1**	**W2**	**W3**	**A1**	**A2**
SiO_2	16.67	47.59	45.57	45.42	46.27	47.27
Al_2O_3	8.49	21.16	20.83	20.59	19.69	19.10
Fe_2O_3	0.39	3.41	2.88	2.71	2.11	3.46
CaO	39.21	13.78	16.11	15.94	12.67	11.18
MgO	12.79	4.63	5.05	4.96	7.71	8.18
SO_3	10.86	7.79	7.33	7.93	8.79	8.21
P_2O_5	0.46	0.12	0.1	0.15	0.18	0.17
Na_2O	10.67	1.01	1.58	1.81	1.93	1.79
K_2O	0.46	0.51	0.55	0.49	0.65	0.64

The tube corrosion test was detailed in our previous work. The furnace temperature was fixed at 650^{o}C in this study. Each test lasted 50 hours and three repetitions were conducted for each condition. Regarding, the oxy-firing flue gas composition, it is made up of 3000 ppm SO_2, 30% steam, 1000 ppm HCl, 5% O_2, 10% N_2 and CO_2 in balance. As confirmed by our pilot-scale test, the steam content in flue gas can go up to 30 vol% and SO_2 is also highly accumulated during the oxy-firing of low-rank brown coal. A total of four tube materials in ***Table 7.3*** was tested, with a Cr content in ascending order of stainless steel SS400 (Cr% nil), low-chrome ferritic steel 12Cr1MoVG (0.9 - 1.2%), high-chrome ferritic steel T91 (9%), and austenite stainless steel SUS304 (18 - 20%). For each test, around 100 *mg* ash was coated on the tube surface. After each test, the used ash was generally brushed away and saved for the test. The used tube was either weighed for its mass change and saved for the future test on the top surface, or quickly mounted together with the ash into epoxy resin to measure the cross - section.

Table 7.3 Tube materials tested in this study

Specimen	Steel grade	Compositions	Cr *wt%*
SS400	Carbon steel (JIS SS400-ASTM A283)		Nil
12Cr1MoVG	Low chrome ferritic steel	1.25 Cr - 1 Mo-V	0.9-1.2
T91	High chrome ferritic steel	9Cr-1Mo-V-Nb	9
SUS304	Austenite stainless steel (JIS SUS304-ASTM S30400)	18Cr-8Ni	18-20

The cross-sections of the corroded tubes were carried out on a computerized photo metallurgical microscope (Olympus) to establish the thickness of scale and depth of intergranular penetration. Prior to the analysis, the tube cross-sections were polished by the use of silicon carbide paper with a grit of 2400. In addition, scanning electron microscope (SEM) was used to map the elemental distribution on the tube cross - section. The analysis was conducted by JEOL, 7001F to identify the distribution of major elements of interest, including Fe, S and O. Prior to the SEM observations, the tubes were carbon sputtered.

The K-edge X-ray adsorption near-edge spectroscopy (XANES) spectra of S and chromium (Cr) were conducted to specify the oxidation of these two interests on the tube top surface. Compared to bench – scale X-ray diffraction (XRD), XANES is highly sensitive and able to detect the elements with a concentration on the ppm level. The beam size of around 1 μm can also easily pinpoint the tube-ash interface which is generally on the sub-micron scale. The XANES spectra were collected from beamline BL16A1 at the National Synchrotron Radiation Research Centre (NSRRC). BL16A1 had a fixed exit double crystal Si (111) monochromators with a nominal beam size of 0.25 by 0.25 mm at sample. For the analysis of Cr, pure elemental Cr was used for the calibration at a K-edge absorption energy of 5989 eV. Pure elemental Mo was used for the calibration of S at a K-edge absorption energy of 2481 eV. The peak energy absorption (white-line) position was taken as the base (0 eV), with all subsequent spectra recorded 200 eV below and 800 eV above this point in fluorescence mode. The analysis of S and Cr was only conducted for the top surfaces, as the signal for S from the cross-section of the tubes was very weak and noisy. All spectra were normalised using ATHENA which is part of the DEMETER package. Linear combination fitting (LCF) was used on the normalized sample spectra to determine the mineral composition by using a large number of standards.

After the tube exposure tests, some of the used ash samples were also gently collected from the tube surface, further grounded and characterised by X-ray fluorescence (XRF) for the composition as well as XANES for the oxidation of S. The XANES results are expected to supplement the results for the respective tube surfaces so as to draw an overall picture on the partitioning of S between tube and ash.

The 'Equilib" module in a commercial thermodynamic equilibrium program, Factsage was used to calculate and establish the species in equilibrium that can be formed upon the interaction between flue gas, ash deposit and the inherent metals in the tube. The input for each calculation includes the amounts of individual elements in a tube, individual elements (as a form of oxide) in the ash, and individual components in flue gas based on the compositions of tube, ash and flue gas, masses of a tube and ash, the flow rate (300 ml/min) of flue gas and a total exposure time of 50 hour. The temperature was set at 650^{o}C and the total pressure was 1 bar absolute. Apart from the pure substances, the built - in databases FToxid Slag A or FToxid - Slag B were also ticked during the calculation. Slag A is made up of sulphide whereas Slag B is dominated by sulphates in the FactSage database. The calculation using Slag B only converged for the raw XJ ash deposit that is rich in sulphate. In contrast, both two slag databases converged for the washed coal ashes that are lean in sulphates. However, the use of Slag B database gives a much lower slag formation propensity, because sulphate is less prone to melt than sulphide at 650^{o}C. Since the formation of sulphide is more of interest and is also confirmed experimentally in this study, the results using slag A database for the washed coal ashes were only interpreted hereafter.

Figure 7.15 illustrates both the mass loss and oxide layer growth rate for the four tubes coated with different ashes, where *x* -axis refers to the ascending sequence of Cr content in the tubes. The tube mass loss is expected to be caused by the evaporation of the metals as chloride/hydroxide, and the spallation of oxide/sulphide fragments which are ductile. For comparison, the blank test without ash coating was also included in ***Figure 7.15.*** As indicated by the mass loss results in ***panel (a)***, the mass loss decreases considerably with increasing the Cr content in the tube, irrespective of ash type. This agrees with our expectation, as Cr and the

other addition metals such as Ni preferentially form a thick, protective oxide layer on the tube surface. With regarding the influence of ash type, it is evident that the raw coal ash is most detrimental, causing the largest mass loss for each tube. The mass loss in the case of raw coal ash is also far higher than the blank flue gas case, demonstrating the significance of solid ash over flue gas on the tube corrosion. The use of silica additive reduces the tube mass loss to a level slightly higher than the blank flue gas case. In contrast, the coating of washed ashes, irrespective of its type was much more effective, mitigating the tube mass loss to a level that is even below the blank case, irrespective of the tube type.

The oxide layer growth rate is shown in ***panel (b)***. Note that, the oxide layer growth rate was calculated by dividing the oxide/interface thickness by the exposure time, 50 hours. The results here further confirms a more effective role of coal washing than the silica addition on the prevention of tube oxidation. Instead of attacking tube surface, the washed coal ashes, in particular those washed by acid can even function as an extra shield, in combination with the high-Cr tubes including T91 and SSS304 to decrease the tube oxidation layer dramatically.

The typical cross-sectional structures for the corroded low-chrome ferritic tube 12Cr1MoVG are illustrated in ***Figure 7.16***. Compared to the case of raw coal XJ ash coating, the other two cases for the coating of W1 and A2 yielded a narrower interface which also refers to as the oxide layer that is formed by the penetration of corrosive components, in particular the oxidising gases such as O_2 and H_2O. Moreover, considering that the tube corrosion was directly related to the penetration depth of oxygen (O) and sulphur (S), efforts were made to map these two elements on the corroded tube cross-section. As shown in ***Figure 7.17*** for the tube T91, the two elements of O and S show distinctively different distribution along the cross - section. O is overwhelmingly dominant and distributes uniformly across the interface, demonstrating that oxidation is the principal mechanisms underpinning the tube corrosion. In contrast, S has a non-continuous distribution, with the preference of the formation of thin strips on the boundary between interface and bulk tube/substrate, or even inside the interface layer. Taking W1 as the example, one can clearly see that a thin S - rich layer, labelled as strip 1 in the S map adheres closely to the tube surface. However, the remaining two strips labelled as No 2 and 3 are embedded deeply inside the interface. Regarding another washed ash W2, only one thin

layer was observed on the boundary between tube surface and the interface. For the acid washed ash A1, the distribution of S is barely discernible.

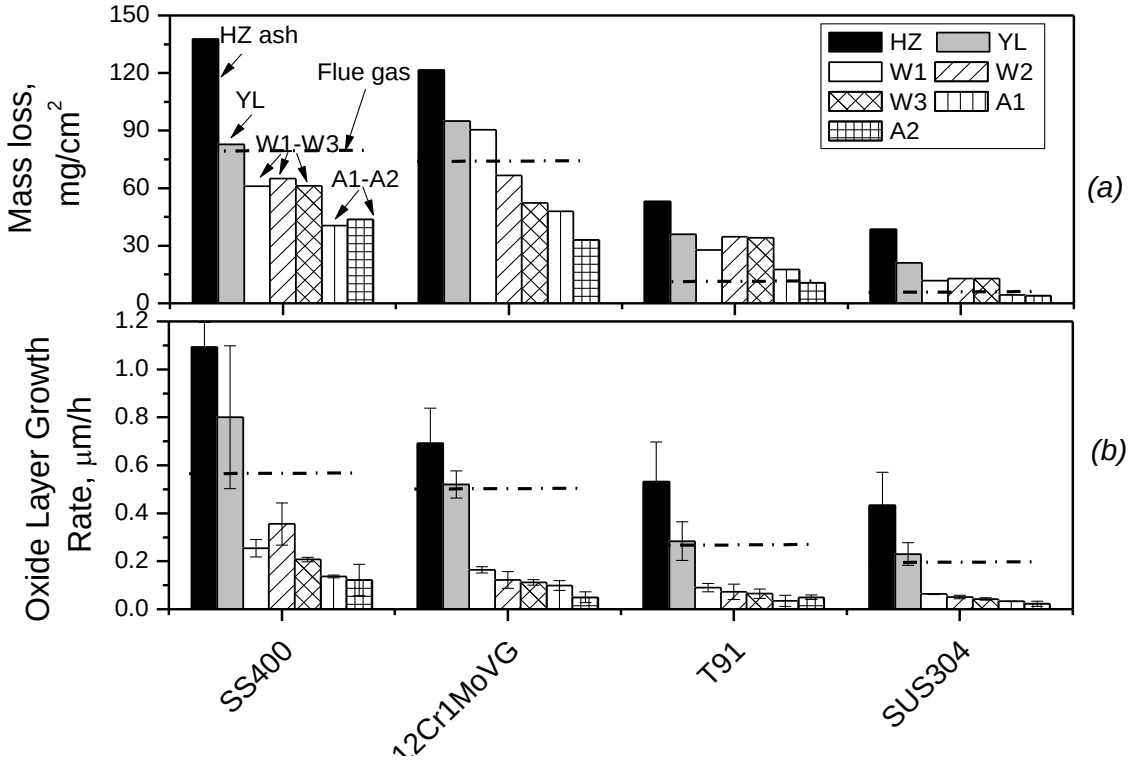

Figure 7.15 Mass loss (panel a) and **o**xide layer growth rate (b) of the tubes exposed to washed coal ashes under the oxy-fuel combustion mode. The dashed lines are results for the respective blank cases with flue gas only.

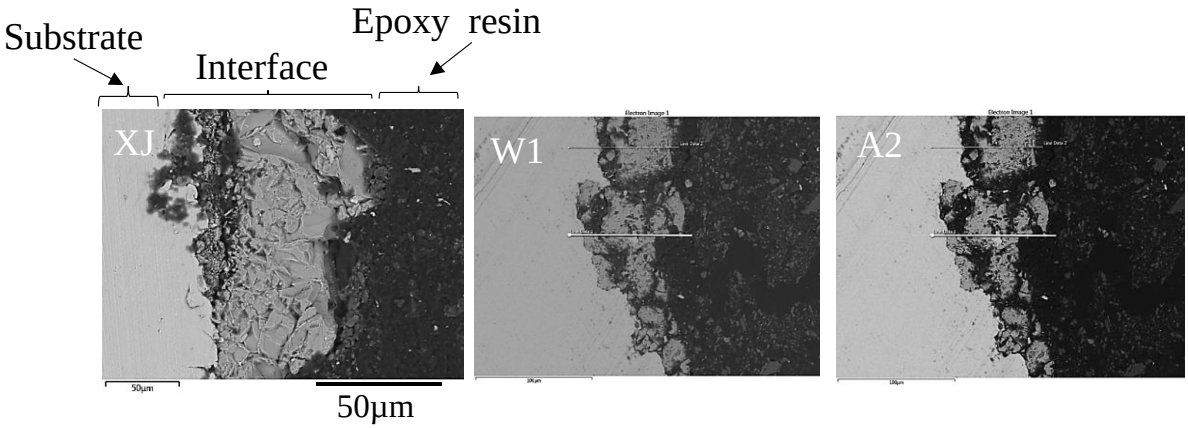

Figure 7.16 Typical micro-structure for the cross-section of 12 Cr1MoVG specimen exposed to different fly ash upon oxy-fuel combustion

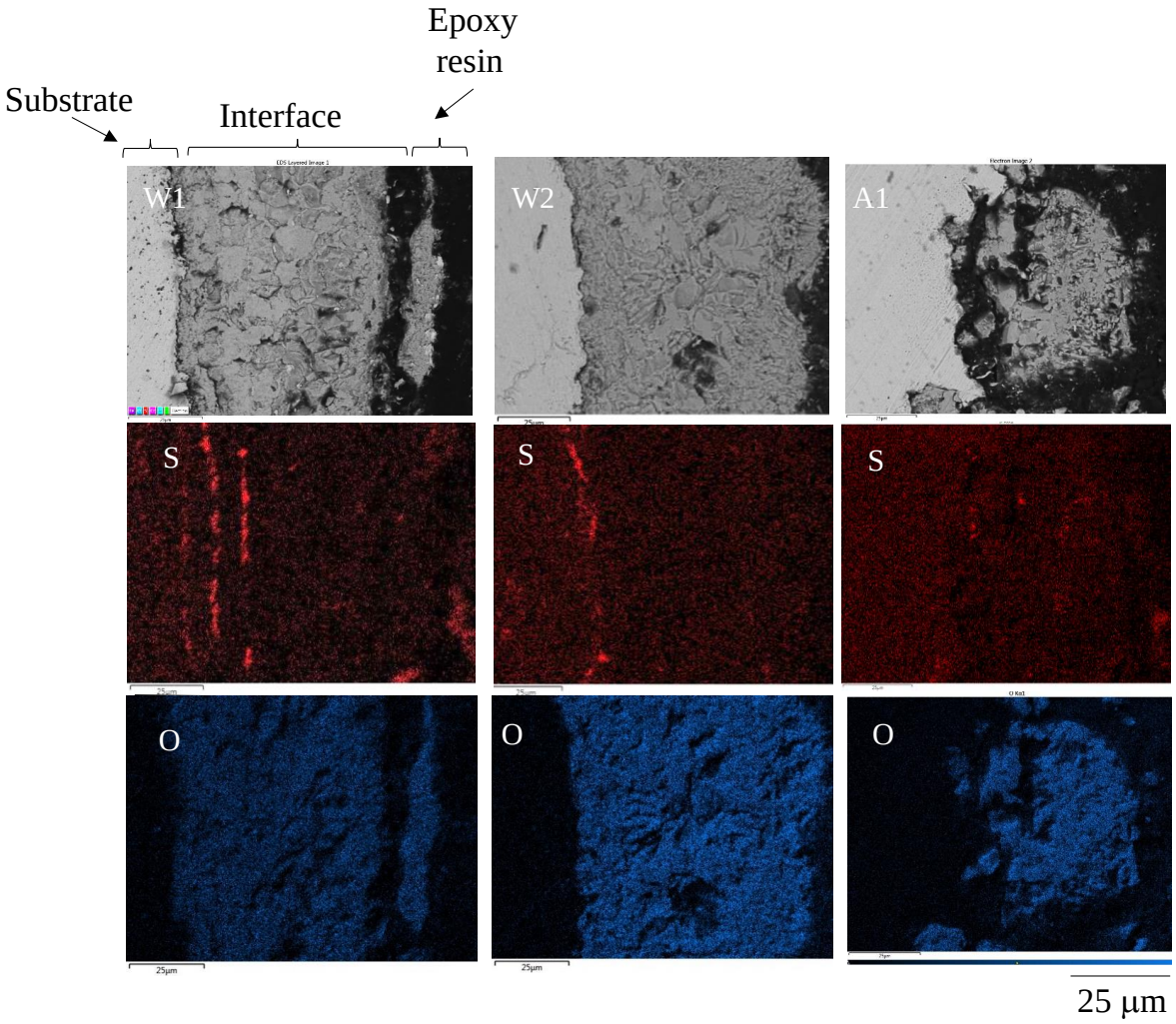

Figure 7.17 The elemental mapping for tube T91 exposed to washed coal

The S observed in the ash-tube interface demonstrates the penetration of this corrosive element either from SO_2 in bulk gas, or from solid sulphates in ash deposits. Regardless of the sulphur source, the resultant S in the interface should be partially ductile and easy to fragment into small pieces that are eventually mixed up with ash deposit. In light of this logic, the contents of S on the corroded tube surfaces were quantified, and plotted versus the respective mass losses of the tubes. Considering the measurement error related to the mass of the tubes, a reasonably linear trend is evident in ***Figure 7.18***. For the most advanced tube SUS304, its mass losses are the least, so are the contents of S remaining on its surfaces. The tube T91 bears a medium – Cr content, and interestingly, the S content remaining on its surface mostly falls in the medium range. As expected, the low-chrome tube 12Cr1MoVG bears the largest mass loss as well as the highest content of S. More interestingly, an identical linear correlation even holds for the three Cr-containing tubes, substantiating that S is the principle element causing the tube wastage. Furthermore, ***Figure 7.19*** for the used ash W1 on tube T91 demonstrates the abundance of ductile S-bearing fragments that are fully mixed with the other particles. The quantified composition for the used ash W1 on tube T91, as listed in ***Table 7.4***, confirmed a remarkable rise on the concentrations of Fe and S, whereas the concentrations of Na and Ca were decreased significantly. Apparently, S is mainly affiliated with Fe, whereas the inherent Na and Ca should partially diffuse out of ash matrix and transfer into the ash-tube interface or even deep inside the bulk tube, forming eutectics that easily melt, flow and fill in the pores within bulk tube and ash deposit.

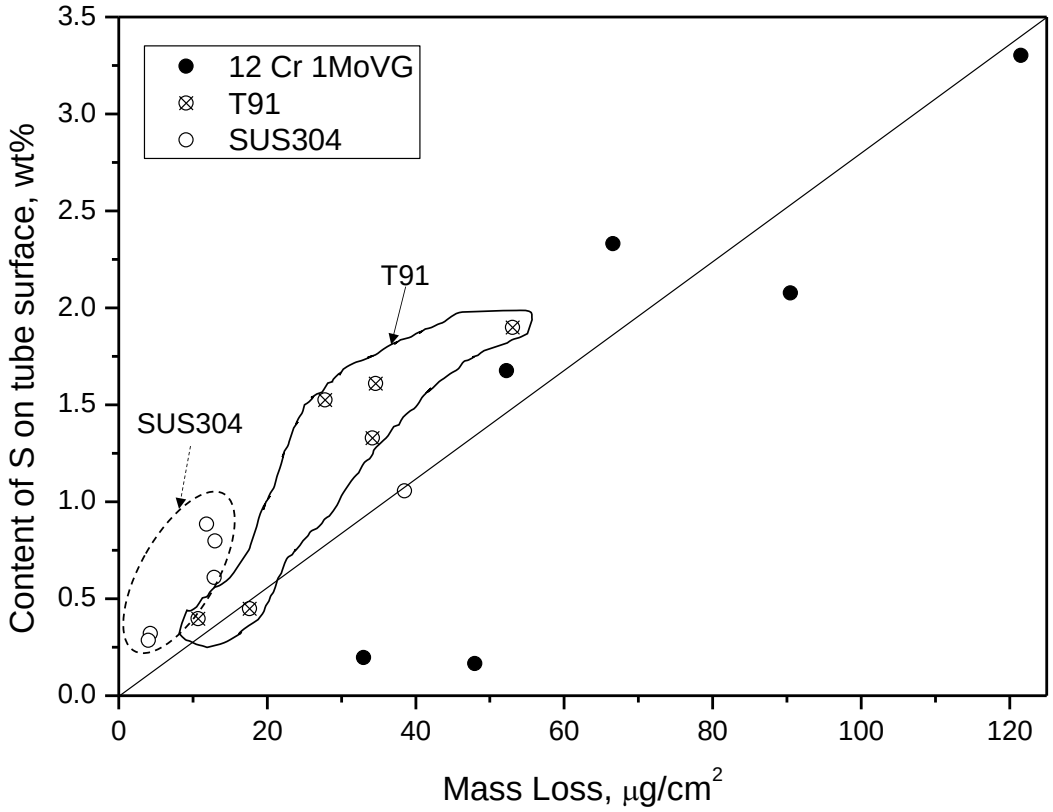

Figure 7.18 Correlation between tube mass loss and the content of S on the corroded tube surface

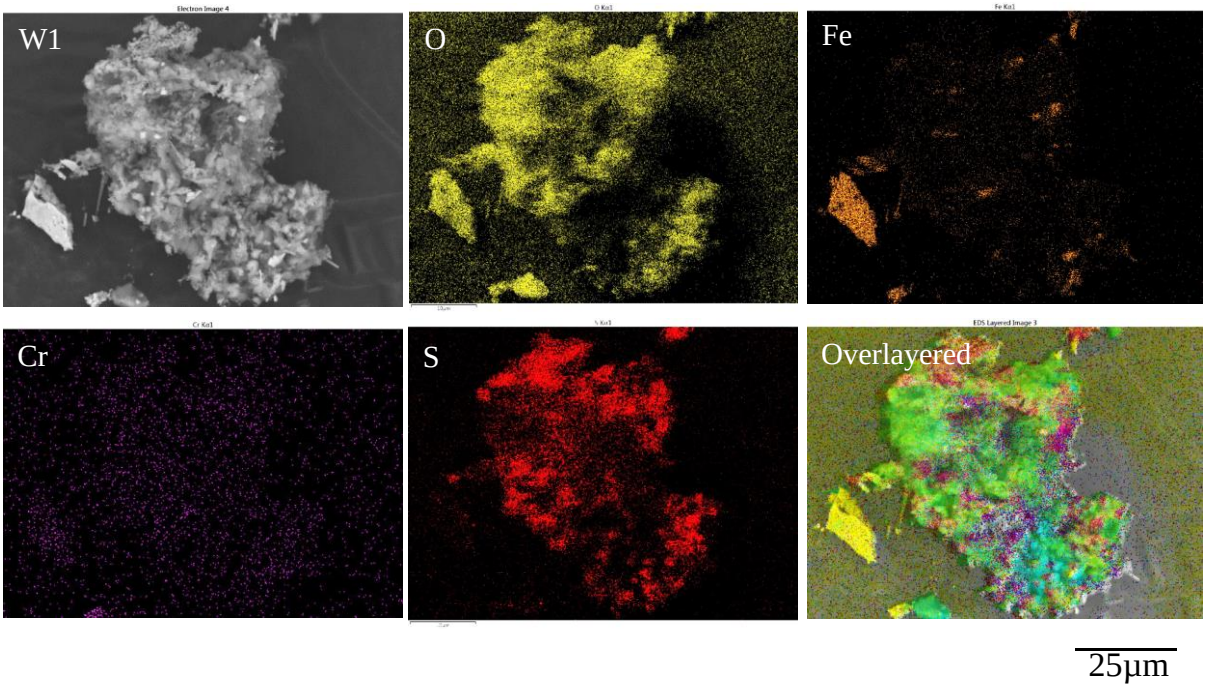

Figure 7.19 Elemental mapping for the used ash particle W1 coated on the tube T91 surface

Table 7.4 Elemental compositions of the W1 fly ash samples before and after tested

Composition, *wt%*	W1 before test	W1 after test
SiO_2	47.59	31.11
Al_2O_3	21.16	14.73
Fe_2O_3	3.41	31.56
CaO	13.78	9.27
MgO	4.63	0.10
SO_3	7.79	12.98
P_2O_5	0.12	0.00
Na_2O	1.01	0.03
K_2O	0.51	0.10

Figure 7.20, illustrates the S K-edge XANES spectra for the three corroded Cr-bearing tubes. Irrespective of the tube material, the peak located at ~2485 eV is the predominant and single peak for 12Cr1MoVG and SUS304. This peak is the fingerprint of sulphates which can be assigned as iron sulphate here. Such a species should be formed by the direct sulphation of iron oxide by bulk flue gas, or via the formation of Na-Fe trisulphate according to the reaction equation 1. Since no other peaks were found for S remaining on the tubes 12Cr1MoVG and SUS304, it is referrable that equation 2 for the reaction between sulphates and iron metal to form sulphide did not proceed on the surface of both low - and high - Cr tubes. This is however not the case for the tube T91 with a medium Cr content. From the panel *b* for T91 coated with W1-W3 ashes, one can clearly see a tiny but non-negligible peak located at 2470 eV or ~2472 eV. The similar phenomenon was observed for the used ashes coated on the same tube. As evident in ***Figure 7.21*** for both the fresh and used ashes, although sulphate is the single, dominant species in the fresh ashes and the used ones on the tubes 12Cr1MoVG and SUS304, the three washed ashes, W1-W3 on tube T91 are the exceptional used ashes that display the unique feature peaks at 2470-2472 eV. This peak is close to the feature peaks for a variety of sulphide standards shown in ***Figure 7.22***. The difference between these sulphide standards is subtle and thus, the sulphides detected in ***Figure 7.21*** can refer to as Fe_2S_3, FeS, NiS, Cr_2S_3, and even CaS/MgS. The formation of Cr_2S_3 can be ruled out here, because ***Figure 7.22*** for the Cr K-edge XANES spectra suggests that chromite/spinel is the predominant Cr-bearing species on the tube surface. The resultant chromite/spinel should function as the protective layer against the oxidation of iron and its corrosion. In light of this, the sulphides in ***Figures 7.20*** and 7***.21*** are very likely related to the metals Fe, Ca and Mg.

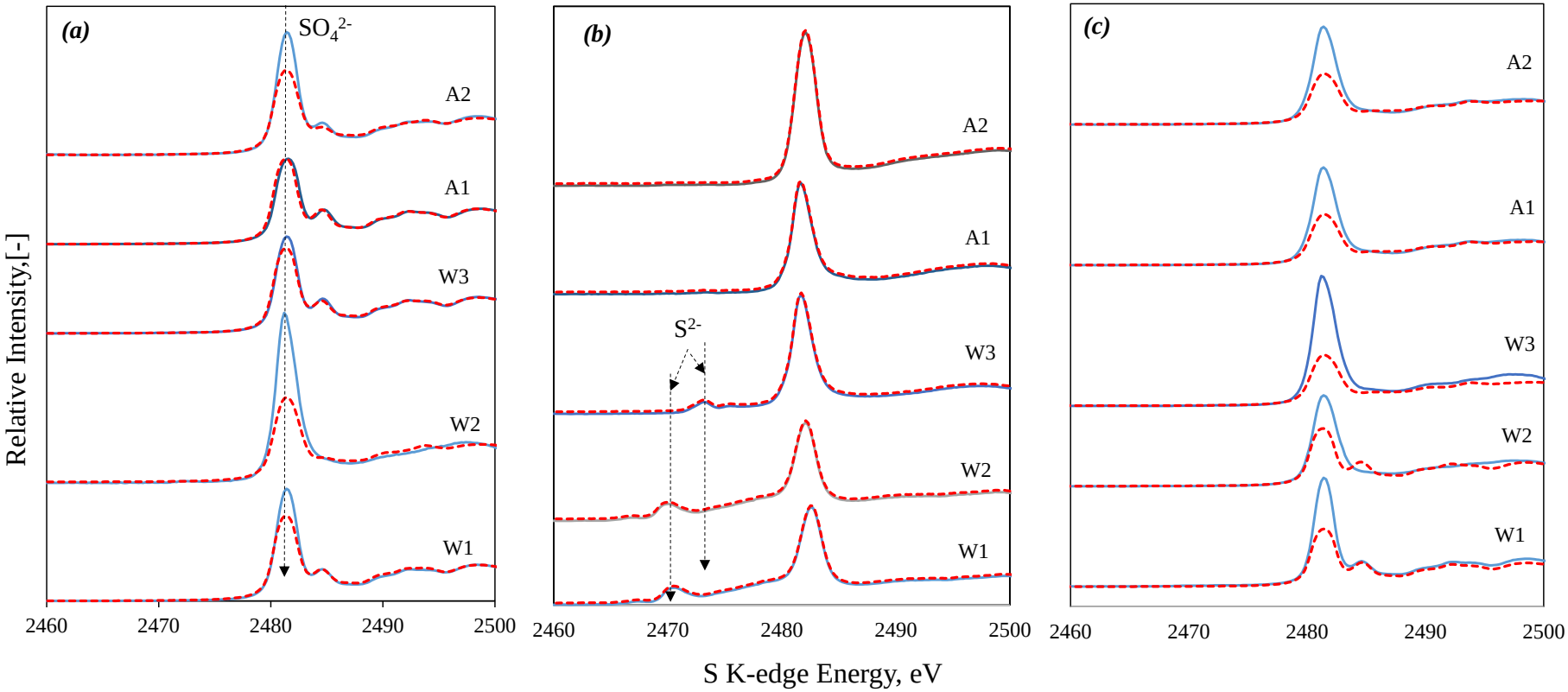

Figure 7.20 S K-edge XANES spectra and the fitting results for the top surfaces of three tubes exposed to different washed coal. In each panel the solid curves refer to the measured XANES spectra, and the dashed curves (in red) are the respective fitted results from ATHENA. Panels (a) to (c) are for the tube 12Cr1MoVG, T91 and SUS304, respectively.

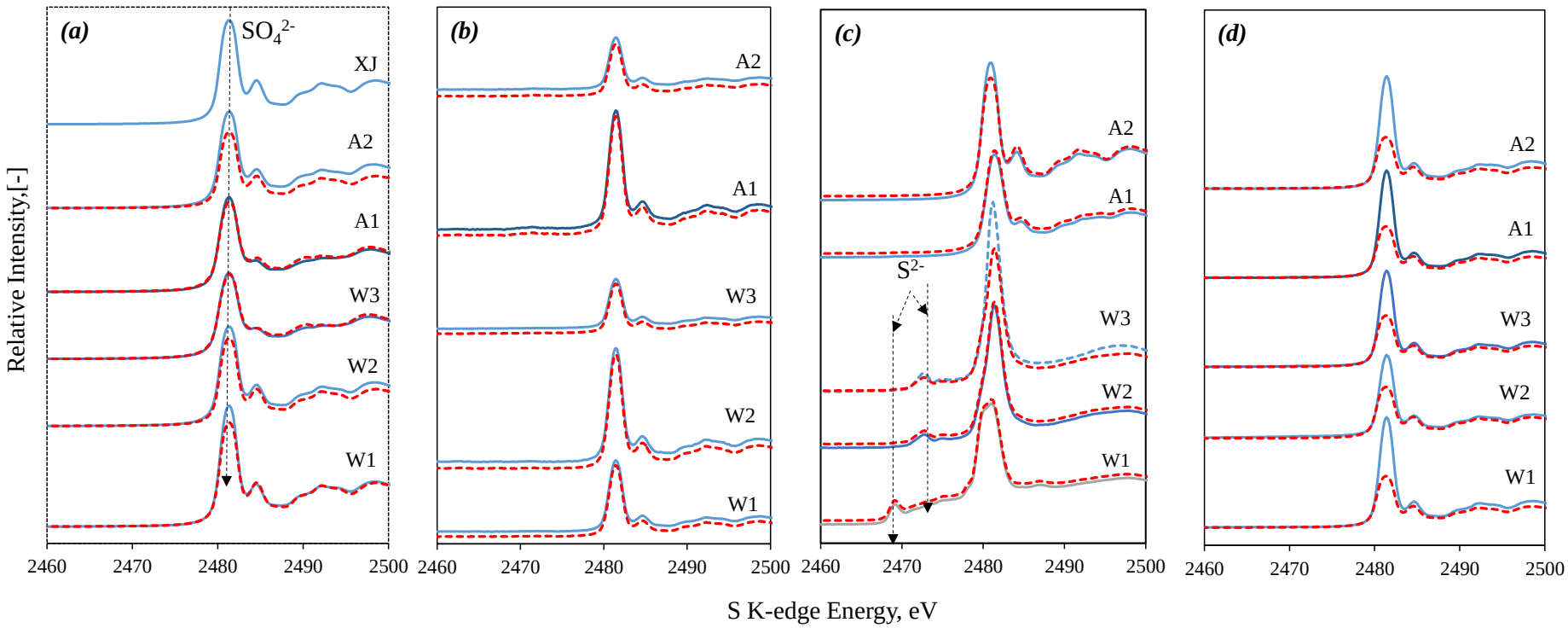

Figure 7.21 S K-edge XANES spectra and the fitting results for the ash samples before and after the tube exposure tests. In each panel the solid curves refer to the measured XANES spectra, and the dashed curves (in red) are the respective fitted results from ATHENA. Panels (a) - (d) are for the fresh ash samples, used ash on tube 12Cr1MoVG, used ash on tube T91 and on tube SUS304, respectively.

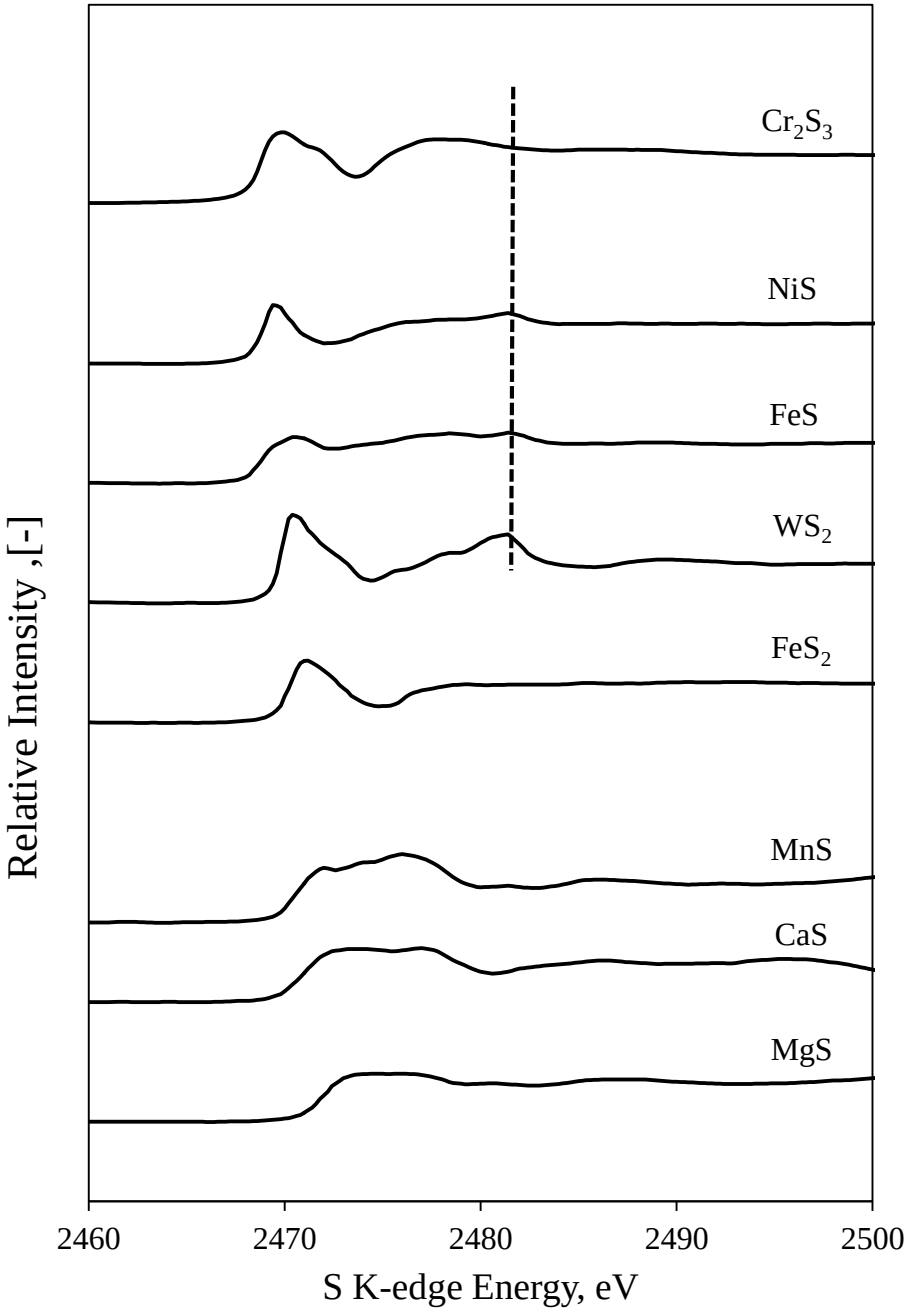

Figure 7.22 S K edge XANES spectra for sulphide standards. Peak at 2481eV indicated by the dotted line is spurious sulphate caused by oxidation

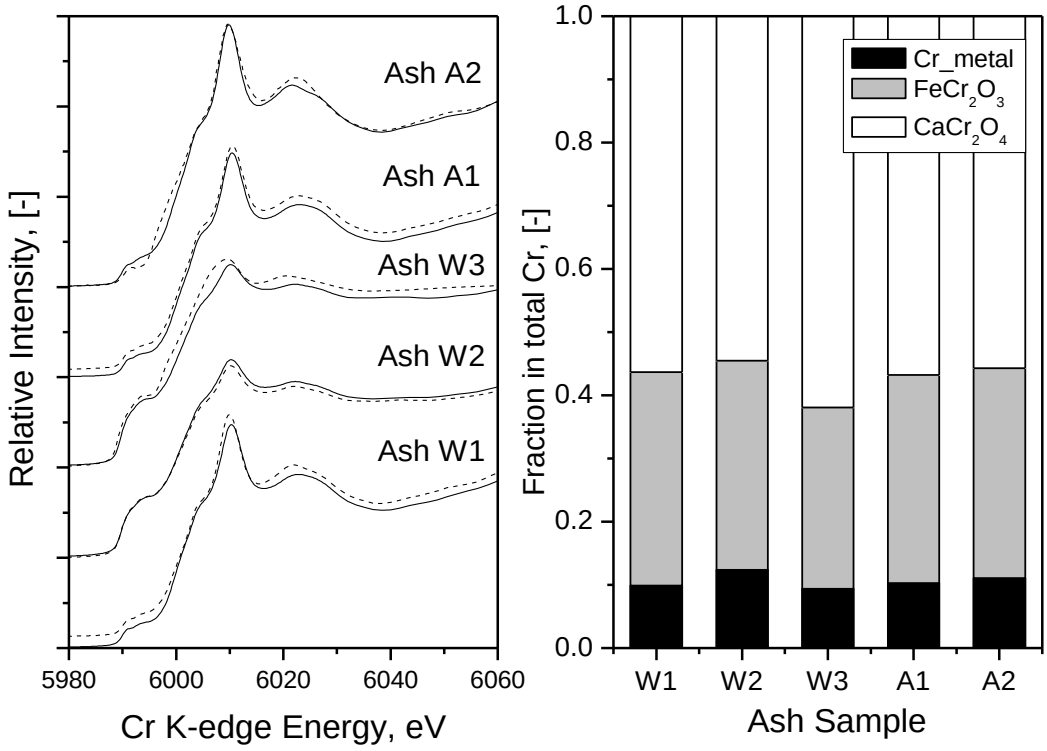

Figure 7.23 Cr-species composition from XANES fitting of on the tube T91 surface

Based on the results above, the behaviour of S is clearly the most critical factor accelerating the high-temperature tube corrosion under the oxy-fuel combustion mode. This broadly agrees with the observations achieved in the conventional air-firing mode. However, three key and new phenomena have been explored from this study, *1)* co - existence of sulphate and sulphide on both corroded tube surface and used ash deposit; *2)* ash - dependent formation of sulphide, and *3)* the unique formation of sulphide on tube T91 upon the coating with washed coal ashes that are lean in sulphates. All these phenomena have yet to be reported in the past. In particular, the last phenomenon related to T91 is for the first time reported here.

With regarding the first phenomena for the splitting of S between sulphate and sulphide, they should be formed according to the reaction equations 1-4 mentioned before. In particular, the formation of sulphate by equation 1 needs to take place firstly upon the contact between loose ash particles and oxide layer formed on the tube top surface. Subsequently, the resultant Na-Fe sulphates, as evident in ***Figures 7.20*** and ***7.21*** partially melt and stick to the tube surface. The molten sulphates can further act as a solvent pool to dissolve the inherent metals such as Fe,

Cr and others in the tube according to the fluxing mechanism. The dissolved metals in turn reacts with the molten sulphates to form the respective sulphide, as suggested by equations 2 and 4. This mechanism is explained visually in ***Figure 7.24(a)*** where the grey, black and light green colours refer to the bulk tube, molten species and loose ash particles, respectively. A thin Cr-O layer is also expected to remain in between the grey and black colours, as has been confirmed in our previous studies and ***Figure 7.23*** in this study. With respect to the formation of molten species, the FactSage prediction results, as shown in ***panels (b)*** and ***(c)*** respectively for raw XJ coal ash and W1 ash on tube T91, confirmed the thermodynamic possibility for the melting of sulphates/sulphides at 650^{o}C. However, the melting propensity of sulphate is far different from sulphide. For the sulphate – bearing slag shown in ***panel (b)***, the oxides are instead much more abundant than sulphates, due to the fact that sulphates are more difficult to melt. The molten sulphates are also dominated by alkali and iron sulphates. In contrast, for the sulphide – bearing slag in ***panel (c)***, sulphide is predominant, which is followed by Cr and Fe oxides. The sulphide is also mainly made up of CaS and FeS that can be formed thermodynamically via equation 3.

The detection of sulphide in ***Figures 7.20*** and ***7.21*** experimentally confirmed a direct involvement of ash deposit on the tube corrosion. For the blank test using pure flue gas only, our previous test have proven that the formation of sulphide was indiscernible. However, the role of flue gas on the formation of sulphide cannot be fully ruled out here. Although having no direct contact with tube surface, the flue gas can react with ash deposit first, forming sulphates that subsequently attack the tube surface according to the fluxing mechanism in ***Figure 7.24 (a)***. The abundant CaO in ash samples in ***Table 7.1*** plus the free oxides derived from equations 2-4 are able to capture SO_2 at 650^{o}C. Moreover, once the S in ash deposit is passed to the tube surface, the S-lean ash deposits has no reason to stop the sulphation reaction with flue gas. To quantitatively clarify the extent of flue gas participating on the tube corrosion, thermodynamic equilibrium calculation was further conducted to evaluate the influences of three flue gas components, SO_2, O_2 and steam/H_2O on the formation of slag. A kinetic modelling was not attempted here because of the lack of the kinetic parameter and the complexity of the oxy-firing flue gas used here. ***Figure 7.25 (a)*** demonstrates the results for the extent of dry gas (SO_2 and O_2) whereas ***panel (b)*** is for the participation extent of steam when the extent of two dry gas components are fixed at 0.2%. Note that, the ash W1 was used for calculation here, and the two dry gas components, O_2 and SO_2 are assumed to have an identical participation extent in the formation of slag and sulphide.

As shown in ***Figure 7.25 (a),*** the attendance of dry flue gas is critical in affecting the amounts of total slag and the two key sulphides, Fe sulphide and Cr sulphide. Compared to the predominant formation of Cr sulphide in the absence of flue gas, the introduction of dry flue gas decreases the formation of Cr sulphide quickly, which drops to nil in the case that no less than 0.2% of dry flue gas participates in the reactions. Simultaneously, the total slag amount and Fe sulphides increase quickly to their maximum when more than 0.5% dry flue gas is involved. However, in the case that more than 2.5% dry flue gas attends the reactions, the slag amount and sulphide drop dramatically to nil, due to the formation of dominant sulphates that are difficult to melt. Back to ***Figure 7.23*** where Cr sulphide was not found, it is obvious that the participation extent of dry flue gas should range between 0.2 – 2.5%. Regarding the ***panel (b),*** it demonstrates the remarkable influence of steam on the formation of molten slag and sulphides. Under the exposure conditions tested here, the participation extent of steam is not nil, but less than 3.5%, otherwise the formation of solid sulphates and gaseous H_2S will be superior. Interestingly, the formation of Cr sulphide is insignificant, irrespective of the steam percentage. This further demonstrates the stability of this protective element in the wet flue gas. However, the total amount of slag decreases while the fraction of Fe sulphide increases upon the rise of steam fraction to participate in the tube corrosion.

Considering that the participation extents of flue gas components are very small, and the solid-state reactions are more critical in attacking the tube directly for the corrosion, it might be the case that the concentration of SO_2 in bulk gas is insignificant. At least, it is not the controlling limit for the tube corrosion. If that is the case, the shift from air-firing flue gas to oxy-fuel gas causes little difference on the penetration rate of sulphur, *i.e.* the concentration of S remaining on the corroded tube surface. This is proven by ***Figure 7.26*** in which the same slope was found the two combustion modes using the same tube material.

The second phenomena for the ash – dependent sulphide formation is intriguing. To reflect the effect of ash composition on the formation of sulphide, ***Figure 7.27*** was plotted by merging ***Figures 7.18, 7.20*** and ***7.21*** to correlate the content of S in ash versus the contents of sulphide formed on both corroded tube surface and used ash, as well as the total content of S remaining on the tube surface. Note that, the contents of sulphides were quantified by the LCF for ***Figures 7.20*** and ***7.21***. It is interesting that the total amount of S on the tube surface and the fraction of

sulphides follow the same trend. That is, the three water washed ashes in particular W1 are more influential in the adherence of S and the formation of sulphide on the tube surface, whereas the other two acid-washed ashes bearing a relatively large amount of S are not in favour of the sulphidation reaction. This difference should be due to the greater reduction on the amount of CaO by acid washing. Therefore, the extent of reaction equation 3 for A1 – A2 is less than for W1-W3. The panel (c) in Figure 10 also suggests a predominance of CaS in the slag formed from the low-S ash deposit. Additionally, although XANES spectra for S in ***Figures 7.20*** and ***7.21*** failed to distinguish different sulphides, it is clear that CaO has a higher whiteline position (close to 1472 eV) than iron sulphide. It is thus very likely that the smallest peak for S in ***Figures 7.20*** and ***7.21*** should be assigned as CaS.

The last phenomena related to the unique formation of sulphide only on the tube T91 is also noteworthy. Thermodynamically, the rise on the contents of Cr and Ni in a tube depreciates the formation of molten slags. As evident in ***Figure 7.28*** one can see a sharp decrease on the amount of total slag and even the fraction of Fe_2S_3 once the Cr content in the tube increases up to 10% that is close to T91. Interestingly, the fraction of FeS in the total slag is slightly improved from the Cr content of 10%. This to certain extent indicates that the sulphides found by XANES should be mainly referred to as FeS. However, the thermodynamic prediction fails to explain the absence of sulphide on the low-Cr tubes. This should be due to the diffusion control inhibiting the formation of sulphides inside a tube. From the gas diffusivity perspective, the top oxide, shown as Cr-O layer in ***Figure 7.24 (a)*** is supposedly protective against gas diffusion. However, for the low-Cr alloy 12Cr1MoVG, the shortage of Cr resulted in a porous and even partially damaged protective layer that is in favour of all the gases including oxygen. This in turn creates an oxidising environment that favours the over-growth of sulphate over sulphide. In contrast, for the highest Cr-tube austenite tube SUS304, its Cr-rich, protective scale is too tenacious for any gas/molten species to permeate through. The medium Cr-tube T91 studied here should fall in between these two extreme tubes, creating a porous layer and reducing environment to promote the formation of sulphides inside. Such a unique feature for 9Cr steel has also been noticed in the other studies on the permeation of C/CO_2 for the formation for carbide.

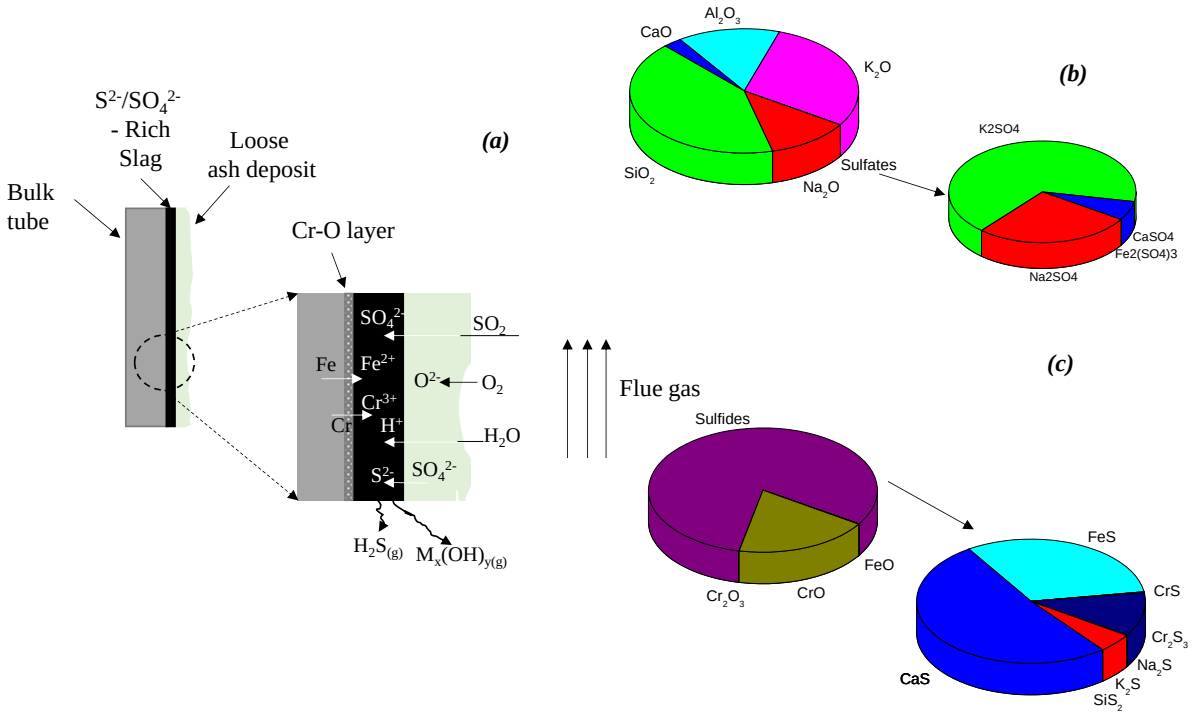

Figure 7.24 Schematic (a) for the formation of slag, sulphide and sulphate in the slag; FactSage predicted slag composition (b) for Hazelwood raw coal ash deposit on tube T91, based on the use of database BSlag + Sulfates; and (c) for the FactSage predicted slag composition for W1 ash deposit on tube T91, based on the use of database ASlag + Sulphide.

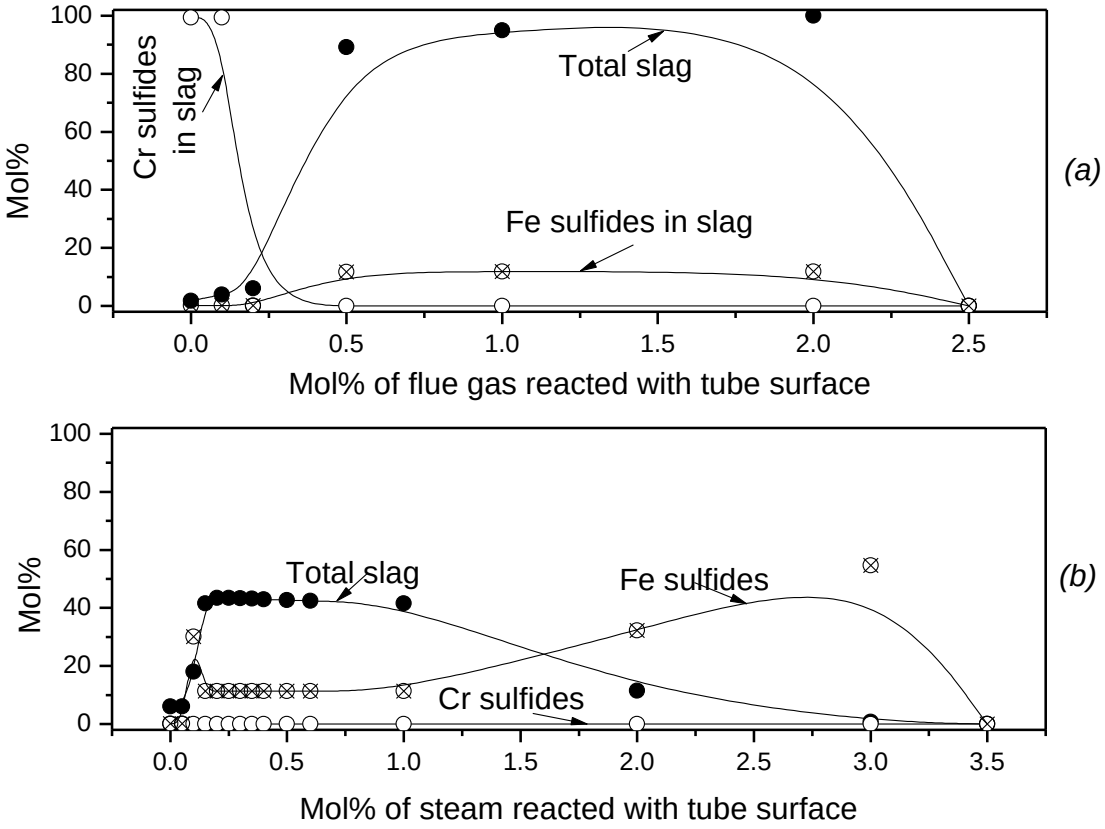

Figure 7.25 Thermodynamic equilibrium modelling on the formation of slag and sulphides on tube T91 surface. Panel (a) is for the percentages of Cr/Fe sulphides upon the ash deposit W1 as a function of dry flue gas reacting with tube surface; (b) for the percentages of Cr/Fe sulphides upon the ash deposit W1 as a function of steam reacting with tube surface. The percentages of O_2 and SO_2 reacting with tube surface were fixed at 0.2%.

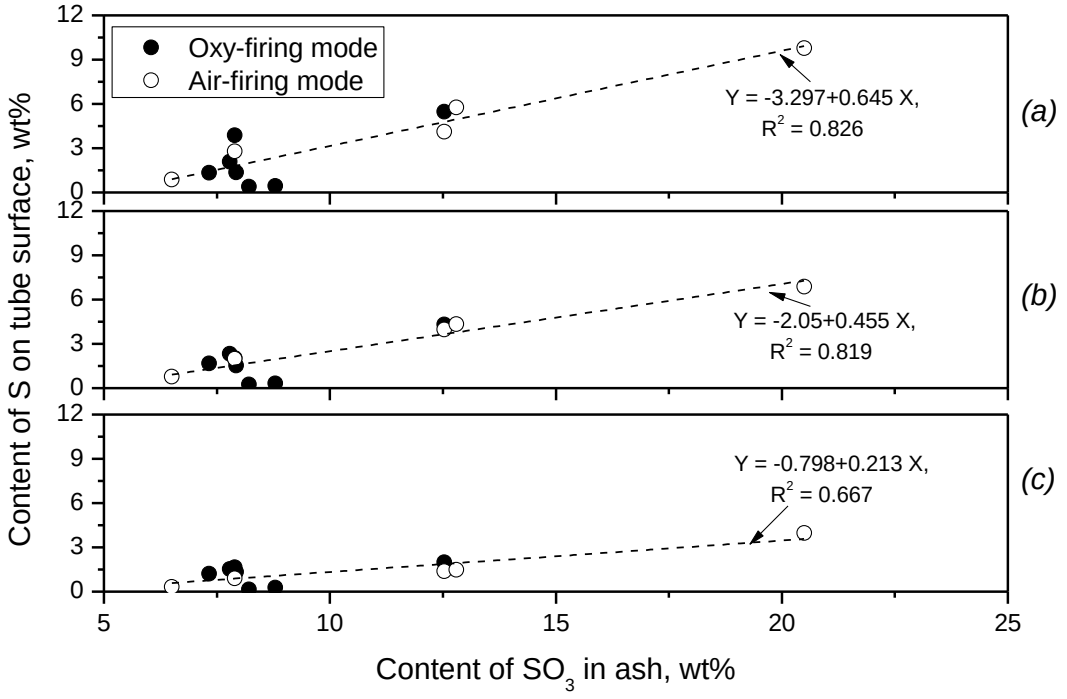

Figure 7.26 Correlation between SO_3 in ash samples with the sulphur on different corroded tubes surface. Panels (a)-(c) are for tube 12Cr1MoVG, T91 and SUS347, respectively.

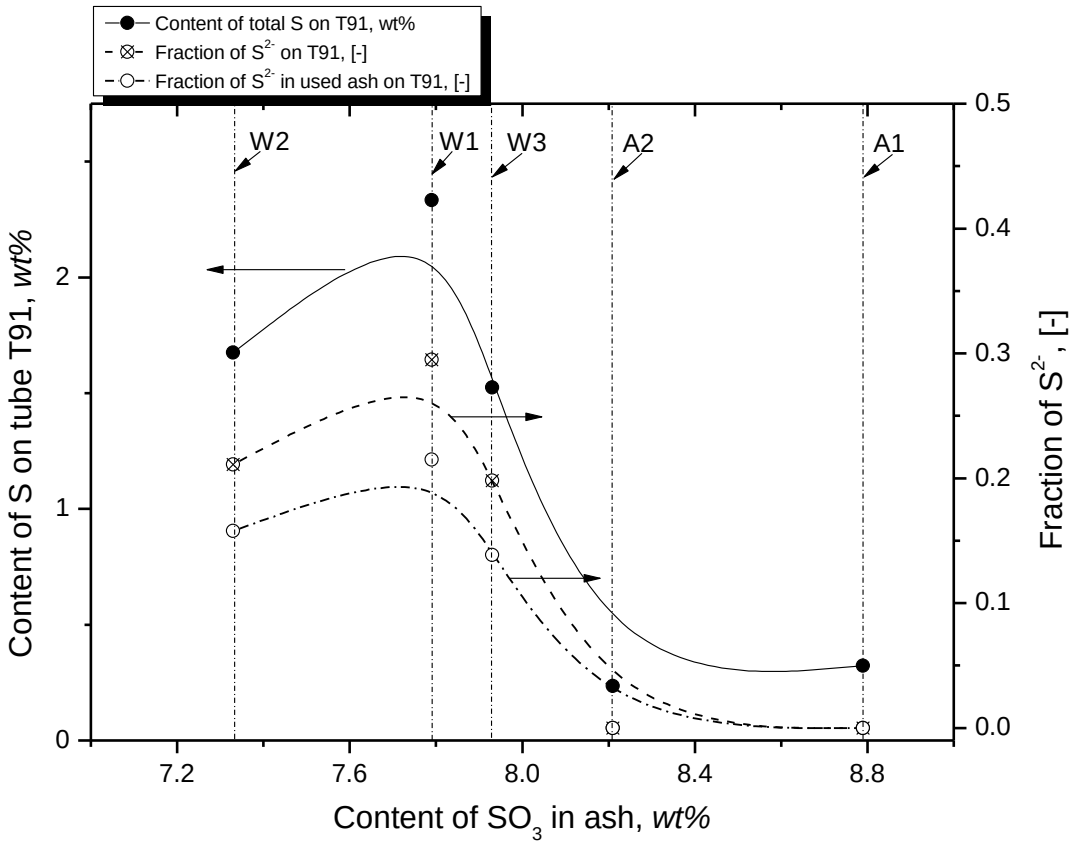

Figure 7.27 Sulphide composition from XANES fitting of tube T91 and ash sample coated with washed fly ash.

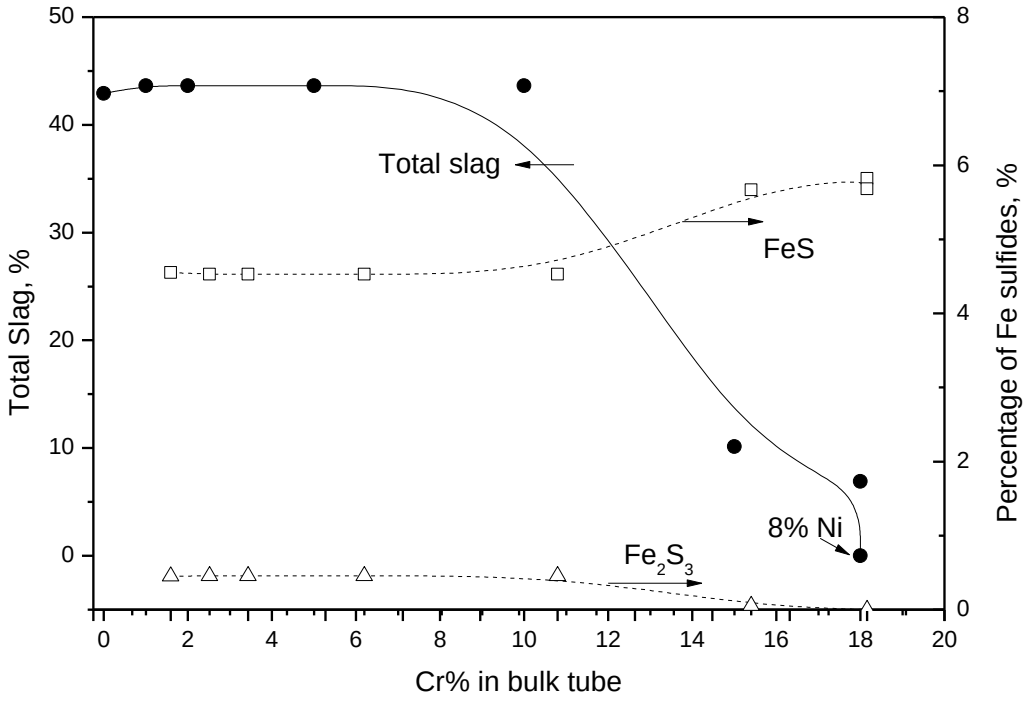

Figure 7.28 Effect of Cr content in bulk tube on the formation of total slag and Fe sulphides, predicted by FactSage. Ash W1 was used as the ash deposit, 0.2% flue gas was assumed to take part in the reactions with tube surface.

7.3 Conclusion

1. For the high-sodium brown coals/lignites including Hazelwood coal, the use of refractory silica as an additive is beneficial in reducing the tube corrosion rate, as well as the ash deposition propensity. This is because the deactivation of sodium via the transformation into less corrosive sodium silicate.
2. Desulfurization of flue gas prior to its recycle is essential to minimise the negative effects of Na sulphate and oxides which even caused the corrosion of the high-Cr alloys. Otherwise, the silica additive should be fed with the low-rank coal together to minimise the capture both Na and other free oxides.
3. The amount of S permeated inside tube is predominantly limited by the availability of the inherent sulphates in ash deposits. However, the participation of flue gas is essential for the tube corrosion. Under the exposure duration of 50 hours studied here, the contribution extent of flue gas is estimated to range from 0.2% to maximum 3.5%. The lignite ash deposit functions as a medium which transfers the S from bulk gas to tube surface, via the formation of intermediate sulphates or sulphide.
4. The formation of sulphide is highly dependent on both ash properties and the tube composition. The high – S ash from raw coal has no potential causing the formation of sulphide. For the low-S ash deposits, the content of Ca as free oxide is critical since the formation of CaS is a critical species assisting in the formation of Fe sulphide in the tube. Compared to water washing, the use of acid is able to remove the free Ca oxide, and hence, eliminates the potential for the formation of sulphide.
5. The medium – Cr ferritic tube T91 is most readily sulphide than the other tubes from both the thermodynamic equilibrium and gas diffusion perspectives. Its Cr content is not high enough to fully avoid the formation of sulphide – bearing slag.

Chapter 8 Characterisation of the corroded tubes upon the use of SEM-EDX, XRD and synchrotron-based X-ray fluorescence spectroscopy (XFM)

Deposits and corrosion on heat transfer tube surfaces play a major role on coal fired boiler performance. Understanding tube corrosion mechanisms allows the deployment or retrofit of advanced tube materials and maintain a long lifetime for an oxy-firing boiler. In this section, properties of the corroded tubes upon the exposure to oxy-fuel gas and the interaction with ash deposits at high temperatures will be introduced, through the characterization by a number of advanced instruments including lab-scale SEM-EDX, XRD and synchrotron-based XFM.

8.1 Characterisation into flue gas only

8.1.1 The interface of tube SS400 (carbon steel) exposed to flue gas only

The tubes were first exposed into flue gas only, without ash coating, to reveal the effects of flue gas components especially CO_2, steam and high-concentration SO_2 and HCl on the tube corrosion. As shown in ***Figure 8.1***, the use of pure CO_2 caused the least corrosion for each tube, suggestive of its relatively inert behavior compared to nitrogen that can cause the nitrification reaction for tube surface. The use of oxy-fuel flue gas is most corrosive, causing the highest corrosion rate for each tube. Additionally, upon the increase of Cr content in the tube, the tube corrosion rate decreased, due to the protective effect of Cr that can be oxidized more quickly than Fe.

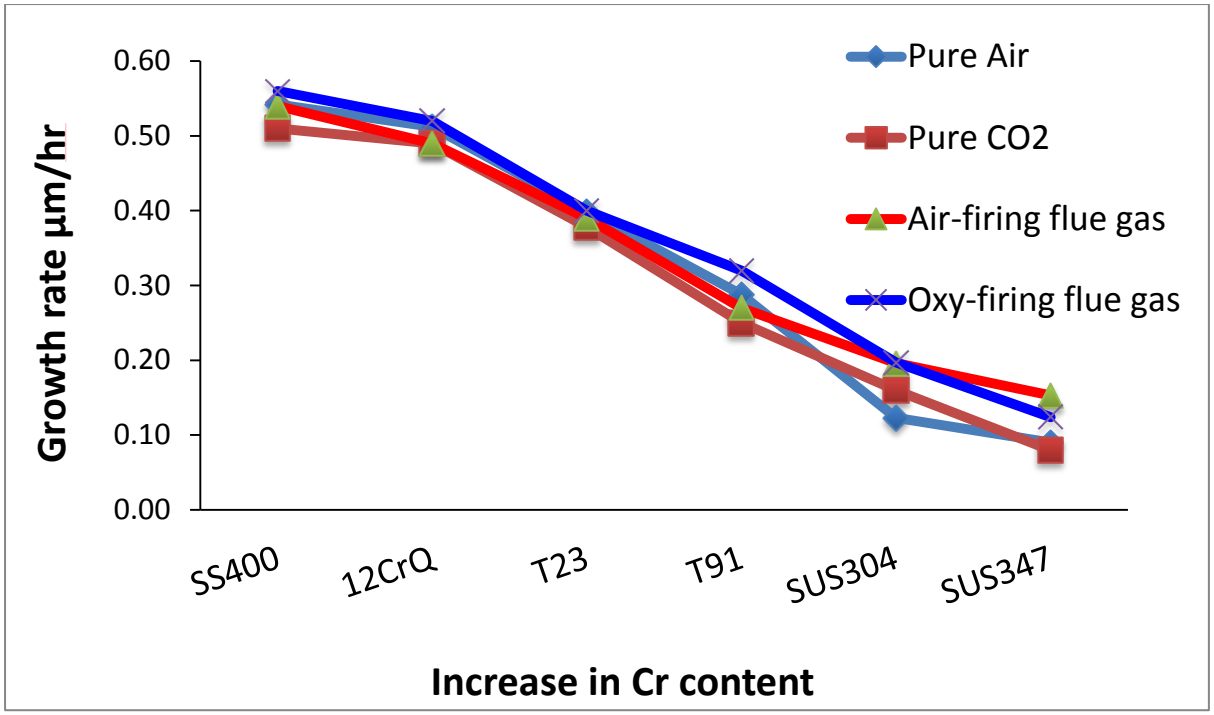

Figure 8.1 Tube corrosion rate upon the exposure to flue gas only, without ash coating

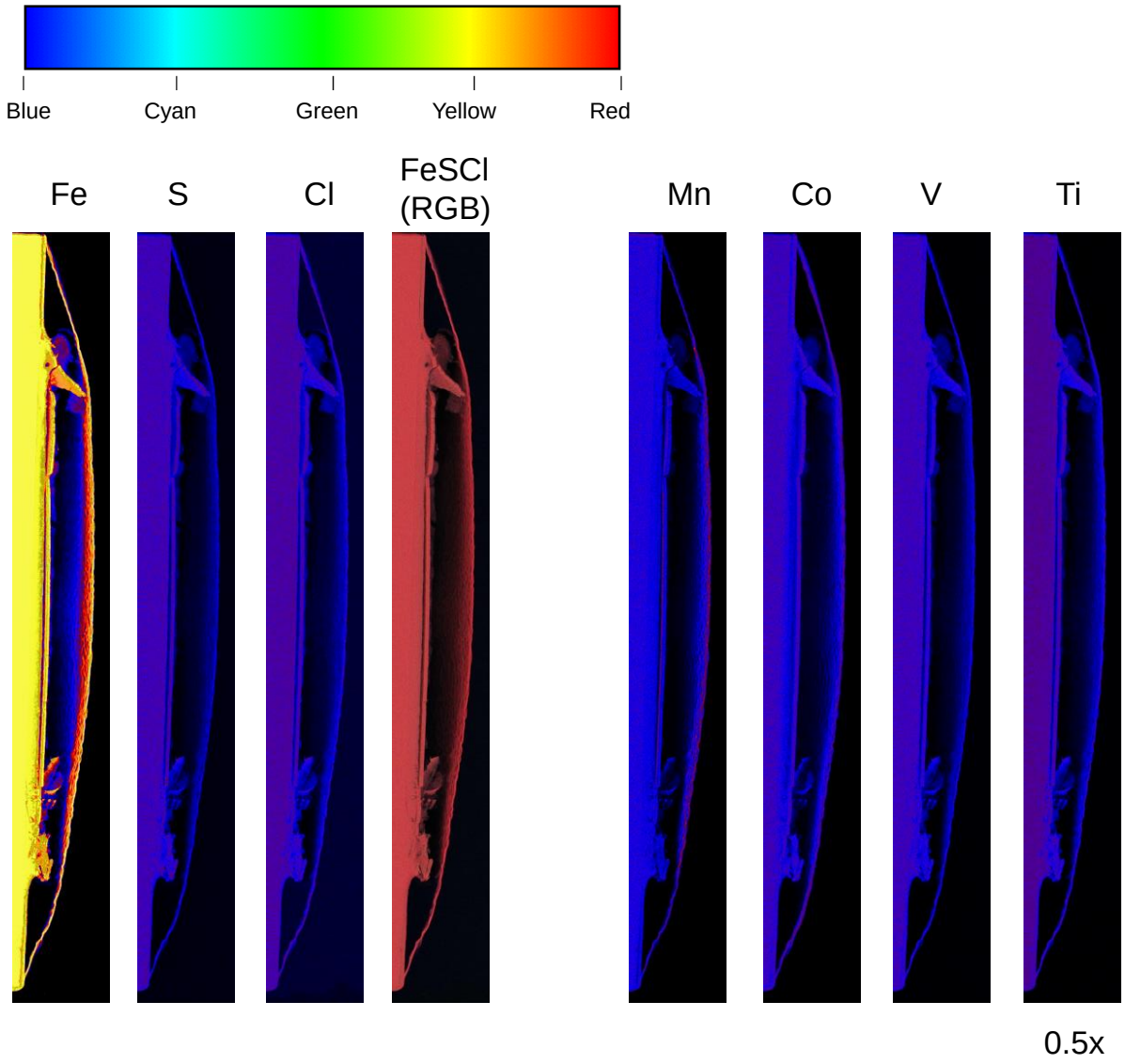

Figure 8.2 Elemental distribution on the corroded tube SS400 interface, characterized by synchrotron XFM

Figure 8.2 demonstrates the elemental mapping for the carbon steel tube SS400 that was exposed to oxy-fuel flue gas, without ash coating. Interestingly, the principal element Fe shows a non-uniform distribution on the top surface of the tube, as well as across the spalled interface. For both the top surface and spalled layer, Fe showed an outward diffusion with it being enriched on the most outer layer. A close look at the other metals suggests the enrichment of Mn and even a few amount of V and Ti on the most outer layer, suggestive of their protective effects. For the two corrosive gases S and Cl, their distribution in both tube top surface and the spalled layer is rather weak, implying the formation of few sulfide/sulfates and chlorides.

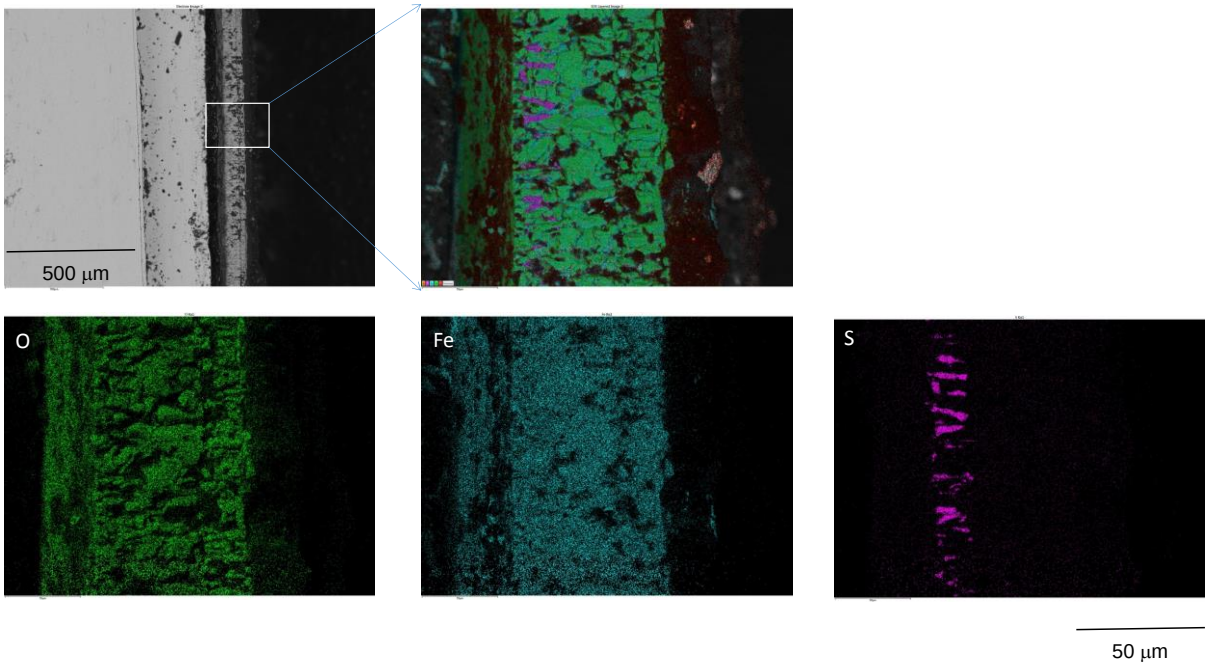

Figure 8.3 Amplified tube interface, characterized by SEM-EDX

Figure 8.3 shows a close-up observation of the tube SS400 interface upon the characterization by lab-scale SEM-EDS. In this case, the sulfur was clearly observed. It however shows a different distribution compared to Fe and O that are evenly distributed across the spalled tube layer. Sulfur is mostly present on the left-hand side of the spalled layer, as scattered stripes that are embedded within the Fe-dominant layer. This is an indicator of the inward diffusion of sulfur. However, the sulfur diffusion should be much slower than oxygen, as evident by the abundance and even distribution of oxygen across the whole tube spalled layer. ***Figure 8.4*** for the Fe-SO_2-O_2 phase diagram suggests that sulfide is the principal species that can be formed from the attack of SO_2 gas, rather than sulfates.

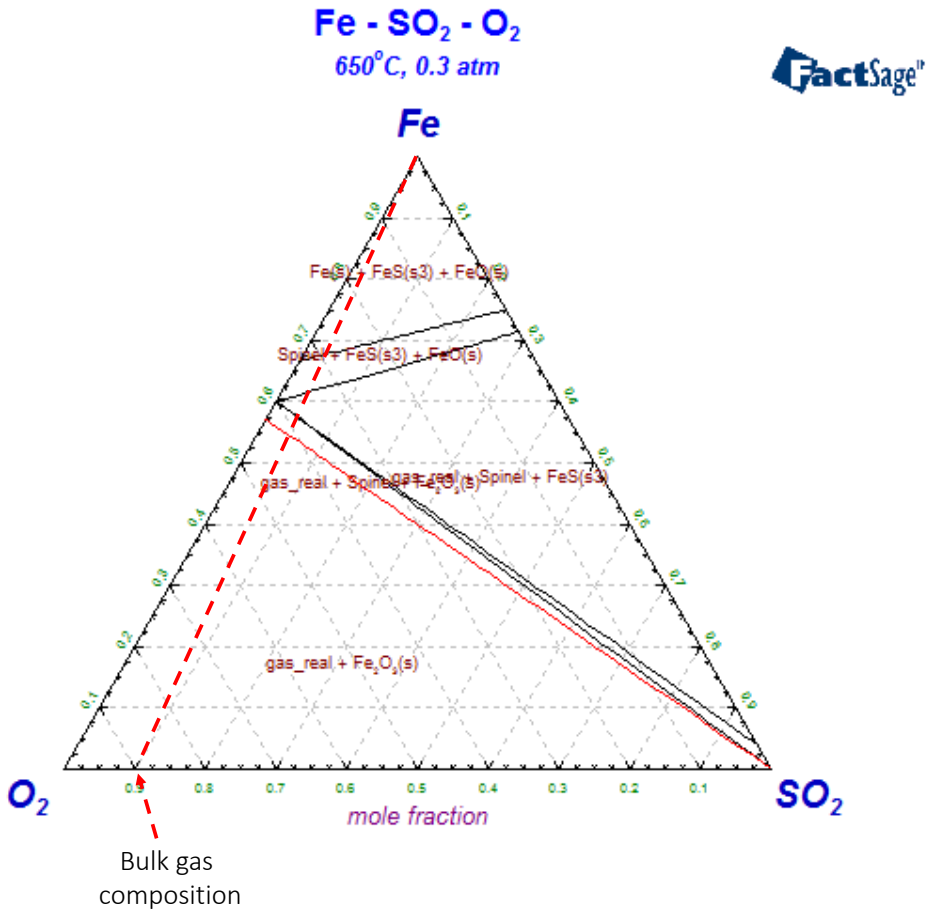

Figure 8.4 Fe-SO_2-O_2 phase diagram at 650°C and 1 atm

8.1.2 The interfaces of tube 12Cr1MoV, T91 and SUS304 exposed to flue gas only

Figure 8.5 shows the XFM map for the individual elements across the cross-section of the tube 12Cr1MoV. Again, one can see a preferential enrichment of the elements including Cr, Mn, V and even Ti on the top of the tube surface which was exposed to flue gas. Here again, the distribution of S and Cl is rather trivial on the tube cross-section, suggestive of their insignificant corrosion effect compared to the other gas components including steam, oxygen and even CO_2. For the two metals of interest Cr and Fe, a close-up observation confirmed a non-uniform distribution on the tube surface. For both two metals, their concentration show a multi-layer distribution across the tube surface, i.e. lowest concentration (in blue) on the most top layer, followed by a medium-layer in red color that refers to the highest concentration, and then a yellow layer/zone that refers to second highest concentration in the grey bar.

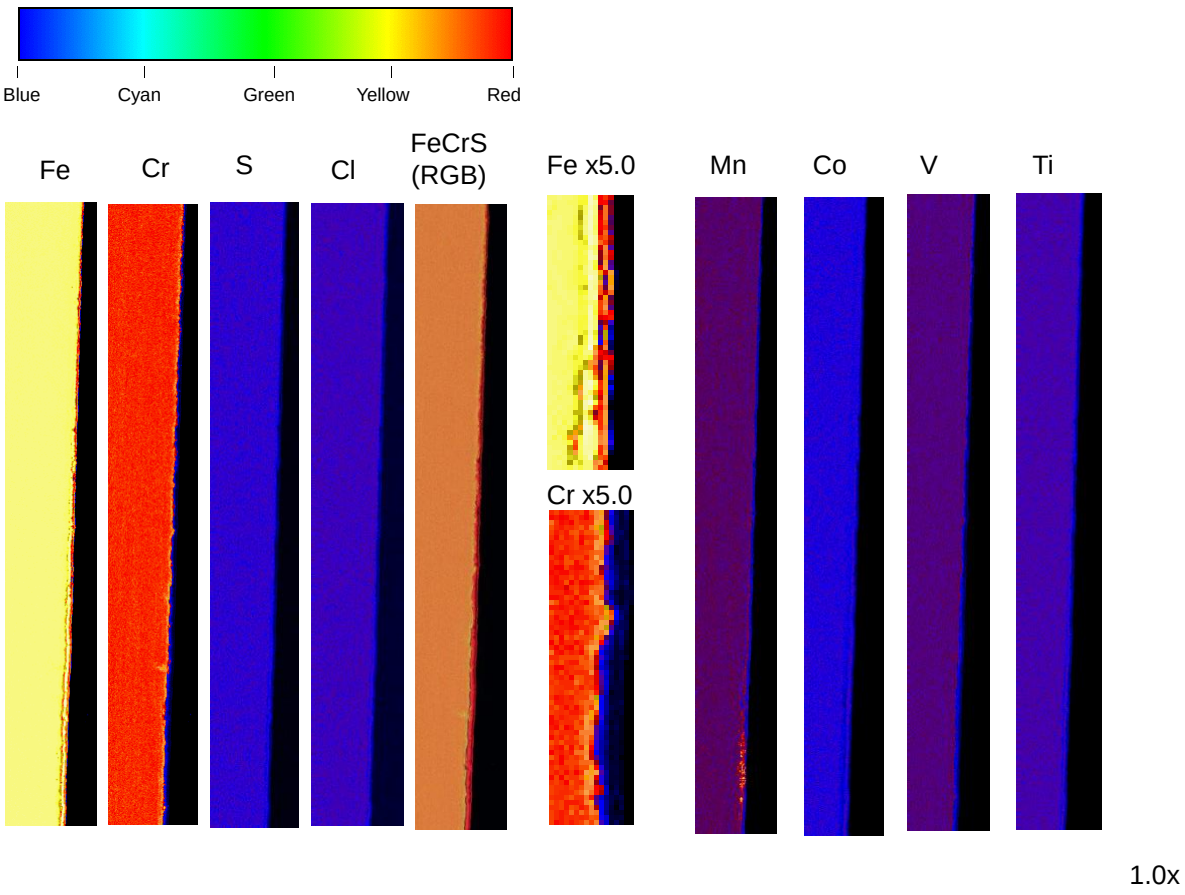

Figure 8.5 Elemental distribution on the corroded tube 12Cr1MoV interface, characterized by synchrotron XFM

A further close-up detection of Cr and its chemical speciation were conducted by both XFM and μ-XAFES. As shown on the left-hand side of ***Figure 8.6***, Cr possesses a multi-layer distribution in its concentration across the tube cross-sectional surface. Again, few of it was bound with sulfur and chloride, implying that oxidation is the principal reaction route for this element. On the right-hand side, one can further see a non-uniform distribution for the individual energies related to Cr on the interface. The energy of 6.009 eV is obviously the brightest, which is the peak for the species including oxide and ferrite.

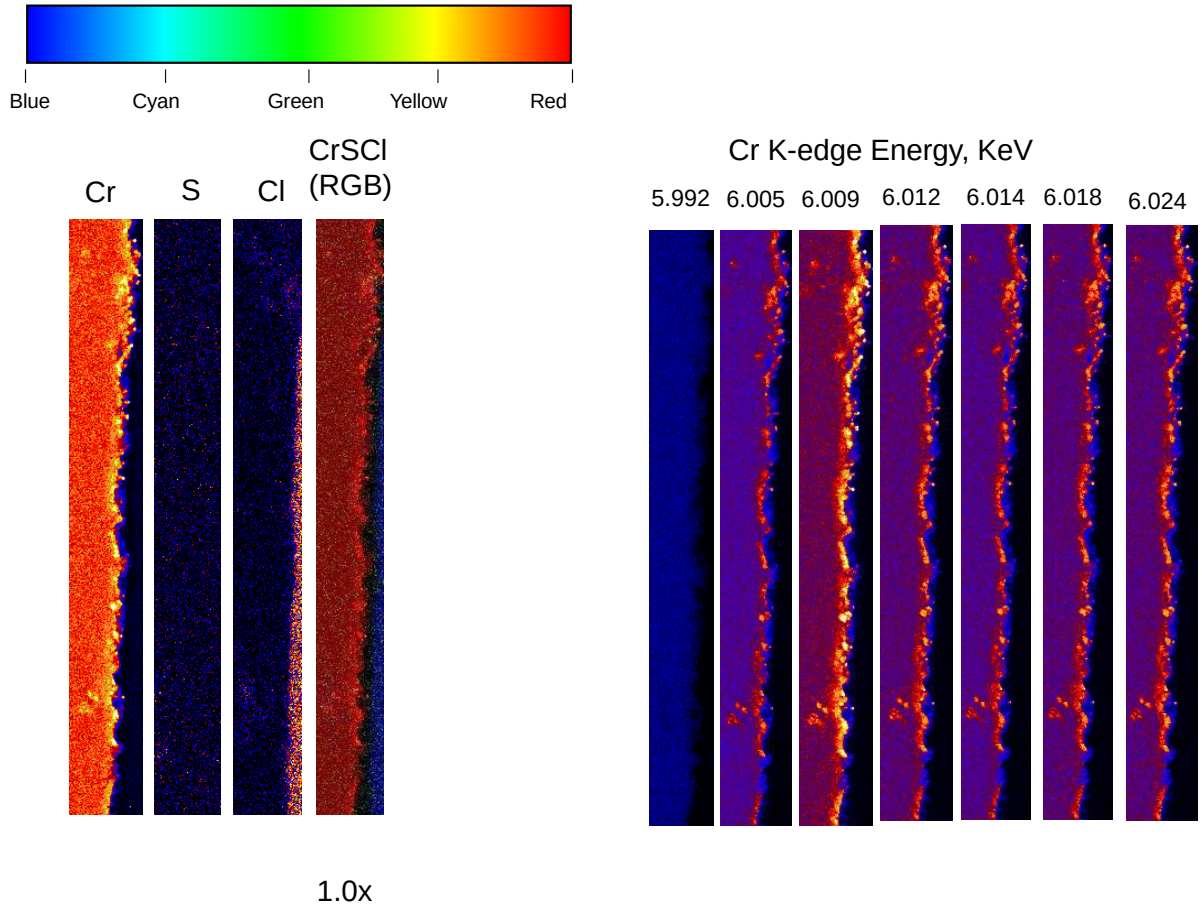

Figure 8.6 RGB mapping for Cr on the 12Cr1MoV interface and its energy distribution, characterized by synchrotron XFM and μ-XAFES

Figure 8.7 shows the μ-XAFES analysis results for a number of spots that are of interest. Apart from position (0) refers to the bulk tube that is predominantly made up of metallic iron (Fe) and chromium (Cr). Cr in the other positions with a color rather than red consists of three major species, Cr metal, chromium carbide (Cr_3Cr_2) and ferrite $FeCr_2O_4$. The fractions of the last two species vary greatly with the position. For position 1 that refers to a detect inside the tube, its carbide fraction is almost the highest, supporting a preferential inward diffusion of $C_{(g)}$ inside the tube. The $C_{(g)}$ should be derived from CO_2 in the flue gas. Following position 1, position 3 close to the position 1 also has a very high carbide fraction, which further confirms the dissociation of CO_2 to form C(g) that can diffuse quickly inside the 12Cr1MoV tube. For the other positions that are located on the yellow/blue stripes/interface, ferrite is most abundant, suggestive of a preferential oxidation of Cr on the outer surface of this tube. A portion of the active oxygen used for the oxidation of Cr should also be derived from the dissociation of CO_2,

which simultaneously produced C(g) that can diffuse through the outer oxide layer inside the tube.

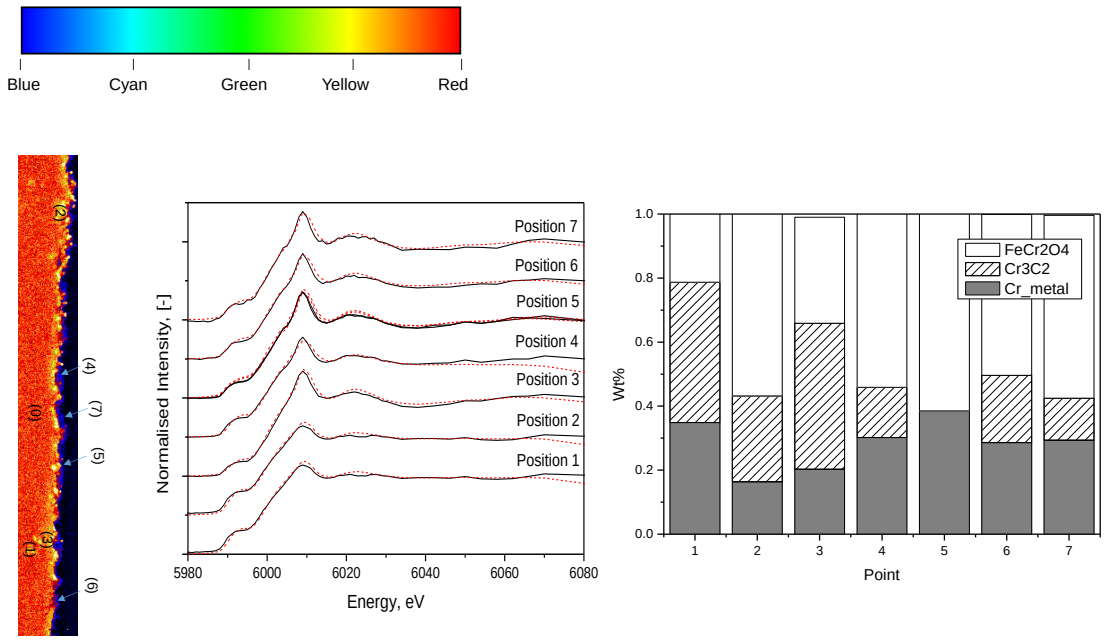

Figure 8.7 XANES spectra for Cr on the interface of 12Cr1MoV, characterized by synchrotron XFM and μ-XAFES

Figure 8.8 shows the elemental distribution for T91 that was exposed to oxy-fuel flue gas only. As expected, the interface with the enrichment of Fe and other elements is very thin, due to the protective effect of Cr that has an average content of 9.1 wt% in the bulk tube. The close-up observation, by five times, indicates the enrichment of Cr on the interface, which even has a multi-layer distribution across the interface. Compared to the bulk tube that is in yellow, a relatively thick layer in orange color was attached to the bulk tube. On top of the orange stripe is the thin red layer and then blue layer. Compared to Cr, Fe in the interface has a weak signal, with only a few of discrete red spots and a very thin blue gas formed on the tube top. Additionally, compared to the other additives from Mn, Co, V and Ti, Cr is most protective.

FGB mapping for Cr-S-Cl and energy distribution of Cr on the tube T91 interface were further analysed, and shown in ***Figures 8.9***, ***8.10, 8.11 and 8.12***. Here again, one can see a little interaction between Cr and S/Cl to form the respective sulfide/chloride on the interface of tube T91. This may be due to a short exposure time employed in this study. For the μ-XANES analysis results shown in ***Figures 8.10***, one can see the predominance of Cr metal in position

1 which refers to the bulk tube. For the positions 2-4 located on the interface, again, carbide is abundant, followed by ferrite or chromium hydroxide. Clearly, compared to the tube 12Cr1MoV, the tube T91 surface is rich carbide. The results in ***Figures 8.11*** and ***8.12*** are for another portion of the tube T91 which is slightly more corroded compared to the portion analysed in ***Figures 8.9*** and ***8.10***. For the portion in ***Figure 8.11***, it has more internal detects which may be a strong indicator of the inward diffusion of corrosive gases. For the Cr K-edge μ-XANES results depicted in ***Figure 8.12***, the first three positions referring to bulk tube and internal detects are rich in carbide, same as that has been confirmed for another tube 12Cr1MoV. Moreover, compared to the internal detects, the medium interface (in orange) including the positions numbered from 4 through to 6 is rich in ferrite and even chloride found in position No 4. More interestingly, for the position No 7 referring to the most outer layer in blue, chromium metal is most dominant, indicating the reduction of the oxidized Cr layer back to Cr metal, which could be due to the reduction effect of some gas components or their derivatives such as hydrogen or carbon that can derived from the dissociation of steam and CO_2, respectively.

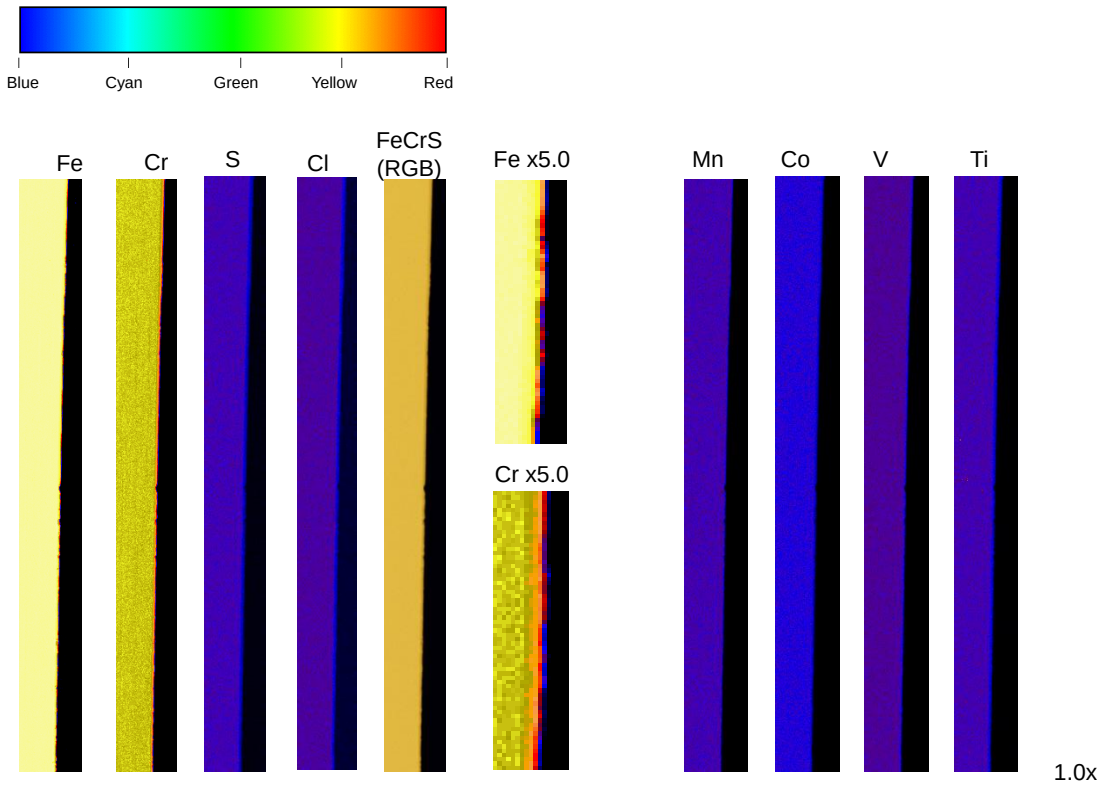

Figure 8.8 Elemental distribution on the corroded tube T91 interface, characterized by synchrotron XFM

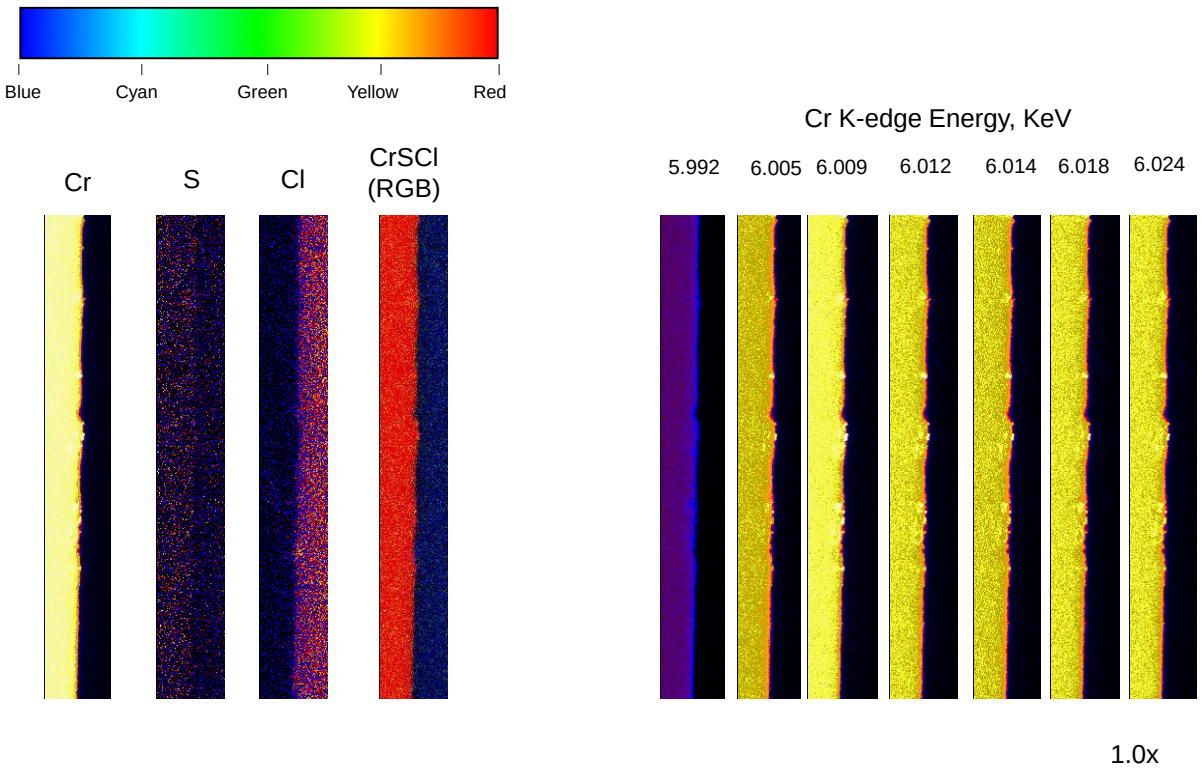

Figure 8.9 RGB mapping for Cr on the T91 interface and its energy distribution, characterized by synchrotron XFM and μ-XAFES

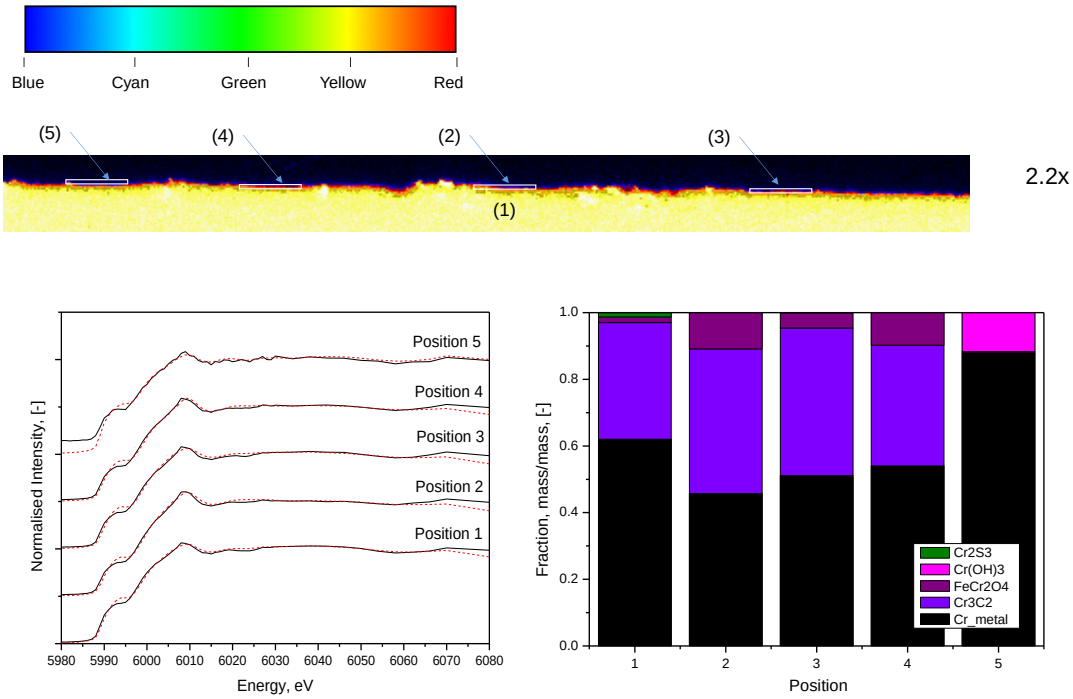

Figure 8.10 XANES spectra for Cr on the interface of tube T91, characterized by synchrotron XFM and μ-XAFES

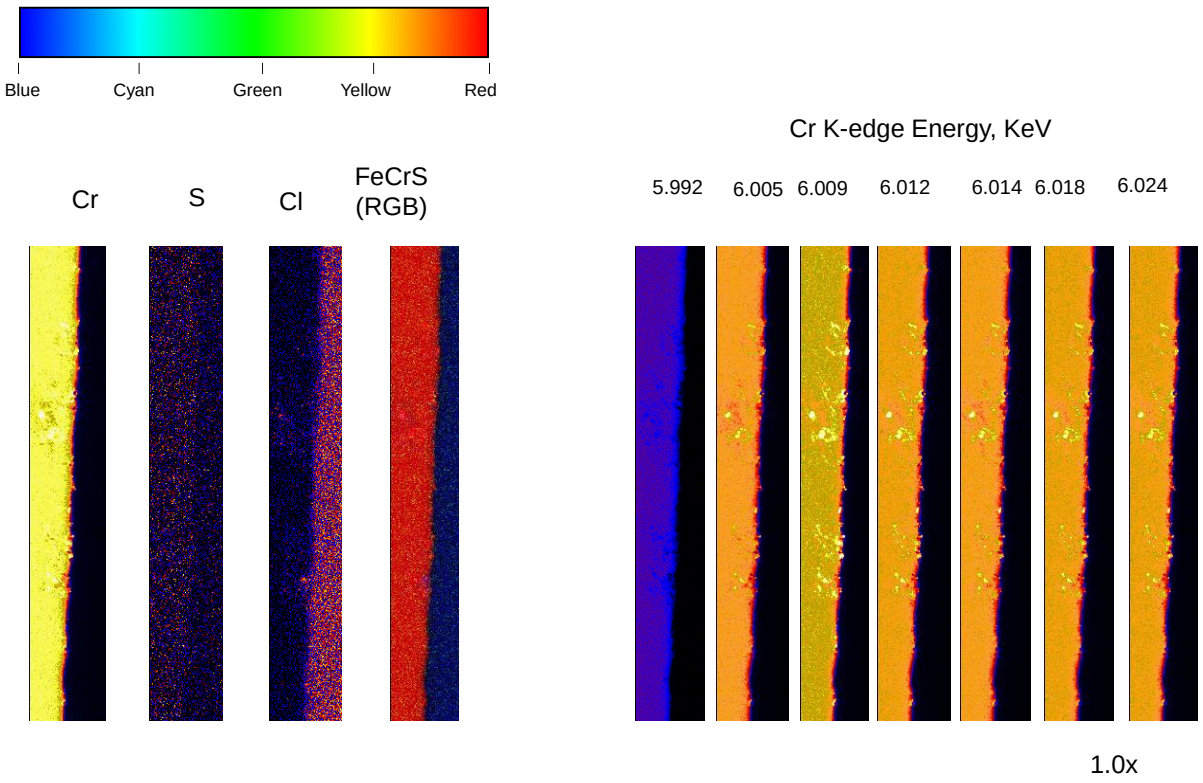

Figure 8.11 RGB mapping for Cr on the T91 interface and its energy distribution, characterized by synchrotron XFM and μ-XAFES

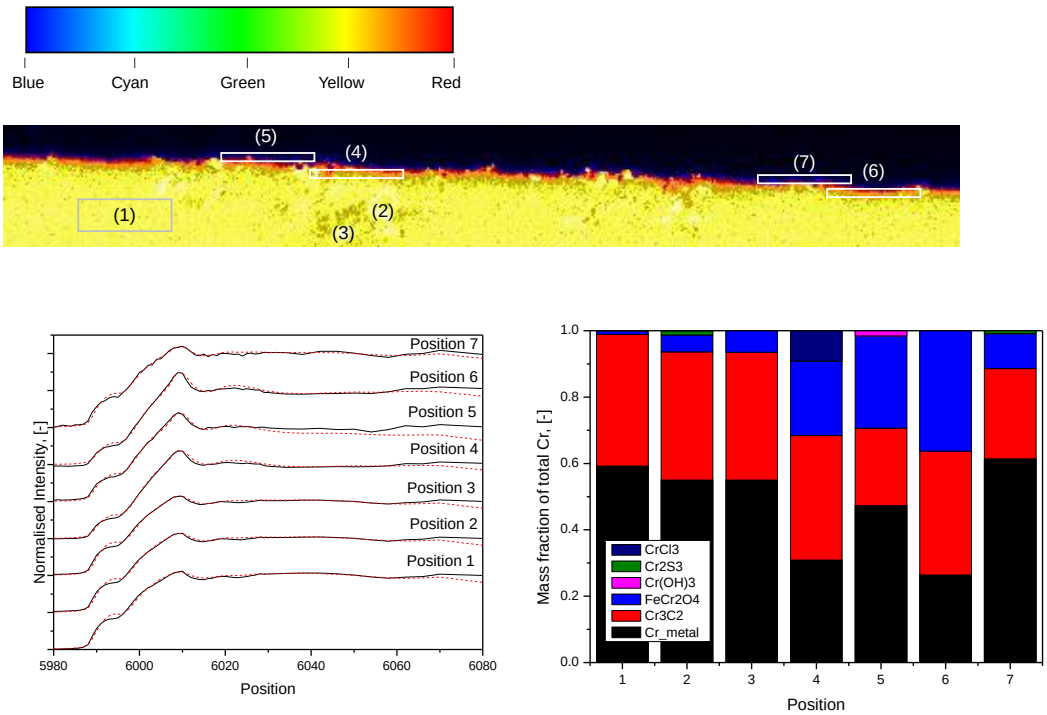

Figure 8.12 XANES spectra for Cr on the interface of tube T91, characterized by synchrotron XFM and μ-XAFES

Figure 8.13 shows the elemental distribution mapping for the interface of the tube SUS304 containing 18 wt% Cr. As expected, the interface formed is much thinner for this tube, due to the strong protection effect of Cr. Apart from Cr, Mn, Ti and trivial Cr are also slightly enriched on the top interface, proving their strong protective effect. The close-up observations of both Fe and Cr on the interface, as inserted in the middle of ***Figure 8.13***, further suggests a multi-layer distribution as that has been confirmed for the tube T91.

The RGB mapping for Cr-S-Cl and the energy distribution of Cr K-edge XANES fingerprints are further shown in ***Figures 8.14, 8.15, 8.16*** and ***8.17.*** Same as on the other two tubes, Cr in the tube SUS304 showed little correlation with S and Cl, implying the formation of few sulfide/sulfate/chloride. More interestingly, for the Cr K-edge energy distribution, the energy of 6.005 eV referring to the shoulder of Cr metal is most abundant. This is an indicator of the lowest oxidation rate for Cr in this tube. The μ-XANES analysis results in ***Figure 8.14*** proved this. As can be seen, the position 1 close to the interface is fully made up of pure chromium metal. For the interface layer referring to position 2 mostly in orange color, both ferrite and carbide appeared. However, for the slightly spalled pieces including No 3 and No 5, the carbide disappeared. Instead, ferrite is dominant and it is followed by hydroxide. For the discrete small pieces that should be formed from the spallation of tube surfaces, including No 4, No 6 and No 7. Again, one can see the predominance of Cr metal that should be formed from the re-reduction of the oxidised tube surfaces, by the reducing gas or derivatives including hydrogen and carbon.

Another portion of the tube SUS304 interface is further shown in ***Figure 8.16*** for the RGB mapping and Cr K-edge energy distribution. ***Figure 8.17*** depicts the respective XANES spectra and fitting results. With regarding the XANES fitting results, it is further confirmed that the bulk tube (position No 1) is less oxidised due to the strong protection role of the abundant Cr in this tube. For the other positions from No 2 through to No 5, they refer to the interface formed that are mainly in orange color. Clearly, both carbide and ferrite were formed. For the discrete spot No 6, it is slightly rich in Cr metal while lean in carbide.

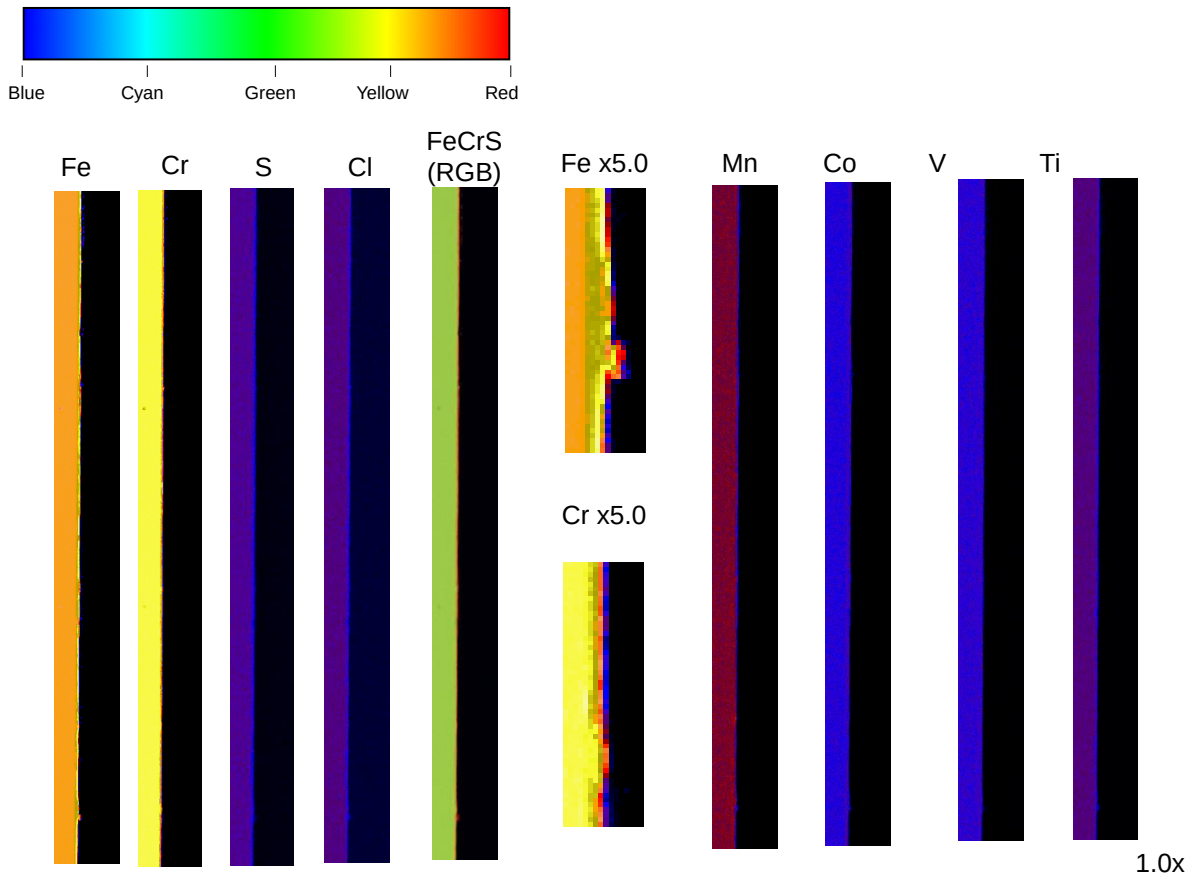

Figure 8.13 Elemental distribution on the corroded tube SUS304 interface, characterized by synchrotron XFM

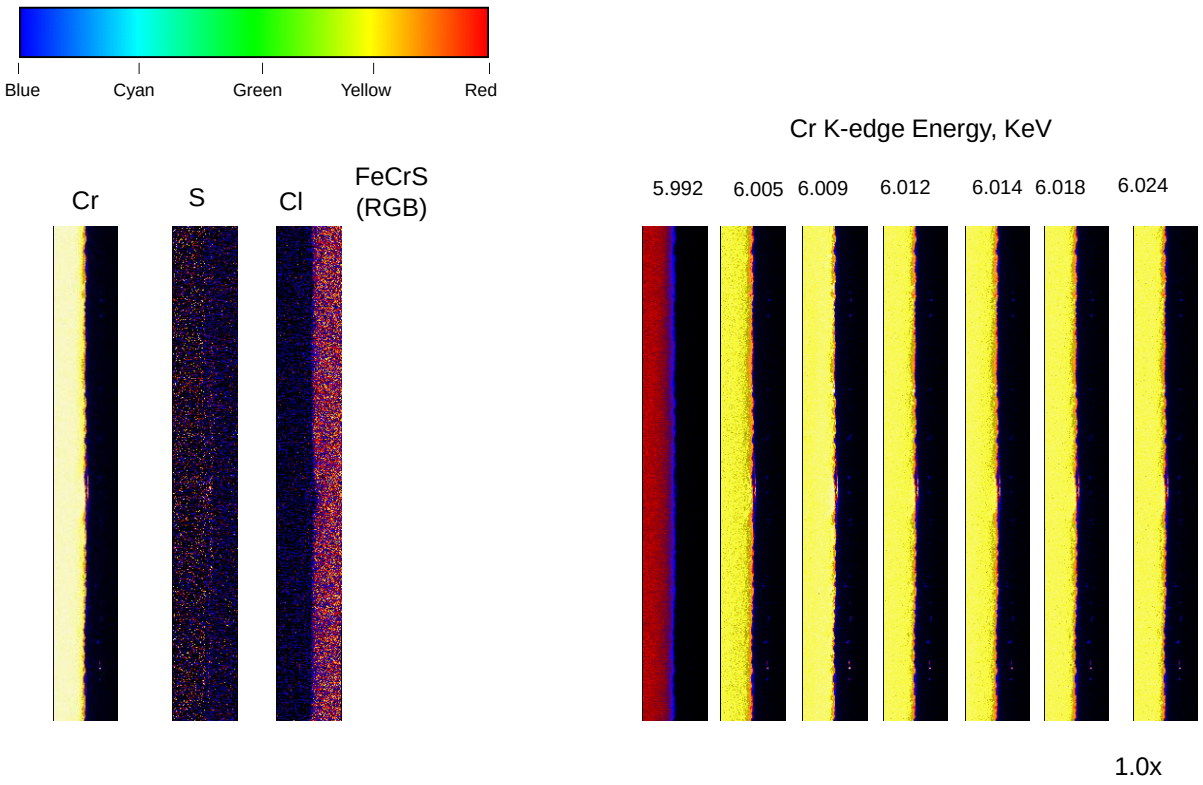

Figure 8.14 RGB mapping for Cr on the tube SUS304 interface and its energy distribution, characterized by synchrotron XFM and μ-XAFES

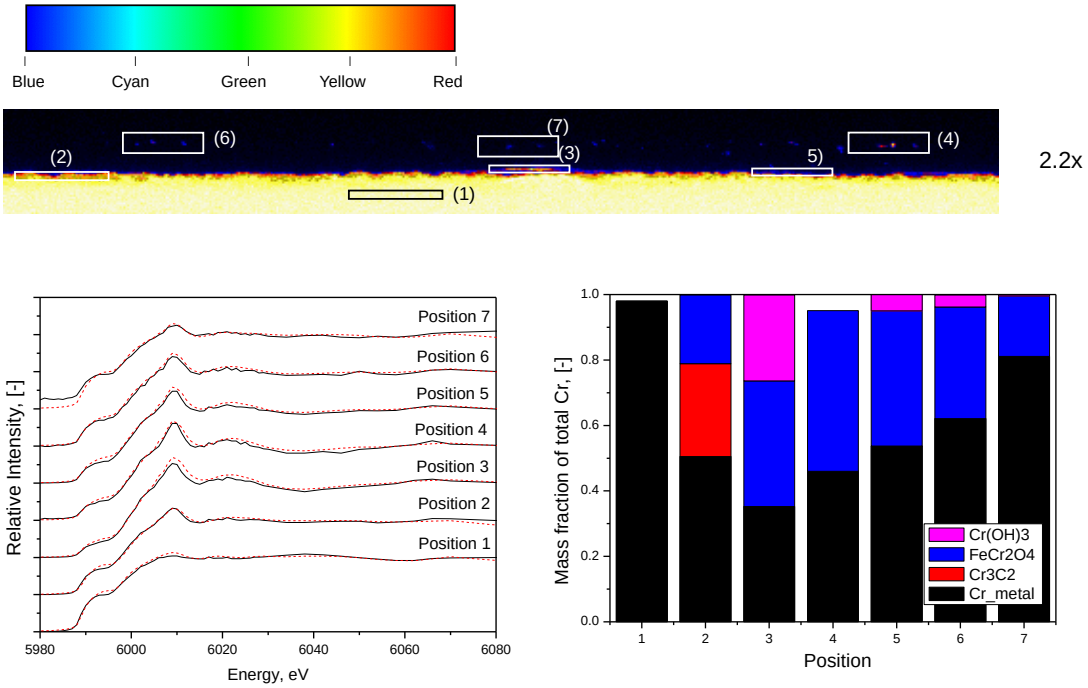

Figure 8.15 XANES spectra for Cr on the interface of tube SUS304, characterized by synchrotron XFM and μ-XAFES

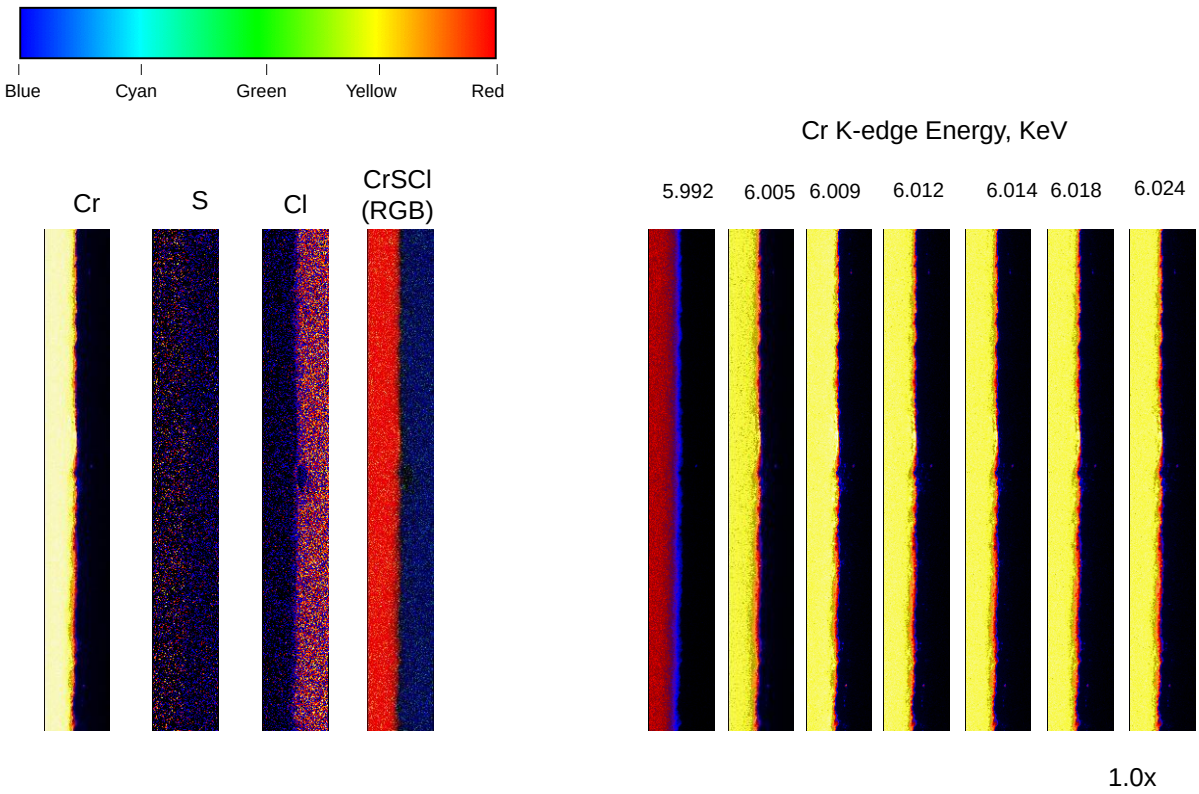

Figure 8.16 RGB mapping for Cr on the SUS304 interface and its energy distribution, characterized by synchrotron XFM and μ-XAFES

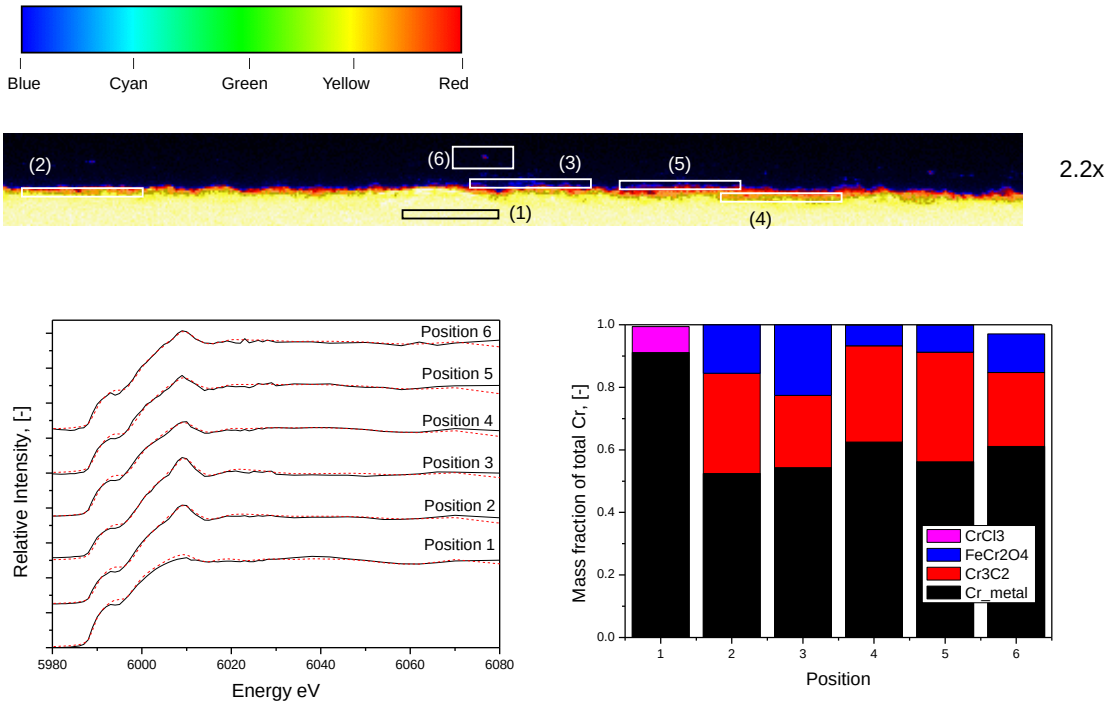

Figure 8.17 XANES spectra for Cr on the interface of tube SUS304, characterized by synchrotron XFM and μ-XAFES

8.1.3 Comparison between three tubes exposed to oxy-fuel flue gas

The discrepancy between three above-mentioned tubes exposed to oxy-fuel flue gas only was further summarized here. First of all, the interface of the three tubes and the Cr K-edge μ-XANES results are depicted in ***Figure 8.18***.

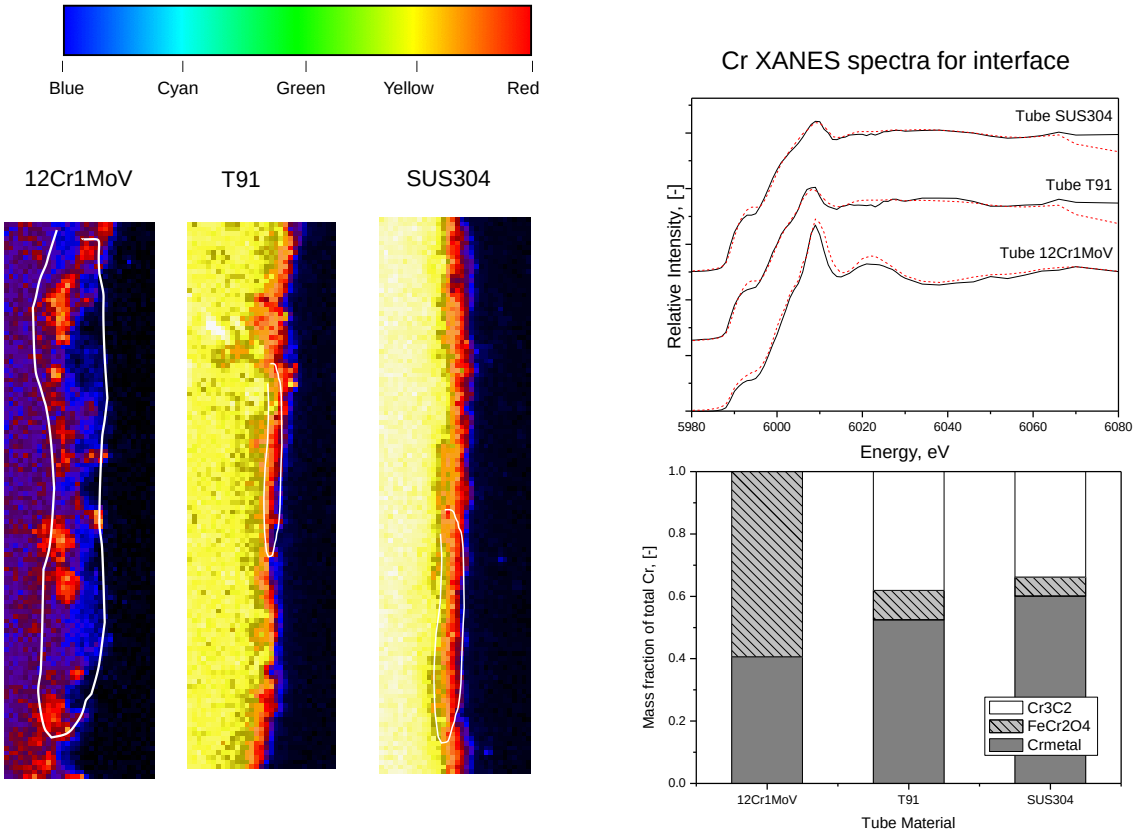

Figure 8.18 Interfaces of the three tubes exposed to oxy-fuel flue gas only, and the respective Cr K-edge μ-XANES spectra and fitting results

To reiterate, the tube 12Cr1MoV was heavily corroded, thereby forming the thickest interface that is mainly composed of two colors, red and blue. The red color referring to the maximum Cr content is a direct sign of the outward diffusion and thus enrichment of Cr on the tube surface, whereas the blue color, on the most outer layer suggests the enrichment of another element that should be oxygen, as suggested by the precious Cr K-edge μ-XANES results such as ***Figures 8.18***.

The Cr K-edge μ-XANES results on the right bottom of ***Figure 8.18*** further confirm the remarkable difference between the three tubes, in terms of the Cr speciation on the interface. As can be seen, ferrite is the principal Cr-bearing species on the 12Cr1MoV tube interface. However, for the interface of the other two tubes, carbide is more dominant than ferrite.

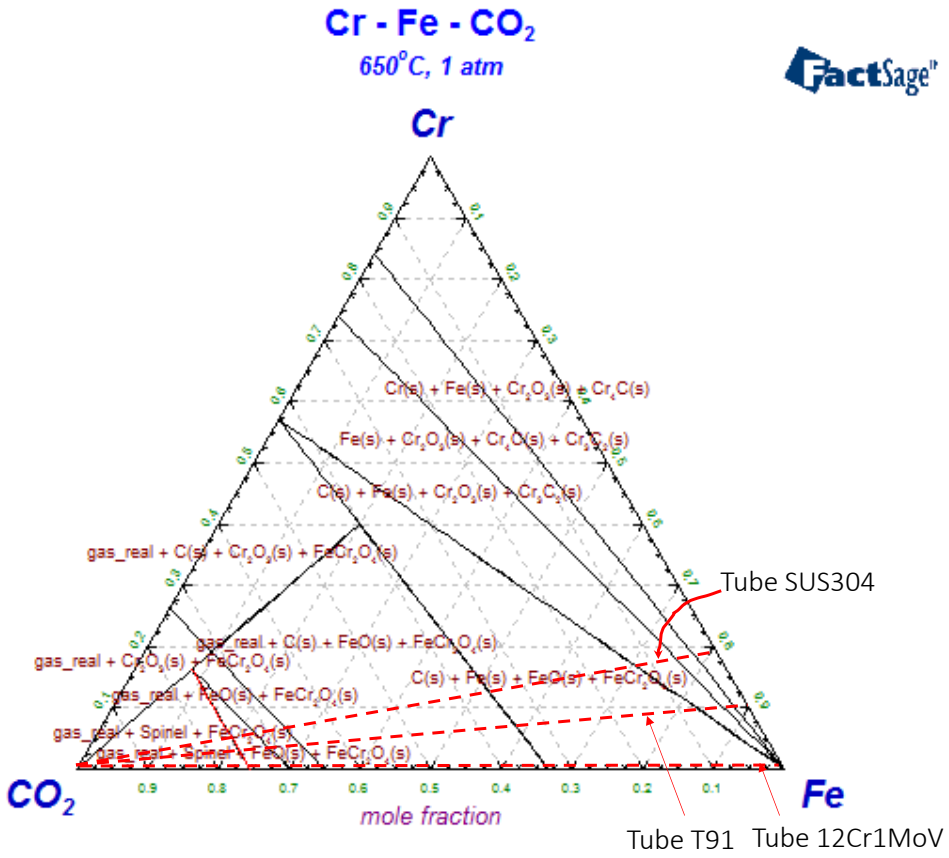

Figure 8.19 Cr-Fe-CO_2 phase diagram at 650°C and 1 atm

Phase diagram of Cr-Fe-CO_2 in ***Figure 8.19*** proves the preferential formation of ferrite (FeCr2O4) for the tube 12Cr1MoV that is close to the Fe-CO_2 line. With the increase on the Cr content, i.e. use of the tubes T91 and SUS304, the formation of Cr_3C_2 is favored under the extremely low pressure of CO_2. The low-pressure CO_2 could be formed under the interface layer where the diffusion of any gas component should be extremely slow. This explained why carbide is abundant on the medium-layer that is in orange color in above figures. Upon the increase of the CO_2 partial pressure, i.e. close to bulk flue gas, the formation of Chromium

oxide (Cr_2O_3) and ferrite are preferred, irrespective of tube material type. Additionally, the solid carbon could also be formed, which apparently has the potential to react with chromium oxide to reduce it back into metallic chromium, as evident in the previous Cr K-edge μ-XANES results.

Although the results in ***Figure 8.19*** have demonstrated the discrepancy between the interfaces of the three tubes in terms of average Cr speciation, one has to bear in the mind that, for each tube exposed to flue gas, there are generally multiple layers formed as interface on the tube surface, as has been evidence in the previous XFM mapping results. Apart from the thickness for individual layers, the Cr speciation in each layer was also found to vary broadly between the three tubes. In light of this, the Cr K-edge μ-XANES results observed for the multiple layers on each tube interface were further summarized qualitatively in ***Table 8.1*** below.

Table 8.1 Qualitative summary of the Cr speciation on the tube interface and its multiple layers

		Average	Outer layer (blue)	Medium layer (orange)	Inside Detects
12Cr1MoV	1st abundant	Ferrite	Ferrite	Cr3C2~ Ferrite	Cr3C2
	2nd abundant	Cr metal	Cr metal		Cr metal
	3rd abundant		Cr3C2	Cr metal	Ferrite
	Trivial				
T91	1st abundant	Cr metal	Cr metal	Cr metal ~Cr3C2	Cr metal
	2nd abundant	Cr3C2	Cr3C2	Ferrite	Cr3C2
	3rd abundant	Ferrite	Ferrite		
	Trivial				Ferrite
SUS304	1st abundant	Cr metal	Cr metal	Cr metal	Cr metal
	2nd abundant	Cr3C2	Cr3C2	Cr3C2	Cr3C2
	3rd abundant	Ferrite	Ferrite	Ferrite	
	Trivial				Ferrite

Clearly, apart from the average, the Cr speciation in individual layers is also broadly different between the three tubes. For the most outer layer that is in blue in the XFM map, ferrite is most abundant on the 12Cr1MoV tube, suggestive of a remarkable oxidation of both Fe and Cr for this tube. This should be due to the least content of Cr within it, which is thus less protective. With respect to the most outer layer for the other two tubes, it is clear that less of it was oxidised

or carburized, thereby still having the un-reacted Cr metal as the principal Cr-bearing compound on the most outer layer. With respect to the medium layer in orange color, it is clear that carbide and ferrite are both predominant on 12Cr1MoV and T91 tubes. However, the un-reacted Cr metal still dominates for the tube SUS304. This further confirms the strong protective effect of Cr, in particular when its content is larger than 9 *wt%* in the original bulk tube. For the discrete detects found inside the bulk tube, the protective effect of Cr for the two tubes T91 and SUS304 is more pronounced. The abundance of Cr_3C_2 carbide for the discrete detects found inside the 12Cr1MoV tube should be due to the fast diffusion of carbon inside this tube, the top surface of which was significantly spalled due to the oxidation corrosion, as evident in ***Figures 8.2*** and ***8.3***.

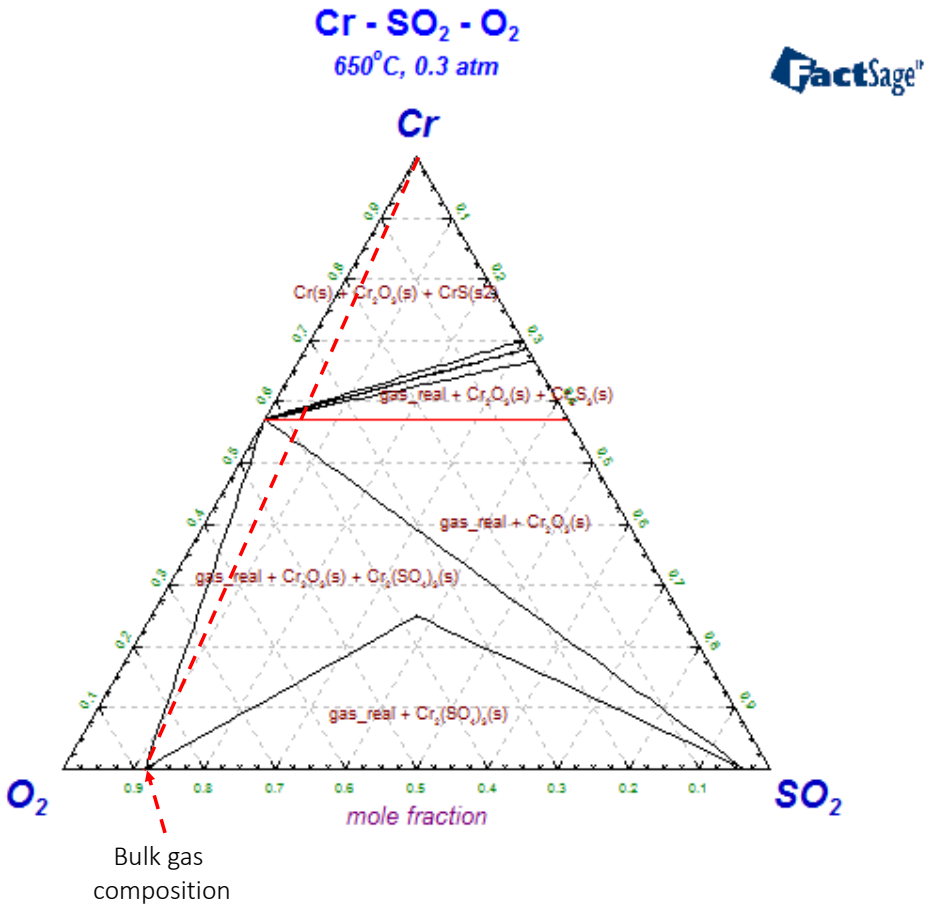

Figure 8.20 Cr-SO_2-O_2 phase diagram at 650°C and 1 atm

Efforts were further made to understand the thermodynamics governing the co-existence of Cr with gaseous SO_2 and O_2. As shown in the Cr-SO_2-O_2 phase diagram in ***Figure 8.20***, the bottom

end of the dashed line refers to the bulk SO_2/O_2 ratio in the flue gas. The formation of both sulfate and sulfide are thermionically favored under the exposure conditions tested in this study. However, the formation of Cr sulphate is only possible in the case that the molar ratio of Cr to (SO_2+O_2) is less than 55%. This could be the case for the top outer layer in blue color in the XFM map. However, such a species was not detected. This suggests a preferred sulphation of iron over chromium on the most outer layer of the tube. Regarding the preference zone for the formation of chromium sulfide, it refers to a larger Cr to (SO_2+O_2) molar than 0.55 for the Cr-rich zones that should include the medium and inside discrete detects observed on the XFM map. However, such a species is trivial and mostly non-detectable by the Cr K-edge μ-XANES analysis. This should also be due to the preferential sulfidation of Fe over Cr inside the tube.

8.2 Co-Existence Ash Deposits and Oxy-Firing Flue Gas

8. 2.1 Cr K-edge XANES analysis of the top surface

Analysis was first conducted on the top surface of individual corroded tubes that were coated either with Hazelwood fly ash or Yallourn fly ash. The resultant XANES spectra and fitting results are shown in ***Figures 8.21*** and ***8.22,*** and ***Table 8.2***, respectively. In terms of Cr speciation, the difference between these two fly ash samples is clearly insignificant.

Statistical analysis was further conducted to quantify the thickness of the corrosion interface for each corroded tube. Based on the interface depth, the corrosion rate or interface growth rate was further calculated by dividing by the exposure time, 50 *hr* employed in this study. As depicted in ***Figure 8.23***, the Cr content in tube material is in reverse proportion to the growth rate, irrespective of fly ash type. For the tube T23 alloyed steel exposed to (HW) fly ash with the lowest Cr content, it was found to have the highest oxide thickness that is consistent with the literature. The effect of fly ash type is marginal, given the fact that the experimental error is relatively large. In addition, the growth rate 0.2-1 *μm/h* found here is broadly consistent with the literature report on the tested alloy tubes with the similar Cr contents [13]. The flue gas-related corrosion rate is comparable to that caused by fly ash only, 0.1-0.45 *μm/h*, further implying the enhanced corrosion upon the exposure of tube to both fly ash and flue gas. The two fly ashes are also different in the corrosiveness. Compared to HW ash, YL also is slightly more corrosive, probably due to the relative abundance of sodium oxide within it.

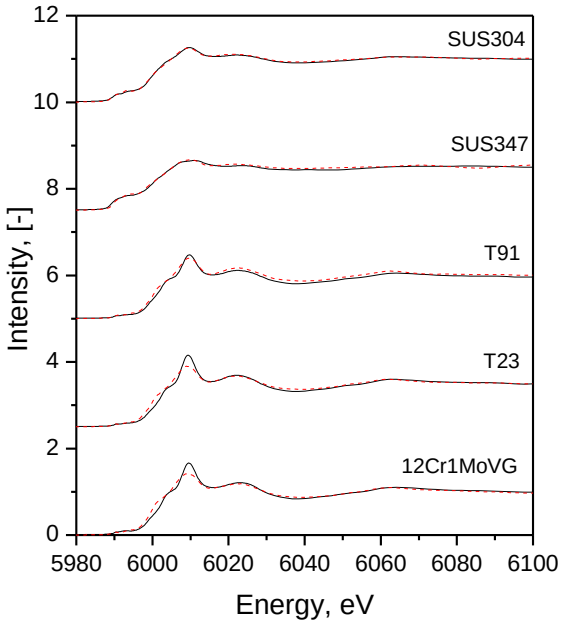

Figure 8.21 Cr K-edge XANES spectra for five different tubes coated with Hazelwood fly ash

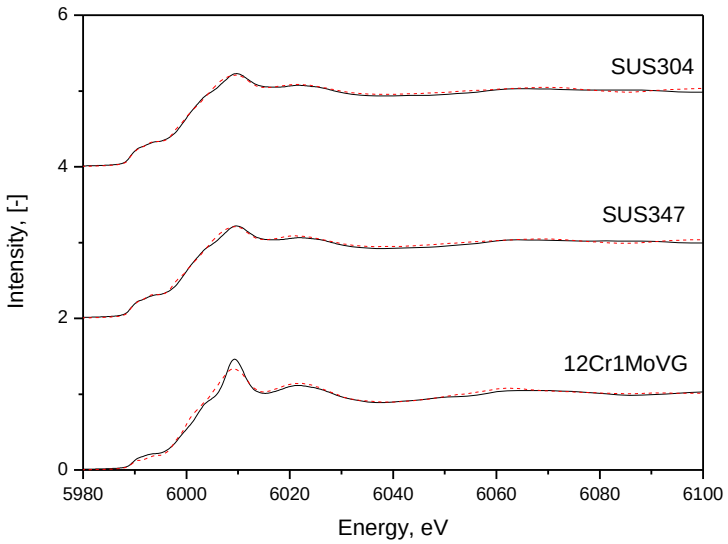

Figure 8.22 Cr K-edge XANES spectra for five different tubes coated with Hazelwood fly ash

Table 8.2 Quantified Cr-bearing species on the top surface of the tubes coated with two Victorian brown coal fly ash collected from their oxy-fuel combustion in pilot-scale furnace

		Cr metal	Cr2O3	Ferrite
Hazelwood fly ash	12Cr1MoV	0.155	0.25	0.595
	T23	0.175	0.28	0.545
	T91	0.25	0.35	0.4
	SUS347	0.538	0.164	0.298
	SUS304	0.301	0.416	0.283
Yallourn fly ash	12Cr1MoV	0.177	0	0.823
	SUS347	0.413	0	0.072
	SUS304	0.449	0.091	0.076

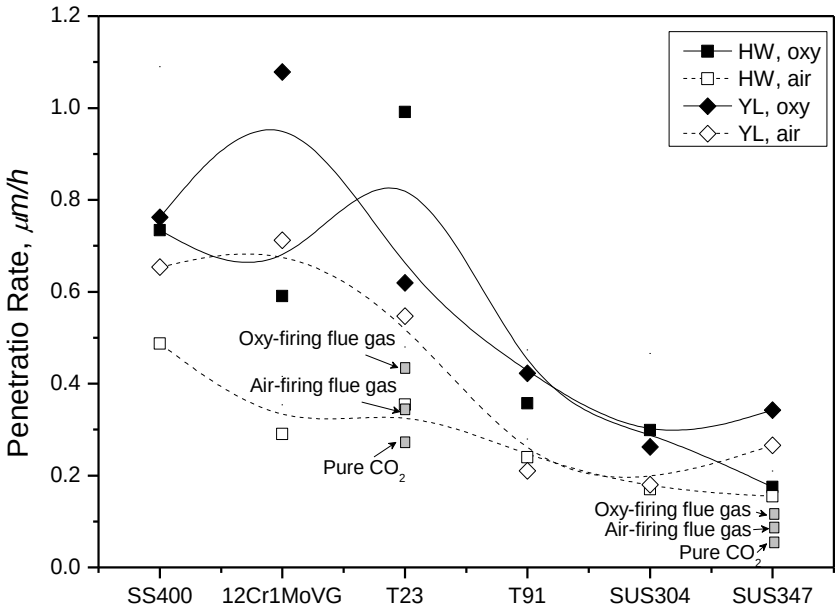

Figure 8.23 Penetration rate of different tubes, calculated based on OM analysis

8.2.2 SEM-EDX observation of the corroded tube SUS347 surface, coated with Yallourn fly ash

Efforts were made to observe the micro-structures of the tube SUS347 that was coated with Yallourn fly ash, under the exposure to both air-firing flue gas and oxy-fuel flue gas. ***Figure 8.24 and 8.25*** illustrate the typical interface that was formed under the air-firing flue gas.

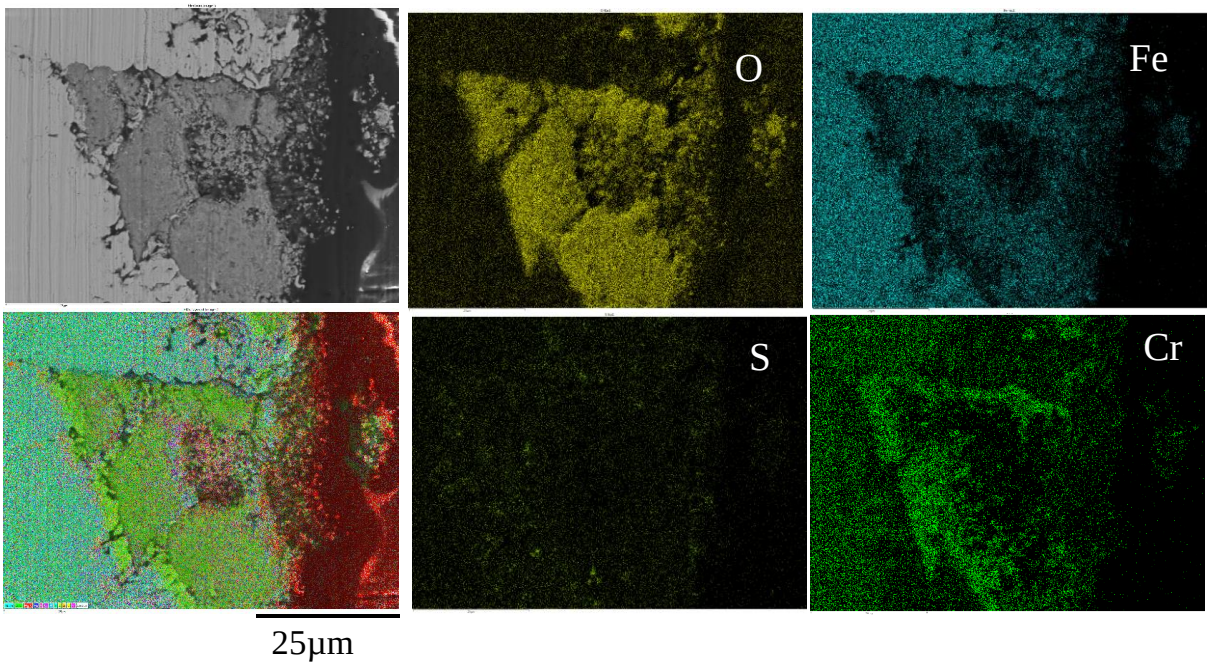

Figure 8.24 SEM microstructure of the tube SUS347 coated with Yallourn ash deposit, under air-firing mode

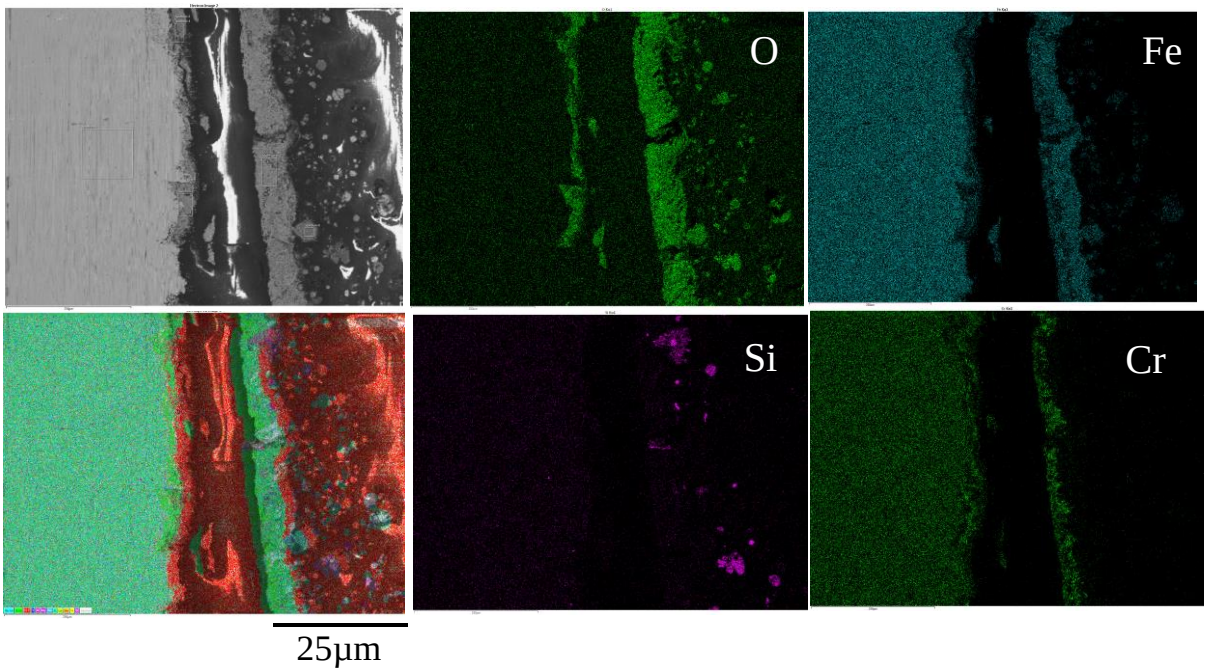

Figure 8.25 SEM microstructure of the tube SUS347 coated with Yallourn ash deposit, under air-firing mode

As can be seen in ***Figure 8.24***, oxygen is the principal element that penetrated inside the tube, whereas Cr was highly correlated with oxygen, implying the preferential formation of chromium oxide to protect the tube surface. Here again, the penetration of sulphur is trivial compared to oxygen. The similar observation can be concluded from ***Figure 8.25***. In addition, ***Figure 8.25*** shows that Si is also protective and forms a thin layer on the top of the Cr-rich layer. Moreover, the spallation of Fe is obvious, resulting in a thin Fe-rich layer which is even on the top of the Cr-rich layer, suggestive of a faster outward diffusion of Fe than Cr upon the Yallourn ash attack.

SEM observation was further made for the same tube SUS347 coated with Yallourn ash deposit, and exposed under the oxy-fuel combustion condition. As evident in ***Figure 8.26***, the tube surface is heavily corroded, caused by the deep penetration of both oxygen and sulphur deep inside the tube. As a counter current, both Fe and Cr diffused outwardly and eventually spalled off.

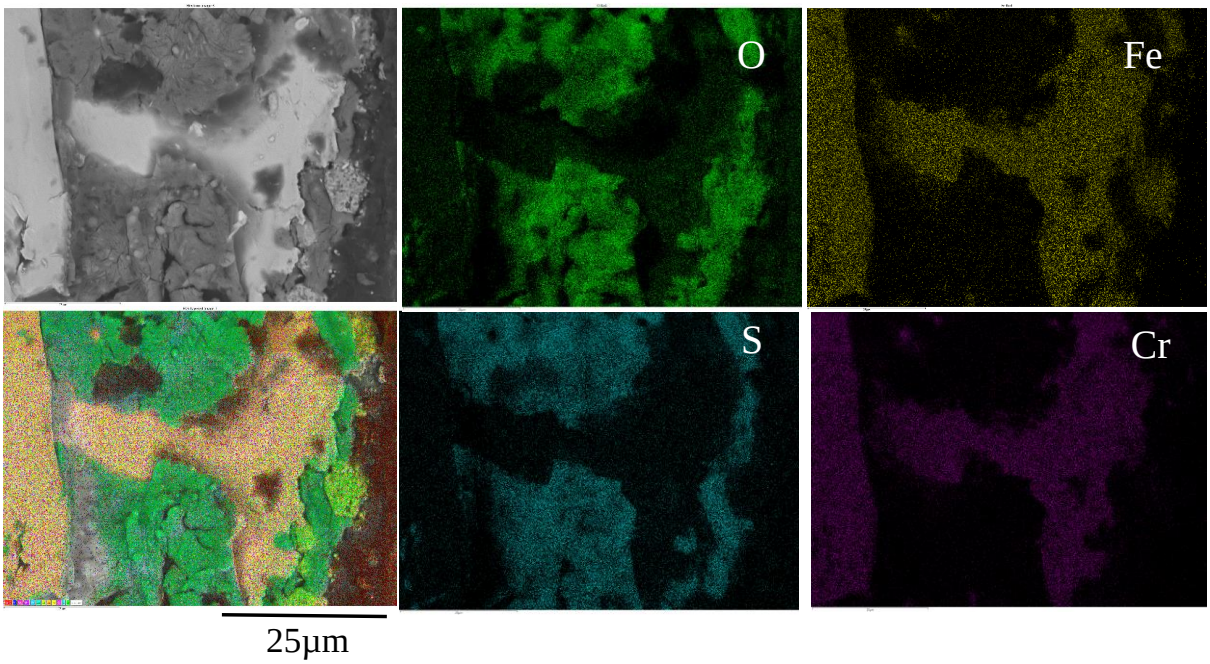

Figure 8.26 SEM microstructure of the tube SUS347 coated with Yallourn ash deposit, under oxy-firing mode

8.3 Synchrotron XFM and μ-XANES analysis of tube interface

The tube T23 was first analysed by the synchrotron XFM. Here again, the tube was coated with Yallourn ash deposit and was exposed in the oxy-fuel flue gas for 50 hrs. As shown in ***Figure 8.27***, because of the corrosive environment, this low-Cr tube surface has been heavily corroded, with the formation of spalled layers that are detached from the bulk tube. The elemental mapping results suggest the formation of different layers on the bulk tube, with the enrichment of different elements in different layers.

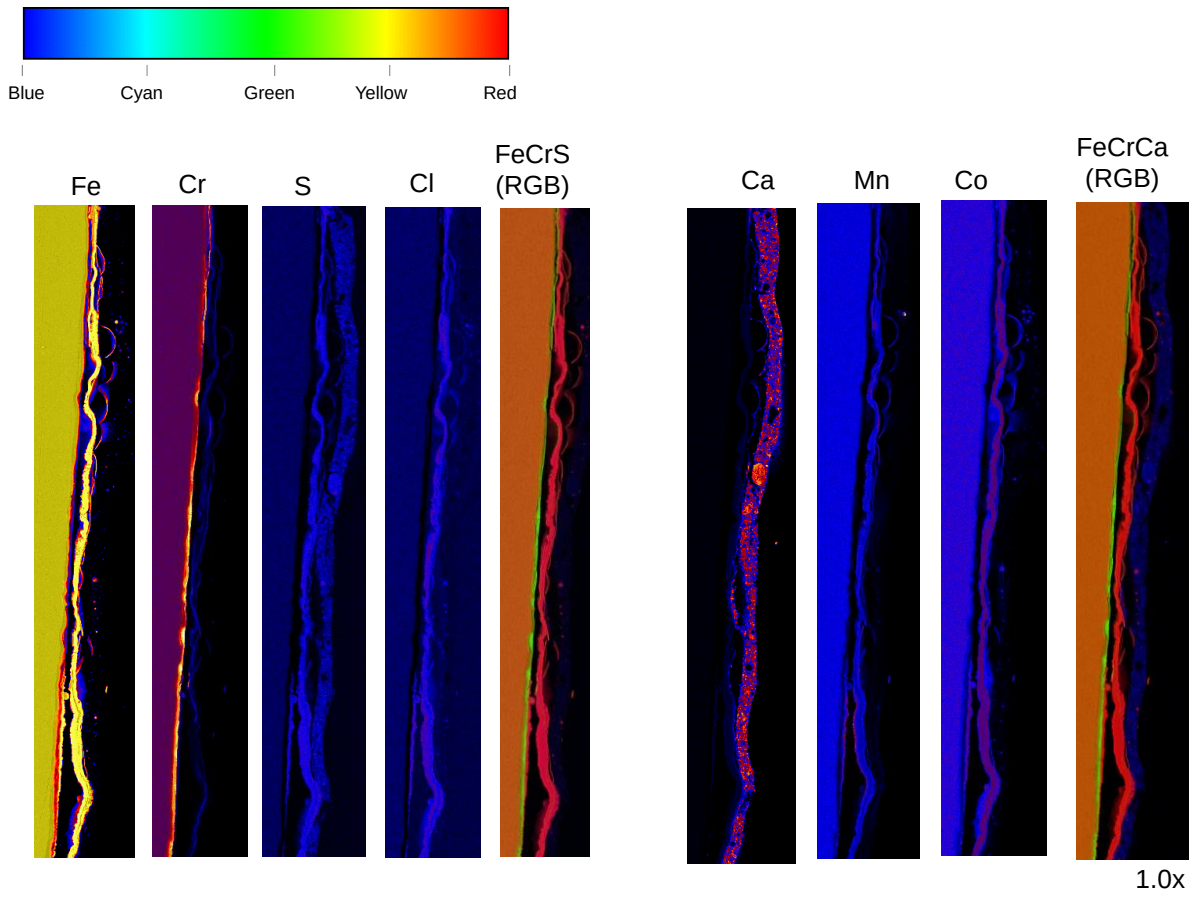

Figure 8.27 Elemental distribution on the corroded tube T23 interface, coated with Yallourn ash deposit, and characterized by synchrotron XFM

Fe is rich in the spalled layer, and correlated well with S and Cl in the spalled layer. A few of Fe was also heavily fragmented into small pieces (in arch shape) that extruded into the ash layer. Instead, Cr formed a thin layer that is still attached on the bulk tube, with a portion of Cr that co-exists with Fe in the spalled layer as well. With respect to the penetration of S, it is clearly insignificant. The RGB mapping for Fe-Cr-S can prove this. With respect to the penetration of Cl, one can see the presence of weak Cl signal (in red) at the bottom of the spalled layer, suggestive of the diffusion of this corrosive gas between the spalled layer and the Cr-rich protective layer on the bulk tube. In other words, the penetration of Cl inside the bulk tube has been effectively prevented by the Cr-layer.

The presence of other elements from Ca through to Co is also noteworthy. Ca is from the Yallourn ash deposit. The Fe-Cr-Ca RGB mapping, as shown on the most right hand, suggests little overlapping between these three elements. The other elements Mn and Co are also corroded. In particular Co is partially enriched in the spalled layer, suggestive of its heavy oxidation and spallation from the bulk tube.

The close-up Cr-S-Ca RGB mapping and μ-XANES analysis, as demonstrated in ***Figure 8.28***, further indicate a weak correlation between these three elements. With respect to the speciation of Cr, its energy distribution on the right hand side of ***Figure 8.28*** indicates that the energy of 6.009 KeV referring to the principal peak for oxide/ferrite is most prevent, which is followed by a strong energy distribution at 6.005 KeV for the shoulder of metallic Cr. ***Figure 8.29*** for the Cr K-edge XANES spectra for different positions indicate the broad variation of the Cr speciation. Compared to the bulk tube that is dominated by Cr metal, the fraction of ferrite is more pronounced in the interface and the spalled layer.

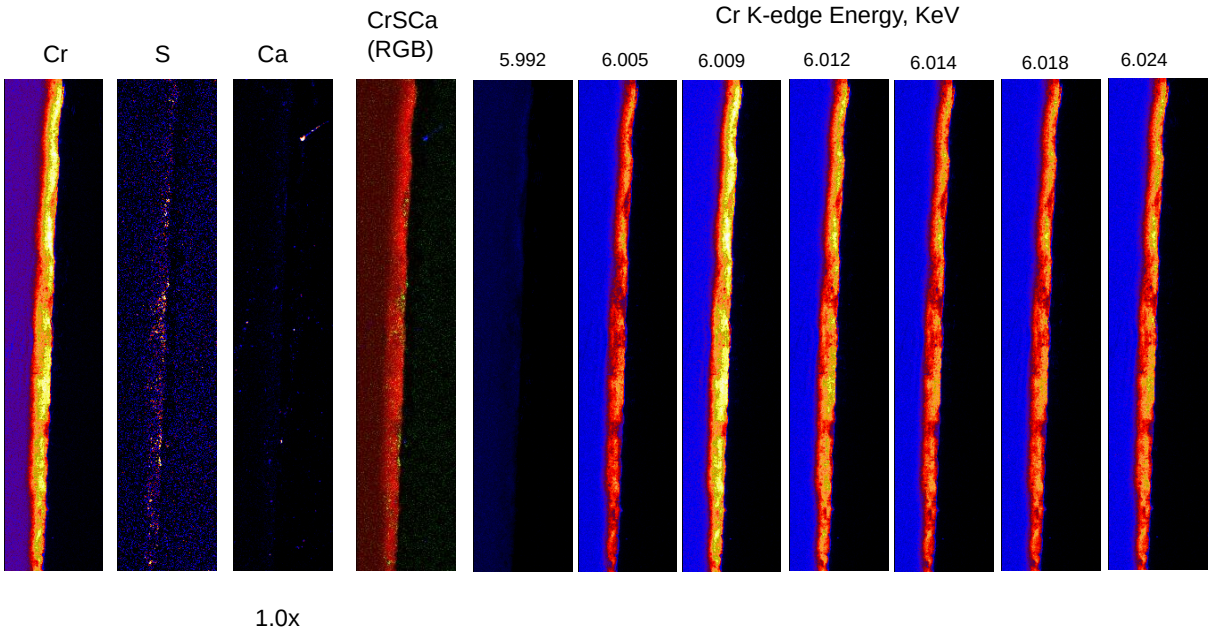

Figure 8.28 RGB mapping for Cr on the tube T23 interface and its energy distribution, characterized by synchrotron XFM and μ-XAFES

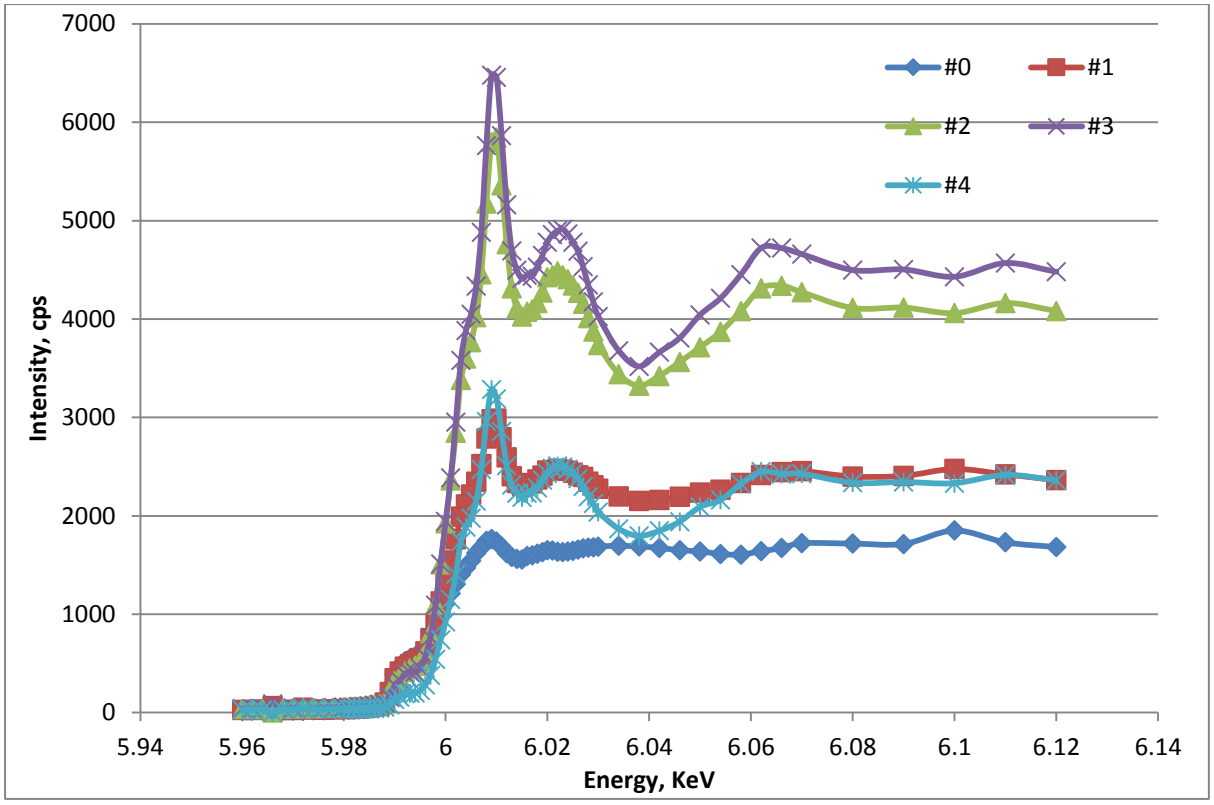

Figure 8.29 Interfaces of the tube T23 coated with Yallourn ash deposit and exposed to oxy-fuel flue gas, and the respective Cr K-edge μ-XANES spectra results

The Yallourn ash deposit is even corrosive for the high-Cr tube SUS347 that was exposed under the oxy-firing mode. As evident in ***Figure 8.30***, a portion of Fe is spalled to form a thick spalled layer that is detached from the bulk tube. Some of the Fe even extruded into the ash deposit. Again, Cr forms a thin but protective layer that is still firmly attached to the bulk tube. For the other elements, Ca is originated from Yallourn ash deposit, whereas Mn and Co from the bulk tube are also mixed and present in the spalled layer. In addition, the Cr-S-Ca RGB mapping in ***Figure 8.31*** indicates a probable correlation between Ca and Cr, due to the formation of Ca chromate/chromite. The Cr K-edge energy distribution on the right hand side of ***Figure 8.31*** further indicates the abundance of the energies of 6.009 KeV and 6.012 KeV. This may indicate the co-existence of multiple Cr-bearing species formed from the interaction of Cr and flue gas, and even with the species in the Yallourn ash. The Cr K-edge μ-XANES results in ***Figure 8.31*** proved the co-existence of various strong peaks for Cr. In particular, a small pre-edge peak allocated at 5.992 was also visible for the positions No 0, 1 and 3. It is a clear sign of the formation of Ca chromate that is toxic.

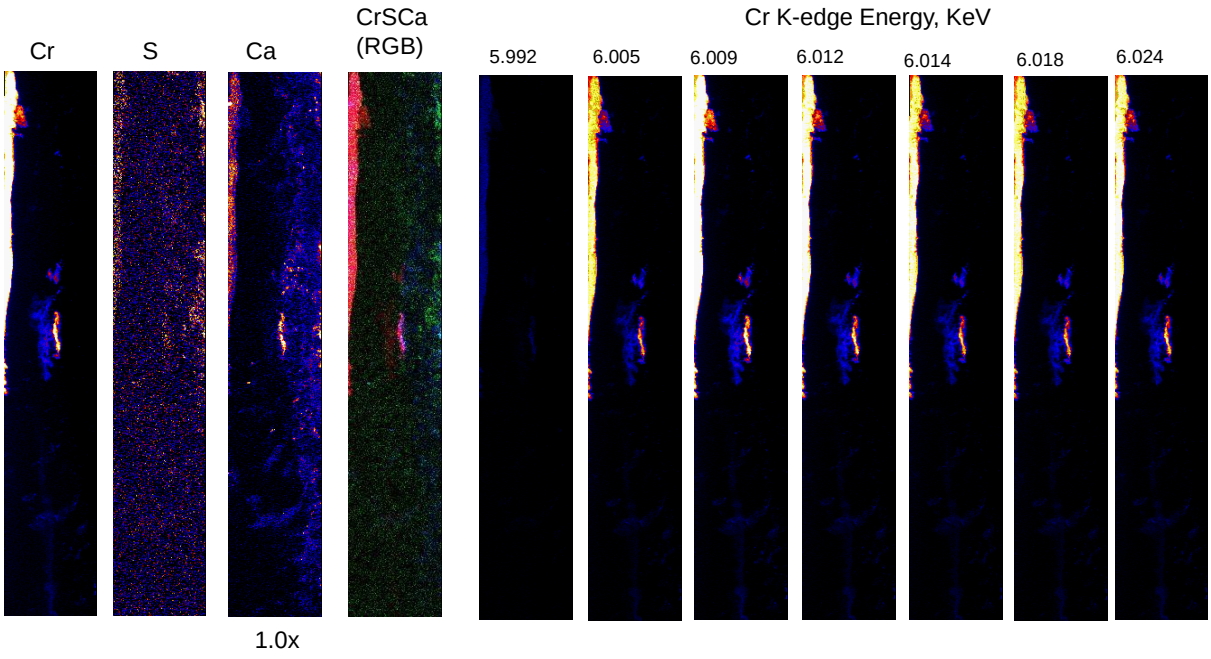

Figure 8.30 RGB mapping for Cr on the tube SUS347 interface and its energy distribution, characterized by synchrotron XFM and μ-XAFES

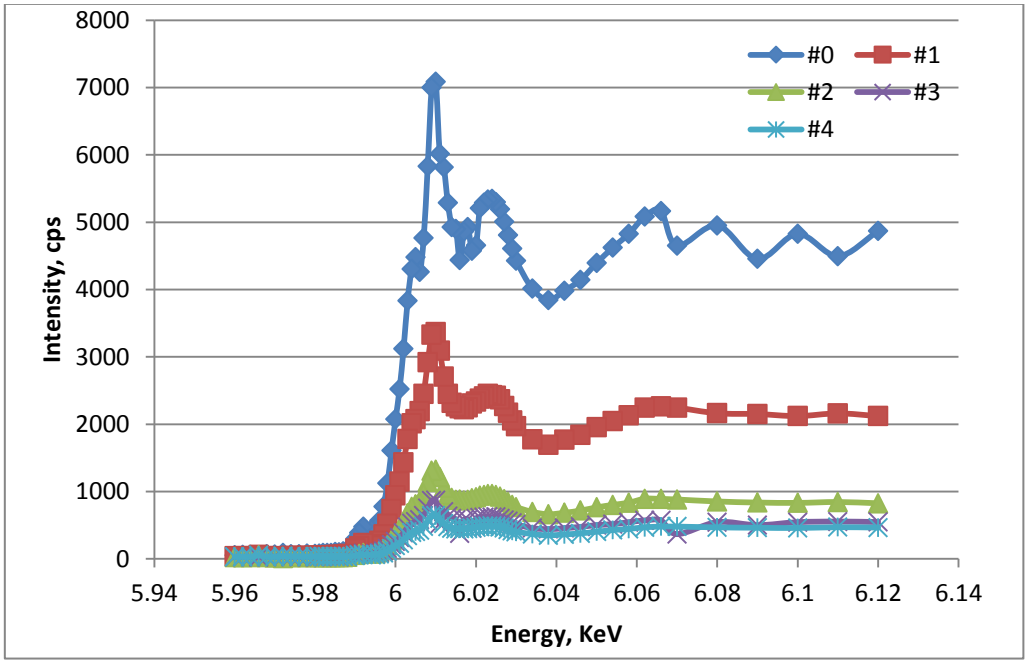

Figure 8.31 Interfaces of the tube SUS347 coated with Yallourn ash deposit and exposed to oxy-fuel flue gas, and the respective Cr K-edge μ-XANES spectra results

8.4 Conclusion

1. For an exposure duration of 50 hrs, the oxy-fuel flue gas shows slightly high corrosion rate for all the tubes exposed under it. The mechanisms for the corrosion of tubes in the oxy-firing flue gas is more complicated. The abundant CO_2 gas in oxy-firing flue gas is not inert, leading to both oxidation reaction and carburisation reaction for both Fe and Cr. In particular, the carburisation reaction extent varied greatly with the Cr content in the tube materials. For the tubes with no Cr (SS400) and low-Cr (12Cr1MoV and T23), the carburisation reaction did not take place. However, for the high-Cr tubes the carburisation reaction is critical.
2. The carburisation reaction for high-Cr tubes mainly takes place in the medium layer that hides behind the top layer. This is due to the extremely low CO_2 partial pressure under the top surface, and the diffusion of C(g) and CO2 through the top layer. With regard to the top layer, it is mainly dominated by oxygen and metallic oxide including ferrite. There is also another layer and even some discrete detects formed behind the medium carburisation-rich layer. This layer and the discrete detects are rich in Cr metal and ferrite that is formed by the diffusion of active oxygen that could be derived from the dissociation of CO_2, O_2 and/or steam.
3. The spallation of tube surface also took place upon the corrosion in oxy-fuel flue gas. For the spalled small pieces, the oxidised Cr was reduced back to the original metallic state, upon the reaction with reducing components including carbon and even hydrogen derived from the dissociation of CO_2 and steam.
4. Compared to Hazelwood fly ash, Yallourn ash deposit is loose and less in amount, due to its high melting point. However, its corrosion effect is comparable with Hazelwood ash deposit. The enrichment of Fe and Na in Yallourn ash caused the considerable corrosion for the SS400 and low-Cr tubes including T23. The use of medium/high-Cr tube material from T91 should be recommended.

9. Overall Conclusions

This three-year research project aimed to understand the new ash – related problems during the oxy-fuel combustion of Victorian brown coals, including sulphation and carbonation rates, the formation rate of SO_3, ash deposition rates and high –temperature tube corrosions. These issues have been examined in lab-scale facilities and/or a $3MW_{th}$ pilot-scale boiler. Apart from experimental investigations, computer modelling based on both thermodynamic equilibrium and kinetics. Additionally, a number of Chinese lignites were studied and compared with Victorian brown coal ashes. Efforts were also made to examine the effect of coal prior washing and the addition of silica on the controlling of ash deposition and tube corrosion.

The key achievements are summarised as follows:

1) Both the sulfation rate and carbonation rate for the Ca-rich Hazelwood fly ash are enhanced under the oxy-fuel combustion mode, due to the preferable formation of calcium sulphate and carbonate. In contrast, these two reactions are less pronounced for the Fe-rich Yallourn fly ash.

2) The formation rate of SO_3 is also highly variable for the different Victorian brown coal fly ashes. For the Ca-rich Hazelwood fly ash, less the SO_3 is formed than calcium sulphate, due to a quick capture of the gaseous S-bearing oxides by the free Ca oxides. The sulphation rate of Ca oxide is preferred and higher temperature and even faster than the carbonation rate. In contrast, the formation of SO_3 is enhanced by the catalytic effect of abundant iron in the Yallourn fly ash.

3) The ash deposition rates for the two Victorian brown coal ashes under the oxy-fuel combustion are higher than their deposition rate under the air-firing mode. For the high-Ca Hazelwood fly ash, the enhanced sulphate is the major reason accelerating its deposition rate under the oxy-fuel combustion mode, whereas the enhanced formation of SO_3 and molten species is believed to the major reason for Yallourn fly ash.

4) For the high-temperature tube corrosion, the solid-state reaction between ash and tube surface is the major reason accelerating the corrosion rate under the oxy-fuel combustion mode. The Ca-rich Hazelwood fly ash is thus more corrosive on tube surface than the Yallourn fly ash. The use of medium and even high – Cr tubes such as T91 is necessary in the oxy-fuel combustion mode.

5) The addition of clay/silica is effective in alleviating the ash deposition rate as well as the high-tube corrosion rate under the oxy-fuel combustion mode. However, its effect is less pronounced than the prior washing/demineralization which reduced the tube corrosion rate to a level close to that of the pure flue gas.

10. Publications

10.1 Published peer-reviewed Journal papers

1. Jabaz I, Zhou S, Zhang L, Jiao F, Yu D, Etschmann B, Ninomiya Y, Paterson D, Spatial distribution of chromium on the corroded tube surface characterized by synchrotron X-ray fluorescence (SXRF) mapping and μ - XANES: co-existence of Ca – rich ash deposits and oxy-firing flue gas, *Fuel Process Technol* 2017, 167: 31-42.
2. Jabaz I, Jiao F, Wu X, Yu D, Ninomiya, Y, Zhang L, Influence of gaseous SO_2 and sulphate – bearing ash deposits on the high – temperature corrosion of heat exchanger tube during oxy-fuel combustion, *Fuel Process Technol* 2017, 167: 193-204.
3. Jabaz I, Chen J, Etschmann B, Ninomiya Y, Zhang L, High-temperature tube corrosion upon the interaction with Victorian brown coal fly ash under the oxy-fuel combustion condition, *Proceedings of the Combustion Institute*, 2017, DOI: 10.1016/j.proci.2016.08.076.
4. Jabaz I, Chen J, Etschmann B, Ninomiya Y, Zhang L, Effect of silica additive on the high-temperature fireside tube corrosion during the air-firing and oxy-firing of lignite (Xinjiang coal) – Characteristics of bulk and cross-sectional surfaces for the tubes, *Fuel* 2017, 187: 68-83.
5. De Girolamo A, Grufas A, Lyamin I, Nishio I, Ninomiya Y, Zhang L, Ignitability and combustibility of Yallourn pyrolysis char blended with pulverized coal injection coal under simulated blast furnace conditions, *Energy Fuels* 2016, 30(3), 1858-1868.
6. Prationo W, Zhang L, Influence of steam on ignition of Victorian brown coal particle stream in oxy-fuel combustion: in-situ diagnosis and transient ignition modelling, *Fuel* 2016, 181, 1203-1213.
7. Wu X, Zhang X, Yan K, Chen N, Zhang J, Xu X, Dai BQ, Zhang J, Zhang L, Ash deposition and slagging behavior of Chinese Xinjiang high-alkali coal in 3 MW_{th} pilot-scale combustion test, *Fuel* 2016, 181, 1191-1202.
8. Prationo W, Zhang J, Cui J, Wang Y, Zhang L, Influence of inherent moisture on the ignition and combustion of wet Victorian brown coal in air-firing and oxy-fuel modes: Part 1: The volatile ignition and flame propagation, *Fuel Proc Technol* 2015, 138, 670-679.
9. Prationo W, Zhang J, Cui J, Wang Y, Zhang L, Influence of inherent moisture on the ignition and combustion of wet Victorian brown coal in air-firing and oxy-fuel modes: Part 2: Contribution of gasification reaction to char oxidation rate, *Fuel Proc Technol* 2015, 138, 680-686.

10. Li X, Wu Z, Zhang L, Liu X, Zhu X et al, An updated acid dew point temperature estimation method for air-firing and oxy-fuel combustion processes, *Fuel Process Technol* 2016, DOI: 10.1016/fuproc.2016.08.033.

10.2 Submitted peer-reviewed journal papers:

11. De Girolamo A, Tan V and Zhang L, Pyrolysis of lignite briquette – experimental investigation and 1 – dimensional modelling approach, Submitted to *Fuel*, April 2017.
12. Wu X, Ji HS, Dai BQ, Zhang L, Lignite ash slagging and flow under the weak reducing environment at 1300oC – establishment of a new slag flow index for basic ashes, Submitted to *Fuel* in July 2017.
13. Ji HS, Wu XJ, Dai BQ, Zhang L, Lignite ash slagging and flow under the weak reducing environment at 1300oC – release of sodium out of slag and its modelling from the mass transfer perspective, Submitted to *Fuel* in July 2017.
14. Jabaz I, Zhou S, Estchmann B, Paterson D, Ninomiya Y, Zhang L, Spatial distribution of Cr – bearing species on the corroded tube surface characterised by synchrotron X – ray fluorescence (SXRF) mapping and μ - XANES: exposure of tubes in oxy-firing flue gas, Submitted to *Corrosion Science* in June 2017.

10.3 Conference papers

15. Jabaz I, Zhang L, Synergism between Gaseous SO_2 and Lignite Ash Deposit on the High-Temperature Tube Corrosion during Oxy-Fuel Combustion – A Case Study of Tubes Coated with Lignite Ash Deposits, Chemeca 2017, Melbourne July 23-26, 2017.
16. De Girolamo A, Liu Z, Zhang L, Pyrolysis of Lignite Briquette – Sensitivity of the Reactivity and Physical structure upon the Variation in Pyrolysis Condition, the 6th Sino – Australian Symposium on Advanced Coal and Biomass Utilisation Technologies, 4-8 Dec 2017, Perth, Western Australia.
17. Zhang L, Jabaz I, Estchmann B, Ninomiya Y, High-temperature tube corrosion upon ash deposition during oxy-firing of Victorian brown coal, Proceedings of the 2016 Chemeca, Sept 25-28, Adelaide, Australia.

18. De Girolamo A, Grufas A, Laymann I, Zhang L, Ignitability and Combustibility of Yallourn pyrolysis semi-coke blended with PCI coal in the simulated blast furnace conditions, Proceedings of the 2015 Australian Comb Symp, Dec 6-9, 2015, Melbourne.
19. Prationo W, Zhang L, Influence of external steam on Victorian brown coal ignition, Proceedings in the 8th International Symposium on Coal Combustion, July 19-25 2015, Beijing, China.
20. Chen J, Suzuki K, Zhang X, Wu XJ, Zhang L, Ninomiya Y, Hot corrosion test of tube materials in brown coal oxy-fuel combustion atmosphere, Proceedings in the 8th International Symposium on Coal Combustion, July 19-25 2015, Beijing, China.
21. De Girolamo A, Lameu N, Zhang J, Zhang L, Ignitability and Combustibility of Yallourn pyrolysis semi-coke in the simulated blast furnace conditions, Proceedings in the 8th International Symposium on Coal Combustion, July 19-25 2015, Beijing, China.
22. Zhang L, Wu XJ, Dai BQ, Using silica-based additive for Xinjiang coal ash slagging and fouling control – what we have learnt through industrial applications, Proceedings in the 8th International Symposium on Coal Combustion, July 19-25 2015, Beijing, China.

Appendix: Ash formation code in Fortran

```
      PROGRAM Fly ash

      IMPLICIT DOUBLE PRECISION(A-H, O-Z)

      CHARACTER FILE*60, NAME*24,pname*24,pcname*24

      CHARACTER*24 CSTFILE, OUTFILE, SUBFILE

      DIMENSION GRIN(100), STOI(100), GRINS(100,100)

      CHARACTER*24 NAMES(100),CNAMES(100,100),TRGTNAMES(100)

      REAL*8 VALUES(100),CVALUES(100,100),GVALUES(100,100)

      REAL*8 MOLS(100),CSUM,TRGTVALUES(100,100)

      INTEGER NOERR, INDEXS,J,I,NC,NPHASE,NPCON,NCOUNT,NTEMP,MC,
     &  NTEMPS(100),NPHASES(100),NPCONS(100),NTRGT,IC,jj

      REAL*8 T,VALUE,GASVALUES(800),ASYS,AGAS,TMAX,TMIN,DT


C READ DATA

      OPEN (UNIT=5, FILE='INPUT21.TXT')


      READ (5,*) OUTFILE,SUBFILE,CSTFILE

      CSTFILE=TRIM (CSTFILE)

      OUTFILE=TRIM(OUTFILE)

      SUBFILE=TRIM(SUBFILE)

C MCOUNT=Number of Cal. between TMIN and TMAX

      READ (5,*) TMAX,TMIN,DT,NCOUNT

C GAS Constituents mol,  Solid Constituents  gram(wt%)
```

```
      READ (5,*) (NAMES(J),VALUES(J),J=1,NCOUNT)
      READ (5,*) NTRGT
      READ (5,*) (TRGTNAMES(J),J=1,NTRGT)
      WRITE(11,*)TMAX,TMIN,DT,NCOUNT
      WRITE(11,*)(J,NAMES(J),VALUES(J),J=1,NCOUNT)
      OPEN (UNIT=11, FILE=OUTFILE)
      OPEN (UNIT=6, FILE=SUBFILE)

C
C Initialize, read the FactSage data-file, change default units
C
C Initialise ChemApp
     CALL TQINI(NOERR)

C Open transparent data-file for reading.
C      CALL TQOPNT('Yutakasa1.cst', 10, NOERR)
       CALL TQOPNT(CSTFILE,10,NOERR)
C Read data-file
     CALL TQRCST(NOERR)

C Close data-file
     CALL TQCLOS(10, NOERR)
C Since we are going to use degrees Celsius as temperature unit
```

```
C throughout the calculations, we will change the unit now
      CALL TQCSU('Temperature ', 'C ', NOERR)


       CALL TQCSU('T ','C ',NOERR)
       CALL TQCSU('A ', 'gram ',NOERR)
C


C Get the number of system comporlents and phases in the data-file. Names
C of system components are those in the data-file.


       CALL TQNOSC (NC,NOERR)
       CALL TQSHOW(NOERR)
       CALL TQNOP (NPHASE,NOERR)
       DO J=1,NC
       CALL TQINSC (NAMES(J), INDEXS,NOERR)
       GRIN(INDEXS) = VALUES(J)
       ENDDO


       T = TMAX
       WRITE (11,*) ' '
C
C At each stage, define the input conditions, calculate chemical equilib-
C ritm, and print the masses of the condensed phases formed (the gas phase
```

```
C is always phase No. 1)
C
      MC=INT((TMAX-TMIN)/DT+1)
      CSUM=0.
      DO K = 1,MC
      NTEMP=TMAX-(K-1)*DT
      T=NTEMP
      NTEMPS(K)=NTEMP
C      WRITE (11,1010) NTEMP
C 1010 FORMAT( ' Temperature/C =' ,I8//'Incoming weights/gram: ' )
      CALL TQSETC( 'T ' ,0,0,T,NUMBER,NOERR)
      DO J=1,NC
      CALL TQSETC( 'IA ' ,0,J,GRIN(J) ,mBER,NOERR)
      CALL TQGNSC (J,NAME,NOERR)
      GRINS(J,K)=GRIN(J)
      NAMES(J)=NAME
C      WRITE (11,1020) NAME, GRIN(J)
C 1020 FORMAT(1X, A, 1X, 1PE12.5)
      ENDDO

      CALL TQCEL(' ',0,0,0,NOERR)
C First, get the equilibrium amount of the gas phase, which is the only
C mixture phase in the system. Note that since we did not change any
```

```
C units, the default amount unit (mol) is used.
      CALL TQCSU('A ', 'MOL ',NOERR)
     CALL TQGETR('A ', 1, 0, AGAS, NOERR)
      MOLS(K)=AGAS
C      WRITE(11,FMT='(A,G12.5)') 'Equilibrium amount of gas phase (mol):'
C     *   , AGAS
C To determine the mole fraction of the gas phase, relative to the whole
C system, we first need to get the amount contained in the system
     CALL TQGETR('A ', 0, 0, ASYS, NOERR)

C      WRITE(*,FMT='(A,G12.5)') 'Mole fraction of the gas phase: ',
C     *     AGAS/ASYS

     CALL TQGETR('A ', 1, -1, GASVALUES, NOERR)
C Print the equilibrium amount of each phase constituent
     CALL TQNOPC(1, NPCON, NOERR)
C      WRITE(11,*) 'Mol fraction of gas phase constituents'
      NPCONS(K)=NPCON
      DO J=1,NTRGT
           DO I=1, NPCON
              CALL TQGNPC(1, I, NAME, NOERR)
                 IF (TRIM(NAME) .EQ. TRIM(TRGTNAMES(J))) THEN
                 GVALUES(J,K)=GASVALUES(I)
```

```
                    ENDIF
                ENDDO
C         IF (GASVALUES(I)/AGAS .GT. 1.E-9) THEN
C         WRITE(11,FMT='(I4,A,G12.5,A)') I, ' : ' // NAME,
C     *       GASVALUES(I)/AGAS

      ENDDO

C       WRITE(11,*)     ' Condensed phases formed:'
        CALL TQCSU('A ', 'gram ',NOERR)
        IC=0
      DO I=2, NPHASE
      CALL TQGETR('A ', I,1,VALUE,NOERR)
      IF (VALUE .GT.0.D0) THEN
        CALL TQGNPC(I,1,NAME,NOERR)
        IC=IC+1
        CNAMES(IC,K)=NAME
        CVALUES(IC,K)=VALUE
        CSUM=CSUM+VALUE
C       WRITE(11,*) i,NAME,',',VALUE
        NPHASES(K)=IC
        ENDIF
        ENDDO
```

```
C
C       Remove amounts which correspond to precipitated species and calculate
C     new incoming weights
C
      CALL TQCSU('A ','mol ', NOERR)
      CALL TQGETR('A ', 0, -1, GRIN, NOERR)
c***
c*     CALL TQSTPC(2,1,STOI,WMASS,NOERR)
c*      WRITE(*,*) 2, PCNAME, (STOI(jj),jj=1,nc),  WMASS
c*     do j=1,nc
c*
c*     CALL TQGNPC(2, j, PCNAME, NOERR)
c*       CALL TQGETR('a ',2, j, VAL, NOERR)
c*            CALL TQSTPC(2,j,STOI,WMASS,NOERR)
c *      write (*,*) j,pcname,val
c*     WRITE(*,*) 2, PCNAME, (STOI(jj),jj=1,nc),  WMASS
c*     enddo
c*********

      DO I=2, NPHASE
      CALL TQGETR('A ', I, 1, VALUE, NOERR)
      IF(VALUE .GT. 0.D0) THEN
```

```
c***
c*       CALL TQGNP(I, PNAME, NOERR)
c*      write(*,*) 'Pname(1)=',pname
c***
        DO J=1,NC
        CALL TQSTPC(I,1,STOI,WMASS,NOERR)
        GRIN(J)=GRIN(J)-STOI(J)*VALUE
        ENDDO
        ENDIF
        ENDDO
        CALL TQCSU('A ','GRAM ',NOERR)
        DO J=1,NC
        CALL TQSTSC(J, STOI, WMASS, NOERR)
        GRIN(J)=WMASS*GRIN(J)
        ENDDO
c**     T=NTEMP-100
        ENDDO

C Incoming weights/gram:
        WRITE(11,*)
        WRITE(11,*)'Incoming weights/gram: '
        WRITE (11,1040)(NTEMPS(J),J=1,MC)
        DO I=1,NC
```

```
      WRITE(11,1010) NAMES(I),(GRINS(I,J),J=1,MC)
      ENDDO

      WRITE(11,*)
      WRITE(11,*)'Incoming weight fraction: '
      WRITE (11,1040) (NTEMPS(J),J=1,MC)
 1040 FORMAT(1H ,'Temp',100(',',I7))
      DO I=1,NC
      WRITE(11,1010) NAMES(I),(GRINS(I,J)/GRINS(I,1),J=1,MC)
      ENDDO
 1010 FORMAT (A,100(',',1PE12.5))

C ***Gas phase constituents
      WRITE(11,*)
     WRITE(11,*) 'Mol of gas phase constituents'
      WRITE (11,1040) (NTEMPS(J),J=1,MC)
      DO I=1,NTRGT
      WRITE(11,1010) TRGTNAMES(I),(GVALUES(I,J),J=1,MC)
      ENDDO

      WRITE(11,*)
      WRITE(11,*) 'Mol fraction of gas phase constituents'
      WRITE (11,1040)(NTEMPS(J),J=1,MC)
```

```
      DO I=1,NTRGT
      WRITE(11,1010) TRGTNAMES(I),(GVALUES(I,J)/MOLS(J),J=1,MC)
      ENDDO
C Condensed phases
      WRITE(11,*)
      WRITE(11,*)'Condensed phases formed:',',','gram',',','Wt fraction'
      DO J=1,MC
      WRITE(11,*) NTEMPS(J)
      DO I=1,NPHASES(J)
      WRITE(11,1020) CNAMES(I,J),CVALUES(I,J),CVALUES(I,J)/CSUM
 1020 FORMAT(1H ,',',A,2(',',1PE12.5))
      ENDDO
      ENDDO

     IF (NTEMP .EQ.INT(TMIN)) STOP ' '
      END
```